UTS UNIVERSITY OF TECHNOLOGY SYDNEY

The hydration, thermodynamic modelling, mechanical properties, and microstructure of Portland cement in seawater

by Peiran Li

Thesis submitted in fulfilment of the requirements for the degree of

DOCTOR OF PHILOSOPHY

Under the supervision of

Principal supervisor: Dr Wengui Li
Co-supervisor: Professor John Zhou

University of Technology Sydney
Faculty of Engineering and Information Technology

January 2023

CERTIFICATE OF ORIGINAL AUTHORSHIP

I, ***Peiran Li***, declare that this thesis is submitted in fulfilment of the requirements for the award of Doctor of Philosophy, in the School of Civil and Environmental Engineering, Faculty of Engineering and Information Technology at the University of Technology Sydney.

This thesis is wholly my own work unless otherwise referenced or acknowledged. In addition, I certify that all information sources and literature used are indicated in the thesis.

This document has not been submitted for qualifications at any other academic institution.

This research is supported by the Australian Government Research Training Program.

Signature: Production Note:
Signature removed prior to publication.

Date: 30/12/2022

ACKNOWLEDGEMENTS

The research plan of this thesis is initially inclined to study more about the mechanical properties, durability, and performance improvement of seawater concrete. However, a 2-year stuck overseas significantly disrupted the experimental plan due to the covid-19 pandemic. I had to rove around and find available labs to continue the experiment, and therefore, the research plan was changed and tended to the simulation and mechanism study.

I would like to thank Dr Wengui Li, my supervisor, for recognising my research plan and providing guidance for experiments and papers.

I would like to thank UTS Mortar and Concrete lab, UTS Science, UTS Environmental Lab and UTS workshop for providing the facilities and equipment. I would also like to thank Mr Rami Haddad, Muller Hailu, Herbert Yuan, Mohammed. Johir and Miss Ann Yan for providing professional technical assistance.

I would like to thank Zhuo Tang for providing great support for my continued experimental study when I was trapped overseas.

I would like to thank my schoolmates from UTS for making my PhD life colourful and memorable.

I am extremely grateful to my parents for their unconditional love and support.

Lastly, I would like to thank my wife for always accompanying, comforting and supporting me during the hardest lifetime

Completing a PhD journey is never a solitary effort, but sometimes, I have to face the deepest loneliness myself from an obsession with constantly pursuing the truth. Most of the time, I obtain a sense of frustration rather than satisfaction, but I do not regret my

choice. If possible, in the future, I want to keep this original intention forever as a romance researcher.

LIST OF PUBLICATIONS

Li, P., Gao, X., Wang, K., Tam, V.W. & Li, W. 2020, 'Hydration mechanism and early frost resistance of calcium sulfoaluminate cement concrete', *Construction and Building Materials*, vol. 239, p. 117862.

Li, P., Li, W., Sun, Z., Shen, L. & Sheng, D. 2021, 'Development of sustainable concrete incorporating seawater: A critical review on cement hydration, microstructure and mechanical strength', *Cement and Concrete Composites*, vol. 121, p. 104100.

Li, P., Li, W., Yu, T., Qu, F. & Tam, V.W. 2020, 'Investigation on early-age hydration, mechanical properties and microstructure of seawater sea sand cement mortar', *Construction and Building Materials*, vol. 249, p. 118776.

Li, P., Li, W., 'Hydration of Portland cement with seawater toward concrete sustainability: Phases evolution and thermodynamic modelling', *Cement and Concrete Composites*, vol. 138, p. 105007.

Li, P., Li, W. ' Portland cement hydrated with seawater: Phase evolution quantified by SED-EDS image analysis' (under the review of *Construction and Building Materials*).

TABLE OF CONTENTS

LIST OF FIGURES

LIST OF TABLES

LIST OF ACRONYMS

ASTM	American Society for Testing and Materials
BFS	Blast furnace slag
BSE	Backscattered Electron
CMT	Chloride migration test
DSC	Differential scanning calorimetry
DTG	Derivative Thermogravimetry
DW	Deionized water
EDS	Energy Dispersive-X-ray Analysis
FA	Fly ash
FW	Freshwater
FWC	Freshwater concrete
ICP-OES	Inductively coupled plasma-optical emission spectrometry
LDH	Layered double hydroxides
MK	Metakaolin
OPC	Ordinary Portland cement
PC	Portland cement
RCPT	rapid chloride permeability test
ROI	Region of interest

RGB	Red, Green and Blue
R-sand	River sand
SCMs	Supplementary cementitious materials
SE	Secondary electron
SF	Silica fume
SLIC	Simple linear iterative clustering
S-sand	Sea sand
SW	Seawater
SWC	Seawater concrete
TG	Thermogravimetry
TGA	Thermogravimetry Analysis
WAT	Water absorption test
w/b	Water to binder ratio
XRD	X-ray diffraction
XRF	X-ray Fluorescence

Cement chemistry

AFm	Aluminate-ferrite-mono
AFt	Ettringite
$[Al(OH)_6]^3$	Aluminate ion

Al_2O_3	Alumina
CC	Calcite
Ca^{2+}	Calcium ions
CaO	Calcium oxide
CAOXY	Calcium oxychloride
C-A-S-H	Calcium aluminium silicon hydrate
Carbo-AFm	monocarboaluminate
C_4AF	Ferrite
C_3A	Aluminate
CH	Calcium hydroxide ($Ca(OH)_2$)
CO_3^{2-}	Carbonate
CO_2	Carbon dioxide
C_2S	Belite
C_3S	Alite
C-S-H	Calcium silicate hydrates
Cl	Chloride
Cl^-	Chloride ions
Fe_2O_3	Ferric oxide
FS	Friedel's salt

G	Gypsum
HNO_3	Nitric acid
K^+	Potassium ion
K_2O	Potassium oxide
KS	Kuzel's salt
MAOXY	Magnesium oxychloride
MgO	Magnesium Oxide
M-S-H	Magnesium Silicate Hydrate
MK	Metakaolin
Na^+	Sodium ion
Na_2O	Sodium oxide
OH^-	Hydroxy ion
P	Portlandite
SiO_4^{4-}	Silicate
SiO_2	Silicon dioxide
SO_3	Sulfur trioxide
$SO4^{2-}$	Sulfate
sulfo-AFm	Monosulfoaluminate
TiO_2	Titanium dioxide

ABSTRACT

Many countries are experiencing freshwater crises due to population growth and infrastructure construction aligned with the enormous freshwater demand. Using seawater (SW) for concrete manufacturing promisingly provides significant economic and environmental benefits, particularly in coastal areas where SW is more accessible. However, the dissolved chemical ions may significantly limit the scope of its application.

In pursuit of a fundamental understanding of SW's impact on the heterogeneous cementitious material structure and mechanical properties, a series of experimental and modelling studies for the hydration performance of Portland cement in SW was investigated in this thesis. Phase identification of the solid and liquid phases was performed by combining thermogravimetry, X-ray diffraction and inductively coupled plasma optical emission spectrometry technology. The Rietveld refinement approach has been adopted to characterize phase evolution quantitatively, which forms an experimental validation as a reference to develop kinetics modelling for cement hydration with SW. By combining the optimized kinetic and thermodynamic equilibrium models, the simulation and experiment results of hydrate phases achieve a good agreement. The use of SW not only increases the hydration rate of clinker significantly but also affects the evolution of phase assemblage. Both thermodynamic calculations and experimental determinations confirmed that Friedel's salt (FS) forms instead of sulfo-AFm in hydrated cement by SW. Additionally, The formation of FS indirectly stabilized the ettringite (AFt) due to the higher concentration of sulfate from the conversion of sulfo-AFm.

Based on the characteristics of cement hydration in SW, the practical study of cement mortar with natural SW and sea sand was carried out. Macroscopic properties were also investigated, including heat evolution, compressive strength, and flexural strength. Although SW increases the early strength by its stimulating effect on cement hydration, the slightly lower compressive strength at the late stage may be due to the additional unhydrated cement and pores.

The secondary electron and backscattered electron imaging technology were adopted to characterize the microstructure of cement paste. By combining SE and BSE images, The area for pores in the microstructure can be accurately segmented with lower data errors. Quantifying hydrated and unhydrated phases was performed by EDS mapping after the data processing of denoising, region segmentation, manual identification, and imaging calibration. The comparison between multiple results shows that the detailed distribution of the phases can be obtained with low data error. Therefore, it is feasible and promising to use EDS mapping to quantify the various cement phases for submicroscopic and microscopic characterization.

Keywords: Seawater; Cement hydration; phase quantification; Thermodynamic modelling; Microstructure characterization; Pore; Compressive strength

CHAPTER 1. INTRODUCTION

1.1 Background

With the world hurtling toward the urban future accompanying increased demand for infrastructure, concrete production has experienced unprecedented large-scale popularity worldwide (Doyle & Havlick 2009; Monteiro, Miller & Horvath 2017). Meanwhile, the tremendous amount of concrete production results in enormous greenhouse gas emissions (Miller & Moore 2020) and massive consumption of freshwater (FW), minerals, and energy (Dhondy, Remennikov & Shiekh 2019) (Malhotra 1999; Mehta 1999). It has been reported that in 2012, over two gigatons of FW was consumed only used as mixing water in concrete production (Miller, Horvath & Monteiro 2016), while there could be ten times more FW involved during the whole manufacturing process if the water for cooling, washing, energy, and transportation is considered (Miller, Horvath & Monteiro 2018). The unsustainability induced by such considerable resource consumption inevitably drives the revolution of the concrete industry (Dong et al. 2019; Mehta 2001; Mehta 2002, 2009; Peduzzi 2014; Sutherland et al. 2017; Torres et al. 2017; Truc & Van Vu 2018). In some island and coastal regions with limited access to FW, long-distance water transportation may significantly aggreviate the cost and energy consumption. Therefore, seawater (SW) is recommended as an alternative to FW for concrete mixing. While in practice, the presence of chloride ions in SW can render severe corrosion in reinforced concrete and subsequently cause

deterioration, limiting the practical implementation. Therefore, appropriate measures are needed in concrete mixtures to alleviate adverse effects of using SW directly.

Although studies in this area have been elaborated and progressed significantly, divergent opinions still exist against using SW as mixing water (Nishida et al. 2015; Otsuki et al. 2014). Otsuki (1985) has proposed that the negative effect induced by SW mixing decreases with age. Therefore a comparable long-term performance can be presented in seawater concrete (SWC) (Japan Concrete Institute 2015). While Neville (2001) pointed out that using SW may cause significant safety issues, such as chloride corrosion that requires careful consideration. In addition, other chemical compositions in SW, such as sulfate and magnesium, may also affect the concrete mechanism properties and durability (Cai et al. 2021; Frias et al. 2013; Mohammed, Hamada & Yamaji 2004; Wang, Liu & Li 2018; Wang et al. 2020) (Khatibmasjedi 2018).

However, the adverse effects do not hinder the application prospect of SW as concrete mixing water. Chloride corrosion can be avoided in plain concrete or those incorporated with noncorrosive reinforcement bars (Sena-Cruz et al. 2018) (Ahmed et al. 2020). Considering the possible environmental interest and economic benefits (Younis, Ebead & Judd 2018), using SW as mixing water for concrete has been a hot topic since 2010.

1.2 Research significance

In order to safely use SW for concrete manufacturing, issues should be first solved on physicomechanical performance, durability reduction, and rebar corrosion from excess

chloride ions (Erdoğdu, Bremner & Kondratova 2001). Investigations found that concrete using SW can cause a 20% reduction in initial slump flow and a nearly 30% loss in initial setting time, compared with concrete using FW (1990; Younis et al. 2018). Meanwhile, SW increases the early strength of concrete by 10–25% within 14 days (Bachtiar et al. 2015b; Ghorab, Hilal & Antar 1990; Nishida et al. 2013; 2010; Younis et al. 2018). The drying shrinkage of SWC is approximately 15% lower than that of concrete with FW (Katano et al. 2013b). Some studies even proposed that using SW does not undermine the concrete microstructure but improves the mechanical performance. For example, studies have found that SW increases the density, compressive strength, and elastic modulus (Etxeberria, Fernandez & Limeira 2016; Etxeberria, Gonzalez-Corominas & Pardo 2016; Li, Zhao & Raman 2018; Wegian 2010; Younis et al. 2018). However, options are divided for using SW when it comes to advanced strength development at the late stage, such as a 13% lower 28-day compressive strength (Kaushik & Islam 1995), a one-year superiority of compressive strength for using SW (Ghorab, Hilal & Antar 1990), and a comparable strength determined to FWC (Islam et al. 2012b; Younis et al. 2018). Furthermore, safety risks cannot still be eliminated from the rebar corrosion and undetermined durability issues.

Therefore, in terms of improving the performance of SWC purposefully and realistically, a fundamental study of SW's impact on the heterogeneous cementitious material structure and mechanical properties is needed. The study is expected to address the

current controversy effectively and guide the future application of SW as a building material.

1.3 Research objectives

Along the above lines, the specific objectives of this study are divided into four parts, which will discuss the following issues in separate sections:

(1) To fundamentally study the effect of SW on cement application, the first section studies the hydration of cement with SW by combining TG, XRD and ICO-OES technology. The Rietveld refinement approach is used to characterize the phase evolution quantitatively and obtain an experimental validation as a reference to develop kinetics modelling for cement hydration with SW.

(2) The second section focuses on the simulation of the hydration process of PC with SW, expected to predict the evolution of phase assemblage of the hydration system. The kinetic clinker dissolution model is optimized for SW hydration based on the experimental quantitative results and thermodynamic model. The simulation evaluates the evolution of various phases of assemblage and pore solution by combining the thermodynamic and modified kinetic models. The quantitative simulation results are also evaluated by experimental results of hydration products.

(3) The third section mainly discusses the property differences between OPC with SW and DW in combination with the hydration characteristics, such as heat evolution of hydration, phase evolution, compressive and tensile strength, and pore structure

development. The applicability of cement mortar with natural sea sand (SS) is also evaluated.

(4) This section deeply investigates and compares the microstructure of cement paste with SW and DW by combining SE and BSE imaging technology. EDS elemental mapping technology is used to quantify the phase based on the stoichiometric, to study and develop the microscopic quantitative characterization method. The multiple quantitative results and perform statistical analyses from different characterizing methods are evaluated and discussed.

CHAPTER 2. LITERATURE REVIEW

This section reviews current and previous studies on the predominant performance differences between SW-mixed and conventional concretes. Particular attention has been paid to the chloride-induced hydration mechanism to provide a scientific and unbiased foundation for an in-depth insight into SW's applicability in concrete manufacturing. Through evaluating both the benefits and limitations of SW mixtures, this work hopes to guide the safer use of SW as a construction material.

2.1 Properties of cement composite with seawater

Due to the long-term transfer from rainwater to the ocean, a great number of alkaline minerals are migrated constantly from the inland rock stratum to SW. The salinity varies in different marine regions that, for instance, the North Sea has a salinity of 3.3%, the Red Sea has that of 4%, while the Baltic Sea has only 0.7% (Neville 2001). The main ions concentration of SW in various marine regions are shown in Table 2.1. Typically, SW has a total salinity of 3.5%, which mainly consists of chloride, sodium, magnesium, sulphate, etc. The concentration of predominant components needed in FW to prepare substitute SW is specified in ASTM D1141-98 (see Table 2.1). In this section, a comprehensive review is provided to summarize the advanced progress of SW-mixed cement composite, followed by a detailed illustration of the mechanisms.

Table 2.1. Concentration of the main ions in SW from various seas

Conc. [mg/l]	Cl^-	Na^{2+}	SO_4^{2-}	Mg^{2+}	Ca^{2+}	K^+	pH	Reference

South China Sea	33400	21700	3840	1040	579	417	7.8	(Li et al. 2019)
Arabian Gulf	26000	15000	3700	2300	500	520	8.2	(Wang, Liu & Li 2018; Younis et al. 2018)
Red Sea	22660	11350	3051	1867	531	1350	–*	(Hamad et al. 2013)
Mediterranean Sea	20800	11640	2820	1360	490	420	8.0	(Etxeberria, Fernandez & Limeira 2016; Fritzmann et al. 2007)
Melbourne	20700	11940	3420	1430	–*	622	–*	(Li et al. 2016)
Norway Sea	19420	9460	2583	1130	351	348	–*	(De Weerdt, Lothenbach & Geiker 2019)
Yellow Sea	19360	10780	2702	1297	408	388	–*	(Yu, Wu & Yang 2017)
Atlantic Sea	19920	10735	2697	1416	424	380	–*	(Montanari et al. 2019)
North Sea	16550	12200	2220	1110	430	500	–*	(Yeginobali 1984)
Marmara Sea	14390	8100	2034	1035	328	340	7.9	(Browne R. D. & Baker A. F. (1979))
Black Sea	9500	4900	1362	640	236	230	7.4	(Browne R. D. & Baker A. F. (1979))
Baltic Sea	3000	1800	410	240	98	67	–*	(Cwirzen, Sztermen & Habermehl-Cwirzen 2014)
ASTM D1141-98	19437	10833	2769	1292	419	398	7	(D-98 2008)

*Not reported

2.1.1 Hydration kinetics

The exotherm from clinker dissolution changes significantly when mixed with SW, in particular, at the early stage. As proposed in the existing literature, a consensus has been

suggested that SW increases the heat flow rate due to the enhanced kinetics of hydration (Guo et al. 2020; Khatibmasjedi et al. 2019; Sikora, Cendrowski, Abd Elrahman, et al. 2019; Younis et al. 2018). In SW mixtures, the accelerated hydration is mainly dominated by the abundant chloride ions (Montanari et al. 2019), which dramatically promotes the hydration of C_3S and C_3A (Li, Li, et al. 2020b). The other ions in SW also affect the cement hydration, such as sulfate, magnesium, and calcium (Farnam, Wiese, et al. 2015; Wang, Liu & Li 2018). The specific effects of these ions on cement hydration will be discussed in Section 3. Based on the aforementioned studies, in general, the exothermic peak of SW mix presents 35–40% higher and occurs approximately 17 – 30% earlier, compared to conventional concrete.

Furthermore, Younis *et al*. (2018) found that the cumulative heat from SW mixtures is higher at an early age, while it becomes almost identical to that of FW mixtures after 7 days. It seems that the heat of cement hydration in SW is released in advance, subsequently being caught up by FW mixtures. The exothermic feature in SW mix is very well accordant with the characteristic of compressive strength growth, which both are dominated by cement hydration. Therefore, Wang *et al.* (Wang, Liu & Li 2018) stated that SW mixing increases the total heat of hydration seems questionable. Besides, differences are also found in the clinkers hydrated in SW. Li *et al*. (Li, Li, et al. 2020b) reported that an increasing water/binder (w/b) ratio in SW mixtures does not further stimulate the dissolution of C_3S, while the dissolution of C_3A is observed to be promoted (see Figure 2.1). The inconsistent results show that the hydration of C_3S is

enhanced by raising the concentration of the influential ions, not by increasing their total content. While as for C_3A, the hydration can simply be promoted by adding more SW-related ions. The results brings the following conclusion that during the accelerating hydration period, some special hydration products were formed by the reaction of C_3A and some ions in SW, for instance, the FS (Friedel 1897). However, the degree of stimulated hydration C_3S by SW is limited in a certain range.

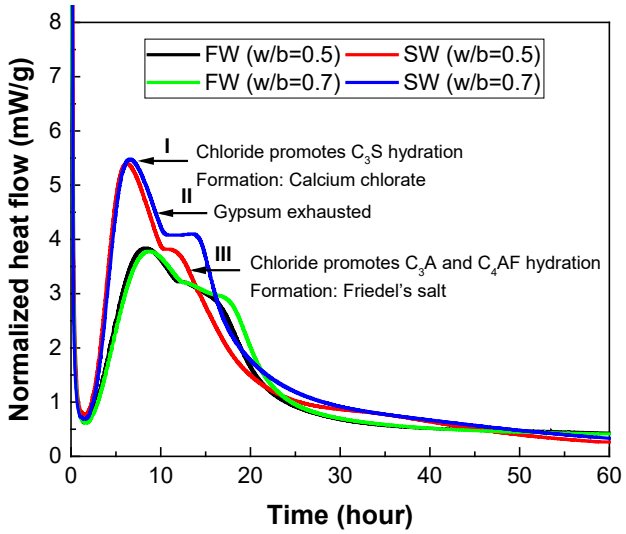

(a) Heat flow of hydration (Li, Li, et al. 2020b)

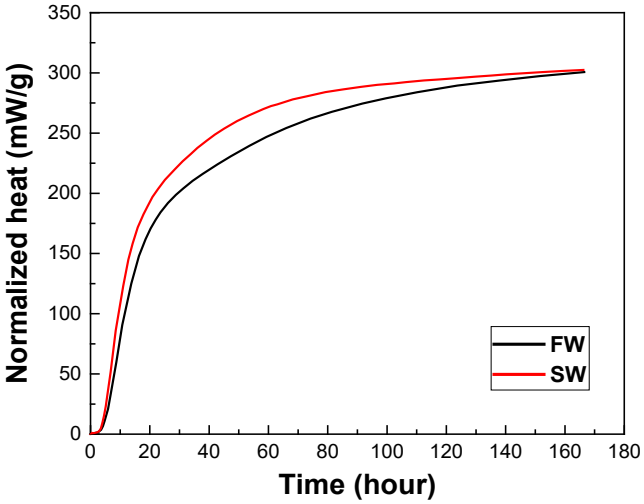

(b) Cumulative heat of hydration (Younis et al. 2018)

Figure 2.1. Heat evolution of OPC hydrated in FW and SW

2.1.2 Fresh properties

It is well understood that in a cast-in-situ construction, the fresh properties of concrete are required to be tested at the time of placement. As a critical evaluating indicator, slump value is widely applied to characterize the workability of fresh concrete. Generally, a higher slump represents better workability, assuming that there is no segregation occurs. Regarding SW-mixed concrete, a consensus has been proposed among the existing studies that SW mixtures presented a higher cohesive, viscous, and compact behaviour, compared with conventional concrete (Sena-Cruz et al. 2018; Wang, Liu & Li 2018). The workability, however, becomes worse, along with a shortened setting period (Jain & Pradhan 2020). According to the research results proposed by Bachtiar *et al.* (2015a) and Ting *et al.* (2020), using SW instead of FW mixing would cause an approximately 30% reduction in slump values. It is, however, worth noting that the influence of SW on slump value is reduced when the w/b ratio increases, as Otsuki *et al*. (2011) also observed that the slump of SW-mixed concrete at a w/b ratio of 0.53 was only 15% lower. Similar observations were reported on OPC concrete blended with (SCMs) in the studies by Sena-Cruz *et al*. (2018), Younis *et al*. (2018), and Katano *et al*. (2013a), in which the reduced slump by SW ranges from 10 to 30% at the decreasing w/b ratio between 0.5 to 0.26. Besides, the initial and final setting times were shortened by 20–25% measured in SW-mixed concrete (Etxeberria, Fernandez & Limeira 2016), which showed a negative effect on the workability. In Wang *et al.* (2018), the rheological behaviours were compared by using SW and deionized water

(DW) as mixing water for cement pastes. The shear stress and viscosity were observed to be remarkably higher in SW mixtures at 5 min and 15 min under the same shear rate, which indicated the stiffer feature in the fresh state. The higher viscosity can be due to the accelerated hydration rate by SW, wherein more solid phases were precipitated to enhance flocculations between the suspended particles. Moreover, there is a consensus that the air content in SW mixtures is typically 5 – 20% lower than that of FW mixtures (Katano et al. 2013a; Khatibmasjedi et al. 2019; Otsuki et al. 2011), probably due to the higher viscosity in the paste matrix. Besides, the water film thickness was calculated a slightly smaller in SW mixtures by Li *et al*. (2019), which led a adverse effect on flowability of the fresh paste. The associated experimental results are summarized in Table 2.2. based on these studies.

Table 2.2. Initial slump flow in SW/cementitious composite

Composite type	W/b ratio	Initial slump flow (mm)			Reference
		FW	SW	SW/FW	
OPC paste	0.25 (with SP 1%)	54	46	0.85	(Li et al. 2019)
OPC concrete	0.32 (with SP 1%)	121	82	0.68	(Ting et al. 2020)
OPC concrete	0.35 (with SP 1%)	122	80	0.66	(Bachtiar et al. 2015a)
OPC concrete	0.53	66	56	0.85	(Otsuki et al. 2011)
OPC 80% + Fly ash 20% concrete	0.26 (with SP 1%)	610	420	0.69	(Sena-Cruz et al. 2018)
OPC 35% + Slag 65% concrete	0.34	600	480	0.80	(Younis et al.

OPC 50% + Slag 50% concrete	0.5	165	150	0.91	2018) (Katano et al. 2013a)

Note: SP is superplasticizer; FW denoted freshwater mixtures; SW represents SW mixtures.

2.1.3 Mechanical properties

Numerous studies have been done on compressive strength to evaluate the effectiveness of SW-mixed composite, as shown in Table 2.3. According to the existing reports, it is generally believed that SWC exhibits higher early strength by 5–30% than FW mixtures within 3 days (Erniati et al. 2015; Li et al. 2015). However, conflicting results have been proposed in the studies regarding the late-age strength of SW-mixed concrete. Based on the experimental results, using SW might produce nearly no impact or, inconsistently, cause serious adverse effects on the late-age strength, which seems contradictory and, thus, causes two opposite views on SW mixtures (Neville 2001; Otsuki et al. 2011). Nevertheless, through the perusal of the related studies, the effect of curing conditions should be considered a very influential factor in strength development. For instance, the strength of cement composites strength can vary after being cured in water or moist condition. Figure 2.2 summarizes the relative compressive strength of SW mixtures versus those of FW mixtures under various curing conditions.

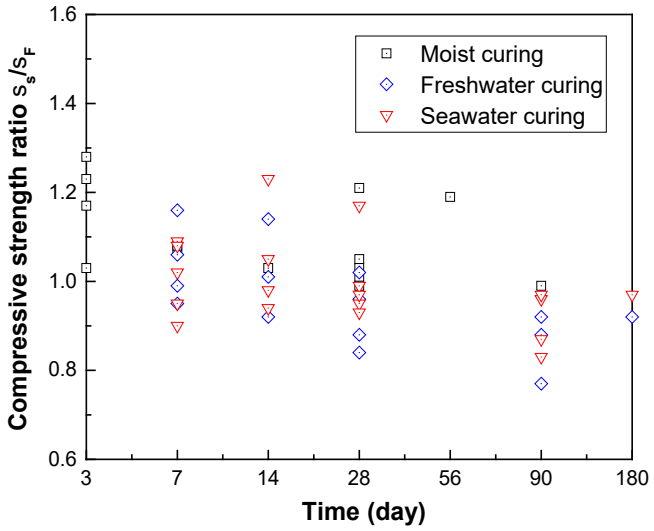

Figure 2.2. Time-dependent changes of compressive strength ratios (mixed with SW/mixed with FW) cured at different conditions (Akinkurolere, Jiang & Shobola 2007; Erniati et al. 2015; Guo et al. 2018; Islam et al. 2012a; Li, Farzadnia & Shi 2018; Li et al. 2019; Li, Li, et al. 2020b; Li et al. 2015; Ting et al. 2020; Wegian 2010)

In moist curing conditions where cement composite has been constantly stored in the standard curing chamber, a higher compressive strength could be retained in the SW mixtures for 28 days or perhaps longer (Ting et al. 2020). The studies from Li *et al.* (2019; 2020b; 2015) and Erniati *et al.* (2015) also proposed similar results. Specifically, SW was identified as improving compressive strength by nearly 60% at 1 day, 7–28% at 3 days, and 0–5% at 28 days, respectively. In a long-term of over 28 days, it has been demonstrated that the compressive strength between FW-mixed composite and SW-mixed composite displays almost no difference.

Slower strength development can be observed in SW mixtures when immersed in FW or SW, compared to conventional concrete under the same curing condition. In Islam *et al.* (Islam et al. 2012a), an approximately 5% lower value in strength was measured in SW-mixed specimens from 7 to 180 days in the water-curing conditions, which was further

reduced with the increasing w/b ratio. In Wegian *et al*. (2010), when the w/b ratio is 0.45, the SWC achieved 0–10% higher compressive strength within 7 days. However, the increase of strength was slowed over time such that the 90-day compressive strength has only reached about 85% of that in conventional concrete. At a higher w/b ratio of 0.5, similar results could also be verified by Guo *et al*. (2018) that comparable early and lower long-term strength was obtained in SW mixtures. These interesting findings indicate that the effect of SW on strength development is complex. On the one side, the SW can stimulate cement hydration to promote early-stage strength. On the other side, the growth rate of strength in SW mixtures is not as high as that in FW mixtures, probably due to the stability of microstructure affected by some specific hydration products formed (i.e., brucite, calcium oxychloride, M-S-H, etc. (Qiao et al. 2018; Wang et al. 2019)). The hydrate phases formed previously may become unstable to decompose when the pore solution changes, based on the principle of chemical equilibrium. Therefore, for cement mixture, a sealed or stable curing condition is beneficial for steady structure development. When the pore solution is much closer to the matrix, the decomposition and leaching effect of cement hydrates will diminish. The conclusion can also well illustrate that SW-mixed concrete achieves better strength development when cured in SW than in FW (see Figure 2.2).

Mohammed *et al.* (2004) investigated the SW-mixed concrete cured in tidal conditions for 20 years, observing a comparable compressive strength between SW-mixed concrete and FW-mixed concrete. For the tidal SW curing, it should, however, be noted that the

external condition was an enormous environment relative to the concrete itself, along with constant dry-wet alternation. In this condition, the higher water absorption and outward leaching effect of alkalis and calcium hydroxide occurred to cause severe deterioration (Khatibmasjedi 2018; Spragg et al. 2017). In addition, the expansive product, calcium oxychloride, may cause serious deterioration to reduce concrete properties (Qiao, Suraneni & Weiss 2018b; Wang et al. 2019) (detailed discussion in Section 3). Therefore, the adverse effect on strength development is quite significant from long-term SW curing conditions, compared to those only use SW as mixing water

Table 2.3. Specific studies on the compressive strength development of SW-mixed composite

Type	W/b ratio	Curing condition	Compressive strength (MPa)			References
			FW	SW	SW/FW	
OPC paste	0.20	Moist curing	84.7 (3 days)	87.3 (3 days)	1.03	(Li, Farzadnia & Shi 2018)
	0.25 (with SP 0–2%)		110.9–123.0 (28 days)	111.7–132.5 (28 days)	1.02–1.08	(Li et al. 2019)
	0.35 (with SP 0–2%)		89.0–99.1 (28 days)	90.8 – 105.5 (28 days)	1.02–1.05	
OPC mortar	0.40	Moist curing	42.1 (3 days)	49.1 (3 days)	1.17	(Li, Li, et al. 2020b)
			51.9 (14 days)	53.7 (14 days)	1.03	
			54.2 (28 days)	54.5 (28 days)	1.01	
OPC concrete	0.45	Moist curing	35.46 (3 days)	45.41 (3 days)	1.28	(Li et al. 2015)
			40.47 (7 days)	51.85 (7 days)	1.28	

			46.17 (28 days)	55.98 (28 days)	1.21	
			50.63 (56 days)	60.18 (56 days)	1.19	
OPC concrete	0.32 (with SP 1%)	Moist curing	60.7 (7 days)	64.9 (7 days)	1.07	(Ting et al. 2020)
			75.2 (28 days)	74.7 (28 days)	0.99	
			91.2 (90 days)	90.1 (90 days)	0.99	
OPC concrete	0.35 (with SP 1%)	Moist curing	9.1 (1 day)	14.6 (1 day)	1.60	(Erniati et al. 2015)
			25.5 (3 days)	31.3 (3 days)	1.23	
			35.2 (7 days)	38.0 (7 days)	1.08	
			50.6 (28 days)	51.9 (28 days)	1.03	
			52.7 (56 days)	53.7 (56 days)	1.02	
OPC concrete	0.40	FW curing	18.3 (7 days)	17.3 (7 days)	0.95	(Islam et al. 2012a)
			24.5 (28 days)	23.5 (28 days)	0.96	
			30.0 (90 days)	27.5 (90 days)	0.92	
			31.5 (180 days)	28.9 (180 days)	0.92	
		SW curing	17.9 (7 days)	17.0 (7 days)	0.95	
			24.2 (28 days)	23.1 (28 days)	0.95	
			28.5 (90 days)	27.4 (90 days)	0.96	
			29.6 (180 days)	28.7 (180 days)	0.97	
OPC	0.45	SW	27.6	30	1.09	(Wegian 2010)

concrete		curing	(7 days)	(7 days)		
			32.1	33.8	1.05	
			(14 days)	(14 days)		
			34.9	34.7	0.99	
			(28 days)	(28 days)		
			30.6	25.5	0.83	
			(90 days)	(90 days)		
OPC		FW	41.2	43.7	1.06	(Guo et al. 2018)
concrete		curing	(7 days)	(7 days)		
			46.1	46.5	1.01	
			(14 days)	(14 days)		
			54.3	45.4	0.84	
			(28 days)	(28 days)		
			65.3	57.1	0.88	
			(90 days)	(90 days)		
		SW	41.3	42.2	1.02	
		curing	(7 days)	(7 days)		
			46.5	45.5	0.98	
			(14 days)	(14 days)		
			50.0	48.3	0.97	
			(28 days)	(28 days)		
			62.5	54.6	0.87	
			(90 days)	(90 days)		
OPC	0.50	FW	39.5	39.1	0.99	(Guo et al. 2018)
concrete		curing	(7 days)	(7 days)		
			45.2	41.5	0.92	
			(14 days)	(14 days)		
			47.2	41.4	0.88	
			(28 days)	(28 days)		
			59.3	45.4	0.77	
			(90 days)	(90 days)		
		SW	42.1	38.0	0.90	
		curing	(7 days)	(7 days)		
			46.2	43.6	0.94	
			(14 days)	(14 days)		
			49.8	46.1	0.93	
			(28 days)	(28 days)		
			55.0	53.3	0.97	

			(90 days)	(90 days)		
OPC concrete	0.60	FW curing	12.1 (7 days)	14.0 (7 days)	1.16	(Akinkurolere, Jiang & Shobola 2007)
			14.0 (14 days)	16.0 (14 days)	1.14	
			15.8 (21 days)	17.0 (21 days)	1.08	
			20.0 (28 days)	20.3 (28 days)	1.02	
		SW curing	12.9 (7 days)	13.9 (7 days)	1.08	
			14.5 (14 days)	17.9 (14 days)	1.23	
			13.1 (21 days)	19.8 (21 days)	1.51	
			18.7 (28 days)	21.9 (28 days)	1.17	

Note: SP: Superplasticizer, FW: FW-mixed composite, SW: SW-mixed composites

2.1.4 Transport properties

In general, concrete deterioration is mainly due to the mass transfer of chemicals that can be transmitted inside and outside through the pore solution. The transport properties are accordingly valued for the service-life prediction of the cement composite. As a prominent feature to characterize the quality of hardened cement mixtures, pore structure dominates the permeability that affects moisture and ions diffusion in concrete. According to the available research, using SW in concrete significantly affects the early-stage pore structure, while a similar long-term pore structure can be observed (Li et al. 2015). The ratio of pores smaller than 10 nm is significantly increased by using SW at 3 days (see Figure 2.3), while the porosity is 5% higher than that of conventional concrete. During the curing time which followed, the porosity decreased remarkably

over time, and gradually, the number of small pores (< 10 nm) overtook the large pores (10 – 5000 nm) at 7 days. However, it appears that the porosity has not markedly altered at 28 days when using SW mixing instead of FW, indicating that the two composites have formed a similar pore structure at the late stage. The result has also been verified by Montanari *et al*. (2019) that at the late stage of 90 days, an identical total porosity ranging between 0.166–0.167 ml/g is determined in both cement pastes mixed with SW and FW.

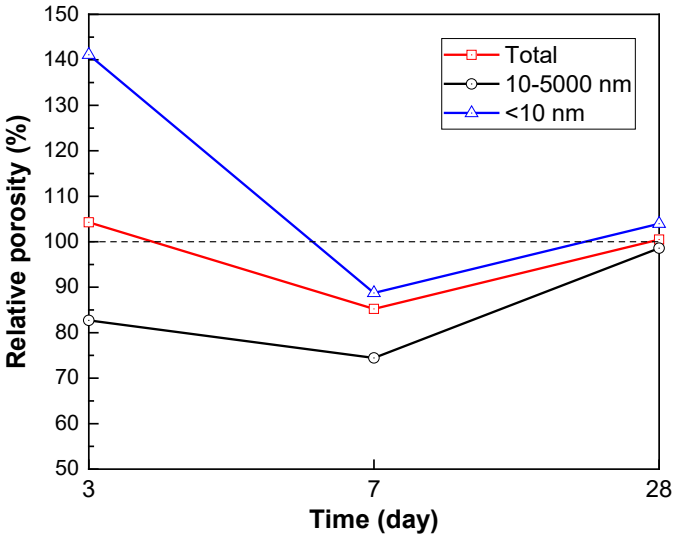

Figure 2.3. Evolution of porosity and the ratios of large and small pores (mixed with SW/mixed with FW) (Li et al. 2015)

Shi *et al*. (2015) studied the SW effect on the pore structure evolution with the aid of mercury intrusion porosimetry (MIP), as represented in Figure 2.4. The results illustrated that most of the pores over 10 nm are converted to finer pores in SW, exhibiting a refined structure at the early stage, after which the distinction between the two mixtures relatively decreases with age. Still, the volumes of pores ranging between 50–1000 nm were slightly higher in SW mixtures at 28 days, and more fine pores less

than 30 nm formed in the SW mixtures at 60 days (Khatibmasjedi et al. 2019), which is well accordant with the slightly higher compressive strength in SW-mixed concrete.

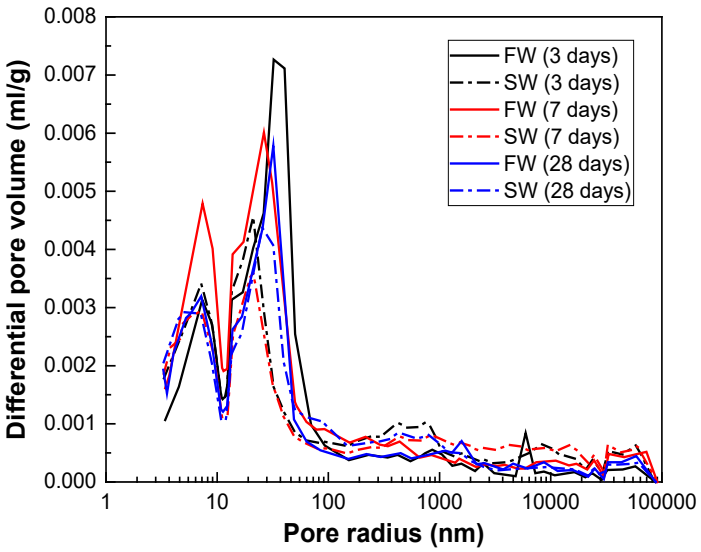

Figure 2.4. The differential pore volume of concrete at 3, 7, and 28 days (FW: concrete mixed with SW; SW: concrete mixed with FW) (Shi et al. 2015)

In Wang *et al.* (2018), the C-S-H gels formed in SW have a high surface area by Brunauer-Emmett-Teller (BET) surface area measurements. It has been found that the cement paste with FW possessed a surface area of up to 14.3 m^2/g, while that of SW paste was 27.4 m^2/g. Additionally, the pores ranging between 2–60 nm are 0.0434 cm^3/g in volume, which was 70% higher than that of FW paste. It can be concluded that a finer structure of C-S-H gels with a higher volume of pores below 5 nm formed with the hydration in SW. Likewise, the permeability performance of SWC was studied by Younis *et al.* (2018) through various methods, such as water absorption test (WAT), chloride migration test (CMT) and rapid chloride permeability test (RCPT). The results demonstrate that the SW mixtures were found to achieve higher impermeability at 28

days. However, the results of the sea mixtures and FW mixtures were comparable over 56 days, revealing that the late-stage permeability is less affected by the mixed SW.

The migration behaviour of conductive ions in the pore solution, such as chloride, sulfate, or possibly hydroxyl ions, dominates the electrical resistance of the concrete. When an electric field is applied, electromigration occurs as the only mechanism of concrete conductivity (Claisse 2005). Montanari *et al.* (2019) demonstrated that the electrical resistivity is reduced by approximately 40–50% in SWC, resulting from a considerable amount of soluble ions involved (as shown in Figure 2.5). Moreover, because the pore solution was concentrated with hydration age, a 40% reduction in the electrical resistivity can be observed in cement pastes with FW at the late stage of 28 days, but only a 25% decrease determined in the resistivity in SW paste.

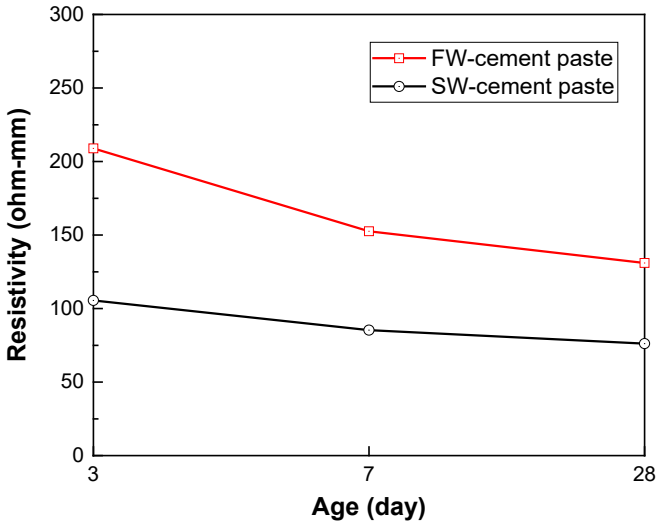

Figure 2.5. Evolution of electrical resistivity in cement paste mixed with SW or SW (Montanari et al. 2019)

2.1.5 Shrinkage

During the cement hydration or drying process of concrete, shrinkage occurs due to the moisture decrease, which may, in some cases, result in structural cracking or deterioration in the service life. According to the distinction of water consumption, the shrinkage behaviour can be divided into autogenous shrinkage and drying shrinkage (Radlinska et al. 2008). Li *et al*. (2018) revealed that using SW increased 30% autogenous shrinkage of OPC paste, resulting from the remarkably refined microstructure by a quicker self-desiccation of cement in SW (Shi et al. 2015). Furthermore, the autogenous shrinkage strains were reduced with an increasing w/b ratio (Khatibmasjedi et al. 2019). The study showed that using SW at a w/b ratio of 0.36 increased the 63-day autogenous shrinkage from 213 to 387 microstrain. If at a w/b ratio of 0.45, SW increased the autogenous shrinkage from 149 to 314 μs (as shown in Figure 2.6). Besides, using SW led to a significantly higher shrinkage in 3 days, which might be due to the stimulated hydration reaction by SW (Shi et al. 2015)

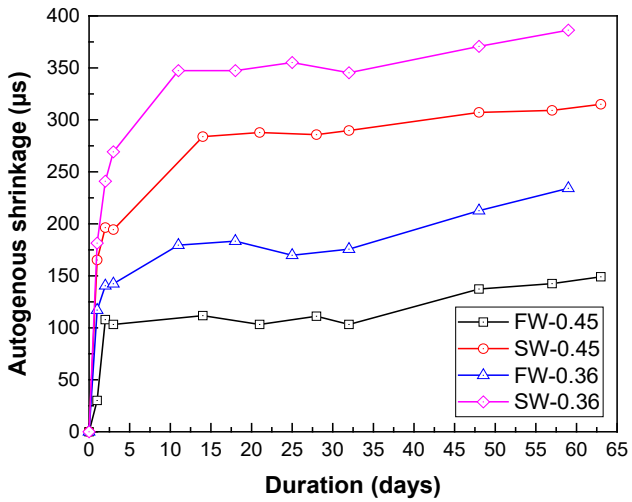

Figure 2.6. Autogenous shrinkage of cement mortar at w/b ratios of 0.36 and 0.45,

respectively (Khatibmasjedi et al. 2019)

Furthermore, drying shrinkage induced by vapour diffusion also occurs in concrete during the external drying process, which inevitably occurs after the moist-curing period (Hajibabaee & Ley 2015). Unlike the autogenous shrinkage, which was scarcely changed at the late stage, the drying shrinkage has grown continuously throughout 65 days (Khatibmasjedi et al. 2019). In Figure 2.7, the drying shrinkage values are quite close in both SW and FW at a w/b ratio of 0.36, approaching 600 μs and 560 μs, respectively. The drying shrinkage becomes prominent in SW mixtures with the increase of the w/b ratio. Khatibmasjedi *et al*. (2019) observed that using SW at a w/b ratio of 0.45, the drying shrinkage reaches 980 μs and exhibits 17% higher than the FW mixtures.

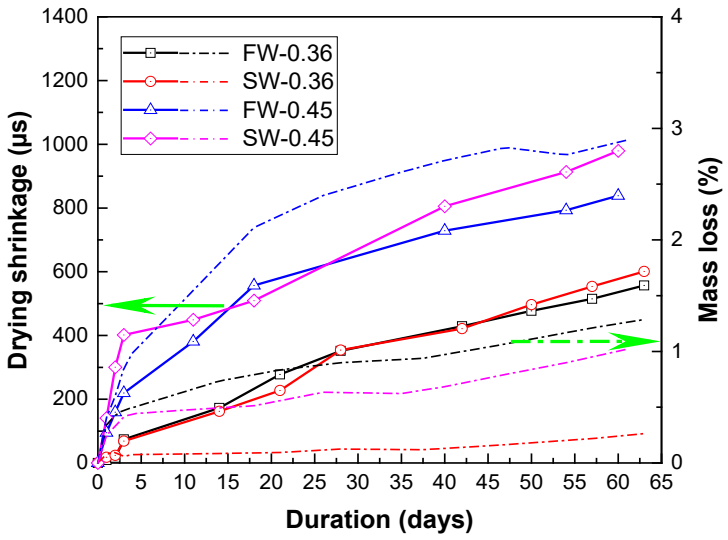

Figure 2.7. Drying shrinkage and mass loss of mortar mixtures (Khatibmasjedi et al. 2019)

The curves of drying shrinkage versus the mass loss are shown in Figure 2.8. The increasing slope of the curves in SW indicates that SW reduced the mass loss during the

drying process. The higher shrinkage can be due to the denser microstructure of hardened cement paste formed in SW (Montanari et al. 2019; Park, Kwon & Song 2011), where the capillary-induced stress caused by the menisci on the liquid surface was higher in finer pores, leading to greater internal shrinkage stress. On the other hand, the chloride-based salts in SW, such as sodium chloride, are hygroscopic (Autelitano, Rinaldi & Giuliani 2019), resulting in slower moisture escaping. Therefore, it can be drawn that SW mixtures are featured with a lower mass loss but a higher shrinkage instead, compared to conventional concrete.

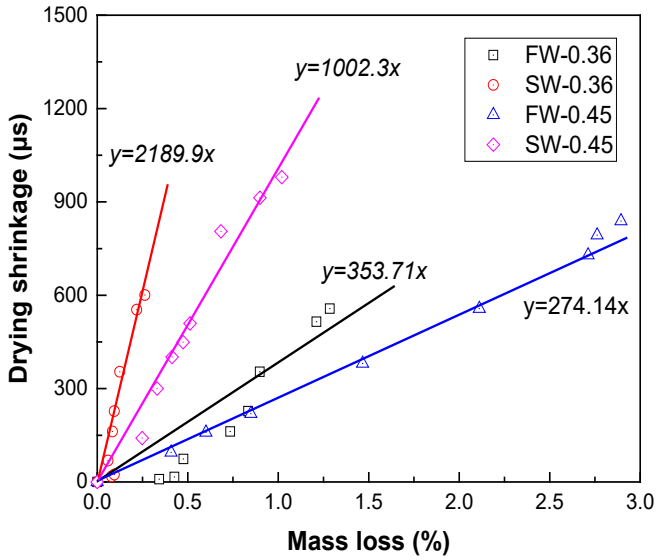

Figure 2.8. Drying shrinkage versus mass loss for cement mortar (Khatibmasjedi et al. 2019)

2.2 Effect of seawater-related ions on cement hydration

Based on the existing studies, the effect of some SW-related ions on cement hydration is discussed separately. This section focuses mainly on the existing ions that play important roles in cement hydration at their specific concentration in SW; however,

multiple chemical reactions occur simultaneously in practice, and the effects are closely related to their actual concentration.

2.2.1 Chloride ions

As the most influential ion in SW on concrete properties, chlorides should be discussed in detail first. The effect of chlorides on hydration can be divided into three parts: 1) the interaction with AFm (aluminate-ferrite-mono) phase; 2) the formation of calcium oxychloride (CAOXY); and 3) the adsorption by C-S-H, as discussed below separately.

2.2.1.1 Interaction with AFm

In Portland cement, chloride can be chemically bound with the layered calcium-aluminate hydrates as AFm hydrates (Matschei, Lothenbach & Glasser 2007a), such as calcium chloroaluminate, commonly known as FS: $3CaO{\cdot}Al_2O_3{\cdot}CaCl_2{\cdot}10H_2O$ (Friedel 1897). Suryavanshi *et al*. (1996) proposed that there are two mechanisms for the formation of FS, namely, the adsorption and the anion-exchange mechanism. Firstly, the bulk of free-chloride ions can be adsorbed directly by the interlayers of the layered AFm structures to balance the charge arising from the displacement of a Ca^{2+} by an $[Al(OH)_6]^3$, as shown in Figure 2.9. Secondly, the free-chloride ions can displace the OH^- from hydroxy-AFm hydrates, such as C_4AH_{13}, C_4AH_{11}, C_4AH_{19}, etc., forming FS coincided with a comparable content of OH^- released in the pore solution. The two separate mechanisms can effectively explain the phenomenon that an increase of OH^-

concentration occurs during the chloride ions binding, and also that the concentration of bound Cl^- is much higher than that of the displaced OH^- from the interlayers.

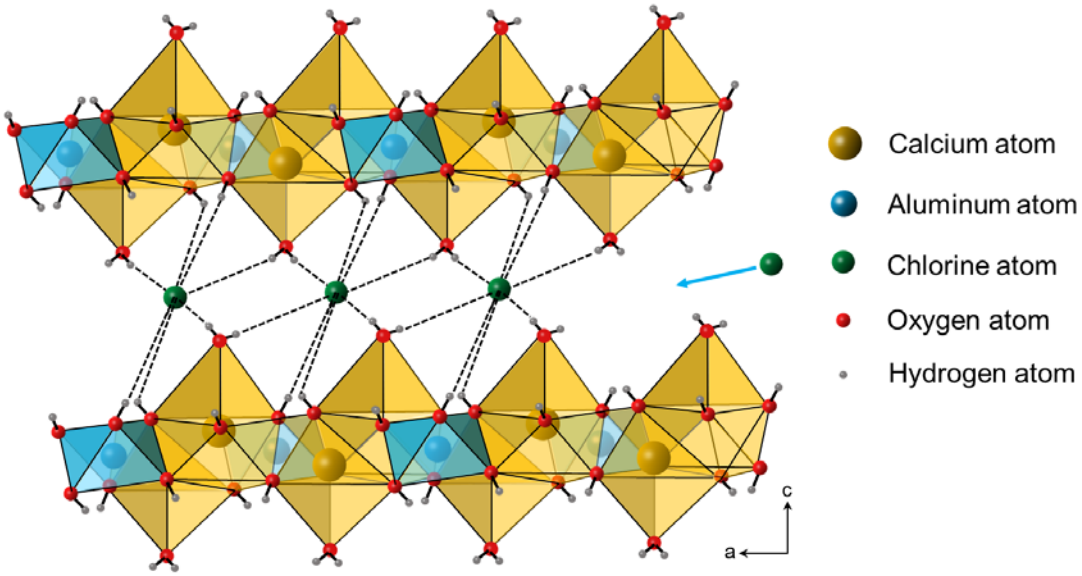

Figure 2.9. Structural representations of AFm phase: hydrogen bond network within an interlayer region (Mesbah et al. 2011; Suryavanshi, Scantlebury & Lyon 1996)

However, it seems not necessary to strictly distinguish the two aforementioned mechanisms. Intending to balance charges, both chloride ions, and hydroxyl ions can be adsorbed by the principal layer of the AFm structure, and the two adsorptions occur simultaneously. During the process, the adsorbed $OH^-$are more easily displaced by Cl^-, due to the fact that OH^- hardly competes with Cl^- in balancing charge. Meanwhile, the free OH^- ions are retained in the pore solution, leading to an increase of pH. Therefore, the increase of alkalinity in pore solution is due to the significant substitution of adsorbed OH^- ions by Cl^-, and it also means that the metastable hydroxy-AFm hydrates hardly coexist with aqueous Cl^- (Matschei, Lothenbach & Glasser 2007b). The same opinion has been put forward by Galan and Glasser (2015) that the ion exchange

mechanism is dominant in the formation of FS (Jones et al. 2003). Suryavanshi *et al.* (1996) also proposed theoretical support but lacks strong evidence. Due to the competitive relationship between hydroxyl ions and chloride ions to bind with AFm, the formation of FS is reduced in high alkaline conditions. In other words, chloride binding is decreased with high alkali content, which was verified by Rasheeduzzafar *et al*. (1991).

Additionally, the formation of FS is not limited to the substitution reaction between free Cl^- and OH^-, which means that the reaction of Cl^- and AFm is more than just one way on a single AFm phase. Some other anions, such as SO_3^{2-} and CO_3^{2-}, can compete with Cl^- in the AFm-related adsorption as well. Hence, the formation of FS also occurs by an ionic interaction from other AFm phases (Birnin-Yauri & Glasser 1998c; Hosokawa et al. 2006; Jones et al. 2003). Additionally, the various bound anions can be partially miscible with each other in AFm phases (Frias et al. 2013) (e.g., Kuzel's salt (KS): $3CaO{\cdot}Al_2O_3{\cdot}1/2CaCl_2{\cdot}1/2CaSO_4{\cdot}10H_2O$; Hemicarboaluminate: $Ca_4Al_2(CO_3)_{0.5}(OH)_{13}{\cdot}5.5H_2O$, etc. (Matschei, Lothenbach & Glasser 2007b)). Therefore, the thermodynamic stabilization of the AFm hydrates is highly associated with the formation mechanism of chloride-related hydrates.

At the temperature of 25 °C under standard atmosphere, monocarboaluminate (CO_3-AFm) is more stable than monosulfoaluminate (SO_3-AFm) in Portland cement, which promotes a progressive substitution of CO_3^{2-} in SO_3-AFm to convert into hemicarboaluminate or, more likely, CO_3-AFm (Matschei, Lothenbach & Glasser

2007b). Similarly to CO_3^{2-}, Cl^- can also displace sulfate in SO_3-AFm, converting to FS as the more stable AFm hydrates. Numerous studies have investigated the chloride effect on the mineralogy of hydrated Portland cement (Cao et al. 2020; De Weerdt & Justnes 2015; Farnam, Dick, et al. 2015; Shi, Geiker, Lothenbach, et al. 2017). Due to the significant competitiveness of carbonate in binding AFm hydrates, the impact mechanism of chloride has to be discussed respectively in the cementitious system with and without carbonates as follows.

In the carbonate-free system, as depicted in Figure 2.10 by Balonis *et al.* (Balonis et al. 2010), Cl^- substitute SO_3^{2-} from SO_3-AFm hydrates, forming an intermediate compound KS at lower chloride concentration (molar ration of $2Cl/Al_2O_3 < 0.70$) and FS at higher chloride concentration (molar ratio $2Cl/Al_2O_3 > 0.70$). Meanwhile, the substituted SO_3^{2-} are released to the aqueous solution, forming AFt subsequently when the required concentration is reached (De Weerdt, Orsáková & Geiker 2014; Ekolu, Thomas & Hooton 2006; Galan & Glasser 2015; Stark & Bollmann 2000). The AFt is hard to decompose due to the higher stability, and thus the content of AFt increases with the presence of chloride, as proposed by Hirao *et al*. (2005) and Cao *et al*. (2020). Additionally, some studies are consistent in that AFt shows no binding capacity to chlorides (Hirao et al. 2005; Midgley & Illston 1984), and thus can coexist steadily with FS at high chloride concentration. In Zibara (2001) and Ekolu *et al*. (Stark & Bollmann 2000), however, AFt was observed decomposed and gradually converted to FS in NaCl solution of 3 M and 2.8 M, respectively.

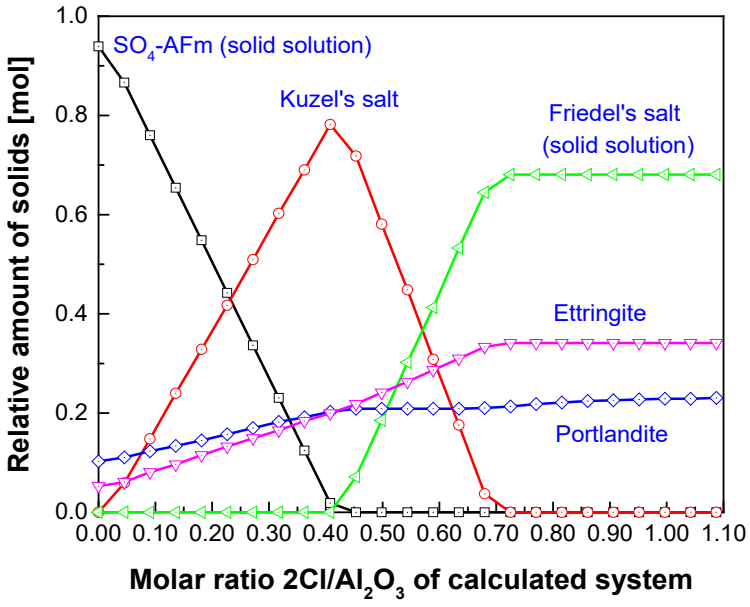

Figure 2.10. Relative amount of solid hydrate phases of a hydrated model mixture consisting of initially 1 mol C_3A, excess of CH, and with fixed initial sulfate ratio (SO_3/Al_2O_3=1), showing phase development and its dependence on changing chloride ratios ($2Cl/Al_2O_3$) at 25 °C (Balonis et al. 2010)

In practice, however, many modern types of cement contain added calcite (CC), leading to a portlandite (CH)–calcium carbonate–carbon dioxide equilibrium in the hydration system (Galan & Glasser 2015). Therefore, hemicarboaluminate or, more likely, monocarboaluminate will form in the carbonate-contained Portland cement. In this hydration system, it can be observed that carbonate ions in AFm phases are gradually substituted by chloride with a rising chloride concentration (Balonis et al. 2010; Frias et al. 2013). The released carbonate ions are subsequently bound as CC. It should, however, be noted that there is no KS appeared even as the intermediate hydration product during the substitution in the carbonate-containing system, which can be attributed to the more stability of CO_3-AFm than that of KS (Loser et al. 2010). The

result reflects that KS is incompatible with CO_3-Afm, and it is destabilized when encountering even small amounts of carbonate in the hydration system. Furthermore, Chang *et al.* (2019) observed that most of FS and KS decomposed after experiencing a 28-day carbonization period with CO_2 concentration being 20%. The results indicate that the bound chlorides in AFm were unstable and prone to be set free again in the carbonization environment.

Some other studies have been conducted to observe the binding of chloride in hydrated calcium aluminoferrite to find that the rate of hydration reaction is slower than C_3A and decreases with increasing iron content as the order C_6A_2F > C_4AF > C_6AF_2 (Csizmadia, Balázs & Tamás 2001). The studies show that both of these aluminoferrites can bind chloride and develop hydrates with similar structures to FS but with iron instead of aluminium (e.g., $3CaO{\cdot}Fe_2O_3{\cdot}CaCl_2{\cdot}10H_2O$) (Sumranwanich & Tangtermsirikul 2004; Suryavanshi, Scantlebury & Lyon 1995), and the iron-containing FS may form solid solutions with other AFm phases.

2.2.1.2 The formation of CAOXY

Apart from the aluminate hydrates, chloride can also be chemically bound during the cement hydration process through the formation of calcium oxychloride compounds: $x\text{Ca(OH)}_2{\cdot}y\text{CaCl}_2{\cdot}z\text{H}_2\text{O}$ (CAOXY) (Farnam, Dick, et al. 2015; Glasser, Marchand & Samson 2008; Jones et al. 2020; Suraneni et al. 2016; Tamas 1966). As calculated by Qiao et al. (2018b), the volume of CAOXY is 303% as large as $Ca(OH)_2$ and thus leads to a volumetric expansion. In hardened cement paste, the expansive pressure caused by

CAOXY is undoubtedly responsible for the deterioration of mechanical properties. The most common compositions range from the dehydrated phase with x:y:z of 1:1:0 compound to the hydrated phase with the ratio of 3:1:15 (3-1-15 compound) and 4:1:10 (4-1-10 compound), depending on the various chloride concentrations and test conditions (Brown & Bothe 2004; Jones et al. 2020). In most cases, however, the formation of CAOXY can be observed in $CaCl_2$ solutions instead of in $NaCl_2$ solutions (Farnam, Dick, et al. 2015; Farnam, Zhang & Weiss 2017; Peterson et al. 2013; Qiao, Suraneni & Weiss 2018a, 2018b; Wang et al. 2019), and a certain concentration is required. Farnam *et al.* (2015) suggested that the minimum concentration of $CaCl_2$ is 11.3% when CAOXY is formed. Qiao *et al*. (2019) determined the required Cl^- concentration for CAOXY formation, which is 1.20 M at 5 ℃ and 3.64 at 23 ℃. Similar results were reported by Brown and Bothe (2004) that the formation of 3:1:15 compound requires a chloride concentration approaching 4 M, and the formation of 1-1-2 compound (hydrated phase with the ratio of 1:1:2) needs about 9 M of chloride concentration, based on the synthetic products in laboratory conditions. Damidot *et al.* (1994) have investigated the CaO-Al_2O_3-$CaCl_2$-H_2O system at 25 ℃ and defined the stable invariant points that FS can coexist with CH and 3-1-15 compound with a Cl^- concentration of 3.285 mol/kg, and FS can coexist with both 3-1-15 compound and 1-1-2 compound with a Cl^- concentration of 6.427 mol/kg. Besides, CAOXY also can be observed in the presence of $MgCl_2$ solution (Julio-Betancourt 2009; Sutter, Peterson, et al. 2006), and the concentration is also required. Wang *et al*. (2019) indicated no

CAOXY formed in solution with 4% $MgCl_2$, but it was detected in solution with 20% $MgCl_2$. However, the existing studies indicated no sign of CAOXY formation when cement paste was exposed to NaCl solution (Galan, Perron & Glasser 2015; Ghazy & Bassuoni 2017; Julio-Betancourt 2009), with an exception in carbonated concrete in one study (Egüez Álava, De Belie & De Schutter 2016). The studies agree well with the conclusion that $CaCl_2$ and $MgCl_2$ solutions might exhibit expansion and crack in cement paste (Peterson et al. 2013), but NaCl is relatively benign (Galan, Perron & Glasser 2015; Ghazy & Bassuoni 2017; Julio-Betancourt 2009), since the expansive product CAOXY does not exist in (Smolczyk 1968). Therefore, CAOXY would hardly form in cement paste hydrated in SW, owing to the fact that the required concentration of $CaCl_2$ and $MgCl_2$ is not reached. Moreover, in practice cases, there is no clear evidence in the existing studies that CAOXY was observed in the OPC hydrated in SW at standard concentration.

2.2.1.3 Chloride adsorped by C-S-H

In addition to chemical combinations, some researchers found that chloride can be physically adsorbed in C-S-H gels due to its large specific area (Theissing 1980; Yogarajah, Nawa & Kurumisawa 2018). It is found that the chloride binding capacity of C-S-H increases with the increase of chloride concentration (Hirao et al. 2005; Yogarajah, Nawa & Kurumisawa 2018; Zhou et al. 2016), and also more chloride can be found held in C-S-H with a higher calcium-silicate (Ca/Si) ratio (Beaudoin, Ramachandran & Feldman 1990; Yoon et al. 2014; Zibara 2001). Therefore, C-S-H gels

with a higher Ca/Si ratio are seemingly more beneficial to reduce the free chlorine in concrete under marine environments. Experimental and modelling results (Friedmann, Amiri & Aït-Mokhtar 2008) suggest that the chloride ions associated with the C-S-H are mainly present in the diffuse layer of the C-S-H surface, which is positively charged in the presence of high calcium concentrations. The finding can well explain that C-S-H exposed to $CaCl_2$ solution has higher chloride adsorption than that exposed to NaCl with the same chloride concentration (Zhou et al. 2016). However, despite the adsorption proposed in most previous studies, an opposite view has been put forward by Plusquellec and Nonat (Plusquellec & Nonat 2016) that C-S-H particles cannot adsorb chlorides, based on the zeta potential measurement. The research observed that the zeta potential was well linearly increasing with the increase of concentration, and thus no adsorption occurred in the process to reduce the zeta potential. This finding questions the common experimental method of calculating the concentration of chlorides that some electrical-attracted chlorides by C-S-H particles are inevitably removed during the filtration process, and thus the reduction of chloride in solution is wrongly attributed to adsorption by C-S-H. As a result, further studies are needed to clarify the chloride-adsorption capacity of C-S-H. Based on the aforementioned discussion, Table 2.4 summarizes the main effect of chloride on cement hydrates.

Table 2.4. Main interactions between chloride ions and cement hydrates

Mechanism	Cement hydrates involved	Comment

Chloride exchange	AFm converts to FS	Anions in AFm, such as hydroxyl, sulfate, and carbonate, can be displaced by chloride to form FS. The stability of related hydrates follows the order of AFt> FS> CO_3-AFm> SO_3-AFm> hydroxy-AFm in the range 0–70 ℃ (Galan & Glasser 2015).
Phase change	Destabilization of CH and formation of CAOXY	CH is converted to CAOXY of 3-1-15 compound or, perhaps, 1-1-2 compound. The reaction occurs in a high concentration of aqueous $CaCl_2$ or $MgCl_2$, and not occurs in aqueous NaCl.
Chloride Adsorption	C-S-H	More chloride can be adsorbed in C-S-H with a high Ca/Si ratio.

2.2.1.4 Effect on chloride in seawater

The properties change of cement composite caused by SW can be well explained through the chloride effects aforementioned. Because the chloride concentration in SW is close to 0.55 M, which is lower than the threshold of that in the formation of CAOXY (1.2 – 9 M (Brown & Bothe 2004; Qiao et al. 2019)), it is still questionable whether the reaction between chloride and CH occurs in SW composites. Therefore, the property differences between SW composite and FW composite can be considered to be dominated by the interaction between chloride and AFm phases. During the SW-mixed hydration process, especially in the early stage, the calcium, aluminate, and ferrite ions are consumed to form FS, thus enhancing the hydration kinetics and accelerating the hydration rate of C_3S, C_3A, and C_4AF. The enhanced hydration in the early stage is responsible for the rapid heat evolution and higher autogenous shrinkage; the ratio of

solid phase is increased to reduce the setting time; the cement hardens faster with higher compressive strength and refined pore structure.

2.2.2 Sulfate and carbonate ions

Sulfates and carbonates, as the other major anions in SW, can also affect cement hydration. Although the content involved in SW is much less than that from gypsum and CC in cement itself, the effect can not be ignored. Similar to the chlorides, the sulfate ions can be bound in AFm and C-S-H, with similar mechanisms aforementioned. Therefore, chloride and sulfate would compete and displace mutually for the binding space, and the chloride binding ability of hydrates is thus reduced (Cao et al. 2020; De Weerdt, Orsáková & Geiker 2014). For example, more AFt would be developed in the presence of sulfate in SW (Frias et al. 2013; Yoon et al. 2016), including that delayed forming by the displaced sulfate by chloride. The AFt possesses higher stability, consuming AFm hydrates, and presenting no chloride capacity as well (Hirao et al. 2005; Midgley & Illston 1984). Analogously, carbonate also presents adverse effects on the chloride binding of cement hydrates. Chang *et al*. (2019) determined that when cement is exposed to a carbonation environment with a CO_2 concentration of 20%, all chloride bound previously in AFm and nearly 90% of that in C-S-H would be released into pore solution after 28 days and 56 days, respectively. While even worse, the chloride binding ability will no longer exist in carbonated cement. Therefore, if SW is used as mixing water instead, there is only a small amount of cement hydrates changed from the limited additional sulfates and carbonates. However, if being long-term exposed to SW, sulfate

attack or carbonation, hydration products such as FS and C-S-H would become more vulnerable to convert and release bound chloride.

2.2.3 Sodium, magnesium and calcium ions

The cations in SW mainly include sodium, magnesium, calcium and other trace amounts of heavy metal ions. Among them, the content of sodium, magnesium, and calcium accounts for approximately 30.6%, 3.7%, and 1.2% of the total mass in SW, respectively (Levitus et al. 2010). It suggested that sodium ion has no specific interaction with the cement hydrates (Barberon et al. 2005). To maintain charge neutrality, some sodium ions have to be removed from the solution when chloride is bound. Therefore, the unstable sodium ions can also be absorbed in C-S-H by reaction with silanol groups (Jones et al. 2003; Suryavanshi, Scantlebury & Lyon 1996) or substituting calcium (Sugiyama 2008; Tritthart 1989; Yoon et al. 2014). Furthermore, one thing should be noted that the associated cations such as sodium, calcium, and magnesium can affect chloride binding. Specifically, calcium and magnesium ions significantly increase the chloride binding capacity of hydrates, while sodium presents no remarkable effect (De Weerdt et al. 2015; Lambert, Page & Short 1985; Machner et al. 2018; Shi, Geiker, De Weerdt, et al. 2017). One of the main reasons is the calcium and magnesium ions, which cause the precipitation of $Ca(OH)_2$ or $Mg(OH)_2$; the pH of the solution decreases and the solubility of Ca^{2+} increase consequently, leading to the formation of higher-Ca/Si C-S-H and M-S-H with higher chloride content (De Weerdt et al. 2015; De Weerdt & Justnes 2015; Jones et al. 2020). The second cause can be the

formation of CAOXY or magnesium oxychloride (MAOXY) (Jones et al. 2020; Qiao et al. 2018; Sutter, Peterson, et al. 2006; Sutter, Van Dam, et al. 2006; Wang et al. 2019). The third one is that in cement blended with alumina-rich SCMs, a higher calcium concentration can enhance the formation of FS, which increases the chloride binding capacity of the composite system (Justnes 1998; Shi, Geiker, De Weerdt, et al. 2017). The schematic diagram of the chloride distribution in cement hydrates is summarized in Figure 2.11. Furthermore, De Weerdt *et al.* (2014) observed an approximately 0.25 M higher chloride bound in $MgCl_2$ than $CaCl_2$, which probably indicates a higher binding chloride enhanced by Mg^{2+}.

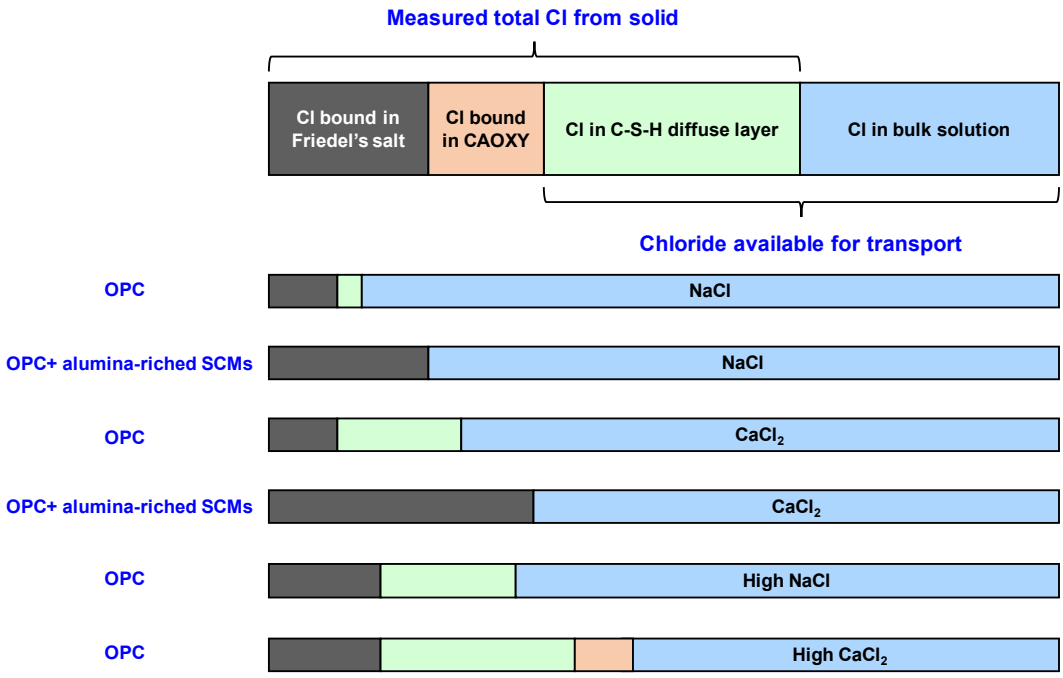

Figure 2.11. Schematic diagram of chloride distribution in hydrates of OPC and alumina-riched SCMs exposed to NaCl and $CaCl_2$ solutions (Farnam, Dick, et al. 2015; Qiao et al. 2019; Shi, Geiker, De Weerdt, et al. 2017; Yoon et al. 2014)

2.2.4 Chloride binding in hydrates

Chloride binding happens during the cement hydration process, which significantly limits the free chloride penetration. Therefore, the threshold concentration of chloride-induced corrosion can be affected by the chloride binding capacity of cement hydrates, and it further influences the service life of the concrete. The chloride binding of cement hydrates can be affected by various factors, such as hydration degree, cation of chloride salt, carbonation, etc. (Loser et al. 2010; Yuan et al. 2009). Among them, chloride binding is significantly associated with chloride concentration and different binding mechanisms. In general, the relationship between the adsorbed chloride and free chloride in OPC is considered as non-linear isotherms:

Freundlich equation: $$C_b = \alpha \cdot C_f^{\beta} \quad (1)$$

Langmuir equation: $$C_b = \frac{\alpha \cdot C_f}{1 + \beta \cdot C_f} \quad (2)$$

where α and β are binding constants at a given temperature, C_b is the absorbed amount of chloride per gram of the solid at equilibrium, and C_f is the chloride concentration in solution at equilibrium.

Tang and Nilsson (1993) investigated the chloride binding capacity of OPC concrete and found Freundlich isotherm is better suited for high chloride concentration (> 0.01 M) and Langmuir is more applicable for low chloride concentration (< 0.05 M). However, it should be noted that because the two equations are empirical and designed to fit data, the constants α and β serve no practical concern and may vary in a wide range.

2.2.4.1 Chloride binding capacity of AFm phase

The chloride binding capacity of sulfo-AFm has been investigated by Hirao *et al*. (2005). They found that the relationship between bound chloride and sulfo-AFm phase follows Freundlich isotherm, in mg of bound Cl/ g of sulfo-AFm:

$$C_{b,\,sulfo\text{-}AFm} = 51.89 \cdot C_f^{0.58} \tag{3}$$

where the molecular formula of sulfo-AFm is $C_4A\overline{S}H_{10}$ at 11% relative humidity (RH).

While as for another AFm phase, hydroxy-AFm, the chloride binding capacity is higher since hydroxyl ions are more easily substituted by chloride in AFm (see section 3.1). As the study by Birnin-Yauri and Glasser (1998a), pure FS can be observed to be stable at 20 ℃ when chloride concentration ranges over 14.5 mM, indicating that all hydroxy-AFm phase has been bound chloride and converted to FS. The binding capacity, in mg of bound Cl/ g of hydroxy-AFm, is thus a constant when chloride concentration is over 14.5 mM:

$$C_{b,\,hydroxy\text{-}AFm} = 126.5 \tag{4}$$

where the molecular formula of sulfo-AFm is C_4AH_{13} at 11% RH.

2.2.4.2 Chloride binding capacity of C-S-H

Some studies investigated the chloride binding capacity of the C-S-H phase and, however, the suggested isotherms vary in a wide range, with poor fit compared to experimental data (Elakneswaran, Nawa & Kurumisawa 2009; Hirao et al. 2005; Zibara 2001). Hirao *et al*. (2005) described that the relationship between chloride concentration

and bound chloride follows a Langmuir isotherm in C-S-H, while a Freundlich isotherm was considered by Elakneswaran *et al*. (2009), in mg of bound Cl/ g of C-S-H:

$$C_{b,C\text{-}S\text{-}H,H} = 21.84 \cdot \frac{2.65 \cdot C_f}{1 + 2.65 \cdot C_f} \tag{5}$$

$$C_{b,C\text{-}S\text{-}H,E} = 12 \cdot C_f^{0.63} \tag{6}$$

Zibara (2001) also investigated the chloride binding capacity of C-S-H. Although the specific equation is not given, the binding isotherm of cement minerals of C_2S and C_3S has been determined, in mg of bound Cl/ g of solid:

$$C_{b,C_3S} = 6.65 \cdot C_f^{0.334} \tag{7}$$

$$C_{b,C_2S} = 7.89 \cdot C_f^{0.136} \tag{8}$$

By considering the almost same hydration products for C_2S and C_3S and the amount of C-S-H generated, Florea *et al*. (2012) combined the two isotherms and the ratio of two minerals as the isotherm of C-S-H provided by Zibara (Zibara 2001):

$$C_{b,C\text{-}S\text{-}H,Z} = 6.65 \cdot C_f^{0.334} \cdot \delta_{C_3S} + 7.89 \cdot C_f^{0.136} \cdot \delta_{C_2S} \tag{9}$$

where δ_{C_3S} and δ_{C_2S} is the mass fraction of C_3S and C_2S. Florea *et al*. (Florea & Brouwers 2012) evaluated the three binding isotherms of C-S-H to their experimental data. The $C_{b,C\text{-}S\text{-}H,Z}$ isotherm in Eq. (9) is considered as the best to express the chloride binding capacity of C-S-H, which presents the lowest relative error and standard deviations to experimental results.

2.2.4.3 Chloride binding capacity of other cement hydrates

As for other phases, AFt and CH, the chloride binding ability is highly debated as most of the existing studies determined no chemical binding exhibited, even when exposed to a high concentration of chloride solution (Ekolu, Thomas & Hooton 2006; Hirao et al. 2005; Zibara 2001); while the physical binding capacity, although insignificant, has also confirmed its existence and even detected in FS (Elakneswaran, Nawa & Kurumisawa 2009). Elakneswaran *et al.* (2009) concluded isotherms of CH and FS, in mg of bound Cl/ g of solid:

$$C_{b,CH} = 0.087 \cdot C_f^{0.62} \tag{10}$$

$$C_{b,Friedel's\ salt} = 0.31 \cdot C_f^{0.46} \tag{11}$$

where the molecular formula of FS is $3CaO \cdot Al_2O_3 \cdot CaCl_2 \cdot 6H_2O$ at 11% RH (Taylor 1992).

As mentioned by Elakneswaran *et al.* (2009), the sorption capacity of AFt was lower than CH and FS, but higher than tobermorite. However, the capacity of the tobermorite described in Eq. (7) is higher than those of CH and FS in Eqs. (10) and (11), which seems contradictory. Hence, the binding capacity of AFt is still not clear. Assuming that the minimum binding capacity of AFt is as same as that of C_3S, Florea *et al*. (2012) suggested the total bound chloride by AFt, which also takes into account the effect of the delay formed AFt from chloride substitution (section 2.2.2):

$$m_{cl,AFt} = C_{b,AFt} \cdot \frac{m_{AFt} + m_{delayed\ AFt}}{m_{sample}} = 6.65 \cdot C_f^{0.334} \cdot \frac{m_{C_6A\bar{S}_3H_{12}} + 0.3 \cdot m_{Friedel's\ salt}}{m_{sample}} \tag{12}$$

where the molecular formula of AFt is $C_6A\overline{S}_3H_{12}$ at 11% RH (Taylor 1992); m_{AFt}, $m_{delayed\ AFt}$, $m_{C_6A\overline{S}_3H_{12}}$, $m_{Friedel's\ salt}$ and m_{sample} refer to the mass of initial AFt, delayed formed AFt, formed FS and the sample, respectively.

Table 2.5 and Figure 2.12 summarize the chloride binding capacity of various cementitious phases at 11% RH based on the fitted isotherms, determined by existing studies. It can be concluded that the hydroxy-AFm phase, exhibiting a constant binding capacity versus chloride concentration, provides the greatest contribution to chloride binding, which can be completely converted to FS in chloride concentration over 0.015M. The binding capacity of sulfo-AFm increases with the increase in chloride concentration, from 13% at 0.3M to over 33% at 3M (Florea & Brouwers 2012). Therefore, the AFm phase provides the greatest contribution to chloride binding, accounting for around 70% of the total chloride binding capacity of OPC. The second strongest chloride binding is C-S-H that the binding ability remains stable and effective in a wide range of chloride concentrations, which comprises 25 to 28% of total bound chloride (Florea & Brouwers 2012). Although the content of CH is higher in OPC hydrates, the corresponding chloride binding ability of CH and FS is only 2 – 5%, due to the insignificant adsorption. While as for other cement hydrates, the chloride binding capacity is very low and can be ignored.

Table 2.5. Chloride binding capacity of cementitious phase

Phase	Isotherm	Chloride binding capacity	Reference
Hydroxy-AFm	Constant	$C_{b,hydroxy-AFm} = 126.5$	(Birnin-Yauri & Glasser 1998a)

Sulfo-AFm	Freundlich	$C_{b,sulfo-AFm} = 51.89 \cdot C_f^{0.58}$	(Hirao et al. 2005)
C-S-H	Langmuir	$C_{b,C-S-H,H} = 21.84 \cdot \frac{2.65 \cdot C_f}{1 + 2.65 \cdot C_f}$	(Hirao et al. 2005)
C-S-H	Freundlich	$C_{b,C-S-H,E} = 12 \cdot C_f^{0.63}$	(Elakneswaran, Nawa & Kurumisawa 2009)
C-S-H	Freundlich	$C_{b,C-S-H,Z} = 6.65 \cdot C_f^{0.334} \cdot \delta_{C_3S} + 7.89 \cdot C_f^{0.136} \cdot \delta_{C_2S}$	(Florea & Brouwers 2012; Zibara 2001)
CH	Freundlich	$C_{b,CH} = 0.087 \cdot C_f^{0.62}$	(Elakneswaran, Nawa & Kurumisawa 2009)
FS	Freundlich	$C_{b,Friedel's\ salt} = 0.31 \cdot C_f^{0.46}$	(Elakneswaran, Nawa & Kurumisawa 2009)
C_3S	Freundlich	$C_{b,C_3S} = 6.65 \cdot C_f^{0.334}$	(Zibara 2001)
C_2S	Freundlich	$C_{b,C_2S} = 7.89 \cdot C_f^{0.136}$	(Zibara 2001)
AFt	Freundlich	not clear	(Elakneswaran, Nawa & Kurumisawa 2009; Florea & Brouwers 2012)

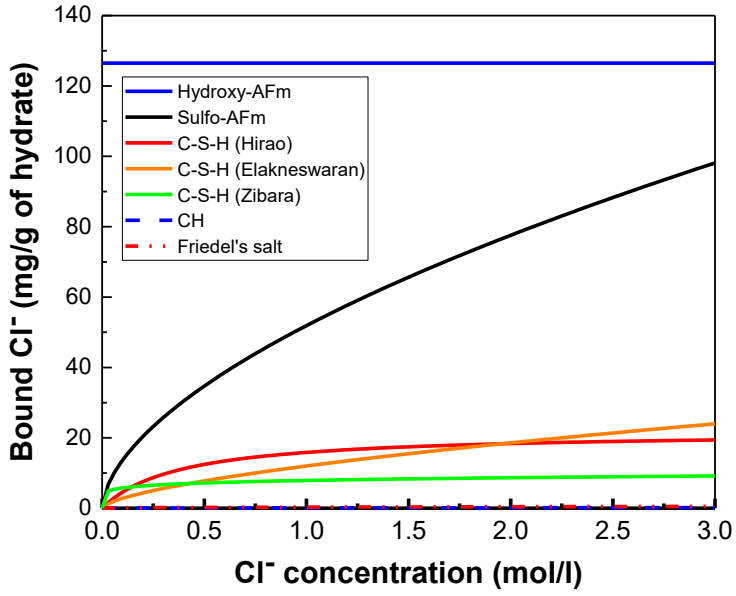

Figure 2.12. Chloride binding capacity of cement hydrates including hydroxy-AFm, sulfo-AFm, C-S-H, CH and FS at 11% RH (Birnin-Yauri & Glasser 1998a; Elakneswaran, Nawa & Kurumisawa 2009; Florea & Brouwers 2012; Hirao et al. 2005; Zibara 2001)

2.2.4.4 Chloride binding in SW

Sodium chloride is the main chloride source in SW, and the magnesium and calcium content is too low to cause any significant enhancement of chloride binding (De Weerdt, Orsáková & Geiker 2014). Therefore, the chloride binding of Portland cement hydrated in SW is similar to that in NaCl solution, which performs lower than that in calcium chloride or magnesium chloride. According to the aforementioned binding capacity, in SW concentration (0.546 M), the total bound chloride by cement hydrates can be divided as 49% to hydroxy-AFm, 20% to sulfo-AFm, 28% to C-S-H, and 3% to CH and FS (Florea & Brouwers 2012), as described in Figure 2.13. In Figure 2.14, a schematic diagram is given to summarize the preferable chloride distribution in SW mixtures. It is proposed that the conversion of the AFm phase to FS seems the only significant mechanism for chemically binding chloride; most of the binding mechanisms are either lower effective or else do not work in low chloride concentration. It should also be noted that chloride absorption is the dominant binding mechanism which is probably reversible. Free chlorides and bound chlorides are accordingly hard to distinguish rigorously (Galan & Glasser 2015).

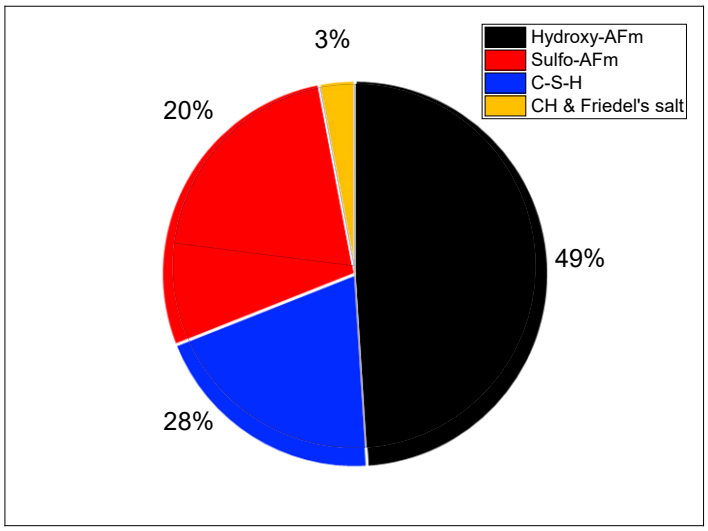

Figure 2.13. The distribution of bound chloride in OPC hydrates in SW (Florea & Brouwers 2012)

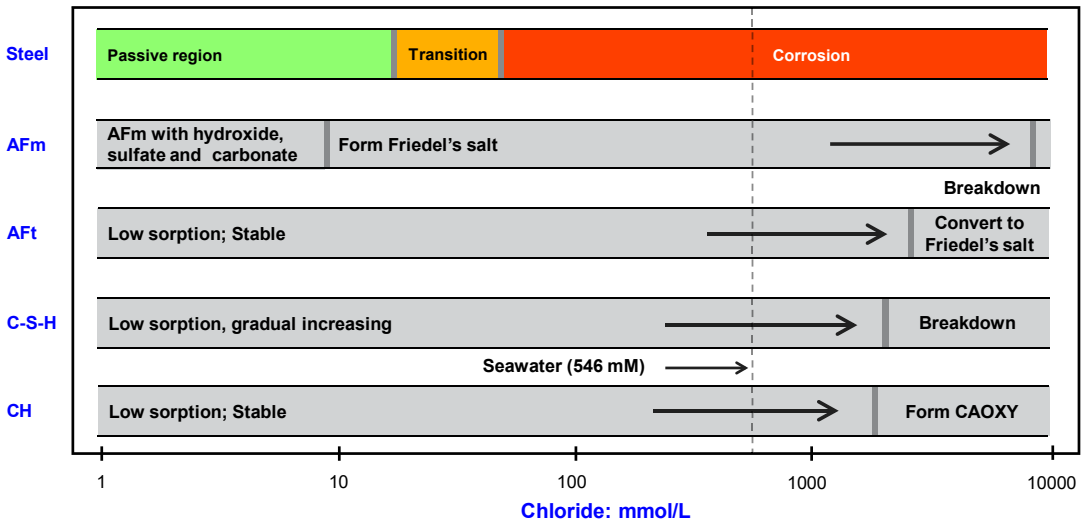

Figure 2.14. Chloride binding mechanism and distribution versus chloride threshold for steel corrosion in a range of concentration (1 – 10^4 mM), assuming aqueous pH is 12.5 and the temperature is 25 °C. Data from the study of Chalhoub *et al*. (Chalhoub, François & Carcasses 2019), Jones *et al*. (Jones et al. 2020), Damidot *et al*. (Damidot & Glasser 1992), Stark *et al*. (Stark & Bollmann 2000), Zibara (Zibara 2001), and Hou *et al*. (Hou et al. 2018)

2.3 Performance of seawater-mixed concretes

Based on the existing studies, the negative effects and specific properties of SW-mixed concrete are discussed. To alleviate the potential defects, various methods have been proposed and adopted to improve concrete performance, as discussed separately.

2.3.1 Superplasticizer and retarder

It is generally believed that SW cement paste has lower workability and flowability due to the rapid hydration effect at an early age (Younis et al. 2018). Therefore, using a superplasticizer (SP) and retarder is recommended in SW-mixed concrete. Li *et al.* (2019) compared the SP effect of cement paste with FW and SW in Figure 2.15. The result showed that the slump increases significantly when SP is added over 1%, though the slump of SW remains a slightly lower value than that of FW. The difference between the two samples is gradually narrowed in slump value if SP dosage reaches 2% or more, indicating the lower workability in the cement-SW mixtures can be thoroughly improved by SP. Furthermore, the improvement was about 12 – 18% of compressive strength in FW, but even 16 – 23% of that in SW, which exhibits the increase of compressive strength by SP is even greater in SW. Younis *et al*. (2018) improved the fresh properties of SW-mixed concrete to achieve a comparable degree to FW-mixed concrete, by adding a retarder with a concentration of 0.25 L/m^3 and an additional 15% more superplasticizer. Meanwhile, if the excessively rapid hydration in SW is eliminated by using the chemical additives, the mechanical performance can also be effectively improved (Younis et al. 2018).

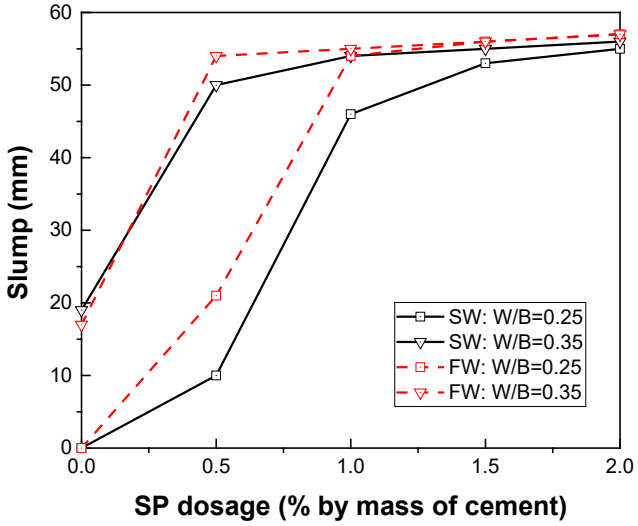

(a) Slump versus SP dosage

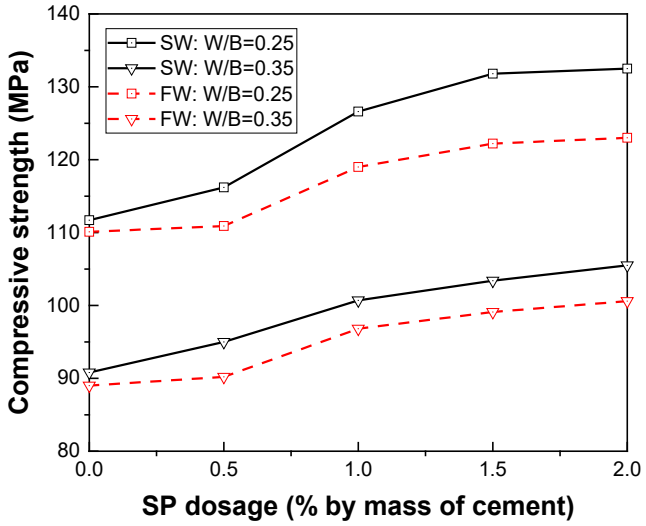

(b) Compressive strength at 28-day versus SP dosage

Figure 2.15. The effect of SP on slump and compressive strength in SW and FW (Li et al. 2019)

2.3.2 Supplementary cementing materials

Generally, the use of supplementary cementing materials (SCMs), such as blast furnace slag (BFS), fly ash (FA), silica fume (SF), and metakaolin (MK) that can modify binder mineralogy has shown a great influence on durability (Choi, Kim & Lee 2006; Gruber et al. 2001), by improving mechanical properties (Japan Concrete Institute 2015; Shi et

al. 2011), reducing chloride diffusivity (Thomas & Bamforth 1999), increasing chloride binding (Justnes 1998; Shi et al. 2012; Thomas et al. 2012) and refining pore structure (Linderoth, Johansson & Wadsö 2020; Skibsted & Snellings 2019). The main mineral composition as silica, alumina, and CC oxide content of SCMs used in related studies is summarized in Figure 2.16. For the potential defects in SW mixtures, the effect of SCMs has been investigated, which can be divided into two parts and are discussed separately herein.

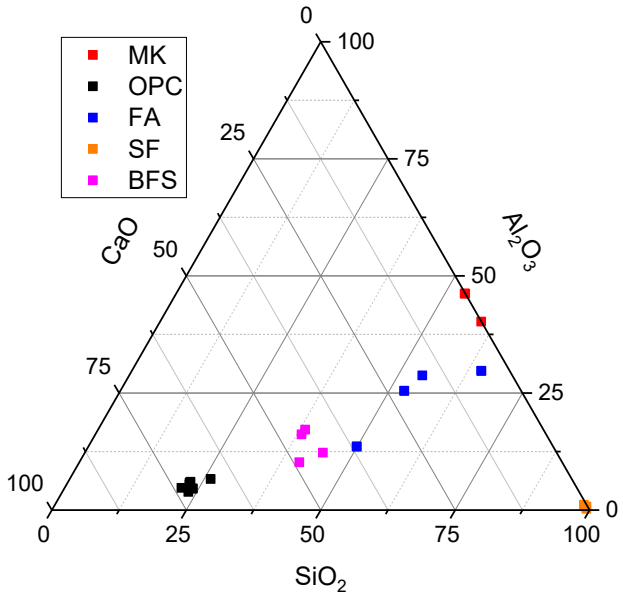

Figure 2.16. The ternary diagram of silica, alumina and calcium oxide content in SCMs (Data from the SCMs used in the related studies).

2.3.2.1 Effects on fresh and hardened properties

Numerous studies have investigated the effect of BFS in SW composites and are consistent with the finding that BFS increases the mechanical properties of SWC. Table

2.6 summarizes the SCMs effect on the compressive strength in the SW-mixed composite. Katano *et al.* (2013a) used BFS to partly replace OPC with a ratio ranging from 30% to 70%. The result shows that the compressive strength decreases with the increase of BFS. However, a higher strength can be observed in SW-mixed composite relative to the FW-mixed composite, and the enhancing effect is even greater at the early stage, despite the lower strength value. For example, when the blending ratio of BFS is 30%, the compressive strength is 37% higher in SW mixtures at 7 days, and the figure reaches 50% or more when the blended ratio is over 50%. The result indicates that SW can promote the hydration of BFS, due to the higher content of alumina than OPC to develop more AFm hydrates. Similar observations have also been identified by Otsuki *et al.* (2011) that the compressive strength ratio has the largest value of 1.62 on the first day of hydration. The test results demonstrate that the hydration degree of BFS in the SW-mixed composite is 5-30% higher than that in the FW-mixed composite. Li *et al.* (2018) also observed enhanced hydration stimulated by SW, which presents as an early occurrence of the main hydration peak for nearly 2 hours. Due to the stimulated hydration in SW-mixed composite, a slightly lower slump is presented in the BFS-mixed mixtures than OPC (Otsuki et al. 2011), while a small increase of slump value is determined in some other studies (Nishida et al. 2015; Otsuki et al. 2014). The differences vary only over narrow limits, proving that the effect of using BFS on the workability of SW mixtures is not significant. Li *et al*. (2015) studied the SW mixtures incorporated with MK. The result showed that the porosity was decreased with a refined

pore structure. Analogously, Cheng *et al.* (2018) investigated the SW mixtures incorporated with MK and BFS and measured that the permeability of concrete was reduced and the mechanical properties of ITZ were improved, due to the filling effect and pozzolanic reaction of SCMs (Cheng et al. 2018). Khatibmasjedi (2019) found that adding 20% FA significantly increased the drying shrinkage from 738 μm to 1370 μm in SW-mixed composite after 60 days, which further aggravates the cracking risk of SW mixtures. Therefore, attention should be taken when combining use SW and FA in cement mixtures.

Table 2.6. The SCMs effect on the compressive strength in SW-mixed concretes

Cementitious type	W/b ratio	Curing condition	Compressive strength (MPa) FW	SW	SW/FW	Reference
OPC 70% + BFS 30%	0.5	Moist curing	21.52 (7 days) 31.76 (28 days) 39.94 (91 days)	29.40 (7 days) 38.09 (28 days) 47.50 (91 days)	1.37 1.20 1.19	(Katano et al. 2013a)
OPC 50% + BFS 50%	0.5	Moist curing	15.33 (7 days) 26.09 (28 days) 36.97 (91 days)	23.00 (7 days) 29.49 (28 days) 31.51 (91 days)	1.50 1.13 0.85	(Katano et al. 2013a)
OPC 30% + BFS 70%	0.5	Moist curing	10.76 (7 days) 20.23 (28 days) 27.01 (91 days)	17.16 (7 days) 20.42 (28 days) 22.61 (91 days)	1.59 1.01 0.83	(Katano et al. 2013a)
Ground BFS cement	0.5	Moist curing	45.35 (7 days) 57.51 (28 days)	48.27 (7 days) 64.32 (28 days)	1.06 1.12	(Etxeberria, Gonzalez-Corominas & Pardo 2016).
OPC 80% + FA 20%	0.5	Moist curing	20.56 (7 days) 30.43 (28 days) 35.79 (91 days)	23.55 (7 days) 32.33 (28 days) 38.95 (91 days)	1.15 1.06 1.09	(Katano et al. 2013a)
OPC 30% + BFS 70%	0.5	Moist curing	4.62 (1 day) 28.95 (7 days)	7.48 (1 day) 35.00 (7 days)	1.62 1.21	(Otsuki et al. 2011)

			45.79 (28 days)	49.42 (28 days)	1.08	
			60.21 (91 days)	63.51 (91 days)	1.05	
OPC 80% + FA 20%	0.26 + SP 1%	Moist curing	66.5 (28 days)	58.0 (28 days)	0.87	(Sena-Cruz et al. 2018)
OPC 35% + BFS 65%	0.34	Cured in FW	38.04 (3 days)	39.22 (3 days)	1.03	(Younis et al. 2018)
			50.72 (7 days)	41.24 (7 days)	1.05	
			68.76 (28 days)	62.22 (28 days)	0.90	
			73.46 (56 days)	68.10 (56 days)	0.93	
OPC 35% + BFS 65%	0.34	Cured in SW	40.0 (3 days)	39.22 (3 days)	0.98	(Younis et al. 2018)
			53.59 (7 days)	53.07 (7 days)	0.99	
			67.19 (28 days)	61.70 (28 days)	0.92	
			71.11 (56 days)	68.10 (56 days)	0.96	
OPC 85% + SF 15%	0.2 + SP 2%	Moist curing	89.31 (3 days)	91.35 (3 days)	1.02	(Li, Farzadnia & Shi 2018)
OPC 70% + SF 30%	0.2 + SP 2%	Moist curing	89.97 (3 days)	91.42 (3 days)	1.02	(Li, Farzadnia & Shi 2018)
OPC 75% + BFS 25%	0.2 + SP 2%	Moist curing	84.40 (3 days)	88.45 (3 days)	1.05	(Li, Farzadnia & Shi 2018)
OPC 50% + BFS 50%	0.2 + SP 2%	Moist curing	80.75 (3 days)	84.59 (3 days)	1.05	(Li, Farzadnia & Shi 2018)

2.3.2.2 Effects on chloride binding capacity

SCMs alter the composition of cement hydrates and, thus, the chloride binding capacity (Justnes 1998; Shi et al. 2012; Thomas et al. 2012). For example, MK, which comprises approximately 40% alumina presents a superior capacity of binding chloride as the formation of AFm hydrates (Li et al. 2015; Shi et al. 2015). Shi *et al.* (2015) added MK (0 – 6%) in SW mixtures to determine the chloride binding effect. The result indicates 48 – 55% of total chloride bound by 3 days and 67% of that by 28 days. Due to the

negligible calcium oxide content in MK, it is also suggested that calcium is necessary to stimulate the binding ability of MK, which reveals the MK to lime ratio as the influential factor (Zibara 2001). Lesser chloride binding, by contrast, can be detected in BFS and FA, which contains alumina (10 – 25%). Dhir *et al.* (1996) found that at a high BFS replacement level of 67%, the chloride binding is 5 times that of OPC measured at 5 M chloride in 14 days. The high chloride binding capacity for BFS also was verified by Li *et al*. (Li, Farzadnia & Shi 2018) that chloride concentration of 1.75mg/g can be decreased to 1.46 mg/g and 1.33 mg/g for specimens with 25% BFS and 50% BFS, respectively in 3 days. Nevertheless, it should be noted that there is an optimum BFS replacement for binding capacity, and when adding BFS to excess, the chloride binding becomes lower than OPC, which is supported by Zibara (2001) who even studied the 100% BFS paste. By contrast with BFS, FA seems too inert to bind chloride at the early stage. Otsuki *et al.* (2014) observed a similar chloride binding capacity in OPC and OPC with 30% FA-replaced blends exposed to SW for 4 months. Shi *et al.* (2011) found that however, adding FA reduced the chloride binding instead of increase as also proposed by Cheewaket *et al.* (2010). Therefore, there is no clear generic relevance in the chloride binding capacity of FA, probably due to the large diversity in mineral composition (see Figure 2.16) and the degree of hydration (Zibara 2001). Furthermore, it should be noted that not all of the alumina in fly ash possesses chloride binding ability. For instance, much of alumina in fly ash is presented in crystalline components such as mullite, which cannot form AFm phases during further hydration (Thomas et al. 2012).

Another reason is that strätlingite is formed when FA or BFS is added as the AFm phase with aluminosilicate anion $[AlSi(OH)_8]^-$, which also presents no chloride binding capacity (Galan & Glasser 2015).

SF contains almost no aluminate and, hence, has the lowest binding ability and results in greatly reduced chloride binding capacity in OPC (Mangat & Molloy 1995; Shi et al. 2011; Thomas et al. 2012). Nilsson *et al*. (1996) propose the effect of SF on chloride binding in three ways: (1) increase of the specific area of pores and C-S-H which increase chloride binding; (2) reactions with C_3A consuming the AFm phase which may decrease chloride binding; (3) reactions with alkalis reducing pH, which may increase binding. For the third effect, the decrease in pH resulted from the substitution of OPC, corresponding to a diluted chloride binding of OPC. However, adding SF leads to the formation of C-S-H with a lower Ca/Si ratio, which has been proved to reduce the amount of chloride adsorbed on the surface of C-S-H (Beaudoin, Ramachandran & Feldman 1990; Yoon et al. 2014; Zibara 2001). In FA and BFS, the formation of low Ca/Si C-S-H also occurs, while the shortages are filled up by higher content of alumina and results in increased binding (Thomas et al. 2012). Therefore, it shows a negative in SF but positive in FA and BFS on enhancing chloride binding of OPC.

2.4 Mechanism discussions

The SW-mixed concrete has been studied for over a century (Abrams 1924), while the general view on using SW in concrete structure remains conservative. Still, construction

specifications in various countries can be summarized as mentioned by Neville (Neville 2001) that SW must never be used in reinforced concrete; never be used in prestressed concrete; and preferably not be used in plain concrete, which often contains some steel. The high chloride content has always been the trickiest problem in SW-mixed concrete that significantly increases the risk of corrosion in reinforcement and structure failure. In this section, the most concerned research problems of SW mixtures will be discussed in detail, based on the current studies.

2.4.1 Characteristics and deterioration in seawater concrete

The effect of chloride is the main factor leading to the discrepancy between SW and conventional mixtures. Due to the chloride promoting hydration, the rapid exotherm, shorter setting period, and higher early strength are presented in SW mixtures undoubtedly. However, it seems that SW mixtures are more sensitive to the environment: no matter in FW curing, SW curing, or tidal curing, SW mixtures present lower mechanical properties than those of FW mixtures at the late stage, except for the moist curing condition. The lower strength development in SW mixtures may be explained by the higher water absorption and the significant leaching effect of alkalis and calcium hydroxide (Khatibmasjedi 2018). Furthermore, the shrinkage of SW mixtures, especially the drying shrinkage, is aggravated by its hygroscopic property, which should be noted: a 17% higher drying shrinkage can be observed in SW-mixed concrete and, more seriously, over 80% higher drying shrinkage in SW mixtures with

20% of FA, compared to the FW-mixed concrete (Khatibmasjedi et al. 2019). Hence, the high risk of shrinkage cracking can also cause deteriorations in SW mixtures.

2.4.2 Limited chloride binding effect in seawater concrete

It seems feasible to reduce chloride content by cementitious materials themselves through chemical binding or physical adsorption. However, it is doubtful that the low chlorine required for reinforcement protection can be reached through the practical binding effect. First, assuming that all chloride ions have been bound by OPC, there will be more than 30% of the chloride bound by C-S-H and other cement hydrates by physical adsorption (see section 3.4). Compared to the chemical binding of chloride forming FS, the physical adsorption is reversible (Galan & Glasser 2015) that the bound chloride can be released easily when the external concentration changes. Second, during the long-term carbonization, the C-S-H phase decomposes inevitably and the chloride binding capacity is significantly reduced. Also, the FS converts to carbo-AFm gradually, with the chloride substituted no longer bound afterward. In these two aspects, the chloride binding effect of OPC appears to be temporary and limited, because chloride ions failed to be weeded out from the mixtures throughout the process; even if applying some effective SCMs, the risk of chloride corrosion cannot be eliminated in SW mixtures. Therefore, SW should not be used in concrete contains steel reinforcement or components. In other words, the research on anti-chloride-corrosion materials is the more significant development trend of SWC.

2.4.3 Applicability of seawater concrete

Now that chloride corrosion has always been a risk in SW mixtures, concrete without steel has a great potential for application, such as plain concrete and fiber-reinforced polymer (FRP) composites (Ahmed et al. 2020; Li, Zhao & Raman 2018; Sena-Cruz et al. 2018; Soares et al. 2020; Xiao et al. 2017). Because no component can be corroded by chloride ions, special consideration on corrosion is no longer required in SW mixtures. The use of SW can be regarded as adding an accelerator of sodium chloride, calcium chloride, and magnesium chloride that leads to rapid development of early strength. Three aspects should also be noted in SW mixtures. Firstly, the main chloride source in SW is sodium chloride, which is alkaline in a reactive state. Hence, the risk of alkali-aggregate reaction in SW mixtures is increased (Kawamura & Takeuchi 1996; Nixon et al. 1988). Secondly, considering the leaching effect on strength reduction, it is not advised to use SW mixtures as long-used structures in water-level fluctuation zones, or those exposed to rain. Thirdly, continuous dampness and efflorescence occur on the surface of the SW mixtures, due to the moisture absorption in higher salinity. Therefore, in the structures where the appearance is considered, or a plaster finish is to be applied, the SWC mixtures are not recommended (Neville 1995).

2.4.4 Discussions of prospects on seawater concrete

Since there are many shortages observed in SW mixtures, it should, cautiously, be worth considering the prospects of the application. The most significant advantage of SWC is to obtain the water easily, rapidly, and locally, which is prominent in some

coastal areas and island areas where the FW resource is scarce. Unfortunately, since convenience has been chosen, the performance of concrete has to be sacrificed, manifesting SW as a two-edged sword. Due to the risk of corrosion and deterioration that cannot be eliminated, SW mixtures should never be used in concrete components that are crucial to structures. The long-term safety of structures should not be belittled, although using SW saves manpower and material resources. Besides, many researchers believe that using SW in concrete is helpful to relieve the stress of FW shortages, while it is too idealistic. Considering the water used in concrete manufacturing, such as water for cooling clinker, water for washing aggregates, water for energy, and water for transportation et al. The mixing water accounts only for 10 – 15% of total water consumption and 2.5 – 4% of water withdrawal for concrete production (Miller, Horvath & Monteiro 2018). Therefore, improving the durability of concrete for prolonging its service life is an effective way to alleviate water shortages, not just using SW directly as a mixture.

However, SWC is a promising research prospect, because technology is progressing through intrepid exploration. Research needs are still promoted by the trends of development in SW mixtures, summarized as follows: firstly, SW mixtures are available to cover the demand of non-crucial and short-term structures, and meanwhile, specification is needed to standardize the use of SW, due to the varying salinity in different marine areas; secondly, SW mixtures can be used in some structural concrete, where FRP is applied instead of steel to avoid corrosion. Once the problem of the poor

modulus of elasticity, shear strength, and durability of FRP can be solved, a great potential would be exhibited in the use of SW mixtures; thirdly, in areas where FW is significantly scarce and SW has to be used in construction, it is feasible to use SW even in reinforced concrete, as long as the chloride concentration is reduced as far as possible through desalination combined with using SCMs.

2.5 Conclusions

Massive resource consumption in concrete production has been an increasing environmental concern. Utilizing SW instead of FW as mixing water is a feasible measure to alleviate water shortages in coastal and island regions. The study in this section has critically reviewed the SW-induced performance changes of OPC, specifically, in the aspects of fresh properties, mechanical properties, transport properties, shrinkage properties, and hydration kinetics. Due to the accelerated early hydration, SW mixtures present lower workability, higher early strength, denser early structure, and greater shrinkage. The long-term properties of SW mixtures are more vulnerable to environmental factors, developing slower in underwater or tidal conditions due to the leaching effect of alkalis and calcium hydrates. Additionally, according to the discussed effect of various SW-related ions, the hydration mechanism in SW is dominated by chloride. The AFm phase, such as hydroxy-AFm and sulfo-AFm, is the most effective chloride binding phase with the highest binding capacity. The physical adsorption of chloride by C-S-H and other cement hydrates accounts for only 30% of total bound chloride. The chloride binding effect of cement hydrates is irreversibly

deteriorated when carbonation occurs, indicating the chloride binding is temporary and limited. Although the performance of SW mixtures can be improved through the additive and admixture, the risk of chloride corrosion cannot be eliminated, and it would significantly limit the scope of its application. Therefore, SWC should not be used in components that are crucial to structures, unless anti-chloride-corrosion materials are applied instead, or desalination of SW is conducted. In short, this review summarizes and compares the sustainable but defective SW mixtures and proposes the viewpoints, based on the advanced research progress.

CHAPTER 3. HYDRATION OF PORTLAND CEMENT WITH SEAWATER: PHASE EVOLUTION

This section identified the compositions of cement clinker, cement hydrates, and pore solutions of pastes made with DW and SW over the hydration time. Phase identification of the solid and liquid phases was performed by combining TG, XRD and ICP-OES. The Rietveld refinement approach has been adopted to characterize phase evolution quantitatively.

3.1 Raw materials

Portland cement (PC) was used in this study, conforming to Chinese standard GB 8076–2008, which was used as the reference cement without blending any supplementary cementitious materials. Through X-ray fluorescence (XRF) and quantitative X-ray diffraction (QXRD) with the Rietveld refinement method, the chemical compositions of the PC and phase compositions were determined in Table 3.1. In addition, the soluble alkalis were measured in the paste suspension with a w/b ratio of 10 after 5 min agitation, and they were presented as alkali sulfates (Lothenbach et al. 2008). By comparing the results from XRF, the missing part of alkalis in phase composition was considered in the clinker phases as the solid solution, which was released gradually with the dissolution of the clinker.

Table 3.1 also shows the physical properties of PC and the mineral composition obtained through the Bogue calculation (Bogue 1955a). Substitute SW, in which the

concentration is close to natural SW, was prepared according to the ASTM (2013). Table 3.2 gives the theoretical concentration of SW prepared according to the standard and the practical concentration used in the study, determined by IPC-OES (Spectro Blue, Analytical Instruments GmbH). The DW of the identical mass was used to prepare the reference sample.

Table 3.1. Composition of the PC

Oxide composition	Content (wt.%)	Phase composition	Content (wt.%)
CaO[a]	63.57	Alite [b]	57.4
SiO_2[a]	20.58	Belite [b]	17.0
Al_2O_3[a]	4.97	Aluminate [b]	7.60
Fe_2O_3[a]	3.76	Ferrite [b]	10.58
MgO[a]	1.00	Periclase [b]	0.10
SO_3[a]	2.10	Gypsum	2.67
Na_2O[a]	0.48	Cao (free)	0.95
K_2O[a]	0.72	K_2SO_4 [c]	1.20
free-CaO[a]	0.75	Na_2SO_4 [c]	0.37
Ignition loss	1.40		
Present as a solid solution in the clinker phases			
K_2O [d]	0.07		
Na_2O[d]	0.32		
MgO[d]	0.90		
SO_3 [d]	0.10		

Note: the specific surface area is 355 m^2/kg; the specific gravity is 3.12g/cm^3

[a] Determined from XRF results

[b] Calculated from Rietveld analysis

[c] Calculated from the concentration of the solution dissolved in the soluble alkalis

[d] Calculated from the chemical molecular weight

Table 3.2. Ions concentration of the SW used for mix design (mmol/l)

Dissolved ions	Na^+	K^+	Ca^{2+}	Mg^{2+}	Cl^-	SO_4^{2-}
Value in the standard	484.3	10.5	10.6	54.9	565.5	29.2
Value in the study	462.0	9.6	12.0	52.0	558.1	30.9

3.2 Experimental methodologies

All experiments were conducted using a PC paste prepared with DW and SW at the same w/b ratio of 0.5. The cement paste was cast into the sealed polyethylene cylinders (to avoid the ingress of CO_2) and stored at an ambient temperature of 20 ℃. The evolution of the mineralogical composition of hydrated PC paste was characterized using thermogravimetric/derivative thermogravimetric analysis (TG/DTG) and XRD/Rietveld analysis at various testing time intervals. To verify the simulation results of the evolving dissolution-precipitation kinetics of minerals and the experimental concentration of the solution, ICP-OES was adopted to determine the ion concentration of the pore solution.

3.2.1 Thermogravimetric analysis

For TG analysis, the apparatus STA449 F5 JUPITER was used to determine the thermal decomposition of samples. Representative cement paste cured for the designated time (the short-term samples of 1, 2, 8, 12, and 18 hours; the other samples of 1, 7, 28, 60, and 90 days) were prepared with DW and SW. The samples were ground into powder or

filtered if the cement paste was not set after the designated time. Isopropanol was used to remove the free water by solvent exchange for 7 days, which was renewed after 1 hour, 1 day and 3 days. The samples were then dried in a vacuum desiccator with water-absorbing agents afterwards for more than 3 days. 30 mg of each sample was determined the mass change in an alumina crucible at 10 ℃/min up to 1000 ℃, purged with nitrogen. CH was calculated from the thermal decomposition between 420–470 ℃. The mass loss curve of CH was identified between the extended lines from the onset to the end at the temperature of the inflection point to eliminate the influence of C-S-H dehydration.

A linear relationship can be obtained between the content of CH and the corresponding peak area from the differential scanning calorimetry (DSC) curves, according to the enthalpy change before and after the dehydration. The method was used to verify the calculation of CH, as described in the previous study (Li, Li, et al. 2020a). However, the AFt and FS cannot be accurately determined due to the peaks of the dehydration temperature overlapped and hardly to be separated. Therefore, XRD analysis was required with the result of TG to qualify the other minerals and carry out semi-quantitative calculations.

3.2.2 X-ray diffraction analysis

As for sample preparation for the XRD test, representative samples of hydrated cement paste made with SW and DW were crushed into particles with a diameter of 2–3 mm after being cured for 1, 2, 8, 12, 18 hours, and 1, 7, 28, 60, and 90 days. The crushed

particles were dried by isopropanol and the vacuum desiccator with the same process as the TG-related samples. Before XRD determination, the dried samples were crushed into powder and mixed with rutile (20% in mass) as the internal standard substance for the subsequent quantitative calculation. The XRD patterns were collected through an X-ray Diffractometer (X'Pert^3 Powder, Malvern Panalytical) with 2θ, the diffraction angle, ranging from 4° to 80° at 0.02°/step, employing Cu–K alpha radiation (λ = 1.54056 A°). The Rietveld refinements were performed by the X'Pert Highscore Plus. The structural information of the identified crystal phases was initially taken from the Crystallography Open Database (CoD). The scale factor, lattice cell, peak shape, and preferred orientation parameters of the related anhydrous phases were adjusted to obtain accurate initial models. Appropriate pattern fitting for the good refinements (weighted profile R-factor (Rwp) was lower than 10%, and goodness-of-fit (GoF) kept in the acceptable range (Toby 2006)) was strived achieved. The strictly determined CH content from TG was used as the reference for the refinement, whose reliability has been proved acceptable (Soin, Catalan & Kinrade 2013). The ill-crystallized phases, such as C-S-H and hydrogarnet, were classified as amorphous phases and calculated in total by the internal standard method.

3.2.3 Extraction and analysis of pore solution

The methods adopted to collect the pore solution depend on the extraction time. For the short-term experiments (1 hour), pore solution was collected by vacuum filtration using 0.45 μm nylon filters. For the hardened pastes (over 1 hour, 1, 7, and 28 days), samples

were in sealed polyethylene cylinders until the designated time. The pore solution was extracted using the steel die pressure method at a loading rate of 1.5 kN/s up to 650 kN. A carbon removal device was used before collecting the pore solution, followed by immediately filtering out the precipitated solid phase using 0.45 μm nylon filters. One part of the collected solution used for element measurement was acidized by HNO_3 (3.6% by volume) to prevent secondary mineral precipitation. Elements including Na^+, K^+, Ca^{2+}, SiO_4^{4-}, SO_4^{2-}, Cl^-, and $[Al(OH)_6]^3$ were determined by ICP-OES. The other part of the solution was used to determine the potential of hydrogen (pH). These processes mentioned above are demonstrated schematically in Figure 3.1.

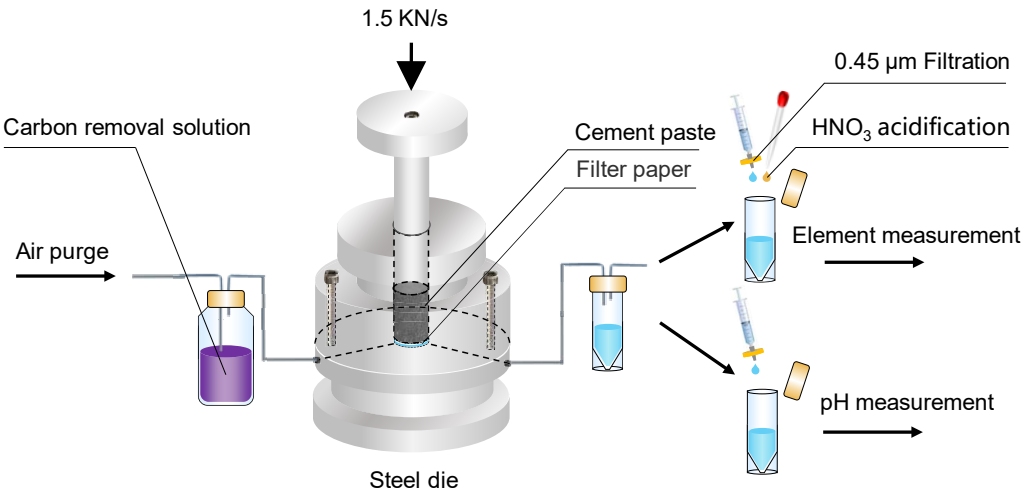

Figure 3.1. Schematic diagram of extraction of pore solution

3.2.4 Microstructure analysis

The microstructure of hydrated cement paste was investigated by the scanning electron microscope (SEM) Zeiss Supra 55vp combined with energy-dispersive X-ray spectrometry (SEM-EDS). The dried XRD-related particles were used as the samples.

Before the SEM test, the samples were crushed and exposed to a new surface, purged with nitrogen to clean the surface and coated with Au/Pt alloy(80/20) with a thickness of 5 nm.

3.3 Experimental results

This section investigated the evolution of the solid phase and liquid phase in the hydration of PC with SW and DW. Quantitative/semi-quantitative analysis was performed by TG/QXRD and ICP-OES to characterize the hydration process.

3.3.1 Phase composition in cement paste

3.3.1.1 Thermogravimetric analysis

The TG/DTG curves of PC hydrated in DW and SW from 1 day to 90 days are shown in Figure 3.2, by which the mass of CH can be calculated in Table 3.3 and used for aligning the quantitative X-ray diffractometry. It can be seen from the weight loss curves that the hydration degree of cement in SW was generally higher than that hydrated in DW, especially at the early stage (within 7 days). Due to the accelerated cement hydration in SW, more AFt was formed in 1 day, evidenced by the characteristic peak at around 100 ℃. Affected by chloride ions, some of the AFt that should have been converted to monosulfoaluminate (sulfo-AFm) at the late stage was transformed into FS. In addition, more AFt can be observed at the late stage, which will be further confirmed and discussed in the following section. Since the cement did not contain carbonated such as limestone, the carbonization did not occur during the whole hydration process. Therefore, weight loss by decarbonization at about 700 ℃ was not observed. In this situation, the formation of CH was not affected by the carbonization,

which, in turn, simplified the calculation to obtain a highly reliable quantified result of CH.

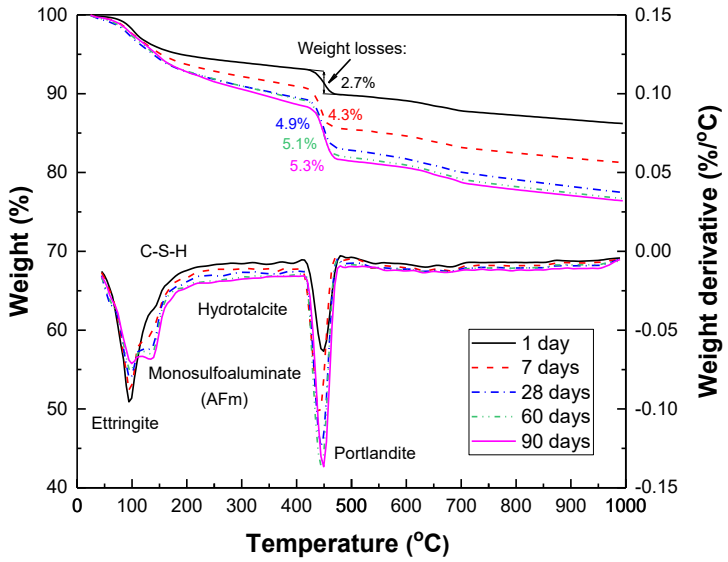

(a) TG/DTG curves of PC hydrated in DW

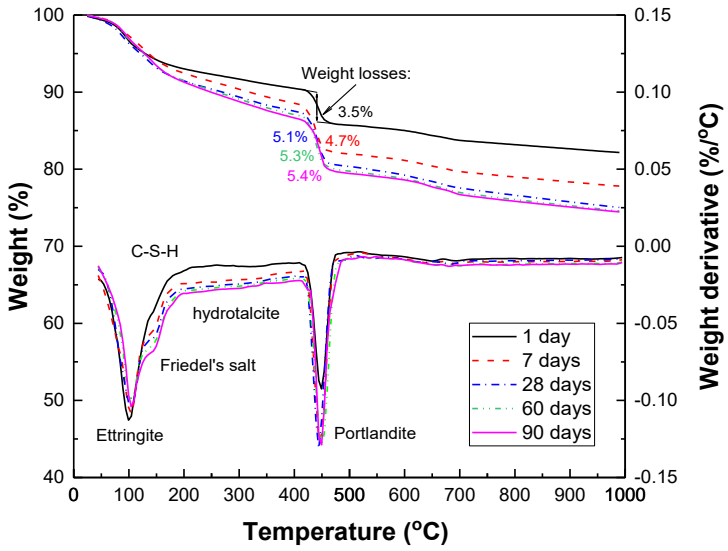

(b) TG/DTG curves of PC hydrated in SW

Figure 3.2. TG/DTG curves of PC hydrated in (a) DW and (b) SW after 1, 7, 28, 60, and 90 days of hydration

3.3.1.2 X-ray diffractometry analysis

Figure 3.3 shows the XRD patterns of PC pastes made with DW and SW hydrated between 1 hour and 90 days. The formation or consumption of the solid phase was closely related to the change in the peak intensity after being normalized by the rutile as the internal standard substance.

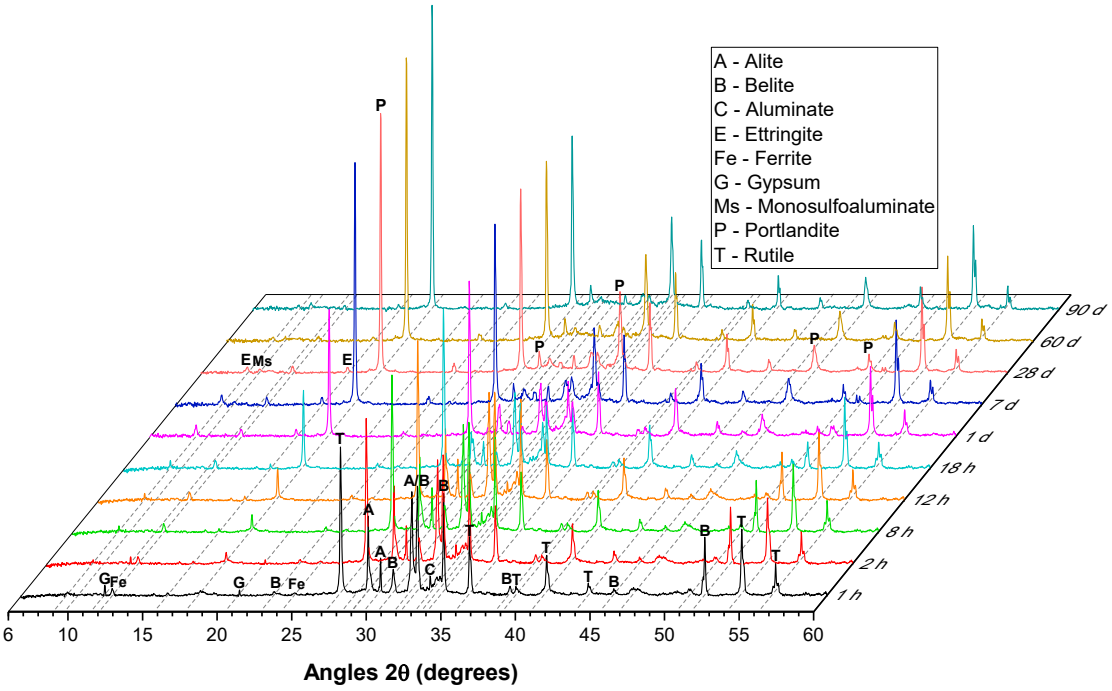

(a) XRD patterns of PC hydrated in DW

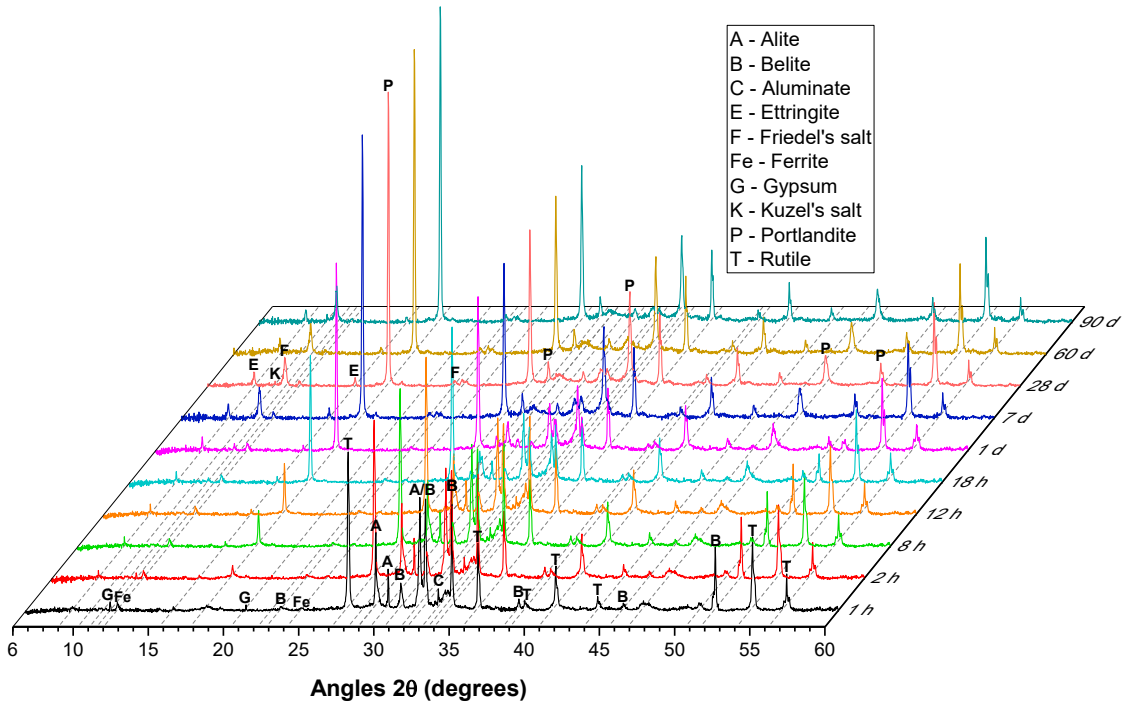

(b) XRD patterns of PC hydrated in SW

Figure 3.3. XRD patterns of PC hydrated in (a) DW and (b) SW after 1, 2, 8, 12, 18 hours, and 1, 7, 28, 60, and 90 days

The evolution of phase assemblage during the PC-SW hydration process was determined by QXRD, calibrated by the quantified CH ratio provided by the TG test. Similar characterization was also performed in the references with the PC-DW hydration process. The result is shown in Figure 3.4 and Table 3.3.

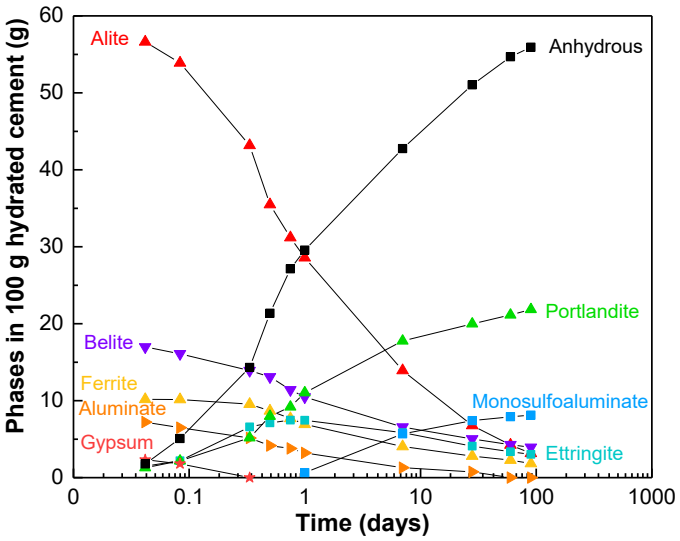

(a) Phase evolution of PC paste with DW

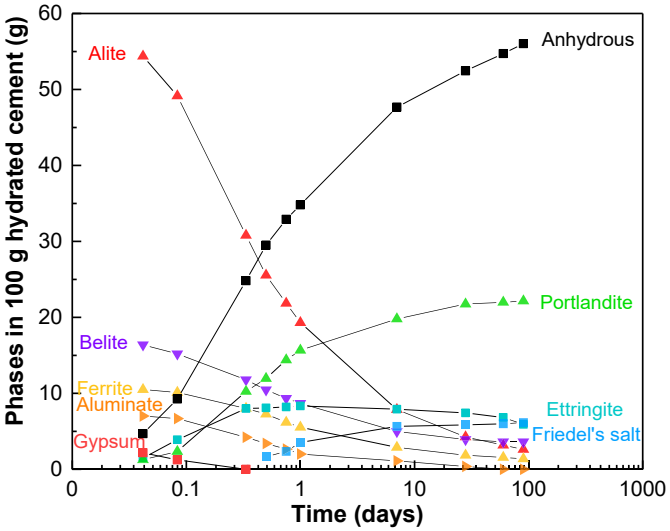

(b) Phase evolution of PC paste with SW

Figure 3.4. Phase evolution of PC pastes made with (a) DW and (b) SW, after 1, 2, 8, 12, 18 hours, and 1, 7, 28, 60, and 90 days

The hydration rate of PC in SW was generally higher than that in DW at the early stage. At the age of 8 hours, the hydration degree in SW was nearly 1.5 times that of DW from the significant variance in unhydrated clinker. The accelerated hydration was mainly dominated by Cl^- (Montanari et al. 2019), which significantly promoted the dissolution of gypsum and clinker and stimulated the formation of the hydrates. However, the

existence of gypsum is crucial to rapid hydration at the early stage. Cai *et al.* (2021) observed that without gypsum, the hydration rate of aluminate was significantly retarded in SW due to the flash setting effect (Taylor 1997) aggravated by rapid precipitation solid phases and enhanced flocculations between the suspended particles (Wang, Liu & Li 2018).

A significantly higher hydration degree of SW samples within 28 days can be observed from the stimulated hydration effect. The main hydrates, such as CH, AFt, and ill-crystallized C-S-H, were formed more in SW. At the late stage of 90 days, however, the hydration ratio of both was eventually comparable; there were nearly 5% of alite, 21% of belite, and 16% of ferrite remaining in anhydrous phases in both DW and SW samples, exhibiting that the acceleration effect in SW did not affect the hydration degree at the late stage.

Besides the accelerated effect on cement hydration, two significant differences in the hydrate phases can be observed in SW samples, which provided more detailed information than the TG test. First, the formation of sulfo-AFm was not observed in the SW samples throughout the whole hydration process, while FS and KS were detected instead due to the interaction between AFm phases and Cl^-. The layered double hydroxides (LDHs), such as FS and hydrotalcite, might be formed as the solid solution (characterized by the broad diffuse peaks at 11–11.5°). Another significant difference is the ratio of AFt at the late stage. At 18 hours, the AFt phase formed in DW was a maximum of 7.48% and then gradually reduced to 3.03% at 90 days. However, the AFt

formed in the SW samples was changed from 8.19% to 5.92% at the identical scope of hydration time. Therefore, the AFt seems to be more stable than that from the DW samples at the late stage. The result is consistent with the results reported in other studies (Frias et al. 2013; Li, Jiang, et al. 2021) and will be further discussed in the result of pore solution test.

Table 3.3. Phase composition of PC at various ages of hydration calculated by TG/QXRD (%)

Time (day)	Alite		Belite		Aluminate		Ferrite		Gypsum		AFt		CH		AFm phases		Amorphous phases	
	DW	SW	DW	SW	DW	SW	DW	SW	DW	SW	DW	SW	DW	SW	DW	SW	DW	SW
0	57.40	57.40	17.0	17.0	7.60	7.60	10.58	10.58	2.67	2.67	–	–	–	–	–	–	N/A	N/A
0.04	56.61	54.38	16.98	16.38	7.22	7.02	10.17	10.49	2.32	2.17	1.49	1.49	1.28	1.25	–	–	1.79	4.69
0.08	53.89	49.14	16.09	15.20	6.49	6.68	10.16	10.12	1.80	1.25	2.18	3.89	2.18	2.35	–	–	5.08	9.25
0.33	43.18	30.79	13.91	11.78	5.15	4.21	9.55	8.02	–	–	6.59	7.99	5.18	10.25	–	–	14.32	24.83
0.50	35.48	25.56	13.09	10.46	4.16	3.39	8.68	7.27	–	–	7.12	8.08	7.98	11.96	–	1.64	21.36	29.51
0.75	31.19	21.86	11.42	9.34	3.78	2.65	7.69	6.18	–	–	7.48	8.19	9.18	14.39	–	2.36	27.13	32.90
1	28.58	19.31	10.47	8.67	3.21	2.01	6.92	5.53	–	–	7.45	8.33	11.04	15.68	0.64	3.53	29.56	34.81
7	13.91	7.87	6.57	4.97	1.29	1.10	4.04	2.89	–	–	5.84	7.92	17.76	19.79	5.69	5.65	42.76	47.68
28	6.78	4.26	5.02	3.92	0.75	0.38	2.80	1.85	–	–	4.09	7.43	19.99	21.75	7.40	5.84	51.04	52.45
60	4.24	3.18	4.27	3.62	0.00	0	2.28	1.56	–	–	3.36	6.82	21.13	21.99	7.91	5.99	54.68	54.72
90	3.16	2.62	3.94	3.62	0.00	0	1.84	1.37	–	–	3.03	5.92	21.85	22.16	8.12	6.15	55.93	56.03

3.3.2 Elemental concentration in pore solution

From the ICP-OES test, the concentration results of the pore solution in PC-DW and PC-SW paste at various hydration times are shown in Figure 3.5 and Table 3.4. With no SW-related ions involved, the concentration of the PC-DW paste was mainly distributed in two ranges, divided by the time when gypsum was completely dissolved. Before the gypsum depletion, the pore solution was dominated by SO_4^{2-}, Ca^{2+}, K^+, Na^+ and OH^-. The continuous dissolution of gypsum kept the high concentration level of Ca^{2+} and SO_4^{2-}, forming AFt and CH as the major hydrates at this stage. The other main constituents of the cement, such as SiO_4^{4-} and $[Al(OH)_6]^3$, were initially very low but increased gradually along with the hydration.

After the gypsum was depleted, a notable change in various ions concentration can be observed between 5 and 24 hours. Due to the lack of direct supply from gypsum dissolution, Ca^{2+} and SO_4^{2-} were significantly decreased by a short formation of AFt and started to convert, or form directly, to AFm phases instead. Meanwhile, the concentration of OH^- had to rise to maintain the charge balance of the solution; SiO_4^{4-} and $[Al(OH)_6]^3$ were then slightly increased with the increasing pH according to the solubility required. With the increasing degree of hydration accompanied by the consuming liquid volume, alkali was released continuously into the gradually concentrated pore solution. Therefore to the late stage, the pH kept increasing gradually and resulted in an increase of SiO_4^{4-} and $[Al(OH)_6]^3$ and a decrease of Ca^{2+} based on the

solubility. Other studies also proposed consistent trends (Le Saoût et al. 2013; Lothenbach et al. 2008; Lothenbach & Winnefeld 2006).

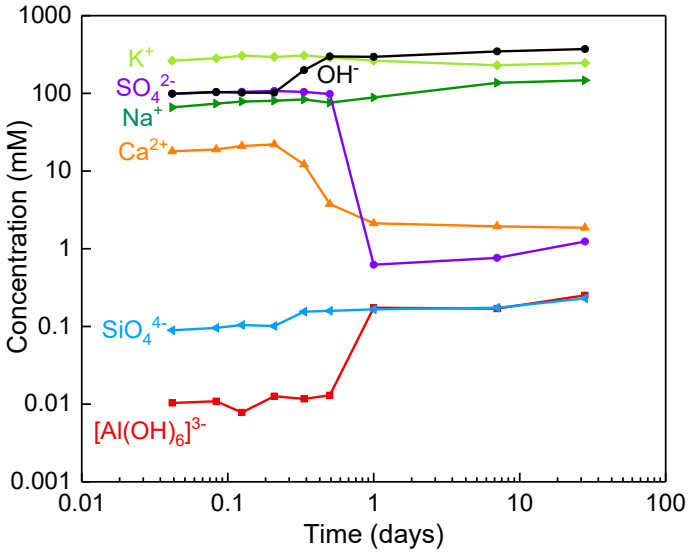

(a) Ions concentration of pore solution in PC-DW paste

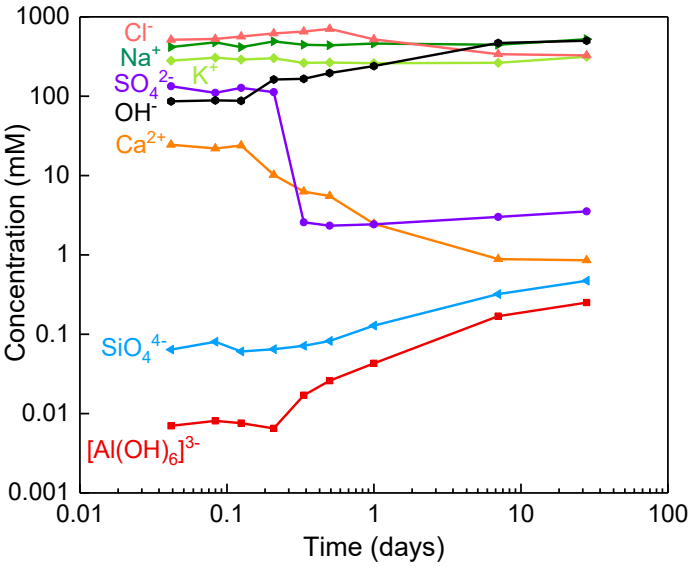

(b) Ions concentration of pore solution in PC-SW paste

Figure 3.5. Ions concentration of pore solution in PC pastes made with (a) DW and (b) SW after 1, 2, 3, 5, 8, 12 hours, and 1, 7, 28 days

SW led to a broadly similar tendency in the ions concentration in pore solution—a significant increase or decrease in the early stage followed by a relatively stable

development. Due to the accelerated effect on hydration, the depletion time of gypsum and the following significant changes in the pore solution composition can be observed earlier (between 3 and 12 hours). Subsequently, the concentration of SiO_4^{4-}, $[Al(OH)_6]^3$, and OH^- increased, and Ca^{2+} decreased steadily in the following period between 1 and 28 days; it differed from the DW samples, whose pore solution concentration was almost constant at the same stage.

The decrease in Cl^- can illustrate such unusual changes. During the high concentration level of SO_4^{2-} before gypsum depleted, the Cl^- was hardly involved in the precipitation of hydrate phases (Li, Li, et al. 2021). In the meantime, the concentration of Cl^- increased slightly due to the decreased volume of liquid. When the SO_4^{2-} was insufficient to form AFt, AFm phases were formed instead as the Al-bearing phases. Although the lower solubility product of sulfo-AFm (Lothenbach et al. 2019) indicated the thermodynamically easier formation, the hydroxy-AFm was more inclined to bind the Cl^- and form FS due to its much higher concentration than SO_4^{2-}. At the following FS formation stage, the free Cl^- decreased gradually along with the increase of OH^- for maintaining charge balance. As a result, the concentrations of SiO_4^{4-}, $[Al(OH)_6]^3$, and Ca^{2+} were changed with the increased pH of the solution afterwards.

Therefore for SW-related cement hydration, Cl^- maintained higher during the whole hydration period wherein FS was formed instead of sulfo-AFm. The concentration of SO_4^{2-} is higher than that of DW samples and thus would stabilize more AFt simultaneously. As the intermediate product between FS and sulfo-AFm, KS may occur

during the period. However, its in-between solubility product indicated poor stability; the content of KS was susceptible to chloride and sulfate concentration, and thus it can be easily converted with the concentration change (Balonis et al. 2010). The evolution of the hydrate phases predicted from the change in the pore solution was consistent with the results observed in the composition of the solid phase above.

Table 3.4. Concentration of the different ions in the pore solution (mM)

Time (day)	$[Al(OH)_6]^3$		Ca^{2+}		K^+		Na^+		SO_4^{2-}		SiO_4^{4-}		OH^-		Cl^-
	DW	SW	DW	SW	DW	SW	DW	SW	DW	SW	DW	SW	DW	SW	SW
0.04	0.010	0.007	18.0	24.51	263.9	280.8	66.0	415.8	98.80	133.2	0.09	0.06	98.8	86.3	515.2
0.08	0.011	0.008	19.0	21.92	281.1	305.3	73.8	477.7	103.0	110.1	0.09	0.08	104.2	88.6	526.5
0.13	0.008	0.008	21.0	23.91	308.1	289.5	78.4	415.4	104.8	127.4	0.10	0.06	102.1	87.6	564.9
0.21	0.013	0.006	22.0	10.36	293.3	301.3	80.4	491.4	107.4	112.5	0.10	0.06	101.9	162.5	618.7
0.33	0.012	0.017	12.1	6.28	306.3	262.9	83.5	445.5	98.0	2.58	0.15	0.07	198.6	165.6	652.3
0.50	0.013	0.026	3.8	5.51	289.5	266.0	76.0	438.3	45.0	2.34	0.16	0.08	299.2	195.9	707.2
1	0.174	0.043	2.1	2.46	263.2	261.1	88.4	461.3	0.62	2.43	0.17	0.13	295.1	239.9	520.2
7	0.169	0.169	1.9	0.88	236.3	263.1	136.6	445.4	0.76	3.02	0.17	0.32	346.7	467.7	338.8
28	0.251	0.250	1.8	0.85	247.2	314.3	147.2	521.9	1.24	3.54	0.23	0.47	371.3	501.2	326.3

3.3.3 Morphological analysis of early hydrate phases

Due to the stimulating effect on cement hydration, the initial hydration rate in SW was higher, forming the hydrate phases rapidly. The secondary electron micrographs of the cement paste show a significant discrepancy in microstructure between 12 to 24 hours. More fine C-S-H nuclei can be observed formed on the surface of clinker particles in SW than DW, as shown in Figure 3.6(a) and (b); the growing CH stacked to become thicker, forming the initial structure of hydrates. At 24 hours in Figure 3.6(c) and (d), a large amount of C-S-H had grown to nearly completely cover the particles, bonding the loose structure and filling the pores remarkably by hydration in SW. While in DW, less clustered C-S-H was formed. The significant differences in microstructure were due to the rapid hydration rate in SW at the early stage.

EDS analysis was performed to identify the specific hydrate phases formed in SW, as shown in Figure 3.6(e) to (i). Needle-like AFt can still be identified after 28 days. The AFm phase formed by conversion was observed surrounding the AFt, identified as FS. As discussed aforementioned, the unconverted AFt might be due to the higher sulfate concentration caused by FS precipitation.

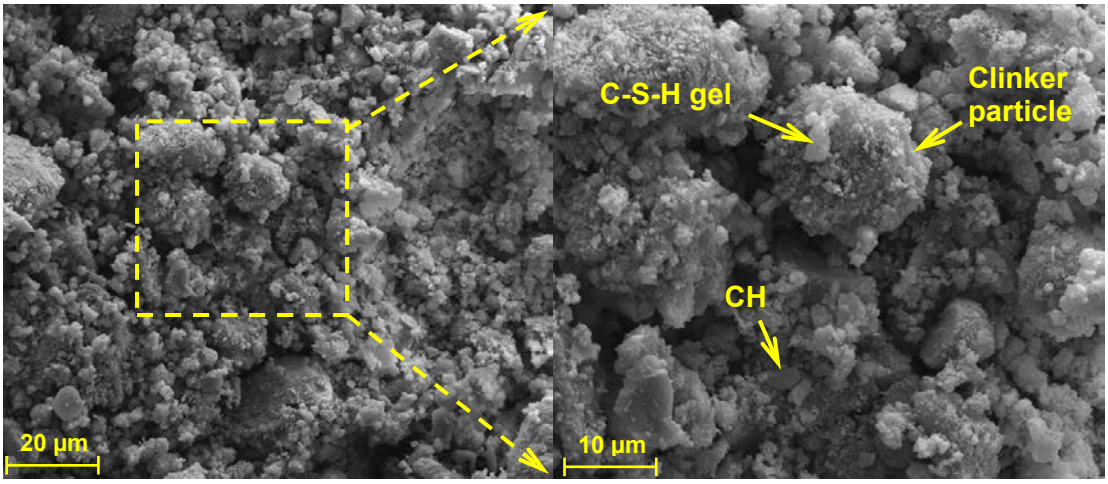

(a) PC paste hydrated in DW for 12 hours

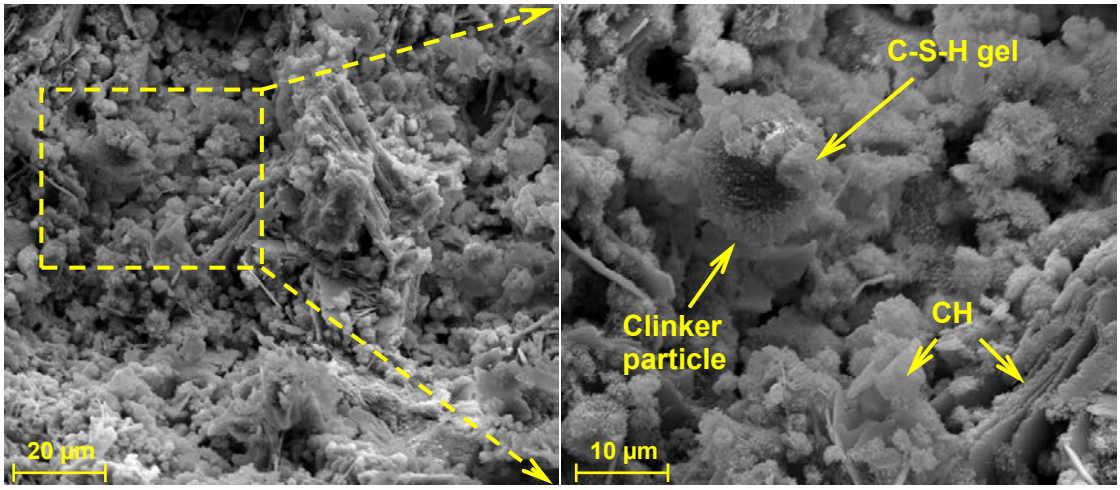

(b) PC paste hydrated in SW for 12 hours

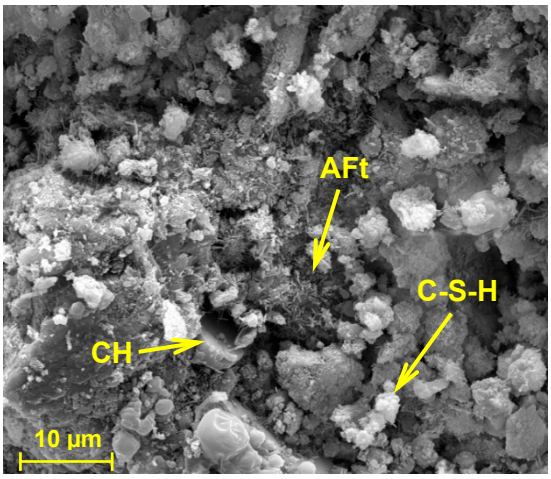

(c) PC paste hydrated in DW for 24 hours

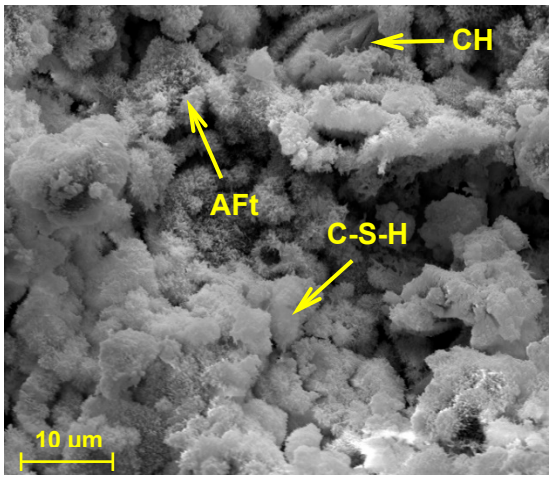

(d) PC paste hydrated in SW for 24 hours

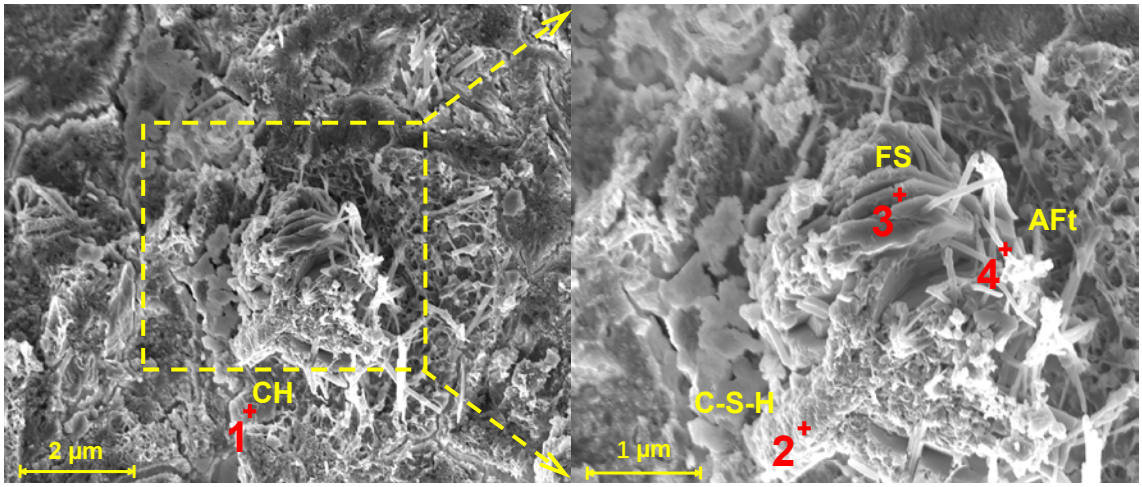

(e) PC paste hydrated in SW for 28 days

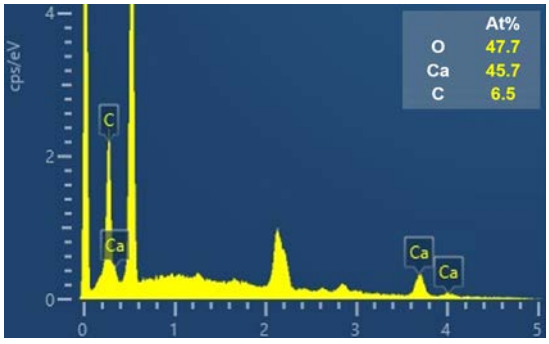

(f) Plot 1 (CH)

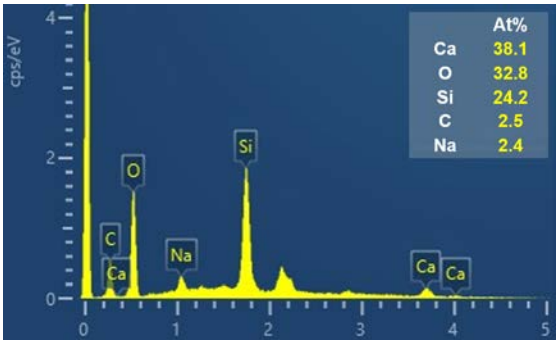

(g) Plot 2 (C-S-H)

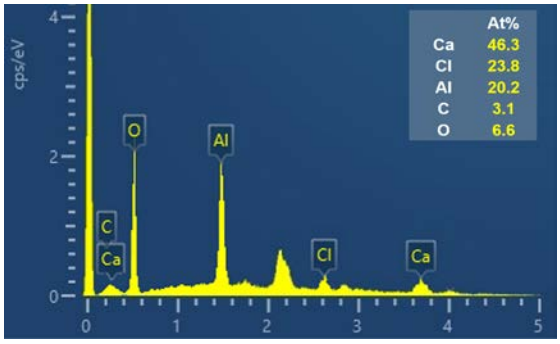

(h) Plot 3 (FS)

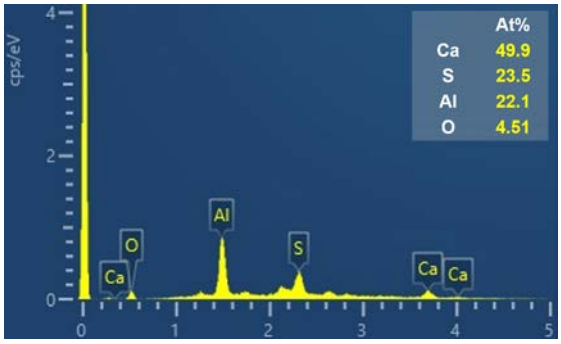

(i) Plot 4 (AFt)

Figure 3.6. SEM-EDS analysis of PC paste hydrated in DW and SW after 12, 24 hours. and 28 days

3.4 Conclusions

This chapter carried out a comprehensive study on PC hydration in SW and DW. The clinker, hydrate phases and pore solution were quantitatively characterized as a function of time. SW stimulated the dissolution of clinkers, increasing the hydration rate at the early stage. The rapidly precipitated hydrate phases accelerated the formation of the cement matrix in SW, which caused a significant difference in the early microstructure between 12 hours to 1 day. The gap in hydration degree between the two cement pastes narrowed after 7 days. Results show that the discrepancy in hydrated clinker phases was only 1.7% after 90 days.

The concentration changes in the pore solution indicated that SW-related ions affected the phase evolution. After the gypsum was depleted, FS was formed instead of sulfo-

AFm. The substitution from chloride ions increased the concentration of SO_4^{2-}, stabilizing the AFt phase at the late stage. The result showed that the SW reduced the conversion ratio of AFt from 60% to 29% in 90 days.

CHAPTER 4. HYDRATION OF PORTLAND CEMENT WITH SEAWATER: THERMODYNAMIC MODELLING

Cement hydration was a continuous conversion process, with the minerals' dissolution and re-precipitation reaching the solid-liquid equilibrium. When the PC was in contact with water, the clinker phase dissolved at various rates, releasing Ca^{2+}, SiO_4^{4-}, $[Al(OH)_6]^3$, Fe^{2+}, and hydroxy in the pore solution, which then co-precipitated to form C-S-H, AFt, CH, and other hydrate phases (Lothenbach & Winnefeld 2006). The formation time and rate of various hydrate phases differed according to their specific solubility products and the chemical kinetics of phase transition. In theory, however, when a specific part of the cementitious phases involved was entirely hydrated, the composition of the hydrates should be invariant if the raw materials, temperature, pressure, and other hydration conditions were unchanged.

Therefore, a model can be set up to simulate the evolution of phase composition as a function of hydration time, which requires the following: i) the phase composition of the PC used in the study; ii) the hydration degree of the clinker as a function of time, and iii) the composition of the hydrates expected to form by the hydrated clinker. As for the first requirement, the PC composition has been determined and given in Table 3.1. The hydration degree of clinker and the predicted hydrates are discussed below.

4.1 Modelling approach

To predict the dissolution degree of clinkers throughout the hydration time, a series of empirical expressions were proposed based on the x-ray measurement (Dalziel & Gutteridge 1986b; Parrot 1984; Swaddiwudhipong, Chen & Zhang 2002; Taylor 1987). In general conditions, there were no significant differences between these approaches.

However, only the empirical formula by Parrot and Killoh (Parrot 1984) specifically predicted the dissolution ratio of clinkers at a very early stage of the first few hours, during which the other approaches predicted no dissolution occurred. Considering the stimulated hydration of cement in SW, therefore, this empirical approach (MPK model) was applied in this study to estimate the hydration degree of each clinker phase. The method proposed the hydration rate R_t of each mineral clinker affected by the three influencing kinetic processes respectively as:

Nucleation and crystal growth (NG):

$$R_t = \frac{K_1}{N_1}(1-\alpha_t)(-\ln(1-\alpha_t)^{(1-N_1)} \tag{4.1}$$

Diffusion (D):

$$R_t = \frac{K_2(1-\alpha_t)^{2/3})}{1-(1-\alpha_t)^{1/3})} \tag{4.2}$$

Formation of the shell (I):

$$R_t = K_3(1-\alpha_t)^{N_3} \tag{4.3}$$

where the α_t represented the hydration degree of a specific clinker after time t (days). The lowest value of R_t was the applied controlling rate at time t, while the corresponding process (NG, D, or I) was considered the dominant kinetic factor at t. The hydration degree at time t is expressed as:

$$\alpha_t = \alpha_{t-1} + \Delta t \cdot R_{t-1} \tag{4.4}$$

At the late stage, it should be noted that the hydration was gradually weakened due to the thickened hydration shell hindering the mass and solute transfer, although there were still unhydrated clinker grains inside. Therefore, the w/b ratio was considered an

influencing coefficient affecting the critical degree of hydration in the long term. For $\alpha_t >$ H w/b, the α_t is expressed as:

$$\alpha_t = \alpha_{t-1} + \Delta t \cdot R_{t-1} \cdot (1 + 3.333 \cdot (\mathrm{H \cdot w/b} - \alpha_t))^4 \quad (4.5)$$

In addition, the effect of the surface area of PC on the initial hydration was considered (Dalziel & Gutteridge 1986a) using the formula from Parrot and Killoh (f(s) = (surface area)/385) (Parrot 1984). The values of related parameters K_1, K_2, K_3, N_1, N_2, and H were listed in Table 4.1, which were initially provided by Parrot and Killoh (Parrot 1984) and adjusted afterwards by Lothenbach *et al*. (Lothenbach et al. 2008). In this study, the same values of the parameters were used to estimate of hydration degree of PC in DW as a reference to evaluate with experimental data. As for modelling the PC hydration in SW, the parameters were optimized to obtain a better fit of the experimental data. The modified values of the parameters were discussed with the modelling results in the following sections.

Table 4.1. Parameters to estimate hydration degree of clinker phases (Lothenbach et al. 2008) in DW

Parameter	Alite	Belite	Aluminate	Ferrite
K1	1.5	0.5	1.0	0.37
K2	0.05	0.02	0.04	0.015
K3	1.1	0.7	1.0	0.4
N1	0.7	1.0	0.85	0.7
N3	3.3	5.0	3.2	3.7
H	2	1.55	1.8	1.65
R-square	0.9973	0.9952	0.9433	0.9837

Note: R-square was calculated from the MPK modelling and quantitative experimental results in Chapter 3

The phase composition and the pore solution concentration of PC paste were calculated using the Gibbs free energy minimization program, GEMS (Kulik 2010), as the prediction of the hydrates formed. The thermodynamic data and solubility products of minerals were provided by the PSI-GEMS thermodynamic database (Lothenbach et al. 2019). By combining the MPK model (Parrot 1984) with the thermodynamic equilibrium model, the estimated content of clinker phases dissolved can be transformed into the predicted hydrated phases and the ions concentration in the pore solution. Therefore, the evolution of the phases of PC hydration as a function of time could be simulated.

4.2 Evolution of solid phases

According to the initial parameters of the MPK model, the hydration degree of clinker in DW can be estimated. Wherein the mass of the remaining unhydrated phases was calculated, as shown in Figure 4.1. The simulation result fitted well with the determined composition of clinker phases from the experiment (R-square was shown in Table 4.1), which indicated that the initial MPK model was applicable to PC hydration in DW. Therefore, the reacted anhydrous phases from the simulation can be converted to the hydrate phases through the thermodynamic equilibrium model and be further evaluated by experimental results in the following section. The dissolution of gypsum was calculated by the thermodynamic equilibrium model. The result showed that gypsum was depleted after 8 hours, which was consistent with the QXRD result.

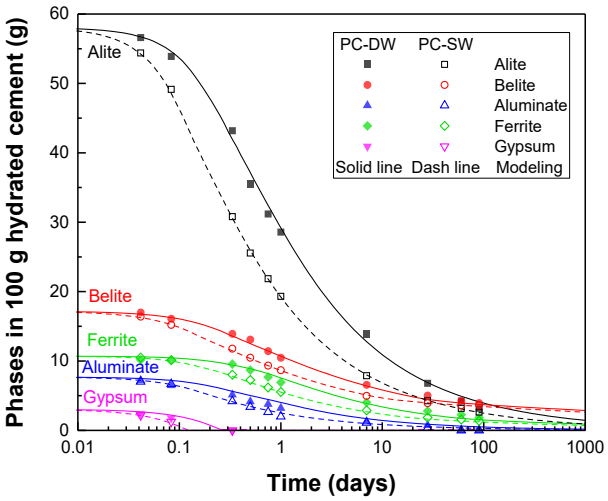

Figure 4.1. Amount of the unhydrated phases in PC paste with DW and SW. The scatter dots refer to the experimental results deduced by QXRD; the solid and dash lines refer to the modelling results of PC hydration in DW and SW, respectively.

As for hydrate modelling in SW, The accelerated hydration effect should be considered. Thus it was reasonable to adjust the values of the parameters as per the guidelines of experimental results. However, changing only one parameter, such as K_1 or N_1, may lead to similar simulation results at the corresponding controlling process, especially at the early stage of hydration when the NG was the dominant restricting factor and lasted for a short time (within 2 or 3 hours). The reason is that in a short time range (such as the NG stage even shortened by the SW effect), the parameters of the empirical formula cannot express significant characteristics when adjusting the fitting curve. On the other hand, the points of experimental results were too limited to fully describe the early hydration process, compared to the significant change at the early stage. Therefore, an acceptable range of each parameter instead of a unique value would be given for the modelling optimisation. Furthermore, the controlling rate was the lowest value of R_t from the three steps at the time t in Eqs. (1) to (3), resulting in a lack of specific restriction in choosing values from the other two non-dominant steps. To ensure that the effective mechanism of the three empirical formulas is consistent with the original

models, modifications were carried out as follows: i) The hydration was accelerated during the process of the NG due to the chloride (Li, Jiang, et al. 2021); thus, the duration of this dominant process should be shortened; ii) As the parameter controlled the critical degree of hydration with w/b ratio, *H* was not required to be adjusted, which can be based on the similar amount of unhydrated clinker determined in DW and SW from experimental result at least within the test range of 90 days; and iii) According to the original model used for PC hydration in DW, the process of diffusion only controlled the hydration rate of aluminate and ferrite between 0.4 to 1.4 days and 1.4 to 2 days, respectively; the subsequent time of hydration was controlled by the I hydration process , which is inconsistent with the assumption proposed by Krstulović and Dabić (Krstulović & Dabić 2000) that the controlling process during the hydration time is changed with the order NG, I, then D. To improve the applicability of the model, the initial kinetic mechanism of hydration was maintained unchanged after the adjustment. The diffusion-related parameters (K_2) were adjusted to a high enough value (given as the minimum threshold) to ensure that diffusion is not the controlling factor at the other time of hydration.

According to the considerations above, the acceptable range of the parameters and the values used in this study (with R-square calculated) were listed in Table 4.2, by which the content of anhydrous phases calculated in SW fitted well with the experimental data in Figure 4.1. The evolution of gypsum was also calculated from the thermodynamic equilibrium model. Due to the chloride effect, the dissolution of each clinker and gypsum was accelerated in SW. The accelerating effect can be observed earlier than 1 hour, influencing the nucleation and crystal growth. The simulation results showed that the maximum difference in hydration rate between the two systems occurred between 8 to 12 hours, which was consistent with the exothermic characteristics of cement

hydrated in SW conducted in the previous and other studies (Li, Li, et al. 2020a; Li, Jiang, et al. 2021; Montanari et al. 2019). The gaps between the remaining clinker phases were narrowed gradually to negligible at 90 days and even later.

Table 4.2. Suitable parameter ranges to estimate the hydration degree of clinker phases in SW

Parameters	Alite	Belite	Aluminate	Ferrite
K_1	**3.2** (2.2–3.2)	**1.2** (0.8–1.2)	**2.4** (1.5–2.4)	**1.0** (0.7–1.0)
N_1	0.7 (0.7–0.9)	1.0 (1.0–1.2)	0.85 (0.85–1.15)	0.7 (0.7–0.9)
K_2	**0.15** (> 0.12)	**0.06** (> 0.05)	**0.13** (> 0.12)	**0.045** (> 0.045)
K_3	**3.0** (2.8–3.0)	**2.0** (1.5–2.0)	**3.0** (2.7–3.0)	**1.2** (1.2–1.4)
N_3	3.3 (3.0–3.3)	5.0 (4.5–5.0)	3.2 (3.0–3.2)	3.7 (3.7–4.1)
H	2.0 (1.8–2.0)	1.55 (1.35–1.55)	1.8 (1.6–1.8)	1.65 (1.45–1.65)
R-squared	0.9998	0.9944	0.9849	0.9915

Based on the calculated hydration ratio of the four clinkers as a function of time, the combination of the thermodynamic equilibrium model was applied to calculate the hydrates formed, as shown in Figure 4.2 with the R-squared listed in Table 4.3. The simulated evolution of CH highly matched the experimental result, which is critical to the accuracy of the entire simulation results compared to the experimental results from QXRD/TG.

Through thermodynamic computing, some mixed phases that were hard to distinguish can be quantified separately by the model. For example, the amorphous phases determined from QXRD mainly consisted of C-S-H and hydrogarnet, with a mass ratio of 3.60 to 1 in both DW and SW samples. The thermodynamic equilibrium was the precondition of modelling, while it was more complex in the actual situation. Therefore, some intermediate phases may form theoretically but hardly be observed in actual

measurement. For example, KS was predicted to be formed after 10 days of hydration in SW. The thermodynamic modelling calculated that 2.6% of KS was formed at the late stage of hydration, which was unstable, closely influenced by the ratio of aluminium to chloride (Balonis et al. 2010) and not observed through the QXRD identification.

In addition, the thermodynamic equilibrium model assumes that the solid-liquid equilibrium was reached with a given reactant content. Therefore, a delay in the experimental results may occur, especially in the late stage when the mass transfer effect is poor. It also caused the coefficient of determination of the fitting curves, R-squared, to be lower to explain the observed value from the actual experimental results. For example, The AFt determined from the QXRD measurement at the early stage was slightly lower than that from prediction. It indicated that the precipitation process of AFt was affected to be slightly delayed. As for the higher content of FS from the experiment, the formation of hydrotalcite could be due to the overlap peaks between FS and chloride-containing hydrotalcite (Machner et al. 2018). Another possibility was that a part of FS measured by QXRD was thermodynamically identified, or theoretically formed, as KS but converted to FS in the actual hydration process. It can be found in thermodynamic modelling that magnesium can also hinder the formation of KS, which is similar to the aluminate's effect. Therefore, the formation of KS is not absolute from hydrated cement with a higher content of magnesium, aluminate, or perhaps ferrite as well.

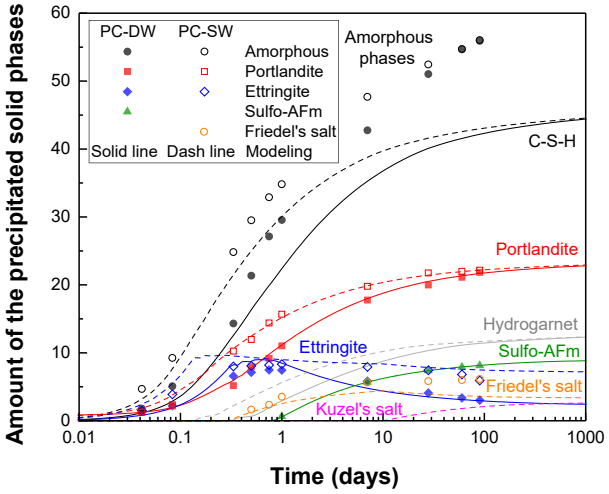

Figure 4.2. Amount of the precipitated solid phases in PC paste with DW and SW. The scatter dots refer to the experimental results deduced by QXRD; the solid and dash lines refer to the thermodynamic modelling results of PC hydration in DW and SW, respectively.

Table 4.3. R-squared between the fitted value and observed value of hydrate phases

Hydrate phases (fitted value—observed value)	DW	SW
CH—CH	0.9981	0.9938
C-S-H + hydrogarnet—amorphous phases	0.9780	0.9954
Gypsum—Gypsum	0.9593	0.9903
AFt—AFt	0.8884	0.8377
Sulfo-AFm—Sulfo-AFm	0.9998	N/A
FS + KS—FS	N/A	0.9321

By using the appropriate models, the simulation of the mass change as a function of time was conducted in Figure 4.3(a) and (b). As aforementioned, the PC hydration in SW affected the composition of the hydrate assemblage and the hydration rate. Starting from the depletion of gypsum at about 2.8 hours, the conversion of AFt caused the formation of different hydrates, which were FS and KS instead of sulfo-AFm due to the chloride. In addition, the effect of other content in SW, such as magnesium and sulfate,

can be regarded as the increased minerals of cement, and finally precipitated as hydrotalcite, AFt, and KS. Table 4.4 shows the thermodynamic modelling results of the composition of C-S-H phases calculated in the CSHQ solid solution model (Lothenbach et al. 2019) (Kulik 2011). By calculation, the Ca to Si ratio of C-S-H formed in SW was 1.551, slightly lower than that in DW (Ca/Si = 1.585) and may affect the strength.

Table 4.4. Composition of C-S-H phase in CSHQ solid solution model

C-S-H (CSHQ solid solution)	DW (mol-%)	SW (mol-%)
JenD Ca/Si=2.25: $C_{3/2}S_{2/3}H_{5/2}$	37.1	34.5
JenH Ca/Si=1.33: $C_{4/3}SH_{13/6}$	23.4	21.2
TobD Ca/Si=1.25: $C_{5/6}S_{2/3}H_{11/6}$	27.6	25.6
TobH Ca/Si=0.67: $C_{2/3}SH_{1.5}$	1.1	1.0
NaSH: $N_{0.5}S_{0.2}H_{0.45}$	5.7	5.8
KSH: $K_{0.5}S_{0.2}H_{0.45}$	5.1	11.8

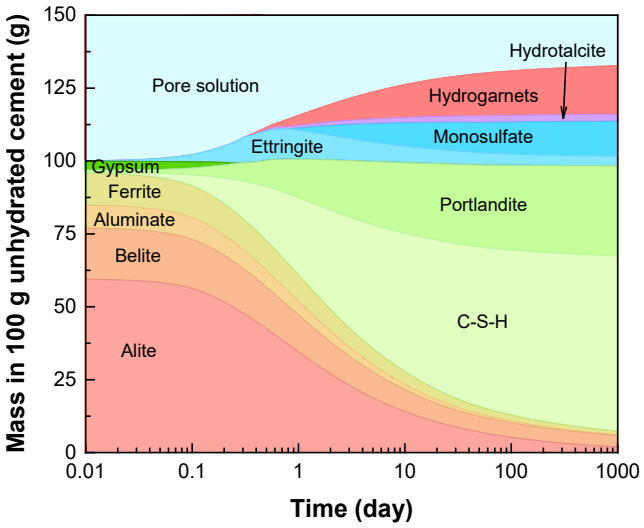

(a) Simulated evolution of mass change of hydrating PC in DW

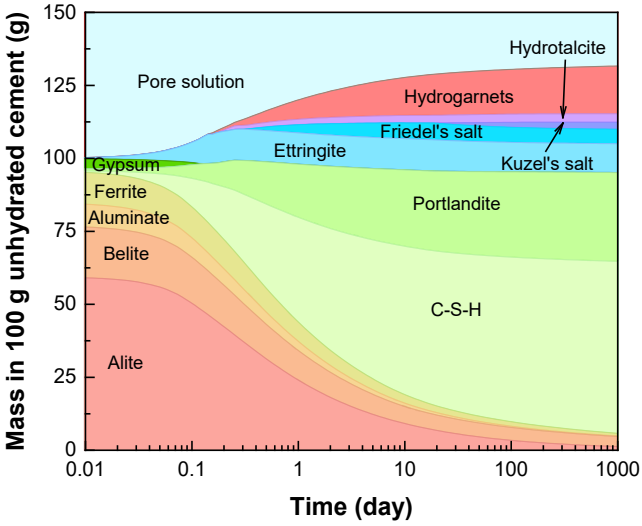

(b) Simulated evolution of mass change of hydrating PC in SW

Figure 4.3. Simulated evolution of various phases in mass during the PC hydration in (a) DW and (b) SW

The PC hydration in SW is also calculated to affect the volume of the hydrating cement in Figure 4.4(a) and (b). According to the modelling calculation, SW instigated rapid volume growth of solid phases significantly at the early stage; the solid volume is 12 %, 7.8%, and 5.7% higher, respectively, after 1,7 and 28 days in Figure 4.4(c), which intensely corresponded with the rapid growth of compressive strength (Li et al. 2019; Li, Li, et al. 2020a; Li et al. 2015; Wegian 2010). At the end of the hydration, the SW increased the solid volume by 3.70% but decreased the liquid phase by 12.2% from the modelling results, although the total volume was almost the same. The result may be due to a high quantity of AFt forming and the precipitation of the inorganic ions from SW. However, the volume change by SW may not be beneficial to the late-stage strength. Once the cement paste was in a high-temperature or humid environment, for example, the AFt could decompose or leach out, creating new pores. Due to the slow hydration rate, the pores formed at the late stage were hard to fill with other hydrates. Therefore, the strength of cement paste made with SW might be more sensitive to the curing condition, which was consistent with the other studies (Li, Li, et al. 2021).

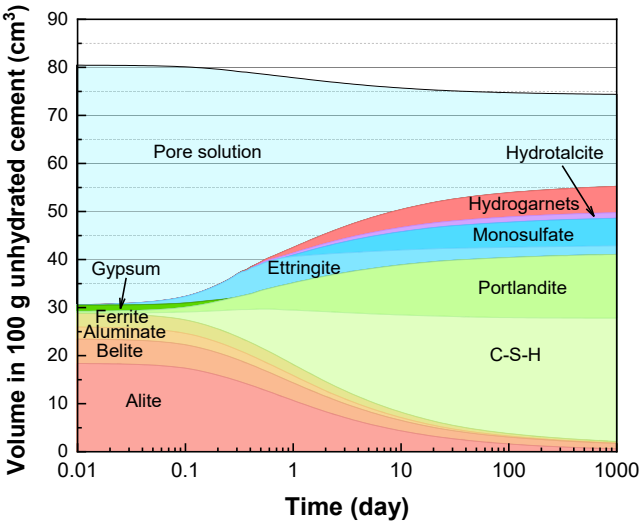

(a) Simulated evolution of volume change of hydrating PC in DW

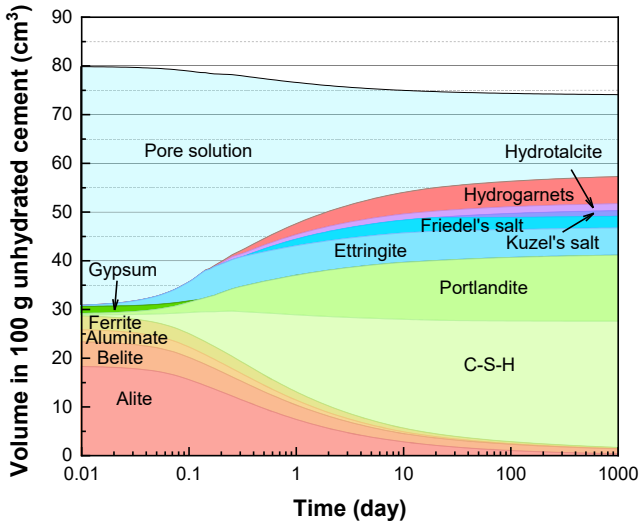

(b) Simulated evolution of volume change of hydrating PC in SW

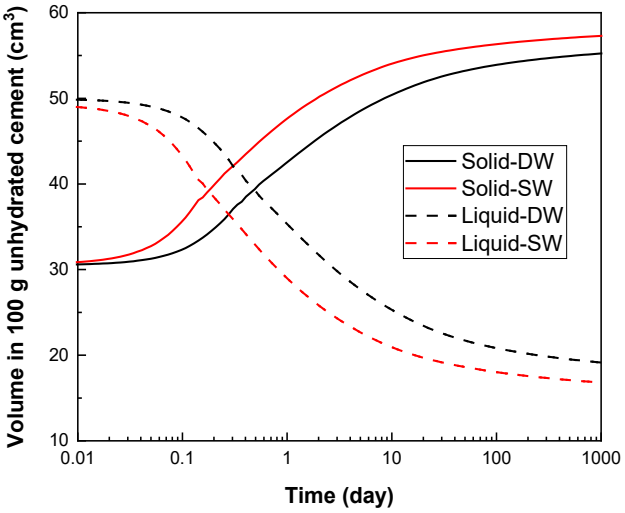

(c) Simulated evolution of the total volume of hydrating PC in DW and SW

Figure 4.4. The modelled evolution of volume change during the hydration of PC in (a) DW and (b) SW as a function of time

4.3 Evolution of liquid phase

To simulate the ions concentration of pore solution, the adsorption of alkalis by C-S-H, which was offered from the dissolution of sulfates alkali, should be considered. The distribution ratio R_d of 0.42 ml/g was used both for Na^+ and K^+ (Hong & Glasser 1999; Lothenbach et al. 2008; Lothenbach & Winnefeld 2006). The modelled composition of the pore solution exhibited consistent trends with the experimental results in Figure 4.5(a) and (b) strongly support developing hydrates during hydration. Unlike the concentration in DW, which was more stable after the significant change, a gradual increase (e.g., aluminate and hydroxy) or decrease (e.g., Ca^{2+} and Cl^-) occurred in SW samples instead. The precipitation of Cl^- indicated the formation of FS over time, along with an increase of sulfate simultaneously from the conversion of AFt or the substitution of AFm phases. The errors of the model, such as the concentration of silicate and aluminate, can be explained by the ideal chemical equilibrium assumed by thermodynamic modelling.

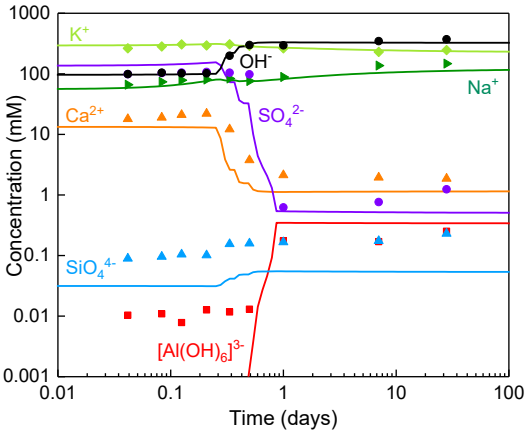

(a) Modelled evolution of pore solution concentration of hydrating cement in DW

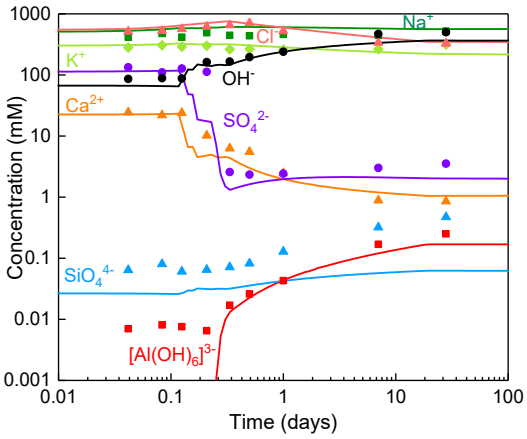

(b) Modelled evolution of pore solution concentration of hydrating cement in SW

Figure 4.5. Concentration of ions in the pore solution of PC hydrating in (a) DW and (b) SW as a function of hydration time. The scatter dots and lines refer to the experimental results and thermodynamic modelling results, respectively.

4.4 Finding in the simulation

Compared to the PC paste made with DW, SW was found to increase the hydration rate of clinker significantly throughout the whole process and affect the evolution of phase assemblage. Both thermodynamic calculations and experimental determinations suggested the formation of FS, instead of sulfo-AFm, in SW. The formation of FS indirectly stabilized the AFt due to the higher sulfate concentration from the conversion of sulfo-AFm. Based on the thermodynamic calculation, the changes in phase

assemblage by SW result in a slight decrease in the Ca/Si ratio from 1.585 to 1.551, as well as a 3.70% increase in solid volume and a 12.2% decrease in liquid volume at the end of the hydration, but the total volume was nearly unchanged. The higher content of AFt may lead to the mechanical properties being more sensitive to humidity and temperature change. The formation of KS was observed by experiment and can be calculated from the thermodynamic model. However, due to its sensitivity to the concentration of sulfate, aluminate, ferrite, and maybe also magnesium, KS was readily converted to other phases, such as FS, and retained in the Al-bearing solid solution. Therefore, in SW, the formation of KS depends on the composition of hydrated PC.

Combining the thermodynamic calculation with the dissolution model of clinker, the evolution of the solid and liquid phase assemblages can be simulated quantitively. The parameters of the empirical equations were modified to be more suitable for modelling the hydration in SW. The simulated results agreed reasonably well with the content of the main precipitated crystalline phases (e.g., CH, AFt) and amorphous determined by QXRD/TG. The findings indicated that the coupled models could successfully simulate the evolution of hydrating phases with SW.

4.5 Conclusions

This chapter presents an approach to simulating cement hydration in SW through thermodynamic modelling. Since SW accelerated the hydration rate determined in Chapter 3, it is necessary to adjust the parameters of the MPK model for simulating the dissolution ratio of anhydrous phases as a function of time. Based on the quantitative experimental results of clinker phases, the range of parameters in Table 4.2 was suggested as proper input for cement hydrated in SW. The corrected simulation result of the hydration rate can be converted into the evolution of hydrated phases by

thermodynamic modelling. To be evaluated by experimental results, a good agreement can be observed in simulation, which, in turn, reinforced the reliability of the modified MPK model for SW hydration.

Through thermodynamic computing, some indistinguishable phases can be quantified separately. The amorphous phases mainly consisted of C-S-H and hydrogarnet, with a mass ratio of 3.60 to 1 in both SW and DW samples. However, since the thermodynamic equilibrium is the precondition of the modelling, a delayed effect may occur in the actual hydration process from failure to maintain the real-time equilibrium. As a result, the expected value of AFt from modelling may be slightly higher; some phases not detected from experimental measurement may be predicted, such as the intermediate KS. Nevertheless, the predictable proportion of main hydrate phases (such as C-S-H and CH) from their R-squared value was higher, indicating the modelling for Portland hydration in SW was of a high reference value.

CHAPTER 5. HYDRATION, MECHANICAL PROPERTIES AND PORE STRUCTURE OF PORTLAND CEMENT WITH SEAWATER

This section investigated the hydration characteristics and mechanical strength development of SW mortar with sea sand. The macroscopic performance differences will be discussed by hydration properties as the mechanism.

5.1 Experimental program

5.1.1 Raw materials

The cement used in the study was the OPC conforming to Australian standard AS 3972 (General purpose and blended cements) (AS 3972 2010). The oxide compositions of the cement measured by X-ray fluorescence (XRF) were summarized in Table 5.1. The content of limestone and gypsum was provided by the cement supplier. After the XRF data was corrected by deducing the chemical composition of the two given minerals, the approximate mineral composition in OPC was obtained through Bogue calculation (Bogue 1955b), which was shown in Table 5.2, as well as the physical properties. Two types of mixing water: (1) DW; and (2) natural SW, were applied. The natural SW was obtained from Congwong Beach on the Sydney coast of Australia. Table 5.3 shows the chemical composition of DW determined by inductively coupled plasma mass spectrometry (ICP-MS), which is close to the world average concentrations of ions in surface SW (Levitus et al. 2010). Natural river sand (R-sand) and washed sea sand (S-sand) are used in cement mortars, which contain few impurities such as clay and sea salt. The particle sizes distribution of the used R-sand and S-sand are shown in Figure. 5.1.

Table 5.1 Chemical composition of the OPC (oxide composites)

Chemical	CaO	SiO_2	Al_2O_3	Fe_2O_3	MgO	SO_3	Na_2O	K_2O	CO_2	LOI*
Component (wt.%)	62.9	20.3	4.5	4.6	1.2	2.6	0.3	0.3	2.0	4.0

Note: LOI* presents loss on ignition

Table 5.2 Mineral composition of OPC and its physical properties

Minerals	C_3S	C_2S	C_3A	C_4AF	Limestone	Gypsum
Content (wt.%)	49.03	21.21	4.14	13.00	3.32	4.55

Note: Specific gravity is 2800-3200; bulk density is 1200-1600kg/m^3 and average particle size (d_{50}) is 8 μm.

Table 5.3 Major chemical composition of SW from Sydney Congwong Beach

Dissolved ions	Na^+	K^+	Ca^{2+}	Mg^{2+}	Cl^-	SO_4^{2-}
Concentration (mol/l)	0.47	0.01	0.01	0.05	0.54	0.03

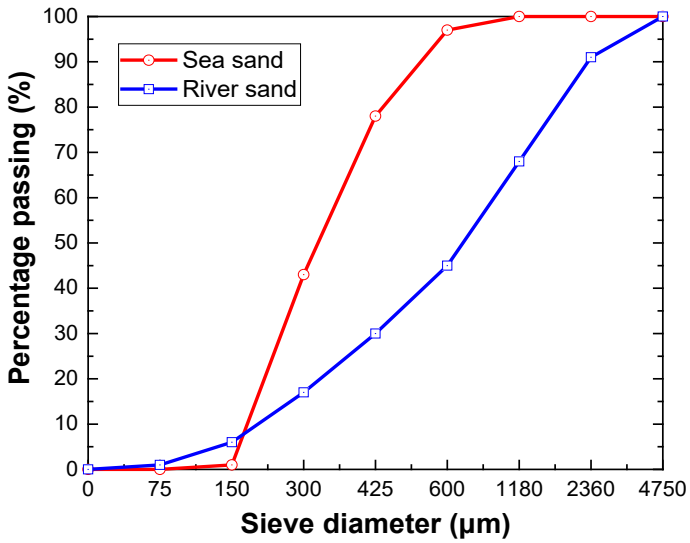

Figure 5.1. Particle size distribution of S-sand and R-sand

5.2 Experimental methods

5.2.1 Heat of hydration

To investigate the effect of SW on the hydration of OPC, an isothermal heat conduction calorimeter (TAM Air) was applied to measure the heat of hydration during the first 60 hours. DW and SW were used to mix water in samples. The w/b ratios of the samples are 0.5 and 0.7. Firstly, 30.00 g cement was weighed and mixed with weighted DW or SW for 60 sec, followed by being injected into ampoules through a syringe. Afterwards, the ampoules loaded with samples and those with references were capped and lowered into the calorimeter simultaneously. Due to the external premixing procedure, very early cement hydration cannot be measured from the calorimeter, and the signal of heat flow became stable after approximately 60 mins. In order to reduce the experimental error, the references applied dry sand (quartz) and DW to respectively simulate the OPC and the certain water used in samples with the same total heat capacity. The composition of the samples with SW and DW was summarized in Table 5.4. The samples were denoted by their "water type + w/b ratio." For example, the "D-0.5" represented OPC with DW at a w/b ratio of 0.5. The final exotherms were corrected by subtracting the baseline obtained before and after the measuring process.

Table 5.4 Mix design of cement paste for hydration heat analysis

Index	W/b ratio	Sample (g)			Reference (g)			Total heat capacity (J/K·g)
		OPC	DW	SW	Quartz	DW	SW	
D-0.5	0.5	9.40	4.70	–	9.40	4.70	–	26.70
S-0.5	0.5	9.40	–	4.70	9.40	–	4.70	26.70
D-0.7	0.7	7.40	5.17	–	7.40	5.17	–	27.17
S-0.7	0.7	7.40	–	5.17	7.40	–	5.17	27.17

5.2.2 Phase quantification

Semi-quantitative X-ray diffraction (XRD), Thermogravimetry/Differential scanning calorimetry (TG/DSC), and Scanning electron microscope-Energy dispersive X-ray spectroscopy (SEM-EDS) were adopted to analyze the phase evolution during cement hydration in DW and SW. The samples were OPC paste with DW or SW at a w/b ratio of 0.5. The pastes were prepared in a Hobart mixer and cast in seated plastic moulds at the size of 50 mm × 50 mm × 50 mm, then cured in a standard curing chamber with a temperature of 20 ℃ and 95% relative humidity. After 1 day of hydration, the samples were demolded and further cured at the previous condition. Afterwards, the samples with different hydration ages were dried with two different treatments. For those hydrated for less than 1 day, the samples were transferred into a vacuum freeze dryer to remove free water after reaching the specified ages; the drying process lasted for 2 days at -55 ℃ in vacuumed condition. For those hydrated longer than 1 day, the hardened cement pastes were crushed into small pieces, and the debris from the inside part of the paste was collected, followed by being immersed into isopropanol for the hydration stoppage. In this way, the ongoing hydration process can be terminated. After being immersed for 7 days, the debris was transferred and stored in a desiccator over silica gel for 3 days. Furthermore, some debris was ground to pass through a sieve with a screen aperture of 75 μm, as the powder samples were applied to TG and XRD measurements.

In terms of TG/DSC analysis, the equipment STA449 F5 JUPITER was used to determine caloric effects and mass changes in the temperature-rise period. About 30 mg of dried powder sample was loaded into an alumina crucible, purged with nitrogen, and heated from 25 ℃ to 1000 ℃ with the temperature increasing rate of 10 ℃/min. With the increase in temperature, the decomposition of hydration products can be determined by mass loss from chemically bound water and carbonate. Thus the content of the

corresponding hydrate phase can be determined. In addition, the endothermic peaks exhibited in DSC curves illustrated the enthalpies of transitions from decompositions of phase. As a result, the area of the endothermic peak can be converted into the value of enthalpy of transition, which helps determine the certain reaction, molar content of the involved substance, and solid composition. Furthermore, some moist samples as contrast groups were also measured, which were not terminated hydration, ground, and dried before, to determine the content of pore solution.

X-ray diffraction analysis was conducted by Bruker D8 Discover with the diffraction angle (2θ) ranging from 5° to 70° and the scan step size of 0.02°. Cu K(alpha) radiation (k = 1.54056 A°) was used as the X-ray source. Before measurement, the powder samples were blended with 10% titanium oxide as the special ingredients of the internal standard method. Semiquantitative analysis of solid mineral phases was conducted through the peak heights and peak areas of the intensity of corresponding phases. Micromorphology analysis was conducted by applying the scanning electron microscope (SEM) Zeiss Supra 55vp combined with energy dispersive X-ray spectrometry (SEM-EDS).

5.2.3 Mechanical strength

Fresh OPC pastes with DW and SW at the w/b of 0.5 were cast into 50 mm cube moulds and vibrated for 10 s before sealed curing at 20 ℃. The compressive strength was tested on specimens at a speed of 0.02mm/s after curing for 1d, 7d, 28d, 60d, and 90 d. OPC mortars were also prepared for compressive strength measurements. Three cubic specimens (50 mm × 50 mm × 50 mm) were prepared for each group of samples. The mix design of cement mortar is listed in Table 5.5. All specimens were cured for 1 day in the chamber before being demolded and further cured in a standard curing chamber (temperature of 25 ℃ and relative humidity of 95%). The cement mortars were

tested at the ages of 7, 14, and 28 days for compression tests. The compression machine of UH500 was applied with a loading rate of 0.1 mm/min in stroke. Cement mortars were prepared for flexural strength measurements. For each group, three prismatic specimens (40 mm × 40 mm × 160 mm) were prepared. The curing condition and tested ages are as same as those for compressive strength. The flexural strength test is in accordance with ASTM C348-18. The cement mortars were tested at the ages of 7, 14, and 28 days.

Table 5.5 Mix design of cement mortar

Index	Cement (kg/m^3)	DW (kg/m^3)	SW (kg/m^3)	R-sand (kg/m^3)	S-sand (kg/m^3)
DR*	800	320	–	1600	–
DS*	800	320	–	–	1600
SR*	800	–	320	1600	–
SS*	800	–	320	–	1600

Note: DR* presents the mortars prepared by DW and R-sand; DS* represents the mortars prepared by DW and S-sand; SR* is the mortars prepared by SW and R-sand; SS* means the mortars prepared by SW and S-sand.

5.2.4 Characterization of pore structure

The pore distribution of cement paste was performed by MIP using Autopore IV 9500. The sample consisted of 50 spherical particles of cement paste dried by the solvent exchange of isopropanol. Each particle was cut into 3 to 5 mm in diameter and exposed its fracture surface. The contact angle of mercury was 130.00°, and the surface tension of mercury was 485.00 dynes per centimetre. The pressure of mercury intrusion ranged from 0 to 32,000 psi, wherein the corresponding measured pore diameter ranged from 350 mm to 5.5 nm.

5.3 Experimental results

5.3.1 Heat evolution of hydration

Hydration heat evolution of OPC was measured with w/b ratios of 0.5 and 0.7 hydrated in DW and SW, respectively. The exotherm of OPC in 60 hours is shown in Figure 5.2(a). The ordinates of the figure, normalized heat/heat flow, are the quantifiable exothermic units released per gram of cement. At the early age of the hydration process, the period exhibiting insignificant heat flow was the induction period, which was caused by the restricted precipitation and the extremely slow rate of dissolution of cement (Costoya Fernández 2008; Fierens & Verhaegen 1976; Odler & Dörr 1979; Sierra 1975). It was observed that the duration of the induction period of hydration in D-0.5 and S-0.5 ranged from 1.54 to 1.56 hours. Furthermore, increasing the w/b ratios from 0.5 to 0.7 had a limited impact on the period of induction. It reveals that the dissolved ions in SW do not have a great influence on the initial dissolution and precipitation process, although there might be a new solid phase formed. The initial hydration is still subjected to the limited surface with low interfacial energy, which is consistent with the dissolution theory based on a geochemical approach to crystal dissolution (Juilland et al. 2010; Kumar, Bishnoi & Scrivener 2012).

In the acceleration period, it was observed that the duration to reach the hydration peak (Peak I) was significantly reduced by 36% for the OPC paste with SW, in comparison to the OPC with DW. Furthermore, the exotherm peak of paste in SW exhibited 44% higher than that with DW. Hence, it demonstrates that the dissolved ions in SW can significantly promote cement hydration. According to previous studies (Farnam, Dick, et al. 2015; Rosenberg 1964), chloride was the dominator that can chemically bind with calcium, aluminate, and ferrite ions to form insoluble phases such as calcium

oxychloride and FS. In this situation, the involved chloride ions contribute to promoting the precipitation of the dissolved mineral ions in the solution. Thus according to the chemical equilibrium, the dissolution rate of unhydrated clinkers was promoted. The stimulating effect is of particular significance to the main mineral tricalcium silicate (C_3S) (Sikora, Cendrowski, Elrahman, et al. 2019).

When the heat flow started to decrease, an exotherm with acromion presented from around 10 to 15 hours or later. The acromion was a part of another peak (Peak II), which overlapped with Peak I. Peak II was formed from the heat of hydration of calcium aluminate (C_3A) and calcium aluminoferrite (C_4AF) (Clark & Brown 1999). During this hydration period, the concentration of sulfate in the solution decreased over time since the gypsum had completely depleted before C_3A and C_4AF. AFt, therefore, became less stable with a lower sulfate solution and subsequently started to convert into the AFm phase (Black et al. 2006). In SW, however, the hydration rate increased during this period, which was greatly affected by the various dissolved ions, especially under the condition with a high concentration of chloride. During the period, it was found from the following analysis of TG and XRD that FS was intensively formed after gypsum was completely consumed. Thus, the formation of FS promoted the hydration of aluminate and ferrite minerals. Furthermore, an extension acromion appeared in samples at a high w/b ratio of 0.7, in which the mass diffusion and transformation were less restricted than the samples at a low w/b ratio. For the OPC with SW at the w/b ratio of 0.7, more ions from SW were involved in cement hydration, and thus the acceleration effect of hydration can be further improved in comparison to the counterparts at the w/b ratio of 0.5.

The accumulated heat evolution in Figure 2(b) showed that the gap of hydration heat released from S-0.5 and S-0.7 started to widen after 5 hours, and S-0.7 released nearly

20% additional heat after 60 hours. For D-0.5 and D-0.7, however, the two exotherms showed a limited difference, releasing less heat than those in SW. It demonstrates that the dissolved ions in SW can promote hydration, especially chloride, which accounted for more than half of the ions in SW. The following conclusions can be drawn through the comparison: the hydration rate of C_3S is greatly affected by the concentration of chloride in the solution, which is correlated with the equilibrium concentration of CAOXY. If the involved chloride is increased, but the concentration of chloride in mixing water is not changed, as samples of S-0.5 and S-0.7, the hydration rate of C3S will not be obviously accelerated. Unlike C_3S, the hydration of aluminate and ferrite can be stimulated with the increasing content of chloride involved, which is due to the further formation of FS.

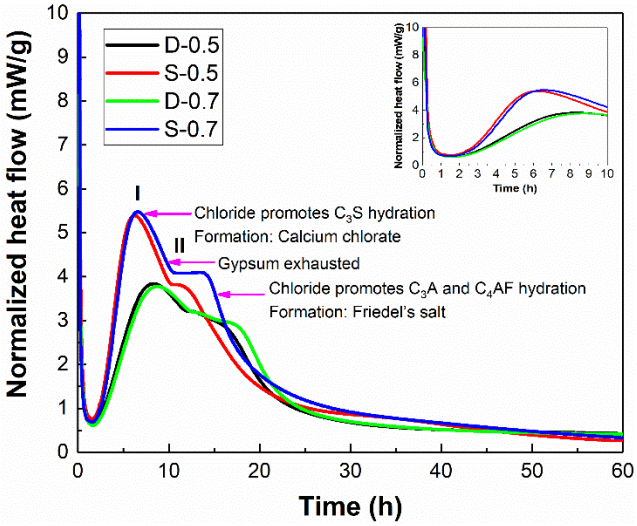

(a) Exothermic rate at w/b ratios of 0.5 and 0.7

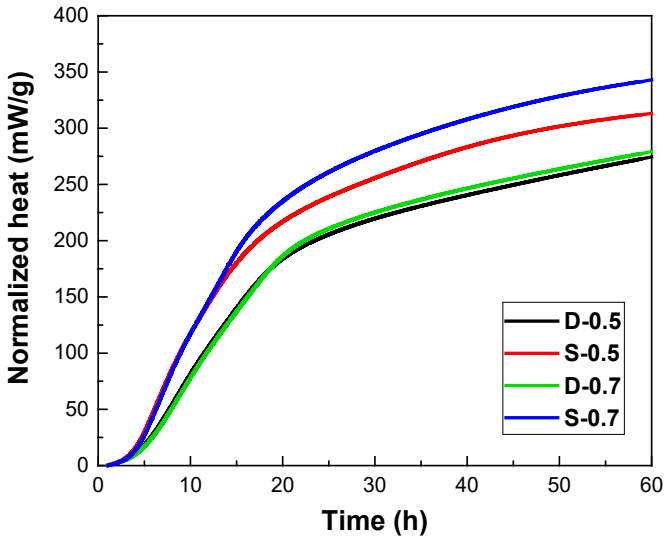

(b) Cumulative heat of hydration at w/b ratios of 0.5 and 0.7

Figure 5.2. Heat evolution of OPC hydrated in DW and SW at w/b ratios of 0.5 and 0.7

5.3.2 Thermogravimetric and X-ray diffraction analysis

The compositions of OPC paste with DW and SW were determined by TG/DSC and XRD analysis. Figure 5.3 shows the TG and the derivative thermogravimetry (DTG) results of OPC paste in DW at various hydration times. The peaks of mass loss displayed in DTG curves indicate that the precipitation of AFt and dissolution of gypsum took place earlier, even in 1 hour of hydration. The other hydrated phases, such as C-S-H and CH, had hardly formed yet during the initial hydration period, which resulted in the DTG curves exhibiting closer to zero significantly. After 8 hours of hydration, it was observed that CH and C-S-H had formed and constituted the main part of the hydrated phase, indicating the hydration reaction of C_3S happened rapidly during this period. The rapid reaction was consistent with the aforementioned characteristic of heat release in the acceleration period.

After 12 hours of hydration, gypsum was completely dissolved and depleted. Due to the decreasing concentration of sulfate in the pore solution, the preformed AFt became unstable and gradually converted to the AFm-formed phase at a slow rate (Lothenbach

& Winnefeld 2006). In DTG curves, it was found that the sample with a 12 hours of hydration had the largest peak at around 100 ℃, compared to the samples with other lengths of hydration time. The peak indicated a maximum mass loss, which was attributed to the dehydration of AFt, water desorption, and water loss from C-S-H gel layers. As an amorphous solid phase, the dehydration reaction of C-S-H occurred continuously from 105 to 1000 ℃ (Khoury et al. 2002), and the amount of dehydrated water increased with the increasing temperature. It was observed in Figure 5.3 that the mass loss increased with the increasing hydration age, especially from 200 to 400 ℃, which illustrated an increasing content of C-S-H with ongoing hydration.

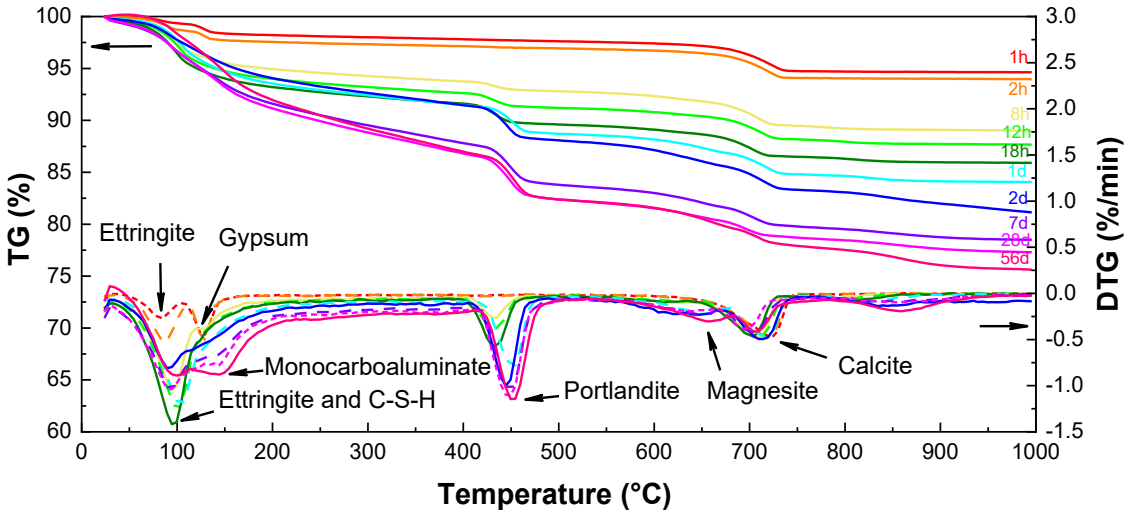

Figure 5.3. TG/DTG curves of OPC in DW after 1, 2, 8, 12, 18 hours, and 1, 2, 7, 28, 63 days of hydration at a w/b ratio of 0.5

The decomposition of CH took place at approximately 420 ℃, followed by the decomposition of the carbonate phase at a temperature over 600 ℃. As the main production of OPC, the content of CH and C-S-H increased with the hydration degree, and their growth rates gradually decreased at the late age. After 28-day hydration, the content of CH and C-S-H was nearly constant and hardly increased. Monocarboaluminate (carbo-AFm), instead of monosulfoaluminate (sulfo-AFm), was detected as the final hydration product of the residual aluminate phase due to the excess

of carbonate ions provided from limestone (Bonavetti, Rahhal & Irassar 2001; Lothenbach et al. 2008). CC is the major mineral phase of limestone added in OPC cement, which was found to slightly decreased during the ongoing hydration period. The other type of carbonate, magnesite, was found to increase at the late age, which decomposed at around 600 °C (Gabrovšek, Vuk & Kaučič 2006).

The following XRD analysis can further support the results from the TG analysis. Figure 5.4 gives the representative diffraction patterns for the OPC paste with DW. It was observed that the amounts of the four main OPC minerals decreased at different rates. Due to the high solubility, C_3A and gypsum reacted rapidly to form AFt which can be detected after 2 hours of hydration. The hydration properties of C_4AF were similar to that of C_3A, but the rate was much slower. When gypsum was completely depleted after 12 hours of hydration, the XRD showed no sulfo-AFm phase (characteristic peak 2-Theta at 9.895°) during the following hydration period. Instead, the content of carbo-AFm (characteristic peak 2-Theta at 11.670°) was found to increase along with hydration. In terms of silicate minerals, a great amount of C_3S was found dissolved in the first 2 days of hydration, and the further hydration rate gradually decreased with the hydration time. After 63 days, the extent of hydration of C_3S was observed to be nearly unchanged in hardened OPC paste. For another OPC mineral, the C_2S hydrated much slower, attributed to the less solubility than that of C_3S. It could be found that some of the C_2S remained unhydrated after 63 days of hydration.

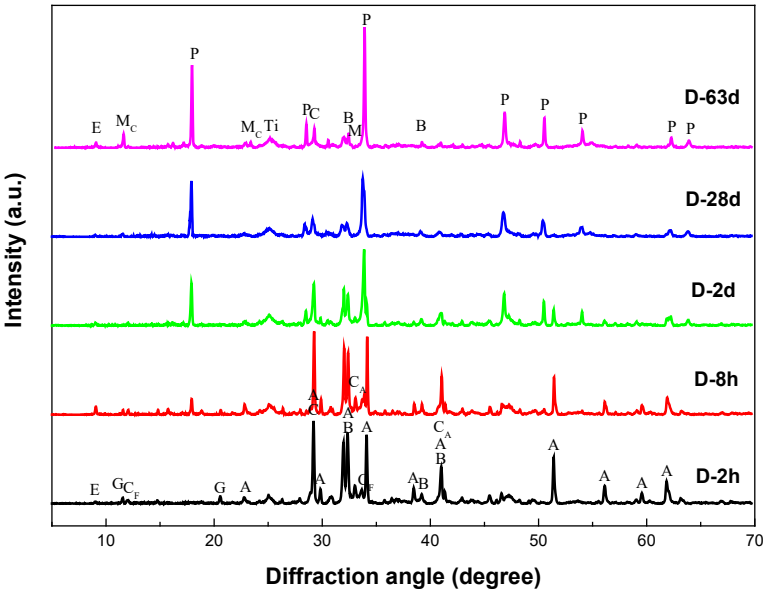

Figure 5.4. XRD pattern of OPC in DW after 2, 8 hours, and 2, 28, 63 days of hydration at w/b ratio of 0.5 (A - C_3S, B - C_2S, C - CC, E - AFt, G - gypsum, P - CH, M – magnesite, M_C - monocarboaluminate, C_A - C_3A, C_F - C_4AF, Ti - titanium oxide for calibration reference)

In Figure 5.5, the cement paste with SW shows a higher weight loss within 7 days than that of paste with DW, which reveals the enhanced early hydration of OPC paste in SW due to the influences of salt ions such as sodium, sulfate, and especially chloride ions. As mentioned above, the presence of chloride could accelerate the precipitation of calcium ions, which was beneficial to the dissolution of minerals. In terms of the sulfate ions involved in hydration, 0.034 molar of sulfate could be supplied from the 5.84 wt.% of gypsum in 100 g of OPC, and 0.0014 molar of sulfate was introduced from SW, which accounts for only 4% of that from gypsum. However, despite the small variation of sulfate content, Figure 5.5 reveals a similar or less amount of AFt formed in SW after 1 hour and 2 hours of hydration. This is probably due to the formation of calcium oxychloride (Farnam, Dick, et al. 2015), which occupies the limited surface of cement particles and restricts the formation of AFt (Costoya Fernández 2008). As a result, the generation of AFt was slightly retarded at the initial stage of hydration.

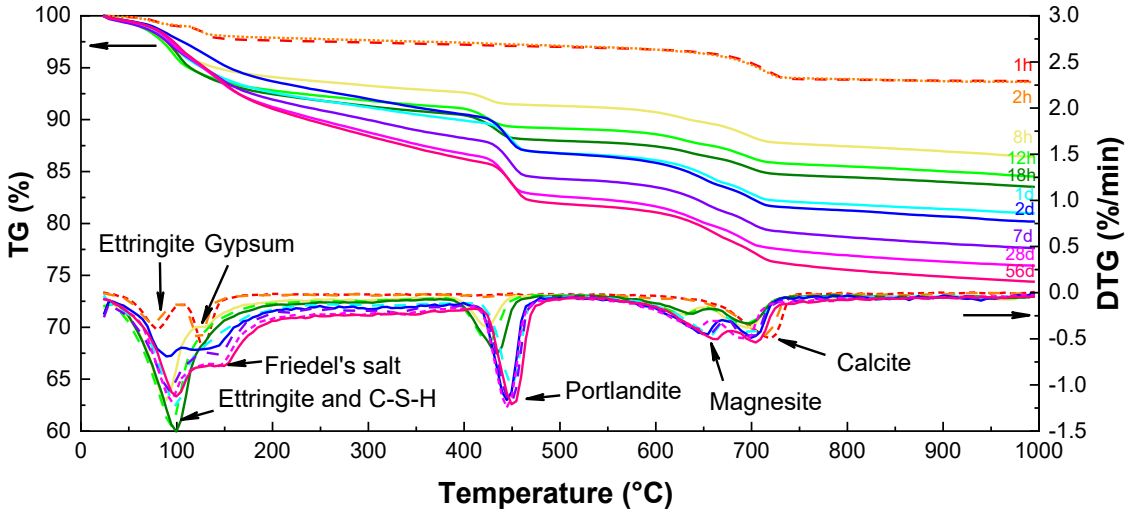

Figure 5.5. TG/DTG curves of OPC in SW; after 1, 2, 8, 12, 18 hours, and 1, 2, 7, 28, 63 days of hydration at a w/b ratio of 0.5

The formation of FS was the most significant difference between pastes with DW and SW. The FS could be dehydrated at 120 ℃ (Birnin-Yauri & Glasser 1998b) and thus cannot be distinguished with carbo-AFm from TG analysis. In the X-ray patterns of cement paste with SW, the characteristic peak (2-Theta at 11.192°) confirmed the presence of FS, as shown in Figure 5.6. In particular, the hydration product carbo-AFm was never formed in cement paste with SW, which was quite different from cement paste with DW. The results suggest that carbo-AFm was instable with chloride ions and could be converted into FS in SW. Also, it was feasible to bind chloride ions by increasing the content of the AFm phase in OPC. Furthermore, it should be noted that more carbonate was observed decomposed over 600 ℃ in cement paste with SW, which was due to the formed magnesite from the excess carbonate from the decomposition of carbo-AFm and the additional magnesium introduced from SW.

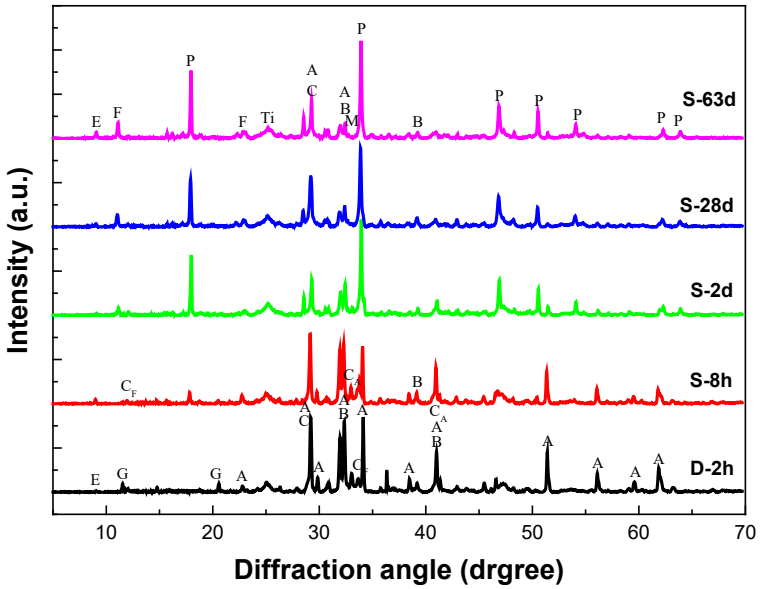

Figure 5.6. XRD pattern of OPC in SW after 2, 8 hours, and 2, 28, 63 days of hydration at w/b ratio of 0.5 (A - C_3S, B - C_2S, C - CC, E - AFt, F – FS, G - gypsum, P - CH, M - magnesite, C_A - C_3A, C_F - C_4AF, Ti - titanium oxide for calibration reference)

5.3.3 Modelling of hydration

The evolution of the solid phase and pore solution was investigated by applying the quantitative analysis of TG/DSC results and semiquantitative analysis of XRD patterns. The peak areas in the DSC curve represented the enthalpy change, which reflected the energy transfer from a certain reaction of decomposition (Kong & Hay 2003) to support the quantitative analysis of mass loss. Taking samples of cement paste with DW in 2 hours and cement paste with SW in 12 hours, as shown in Figure 5.7, the corresponding hydration phase could be quantified through methods combining TG and DSC. Based on these data, a linear regression was used to investigate the correlation between TG and DSC. Figure 5.8 demonstrates a reasonable agreement and close values to the linear relation for evaluating gypsum, CH, and CC. Therefore, the data from DSC confirmed the TG results, which could be the supplementation and correction in the estimation of the solid phase. The extent of OPC hydration was evaluated based on the changes in the

peak intensity of the crystalline phase in XRD patterns. The peak intensity was corrected by the intensity of TiO_2, which was the calibration substance.

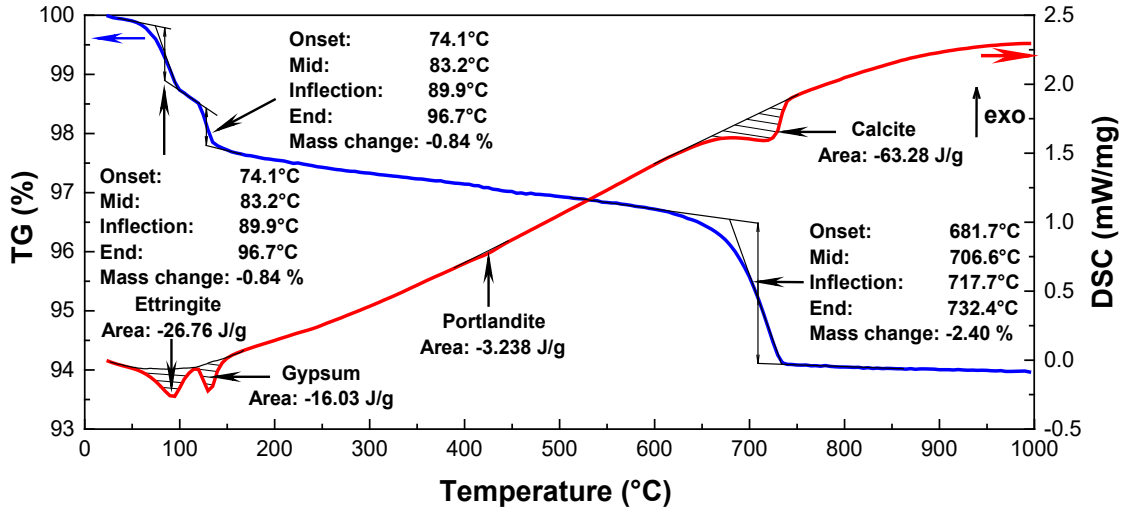

(a) TG/DSC analysis of OPC hydrated in DW for 2 hours

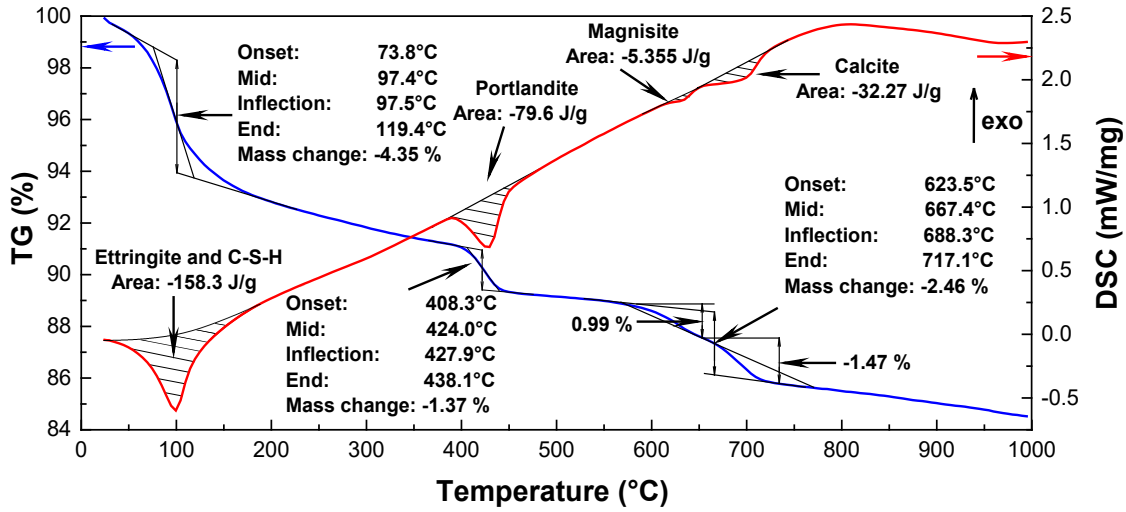

(b) TG/DSC analysis of OPC hydrated in SW for 12 hours

Figure 5.7. Quantitative analysis of TG/DSC in OPC hydrated in DW and SW

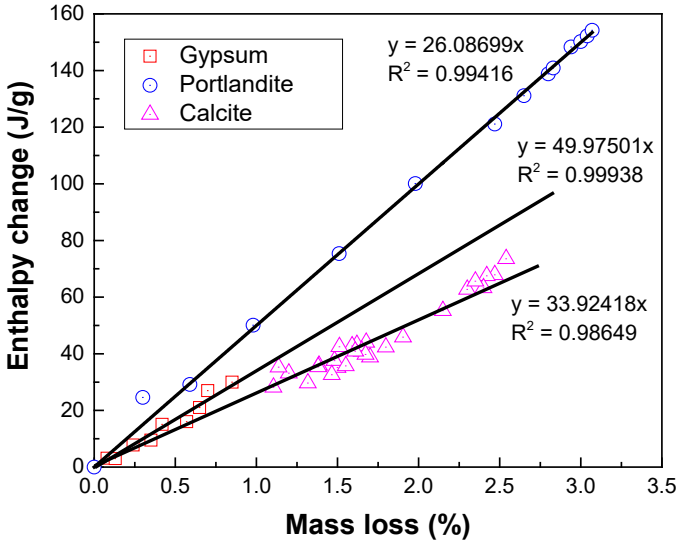

Figure 5.8. Fitting regression of the data from TG and DSC evaluation methods of gypsum, CH, and CC

According to the result, a modelled evolution was set up regarding the various phases from OPC hydration in DW and SW as a function of the hydration time, as shown in Figures 5.9 and 5.10. It was observed that a small amount of gypsum dissolved in the first 1.5 hr, along with the hydration of C_3A minerals, and a small amount of AFt was found precipitated. After 8 hours of hydration, it was noted that 35% of C_3S had dissolved in SW, which was 16% more than that in DW, conformed to the aforementioned greater heat released from the hydration in SW during this period. After 7 days of hydration, the total amount of hydrated C_3S in DW was nearly caught up with that of paste in SW. At the late age of 63 days, the C_3S minerals were almost completely hydrated in DW. However, 8% C_3S was detected as remaining unhydrated in SW, showing that SW might decrease the late-age hydration rate of OPC. Furthermore, the total content of C-S-H in SW was lower, although it was beneficial to form C-S-H rapidly in the early 7 to 15 days of hydration. Overall, the results showed that the amount of C-S-H decreased by nearly 10 wt.% in SW after 63 days of hydration. The

decreases might be due to the increasing proportion of other hydration products such as AFt and FS, which led to a less negative effect on the late age strength of OPC.

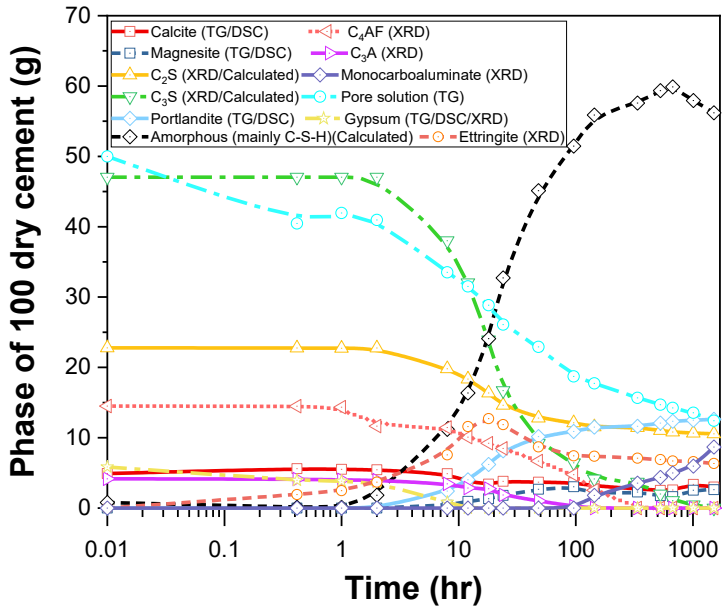

(a) OPC hydrated in DW

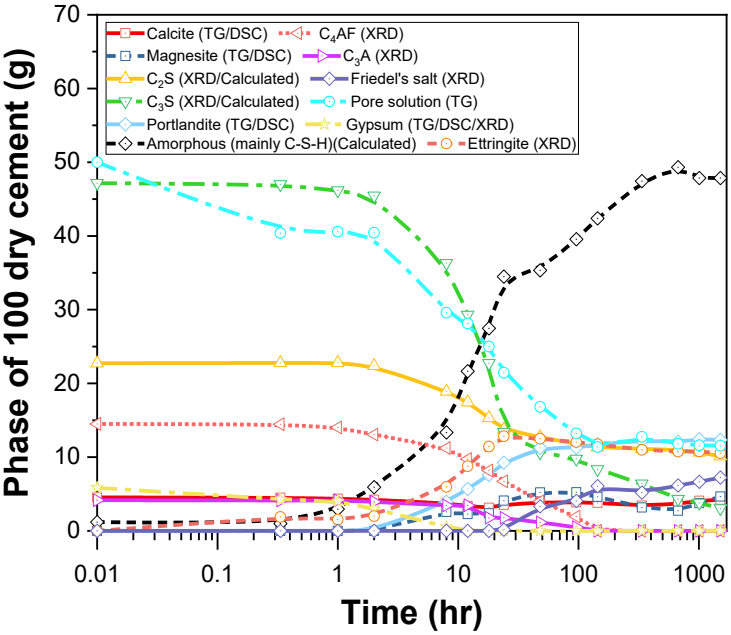

(b) OPC hydrated in SW

Figure 5.9. Evolution of solid phases model and pore solution of OPC in DW and SW

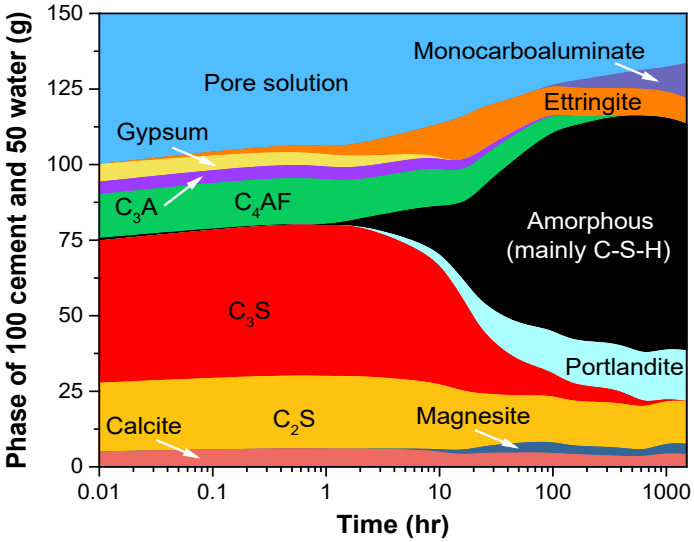

(a) OPC hydrated in DW

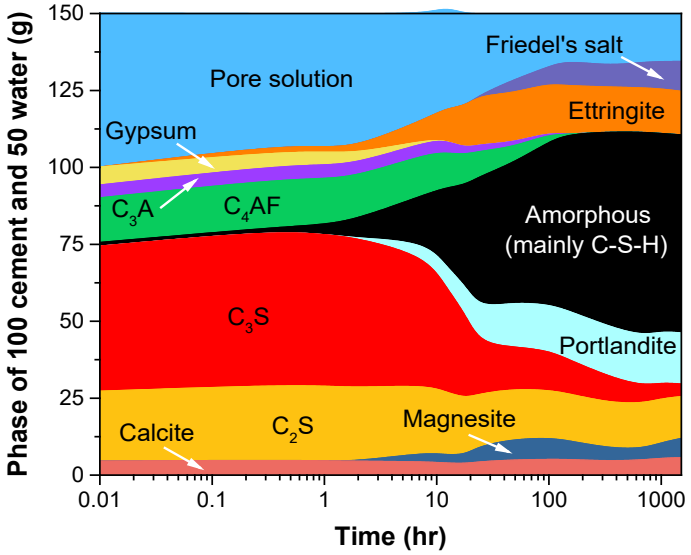

(b) OPC hydrated in SW

Figure 5.10. Phase evolution model of OPC hydrated in DW and SW

The gypsum in DW and SW completely disappeared after 12 hours of hydration. At this moment, the content of AFt was no longer increased but started to convert to the AFm phase. For the cement paste with DW, the content of AFt accounted for 12.7% of the total mass and then decreased to 6.6% after 63 days. With the presence of limestone in OPC, nearly 48% AFt converted to the carbo-AFm phase instead of sulfo-AFm after 63 days since carbonate can replace sulfate ions from AFm to form the stable phase

(Bonavetti, Rahhal & Irassar 2001; Lothenbach et al. 2008). In comparison, AFt in SW increased by 7% compared to that in DW after 18 hours. However, only 22% of AFt had decomposed after 63 days, indicating that the AFt exhibited more stable in SW. The reason is that the introduced chloride ions in SW are more stable to combine the AFm phase than carbonate from limestone. Therefore, the formation of sulfo-AFm became more difficult, which resulted in more uncombined sulfate ions presented in pore solution to hinder the decomposition of AFt.

The hydration ratio of C_3A and C_4AF shows no significant discrepancy in DW and SW. Figure 5.9 shows that C_3A and C_4AF were hydrated completely in 4 and 7 days, respectively. As for C_2S, only a similar 53% of this mineral phase was hydrated after 63 days in both DW and SW, although SW can accelerate the hydration of C_2S by 5% in the first 3 days. The formation of FS can be detected after 1 day of hydration in cement paste with SW, which gradually increased to nearly 7% of the total mass after 7 days and then kept unchanged for the further 56 days. FS is formed mainly from the residual unhydrated aluminate phase and chloride after AFt. The result showed that AFt formed earlier than FS, which can be due to the higher stability and insolubility of AFt than FS (Birnin-Yauri & Glasser 1998b; Hirao et al. 2005). In other words, FS can not be formed when gypsum exists because only AFt precipitates during this period, which was confirmed by the evolution of the solid phase from experimental results, as shown in Figure 5.10. It means that AFt does not have the chloride-binding capacity in the concentration of SW. The conclusion can also be drawn that if aluminate or ferrite minerals were used for binding chloride to reduce chloride concentration in cement, adding gypsum would weaken the binding effect.

Compared to the solid phase from hydration in DW, it was observed that no carbo-AFm formed in SW. The significant differences revealed that the chloride in SW can convert

carbo-AFm to FS by replacing carbonate ions, to form FS which was more stable than carbo-AFm. Furthermore, the study found no carbo-AFm formed throughout the hydration of 63 days, which illustrated that the involved chloride had beyond the binding capacity of the aluminate and ferrite phase in OPC. Due to the replacement effect of carbonate in AFm, the SW paste remained 1.5% more CC and 2.3% more magnesite than those of DW paste. The consumption volume of pore solution can represent the extent of hydration (Powers & Brownyard 1946), from the reaction of free water converting into chemically combined water and hydroxyl. Throughout the entire hydration process, the amount of pore solution in SW was always lower than that of DW, particularly from 2 hours to 15 days of hydration. The rapid consumption in SW can inevitably influence the early strength and workability and may affect construction efficiency (Younis et al. 2018).

5.3.4 Pore-size distribution

Figure 5.11 presents the PSD of cement paste with various hydration ages in DW and SW. The size of the pores in cement paste was mainly distributed in the regimes of 40–50 nm and 200–1000 nm. An average decrease can be observed in the porosity as well as the pore size with the increase in hydration time.

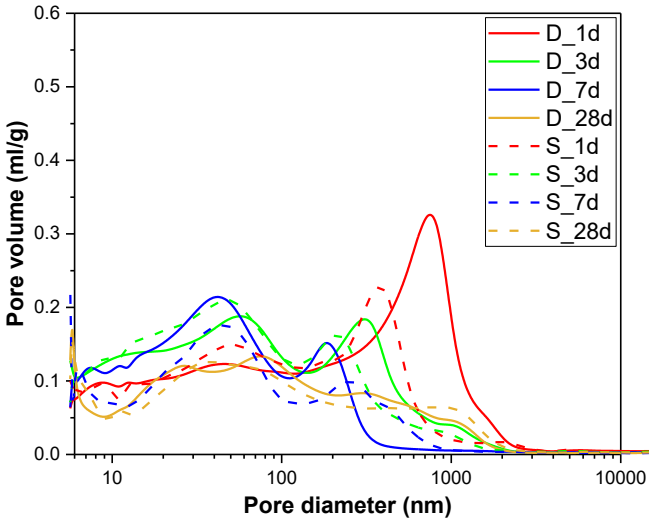

Figure 5.11. Pore-size distribution of cement paste hydrated in DW and SW at 1, 3, 7 and 28 days

Due to the stimulating effect on hydration, SW accelerated the precipitation of hydrate phases to reduce the pores at the early stage, which was significantly before 7 days. The accelerating effect gradually decreased with the growing hydration ratio. After 28 days of hydration, similar PSD can be observed in DW and SW samples. Wherein the result shows that DW led to a higher volume of pores with a diameter between 100 to 500 nm, which may result from the space left from a higher content of AFt converted to AFm phases. However, in SW samples, more AFt can remain stable at the late stages due to the chloride, as discussed in Chapters 3.2 and 4.2. SW caused a higher ratio of pores over 1000 nm, which may be due to the larger space left between the dissolution of clinker particles and the rapid formation of the matrix at the earlier stage.

5.3.5 Compressive strength of cement paste

Figure 5.12 summarizes the development of compressive strength in OPC paste with DW and SW. It could be found that SW increased the compressive strength of cement paste significantly at 7 days due to the accelerated hydration. The gap in the strength between the two pastes was gradually narrowed over time. The pastes developed a

similar compressive strength at the late stage of 90 days. The experimental results were consistent with the calculation from thermodynamic modelling. However, it should be noted that the error value of the strength in SW samples was higher. The late-stage strength was relatively unstable compared to the references, which may be due to the delayed gradual decomposition of AFt that caused the internal reduction of volume after structural hardening.

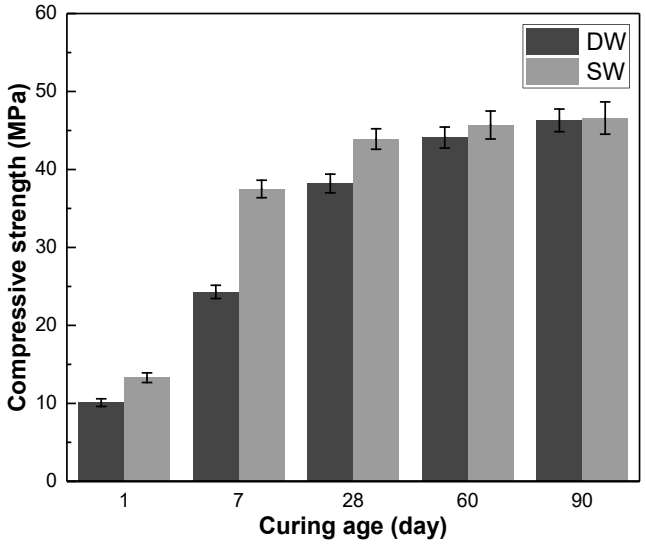

Figure 5.12. The compressive strength of cement pastes hydrated in DW and SW at 1, 7, 28, 60, and 90 days.

5.3.6 Compressive strength of cement mortar

The compressive strength of mortars prepared by DW and SW was investigated, as illustrated in Figure 5.13. It could be found that SW increased the early compressive strength of cement mortar at 7 days by nearly 15% in both specimens with river sand and sea sand. As for the late stage age, however, the compressive strength of the cement mortar with DW increased considerably more than those with SW. Although the specimens with SW had higher compressive strength at 14 days, they were subsequently exceeded by their counterparts with DW after 28 days. It conformed to the promoted early hydration and the slightly retarded hydration of C_3S in SW, which is the primary

mineral phase in OPC, contributing to compressive strength. In addition, river sand was better than sea sand regarding the growth of compressive strength, as a better grading distribution in river sand can obtain a denser structure. By contrast, the particle size distribution in sea sand is relatively concentrated, reducing the filling effect. Its smooth surface, furthermore, weakens the bound properties between cement and aggregates, thus gaining a relatively lower compressive strength.

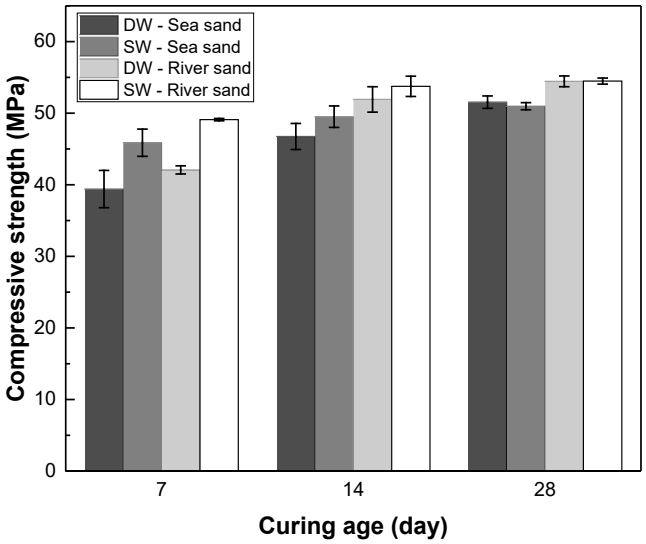

Figure 5.13. Compressive strength of cement mortar with different types of water and sand

5.3.7 Flexural strength of cement mortar

In Figure 5.14, the difference between specimens with SW and DW is less than 8% in flexural strength. However, using sea sand reduces the flexural strength by nearly 25% from 7 days to 28 days, indicating that the ions in SW present less impact but the flexural strength is greatly decreased by the poor particle size distribution of the aggregate.

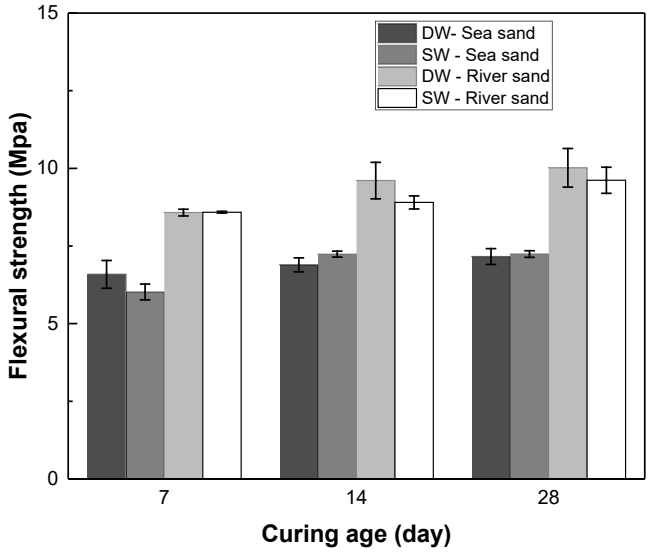

Figure 5.14. Flexural strength of cement mortar with different types of water and sand

5.4 Conclusions

In this study, the hydration properties of OPC in DW and SW have been investigated by analyzing the heat evolution, hydrated phase, hydration kinetics, and microstructures. The main conclusions were as follows:

The hydration of OPC can be accelerated by SW, which is mainly due to the chloride promoting the precipitation of calcium, aluminate, and ferrite. The accelerated hydration rate indicates the positive effect of SW, especially in the stage of 2 to 48 hours. The formation of FS led to the accelerated hydration of C_3A and C_4AF. Therefore the hydration rates of the two minerals were increased at high w/b ratios, with additional chloride involved in hydration.

The hydration rate of C_3S is greatly promoted in SW, especially at the early age of 1 day, due to the involved chloride in hydration. At the same ion concentration, the hydration rate of C_3S is not significantly increased by mixing with more SW. However, the hydration of aluminate and ferrite can be stimulated with the increasing amount of SW involved, which is due to the formation of FS.

Affected by the rapid hydration in SW, the early compressive strength of OPC mortar increased rapidly. For the cement mortar with SW at the w/b ratio of 0.4, the compressive strength of 7 days and 14 days increased by 15% and 5%, respectively, compared to those of counterparts with DW. However, the compressive strength of 28 days is nearly the same as that of specimens with DW. SW can influence the flexural strength of less than 8% from 7 days to 28 days, while using sea sand instead of river sand can decrease flexural strength by 25% due to the poor particle size distribution.

The chloride in SW promoted the early hydration reaction and influenced the hydrate assemblage of the hydrating cement paste. In the presence of chloride, FS was more stable than carbo-AFm in OPC paste. Due to chemical equilibrium, the decomposition rate of AFt at 63 days was reduced from 51% to 22%, and more carbonate was formed, such as magnesite which accounted for 2.3% to 4.6% of the total mass. As a result, the chloride binding capacity of OPC could be weakened by sulfate from gypsum, for that gypsum can react with aluminate to form stable phase AFt, which has no chloride-binding capacity.

It was found that at the later age of 28 days, 8% C_3S remains unhydrated in OPC paste with SW, and the mass of C-S-H is 10% lower than that of OPC paste with DW. The decrease in mass might be due to the increasing proportion of other hydration products, such as AFt and FS, and thus had a less negative effect on the later strength of OPC.

CHAPTER 6. MICROSTRUCTURE ANALYSIS OF HYDRATION RESPONSE OF PORTLAND CEMENT WITH SEAWATER

This section investigated the microstructural hydration features of Portland cement with natural seawater (SW). Special attention was paid to characterizing the pore, hydrated and anhydrous phases through the microscopy techniques of secondary electron (SE), backscattered electron (BSE) imaging and energy dispersive spectrometry (EDS) mapping. The characterization combines the latest BSE and SEM-EDS mapping techniques for obtaining two-dimensional digital images of Portland cement paste in which all major phases and pores are identified. Numerical treatments of maps are conducted to allow intuitive visual identification. Statistical results from different mapping techniques are compared and discussed.

6.1 Experimental program

6.1.1 Materials and sample preparation

The materials used in this section, including OPC, DW, and SW, were the same as those used in Chapter 5 to ensure the uniformity and representativeness of the samples investigated. Cement paste mixing was performed with DW or SW at a w/b ratio of 0.5 using a Hobart mixer according to ASTM C305. Cylindrical plastic moulds of 50 × 100 mm were used for casting. The cast paste samples were sealed and placed at 20 ℃ for 12 hr, 7 days, 28 days, and 63 days until testing. Two drying methods were applied afterwards, which depended on the curing time of the samples. For the 12-hour cement paste samples, a vacuum freeze dryer was used to prevent brittle fracture of the early-stage samples. Before drying, samples were crushed into 2 – 3 mm particles. The drying

process lasted 2 days at -55 ℃ in vacuumed condition to remove the free water. For the other longer-cured samples, particles with a diameter of about 2 mm were collected from the crushed cement paste. Isopropanol was used as the solvent exchange to dry the particles for 7 days. During the drying, the isopropanol was renewed at 1 hr, 1 day and 3 days. The dried particles were transferred into a vacuum desiccator with CO_2 and H_2O absorbing agents to allow the residual isopropanol to evaporate. In these two drying ways, the chemically bound water in hydrate phases was preserved as possible, thus keeping the hydrates unaltered (Scrivener, Snellings & Lothenbach 2016). However, it should be noted that the freeze-drying method was not the condition encountered in conventional cement hydration, especially at the stage of initial structure formation, and the pore structure in freeing-drying samples may be changed.

Samples were tested within 1 day after the drying process to ensure the reliability of experimental results. To inspect the morphology of the hydrate phases, the dried samples were broken to reveal a fresh surface, cleaned with nitrogen to clean the investigated surface, and then coated with Au/Pt alloy (80/20) with a thickness of 5 nm. Carbon Conductive tape was also used to bond the sample to the pin stubs, to improve conductivity and reduce the charge-up effect. As for further quantification of hydrate phases, preparing a smooth surface was significant to acquire reliable experimental results on delicate microstructure. The dried samples were crushed to collect 2 mm slices. To obtain a flat surface, silicon carbide paper #1200 was used for further polishing. Resin mounting was conducted using Leco 812-522^{TM} epoxy, followed by vacuum impregnation. The embedded samples were then polished by an SS-1000 polishing machine with polishing cloth lecloth^{TM} discs. Water-free diamond polishing suspensions were used as abrasives, with diamond lapping oil as a lubricant to prevent further hydration during the polishing process. An ideal mirror-like surface can be

attained by a 20-minute polishing under a pressure of 15 N with a 9 μm diamond suspension, followed by a 30-minute polishing at 20 N with a 3 μm diamond suspension and a 1-hour-polishing at 20 N with a 1 μm diamond suspension.

During the polishing process, the lapping oil was added continuously to cool down the surface's temperature, protecting AFt from thermal decomposition. Isopropanol ultrasonic bath was used to clean the samples before changing the polishing abrasives. The samples were coated with carbon with a thickness of 15 nm to avoid the interference effect of Au to EDS analysis after dried in the vacuum desiccator.

6.1.2 Test methods

The morphology analysis of hydrate phases at high magnification was conducted with a Field emission scanning electron microscope (FESEM) of Zeiss SUPRA 55-VP equipped with an Energy Dispersive X-ray Spectrometer (EDS) of Bruker Quantax 400. EDS point-scan analysis was performed to identify hydrate phases.

The microscope hydrate phases were expected to be quantitatively characterized by analyzing polished samples through Zeiss EVO SEM with EDS. The quantification analysis of pores (500 nm – 100 μm) applied statistical map image analysis, combining SE and BSE imaging. The grey-level statistics analysis of BSE images was also conducted to roughly separate the region of hydrated and unhydrated phases. Furthermore, EDS quantitative mapping technology was applied to obtain data on the atomic proportion of the investigated area, which can quantify various phases based on their chemical composition.

It takes nearly 1 hr to obtain a high-quality EDS mapping database (hypermap). Therefore, during the long scanning time, the conductivity of the samples was critical to avoid image shifting due to the beam drifting effect. In addition, the EDS mapping

scanning process synchronizes with BSE imaging to ensure the two imaging areas are consistent. 15 kV was applied as the accelerating voltage to access K lines of Fe. Whereas clear BSE images with high contrast gradients can be obtained from a scanning beam current of 2 nA, the deadtime value should be carefully considered. As proposed in the existing literature on quantitative EDS analysis, the deadtime was 30-35% from the study of Georget (Georget, Wilson & Scrivener 2021), who used Aztec software to acquire and quantify hypermaps. However, as proposed by Newbury, the deadtime was recommended to be lower than 10% to minimize pulse coincidence (sum peaks) (Newbury & Ritchie 2015). By using Esprit software to acquire and process EDS hypermaps in this study, if the deadtime was over 40% or more, the input counts per second are too high to be handled optimally by the current amp time and may lead to excessive summed peaks, and causing high dispersion after when processing hypermaps, as indicated in Figure 6.1. The significant discrepancy may be due to the different software used. Therefore, based on the performance of EDS detection equipment, the optimum deadtime was 5% - 9%, and the beam current was adjusted from 300 – 600 A, for the different types of polished samples investigated.

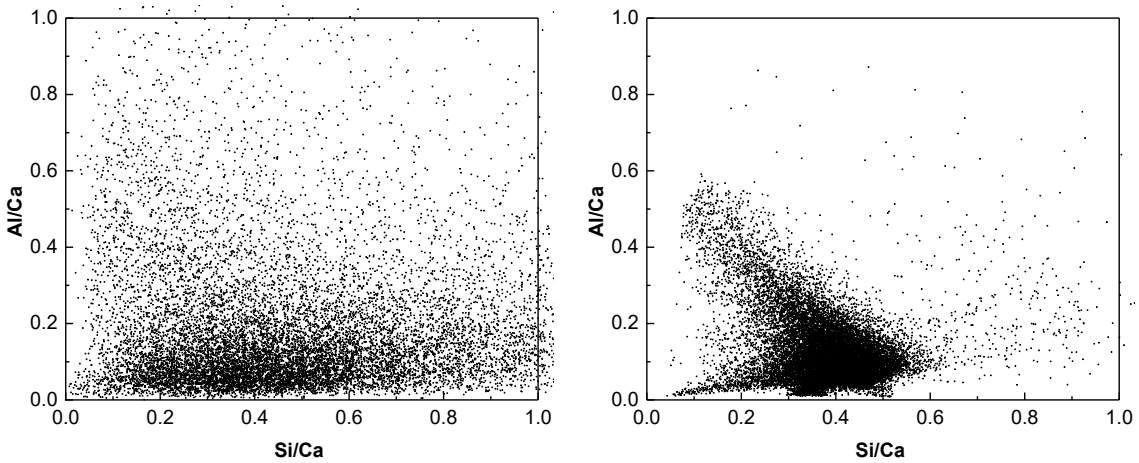

(a) One-eighth of the same hypermap (b) One-fourth of the same hypermap

Figure 6.1. The elemental atomic ratio mapping result of 12-hr cement paste with DW (data acquired with 40% deadtime, quantified at resolutions of the same acquired

hypermap)

The EDS hypermaps were acquired over regions of 440 μm by 330 μm at a resolution of 1024 × 768 pixels. The dwelling time (the time the electron beam stayed on a pixel while acquiring hypermaps) was 256 μs, with the line average (controls the number of times a horizontal line was scanned before proceeding to the following line) of 10, wherein it took nearly 40 minutes to acquire a quantified hypermap.

The quantitative data about the sample composition is derived from the different peak intensities by an extensive mathematical process. In this study, the standard peak-to-background ZAF correction (P/B ZAF) was used as the self-calibrating method. The data of standards for all elements of interest in this study was from the built-in standards library: wollastonite for Ca, corundum for Al, anhydrite for S, quartz for Si, NaCl for Cl, hematite for Fe and MgO for Mg. Due to the limited standards database, the quantification of Na and K was performed by the standardless P/B ZAF method, which can also provide reliable and adequate element results for non-light elements. In addition, the stoichiometric of O was alternatively carried out during elements processing. Although it may not be accurately quantified, it would correct matrix errors effectively by processing the oxides of the dominant (Georget, Wilson & Scrivener 2021).

The resolution of output quantitative processing results also needed to be adjusted; the long processing time severely limited the efficiency of determination. If the resolution remained unchanged (1024 × 768 pixels) or increased, quantifying a map would typically take 10 hours to more than one day but obtain high-quality maps. A finer quantifying calibration could significantly reduce data dispersion. As shown in Figure 6.2, the higher the resolution outputted, the higher the quality of the results. A compromise of one-second resolution of the acquired maps was adopted, which could

produce a satisfactory result in an acceptable one-hour time. In this way, a quantified elemental map was obtained in about two hours.

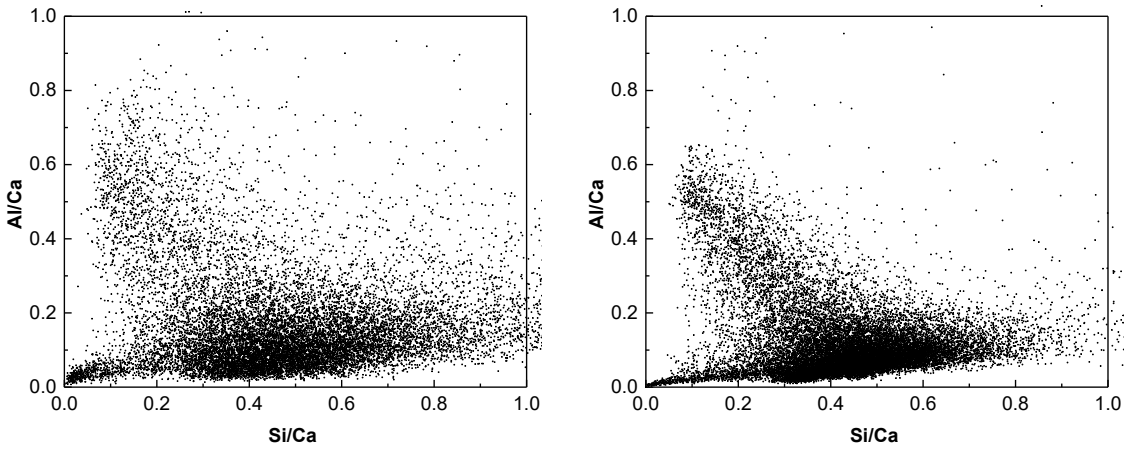

(a) One-fourth of the same hypermap (b) One-to-one ratio of the same hypermap

Figure 6.2. The elemental atomic ratio mapping result of 12-hour cement paste with DW (data acquired with 7% deadtime, quantified at resolutions of the same acquired hypermap)

6.2 Image and data treatment

The characterization combines the latest image and data processing technologies, SEM imaging, and EDS mapping methods for obtaining two-dimensional digital images of cement paste in which all major phases and pores are identified. A sequential approach to the study is presented in Figure 6.3, which will discuss the following issues in separate sections:

1. Region segmentation of BSE image and its defects

2. Correction of pore area by combining SE and BSE images

3. Processing EDS mapping data for phase identification and regional quantification

4. Obtaining two-dimensional digital images for microscopic characterization

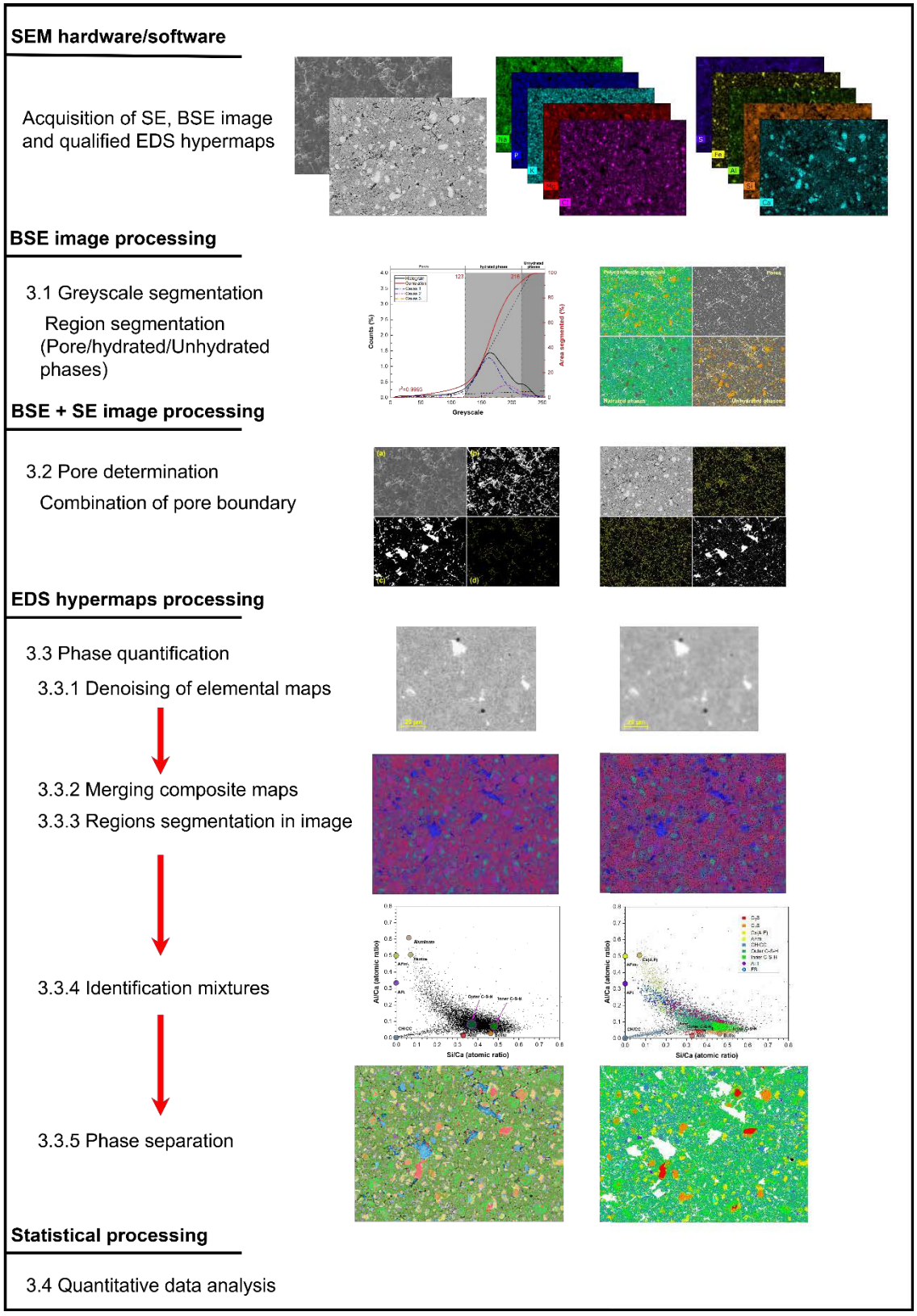

Figure 6.3. Flowchart of the image and data treatment process corresponding to sections of the paper

6.2.1 Greyscale segmentation

Figure 6.4 illustrates typical greyscale segmentation results from a BSE image of the 63-day hydrated OPC paste (the sample S63d_1) with SW, as an example in the following image and data treatment. The deconvolution procedure of the histogram was performed by Peakfit software, using a Gaussian response function with a Fourier deconvolution algorithm. Three Gaussian curves can be revealed in Figure 6.4(b), which represent a local maximum. The first Gaussian curve is primarily assigned to the C-S-H phases, and the second Gaussian curve can be classified as CH. Since the intersection of the two Gaussian curves was close to the peak, segmenting the two phases directly by greyscale discrepancy was not rigorous to some extent; the greyscale of CH and inner C-S-H phases were hard to distinguish, especially at the late stage. Therefore, Gauss 1 and Gauss 2 were counted jointly as hydrated phases.

The third Gaussian curve can be attributed to unhydrated phases. The intersection between Gauss 2 and Gauss 3 was set as the threshold to divide hydrated and unhydrated phases. It should be noted that no sharpened peak occurred in the histogram because the BSE imaging can still detect partly phases inside the larger pores. Therefore, the tangent-slop method (Scrivener 2004; Scrivener et al. 1986) was used as the strategy to determine the threshold to divide the C-S-H phase and pore. Proper area segmentation with other strategies, such as the “overflow” method (Wong, Head & Buenfeld 2006), was also reasonable in common. However, it needs to be emphasized that the pore determination only by the greyscale of BSE was not wholly reliable. Joint strategies would be used to correct the pore phase determination, which was illustrated in the subsequent section. Here, the greyscale values of 123 and 216 were adopted as the threshold for the pores, hydrated, and unhydrated phases of the particular BSE image.

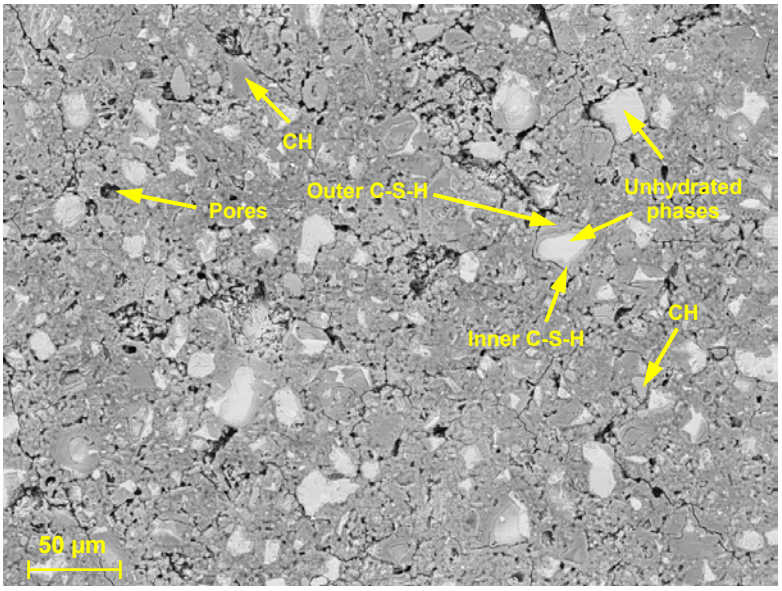

(a) Origin BSE image

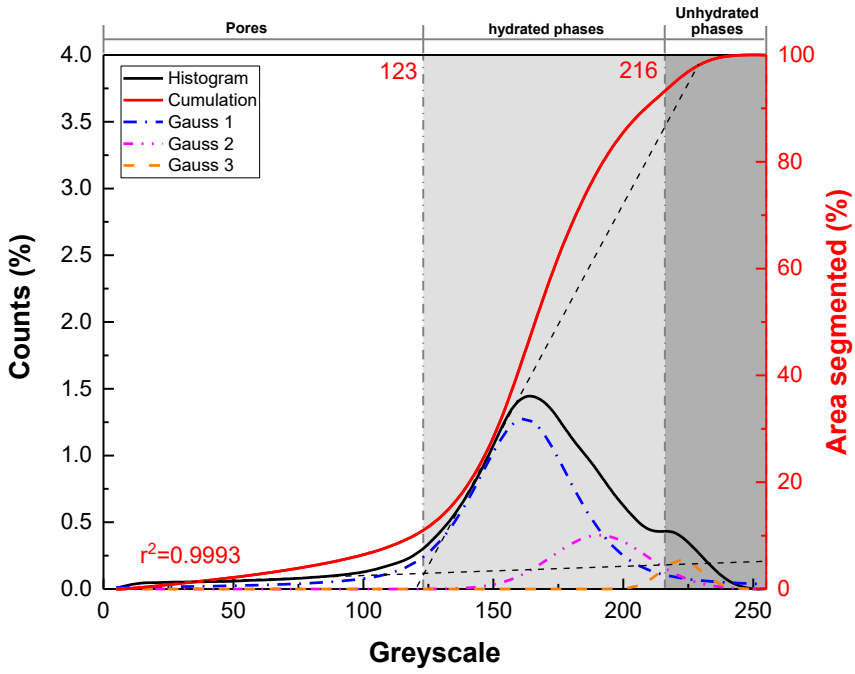

(b) Grayscale histogram

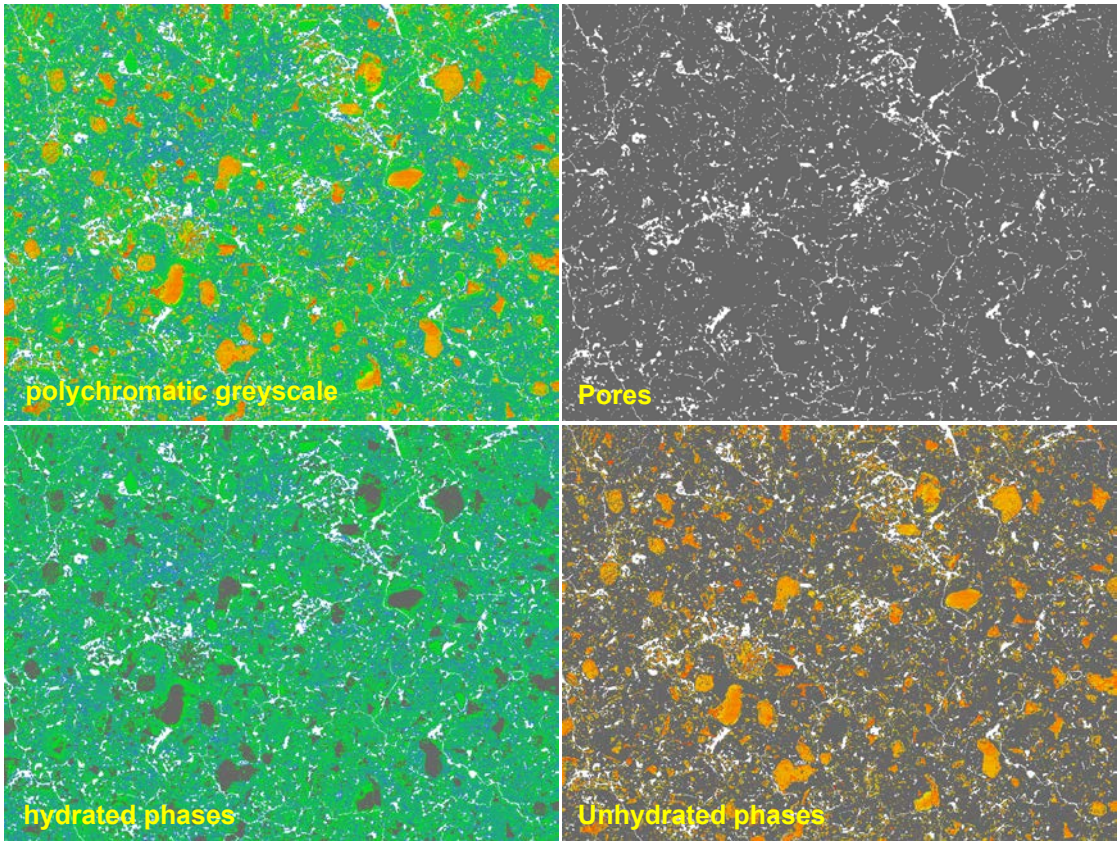

(c) Polychromatic greyscale images based on the specified threshold

Figure 6.4 A typical BSE image treatment for region segmentation in S63d_1

The Polychromatic BSE images can be obtained based on the greyscale segmentation above in Figure 6.4(c). Table 6.1 lists the determined threshold of samples in this study, wherein slight differences in threshold value can be observed even for the samples from the same cement paste. This is because the current intensity was adjusted to obtain qualified EDS hypermaps with enough counts per second, resulting in a brightness change in the BSE image. Due to the various hydrated time, the current intensity of microscopy needed to be adjusted depending on the imaging quality and deadtime for elemental mapping. Thus, there was an unvoided deviation of brightness and contrast of these images, and threshold values should be determined independently for each sample. More details about threshold determination for the samples were plotted in Appendix A.

Even though the phase segmentation might be arbitrary to some extent, it can ensure the reliability of revealing regularity by using the identical processing strategy.

Table 6.1 Threshold values for hydrate phases segmentation of cement paste

Cement Pastes	Pores	Hydrated phases	Unhydrated phases
D12h_1	0 – 53	54 – 140	141 – 255
D12h_2	0 – 48	49 – 145	146 – 255
S12h_1	0 – 117	118 – 192	193 – 255
S12h_2	0 – 106	107 – 182	183 – 255
D7d_1	0 – 125	126 – 200	201 –255
D7d_2	0 – 109	110 – 186	187 – 255
S7d_1	0 – 131	132 – 205	206 – 255
S7d_2	0 – 118	119 – 197	198 – 255
D28d_1	0 – 107	108 – 207	208 – 255
D28d_2	0 – 108	109 – 182	183 – 255
S28d_1	0 – 124	128 – 187	188 – 255
S28d_2	0 – 146	147 – 204	205 – 255
D63d_1	0 – 119	120 – 191	192 – 255
D63d_2	0 – 130	131 – 192	193 – 255
S63d_1	0 – 130	131 – 212	213 – 255
S63d_2	0 – 123	124 – 216	217 – 255

Nomenclature: using “D28d_1” as an example, D denotes deionized water, 28d denotes curing for 28 days, and 1 represents the sample’s number.

6.2.2 Pore determination

Following the discussion above, it is defective for only using BSE greyscale histogram to determine pore area. A slight change in pore-related threshold can significantly increase or decrease the accounted area, mainly because some hydrate phase detected in

the pore was not counted as pore area. Therefore, a method for correcting the pore size was applied by combining SE images, in which the area of large pores was easy to determine.

The charge-up effect was undesirable in SEM imaging. However, it can well depict the boundary of the pores. The binarization of the pores and other phases can be obtained by adjusting the threshold, as shown in Figure 6.5(a) and (b). It must be emphasized that the charge-up area (the white area in Figure 6.5(b)) was larger than the real boundary of the pores. Therefore, a visual adjustment was required to shrink the white area (generally two pixels inward) after filling the internal area (for ImageJ software, the Fill Holes and Erode function may help as Figure 6.5(c)), and the outline of pores based on SE image can be obtained eventually in Figure 6.5(d).

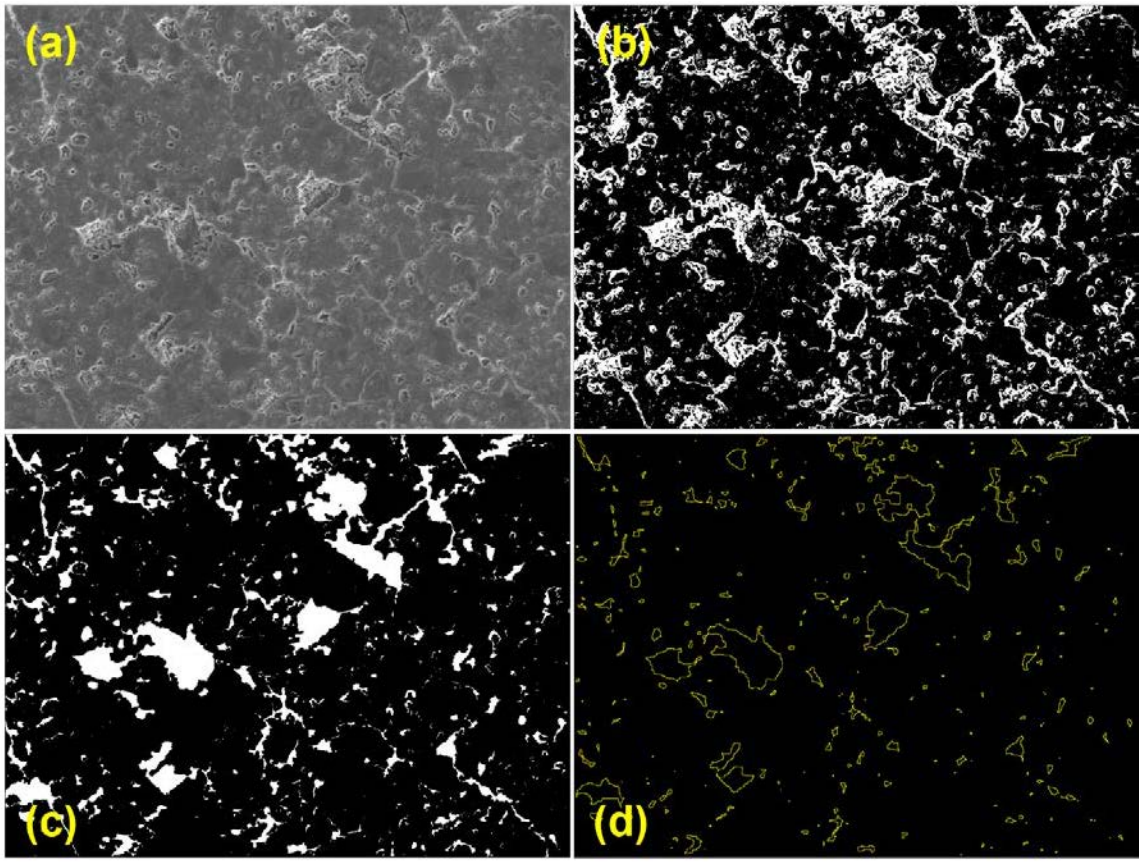

Figure 6.5 Delineation of pore boundary processed by SE image

Notably, the pore determined should consist of hollow reaction shells, cracks, and capillary pores (Wong, Head & Buenfeld 2006). By narrowing treatment, the finer pores (about two or fewer pixels in diameter) might be filtered out inevitably, hence the need for a merged pore boundary. According to the threshold determined from the BSE image above, the outlines of finer pores can be well preserved, as depicted in Figure 6.6(a) and (b). The merged pore boundary in Figure 6.6(c) can be obtained by combining the superiority of two pore-boundary determination methods, resulting in higher reliability in characterizing pores by image analysis. The corrected pore distribution is depicted in Figure 6.6(d), which can be further investigated for quantification.

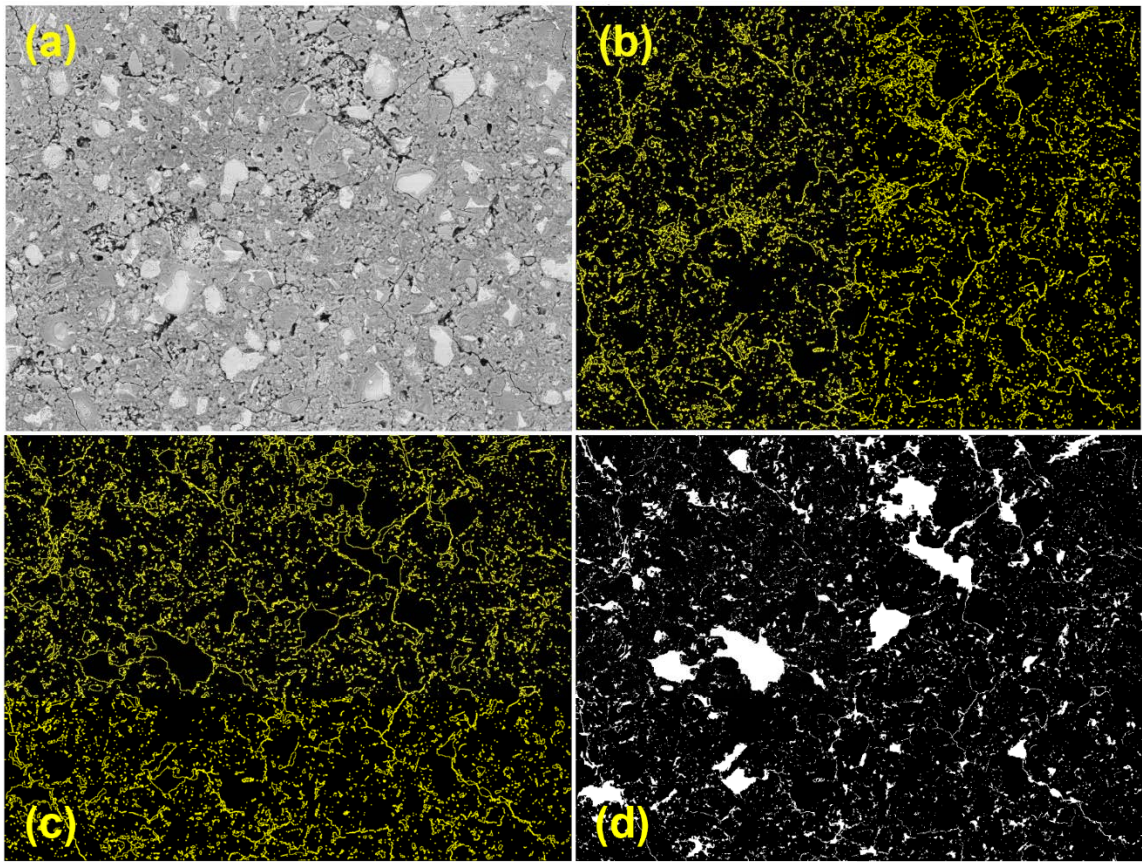

Figure 6.6 Correction of pore area by combining SE and BSE image

6.2.3 Phase quantification

Since the hydrated and unhydrated phases can be roughly determined by image analysis, it should be worth considering the identification and quantification of various phases. A new framework developed by Georget *et al*. (Georget, Wilson & Scrivener 2021), *edxia*, was used to identify phases by the ratio plots. This program was coded in Python (Oliphant 2007), using developed libraries of scipy (Jones, Oliphant & Peterson 2019; Moore et al. 2020), matplotlib (Jones, Oliphant & Peterson 2019) and scikit-image (van der Walt et al.). Based on its open-sourced framework, visual operating interface and creating linked maps with ratio plots, the *edxia* method significantly simplified the data processing.

6.2.3.1 Denoizing of elemental maps

Due to the limited scanning time for the EDS detector, the number of characteristic x-ray counts collected per pixel is usually lower than the threshold needed for dictating a high accuracy (Rossen & Scrivener 2017), which causes maps to be noisy. The noise was featured with the brightness variations as the densely dotted textures on the elemental maps. For instance, a calcium map with noise texture can be observed in raw EDS data displayed in Figure 6.7(a). The noise texture significantly caused a higher spatial dispersion in the pixels' element ratio distribution and brought inconvenience to the later processing while identifying various phases. Thus, image denoising was necessary. Although it may cause a few pixels to be unreliable, most can still provide competent information to distinguish more representative areas readily.

An ideal denoising result should remove hot pixels while preserving the sharp edges (Georget, Wilson & Scrivener 2021). Otherwise, the fuzzy edges of elemental maps would cause mutual encroachment in adjacent areas, distorting the original volume. The left column of Figure 6.7(b) to 6.7(d) displayed the processed Ca map by three

denoising algorithms: the total variation algorithm (Chambolle 2004), the Gaussian filter (Haddad & Akansu 1991), and the mean filter. The other maps (such as Si and Al) were denoised using consistent algorithms, plotting the element ratio on the right column. The denoising effect of each algorithm was controlled by its parameter. The mean filter depends on a radius parameter (the value here was 10.0); the Gaussian filter depends on a scale parameter (the value here was 0.5); the total variation algorithm relies on a weight parameter (the value here was 0.1). For each denoising algorithm, the optimum value of the parameter was not a constant (the larger the parameter value was, the further blurred the map was), and here it can be used as a reference for a reasonable range. In addition, adjusting the parameter value cannot optimize the algorithm, and thus the denoising algorithm selection should be prioritized. By comparing the deionizing methods, a better effect can be obtained by using the total variation algorithm, even converging the dispersed scatters into two strips. The mean filter can obtain a similar result, but the edge in the map was significantly blurred. As for the Gaussian filter, a compromise should be reached between the texture reduction and the fuzzing edge by adjusting the parameter, which limits the denoise extent. Based on the Gaussian function, a Joint bilateral filter (Eisemann & Durand 2004; Petschnigg et al. 2004; Tomasi & Manduchi 1998) was developed to be the non-linear, edge-preserving denoising algorithm for images. It was also a competitive method to reduce the need for compromise while becoming more sensitive to parameters (Georget, Wilson & Scrivener 2021)

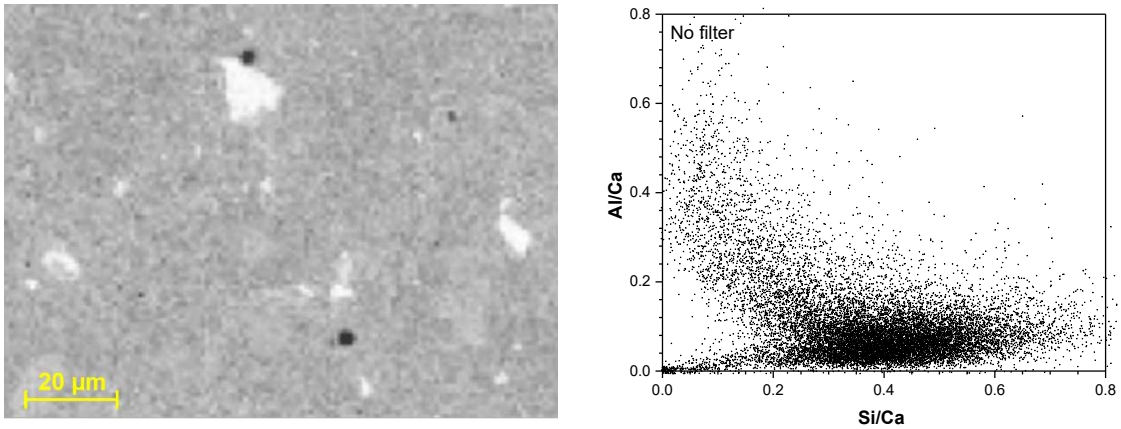

(a) Original Ca maps and atomic ratio plotted without filter

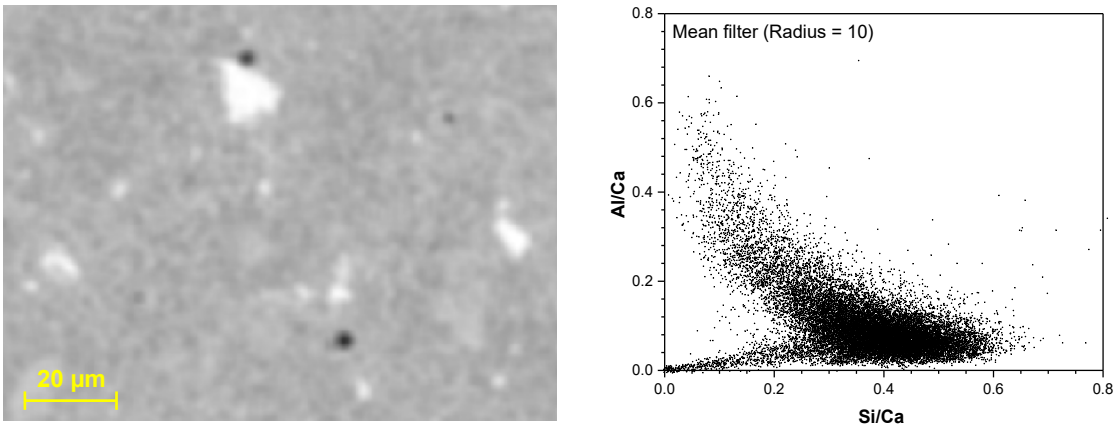

(b) Ca maps and atomic ratio plotted with mean filter (Radius = 10)

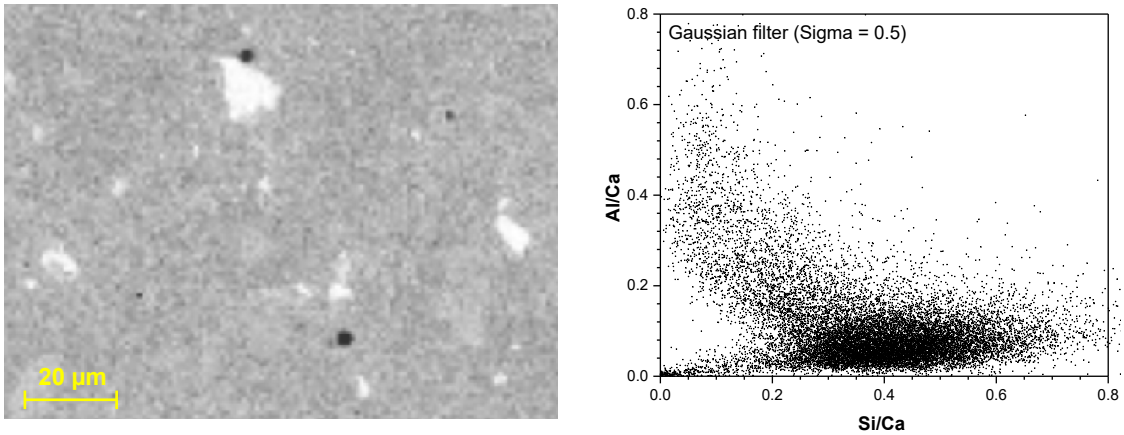

(c) Ca maps and atomic ratio plotted with Gaussian filter (Sigma = 0.5)

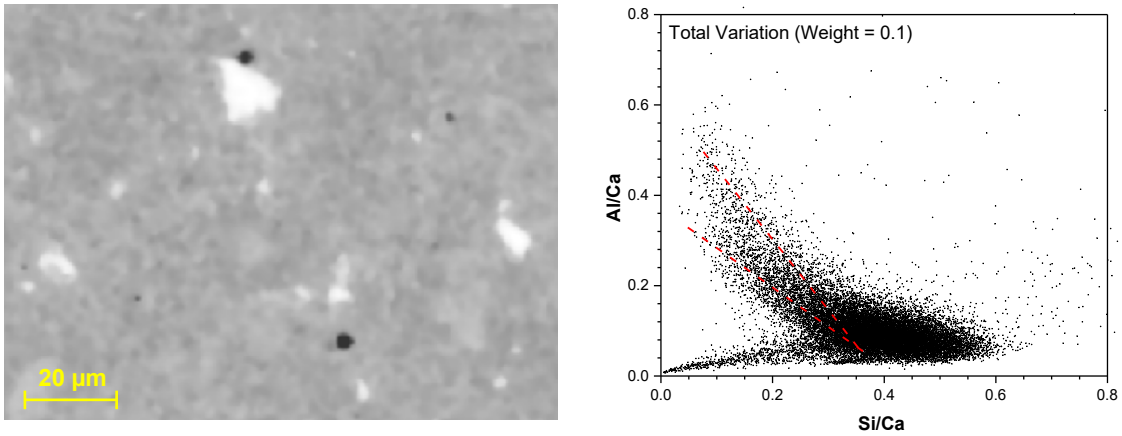

(d) Ca maps and atomic ratio plotted with total variation algorithm (Weight = 0.1)

Figure 6.7 Effect of the denoising algorithm on the Ca map and representative points in the ratio plot

Denoising is not an objective process—it inevitably leads to participant bias. Nonetheless, the information distributed over the many composition ratios was still quantitative on average (Harrisson, Winter & TAYLOR 1987). Because of the best denoising effect achieved from the total variation algorithm, it was used to process the elemental maps.

6.2.3.2 Merging composite maps

The main elements of interest in cement composition are Al, Si and Ca, by which most of the phases can be identified. A composite map with the three elemental distributions can be obtained by merging the elemental maps as the three channels of an RGB image: Si map for the red channel, Al map for the green channel, and Ca map for the blue channel. To enhance the definition of the grains' outlines in the image, the corresponding grey-scale BSE map can be used as the background with a translucent layer of the composite map covered. Figure 6.8 shows the four components of a composite image (a greyscale BSE image and three quantified element maps). The composite image is displayed in Figure 6.9(a). Specific chemical compositions of phases were displayed as colours with the corresponding RGB values; thus, they can be

identified. The background of the legend was set as the average colour of outer C-S-H for a better distinction by visual intuition.

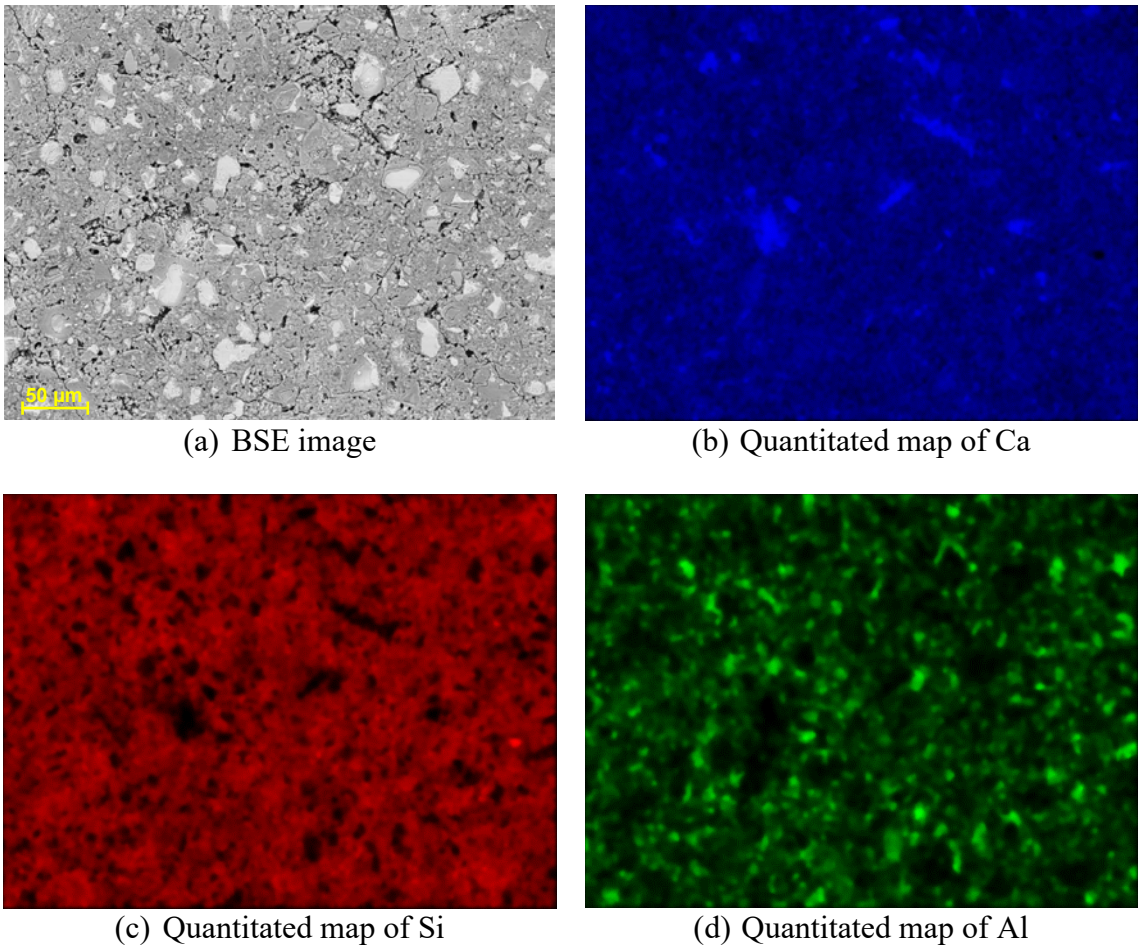

(a) BSE image (b) Quantitated map of Ca

(c) Quantitated map of Si (d) Quantitated map of Al

Figure 6.8 Components of a composite image

The composite map was suitable for fast phase identification, which was adequate for those phases with significant differences in chemical composition, for example, the CH and AFm phases. However, when it is necessary to consider the other elements (such as sulphate, chloride and magnesium), the composite map cannot merge another component unless replacing the original channel or displayed as a grey channel. In addition, the threshold in the composite map was offered by the hue of three quantized elements, not the chemical composition. For example, it was intractable to distinguish

the AFm phases and AFt. Therefore, phase separation based on chemical composition was necessary to go further.

6.2.3.3 Regions Segmentation in image

The segmentation can also apply to BSE images. However, without information on chemical compositions, it typically failed to distinguish hydrate phases through the region segmentation based on only greyscale distribution. Therefore, region segmentation by chemical composition was more beneficial for hydrate phase identification.

A simple linear iterative clustering (SLIC) algorithm was used to perform segmentation (Achanta et al. 2012), which adapted a k-mean clustering approach (Forgy 1965) to generate superpixels (a group of adjacent pixels that share common characteristics). Here in EDS's hypermaps, the similar characteristics were similar chemical compositions. By giving similar pixels the same colour belonging to a superpixel, it would provide perceptual meaning to facilitate phase identification. The segmentation result is displayed in Figure 6.9(b), which constituted 5000 chromatic fragments. The dots were the geometrical centre of each fragment. The main details were retained compared with the composite image in Figure 6.9(a). The segmentation was unnecessary while significantly reducing the data processing time and increasing the signal-to-noise ratio. Meanwhile, the loss of image information was minimized by using the SLIC algorithm. In a full scan image (with 1024 × 768 = 786, 432 pixels), a segmentation in 5000 to 20000 fragments is recommended (Georget, Wilson & Scrivener 2021). The geometric centre of these segmented regions would be used as the representative points with the chemical information to be analysed.

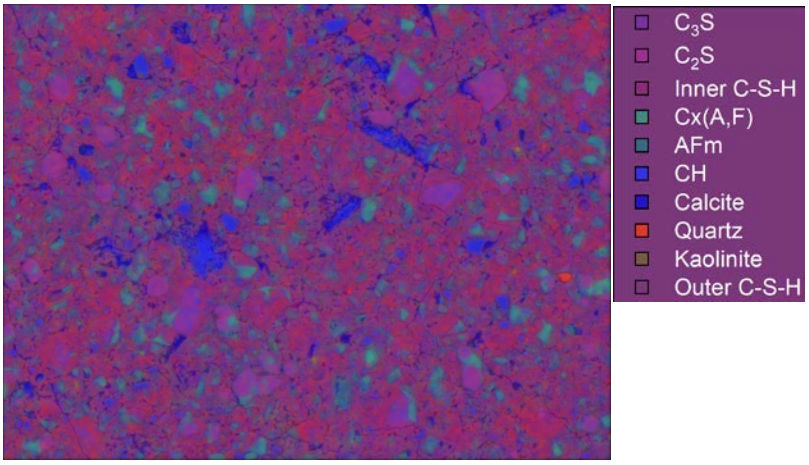

(a) Composite image

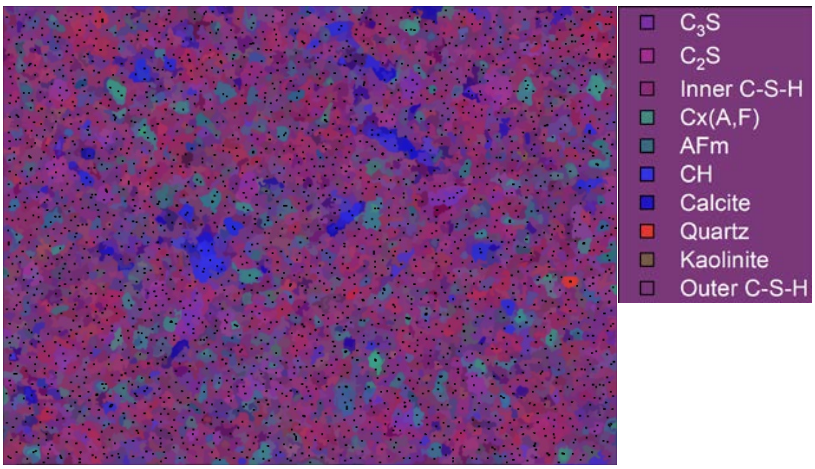

(b) Segmented image (in 5000 pieces)

Figure 6.9(a) Composite image generated from the translucent RGB layer over grey-scale BSE in Figure 6.8, and (b) Region segmented image using SLIC algorithm.

6.2.3.4 Identification and division of mixtures

For identifying cementitious phases, the atomic ratio was commonly adopted (Harrisson, Winter & TAYLOR 1987). A dataset of Al/Ca to Si/Ca plots can be obtained in Figure 6.10 based on the atomic ratio of the representative points. The circle regions representing some pure phases were marked corresponding to stoichiometries from Taylor (Taylor 1997). It can be observed that most of the points were not located ideally

in the regions; they were distributed as mixtures instead of pure phases. The reason may result from the limitation of scanning resolution. The C-S-H matrix contains various small particles, such as anhydrous grains and other hydrate phases. These fine particles were even smaller than the interaction volume of electron beams (the size of one pixel) that cannot be identified to a phase and, thus, would be considered "impurities" in the matrix.

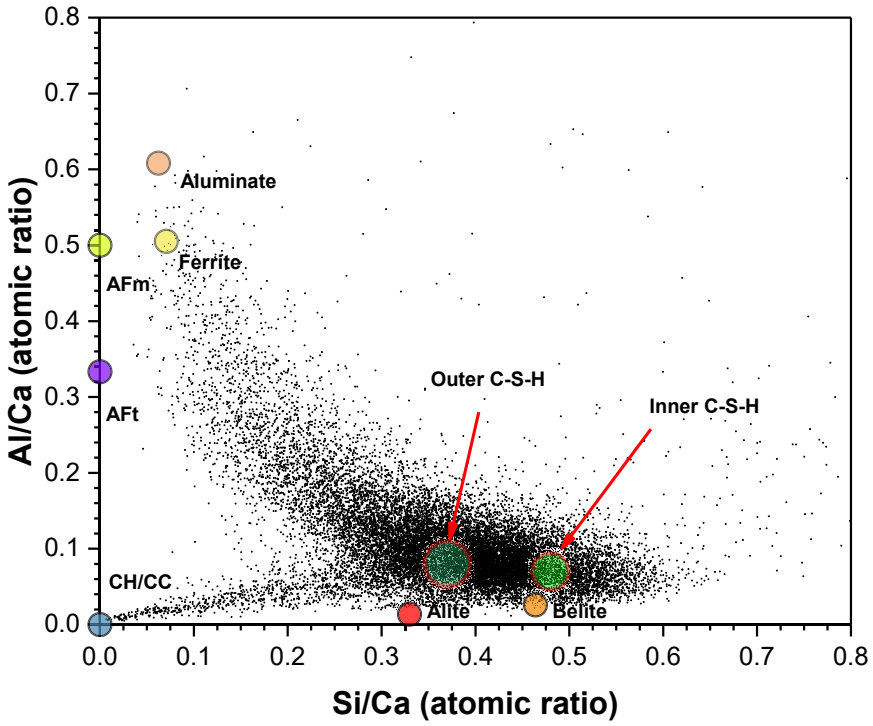

Figure 6.10 Atomic ratio (Si/Ca to Al/Ca) of representative points (in 20,000 fragments) from EDS hypermaps. The pure phases refer to the corresponding stoichiometries proposed by Taylor (1997).

The "impurity effect" inevitably caused a dispersion of point clouds in the result from the EDS mapping on the matrix unless a large amount of pure phase formed within a specific volume. Therefore, the region corresponding to the C-S-H matrix was depicted by the atomic ratio points from the pure C-S-H gels and the sub-resolution phases. The "impurity effect" occurred in other identifiable hydrate phases (such as Layered double

hydroxide (LDH) particles of AFms and other solid solutions), resulting in the mixture lines between the C-S-H matrix and the pure phases. In the Glue interface, the region of interest (ROI) can be separated by setting the thresholds along these lines, which correspond to certain phases by their stoichiometries. Conversely, the ROI can be corrected graphically using the grey-scale BSE image. Finally, after multiple adjustments, a finer ROI can be obtained through the manual selection approach.

6.2.3.5 Phase separation

According to the above approach, Figure 6.11 shows the boundary definition of point clouds and the corresponding false-colour ROI layers displayed on the BSE image. Based on the atomic ratio, the strategy for separating the main phases is listed in Table 6.2. A tolerance ε can be set up out of the scope of the stoichiometry of ideal pure phases dependent on the ratio distribution. The regions of anhydrous particles in the grey-scale BSE image can refine the typical value of ε. Because the composition of the cement and the sub-resolution phases mixed in the matrix may be variable, the boundary of the C-S-H matrix should be determined according to the specific situation rather than a fixed scope.

Compared to the outer C-S-H (the phases formed between clinker grains), the composition of the inner C-S-H (the phases formed in clinker particles) was more homogeneous due to the fewer other phases glued. The related point cloud was adjacent more to the boundary of C_2S. It seems reasonable because the inner C-S-H was more likely to form after the surface of anhydrous particles was completely covered by hydrated phases (Scrivener, Juilland & Monteiro 2015). Therefore more inner C-S-H was formed around C_2S due to its slower hydration rate. The definition of these boundaries can also, or perhaps should, refer to the BSE image. Thus, the scope listed in

Table 6.2 should not be taken as a strict guideline, but it can be considered an empirical rule to mark the phases readily.

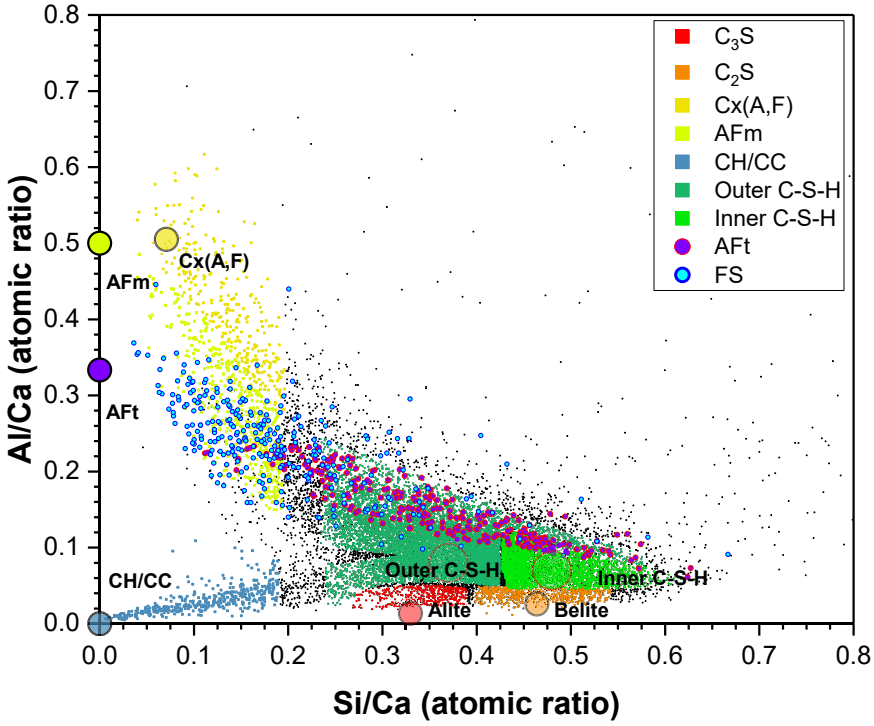

Figure 6.11 Definition of representative point clouds for phase separation

Table 6.2 Strategy for separating phases in cement pastes. ε represents a tolerance dependent on the distribution of representative points in the atomic ratio plot.

Phase	Si/Ca	Al/Ca	Others
C_3S	$0.33 \pm \varepsilon$	< 0.06	
C_2S	$0.5 \pm \varepsilon$	< 0.06	
CxAF	< 0.2	> 0.25–0.5	
AFm	< 0.2	< 0.25–0.5	S/Ca, Cl/Ca
CH/CC	< 0.2	< 0.1	
C-S-H matrix	Variable	Variable	
Quartz	> 1	< 0.1	High value in Si
Gypsum	< 0.2	< 0.1	S/Ca

Kaolinite	> 0.8	> 0.8	Si/Ca = Al/Ca

For the threshold definition of specific aluminium-bearing phases, such as AFt and FS, the Si/Ca vs. Al/Ca plot was insufficient to determine the boundaries; it should correspond to the ratio of sulfate and chloride. The typical crystal size of AFt was approximately 100 nm (refer to Figure 6.15 and Appendix B), which was significantly lower than the mapping resolution (430 nm for one pixel). Therefore, it was not strange to hardly find a representative point in the region of pure AFt phases (as shown in Figure 6.12(a)). Enhancing the resolution of EDS hypermaps was surely an effective measure to identify the sub-resolution phases. However, it can still be detected with the aid of a S/Ca vs. Al/Ca ratio plot. Based on the stoichiometry of AFt, the region rich in AFt of the C-S-H matrix would lead to a higher S/Ca ratio. Some representative points within the stochiometric range, thus, can be assigned as the geometric centres of segmented regions representing Aft phases. It would be, to some degree, disputed in phase identification. One is that, for example, in the regions of AFm phases, some points with a lower sulfate ratio might be caused by a small amount of AFt, not the AFms. Second, as shown in Figure 6.12(b), it can be observed that most of the selected AFt points were distributed in the regions of the C-S-H matrix, indicating that the sub-resolution AFt phase was detected integrally mixed with C-S-H. It seems hasty to assign the whole region as the AFt phases. Therefore, a compromise strategy was needed. For instance, the S ratio of C-S-H close to AFt phases was not assigned to the C-S-H matrix—assigning the AFt phase was a higher priority. Similar strategies were adopted to separate the C-S-H matrix with other detectable sub-resolution phases. The compromise strategy was not rigorous for quantifying these sub-resolution phases, but conducting qualitative comparison was adequate if the points assignment was performed according to the unified compromise strategy.

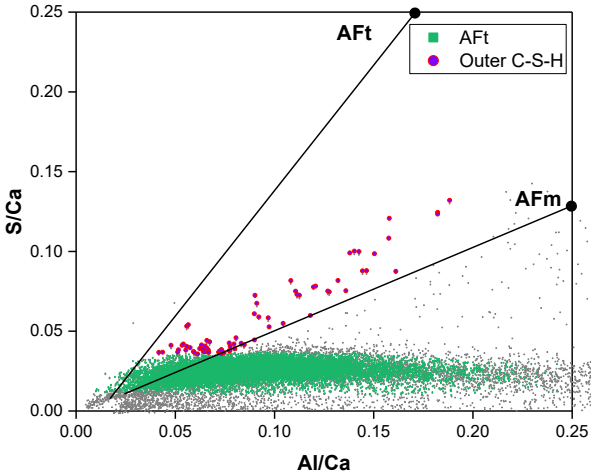

(a) Definition of representative point clouds for AFt/C-S-H

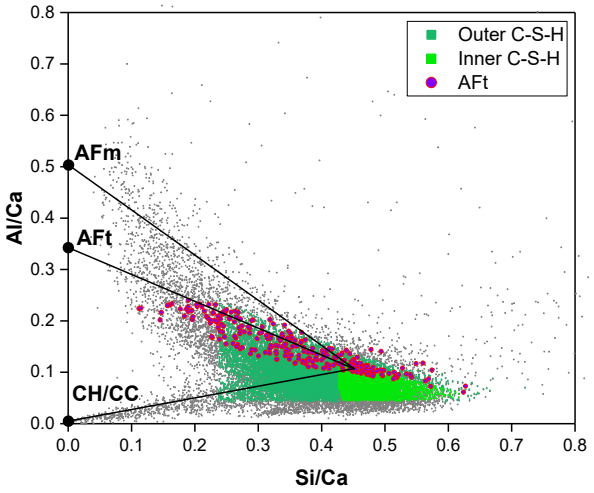

(b) Definition of representative point clouds for AFt/C-S-H

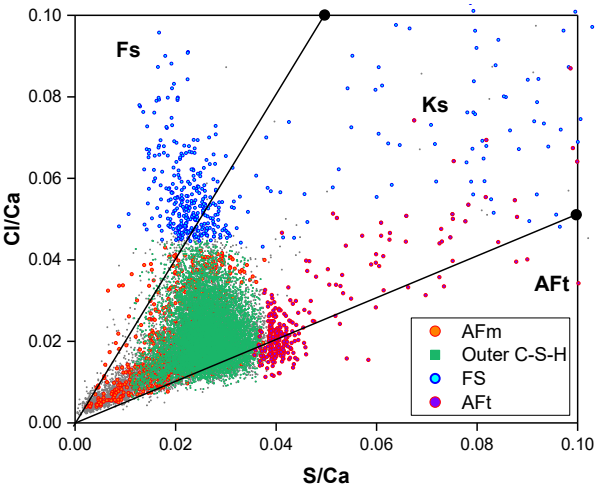

(c) Definition of representative point clouds for FS/KS

Figure 6.12 Boundary definition for specific phases

SW increased the chloride ratio in the cement matrix. The consistent compromise strategy allows representative points for FS and KS to be selected by Cl/Ca vs. S/Ca plot outside the C-S-H matrix in Figure 6.12(c). Similarly, these points were not considered pure phases; they represented AFms with a higher chloride ratio on average. The Cl/Ca vs. S/Ca plot also provided valuable information. For example, it can be observed that most of the AFm phase identified contains lower S and Cl, indicating the formation of carbo-AFm phases, which is consistent with the result in Chapter 5.

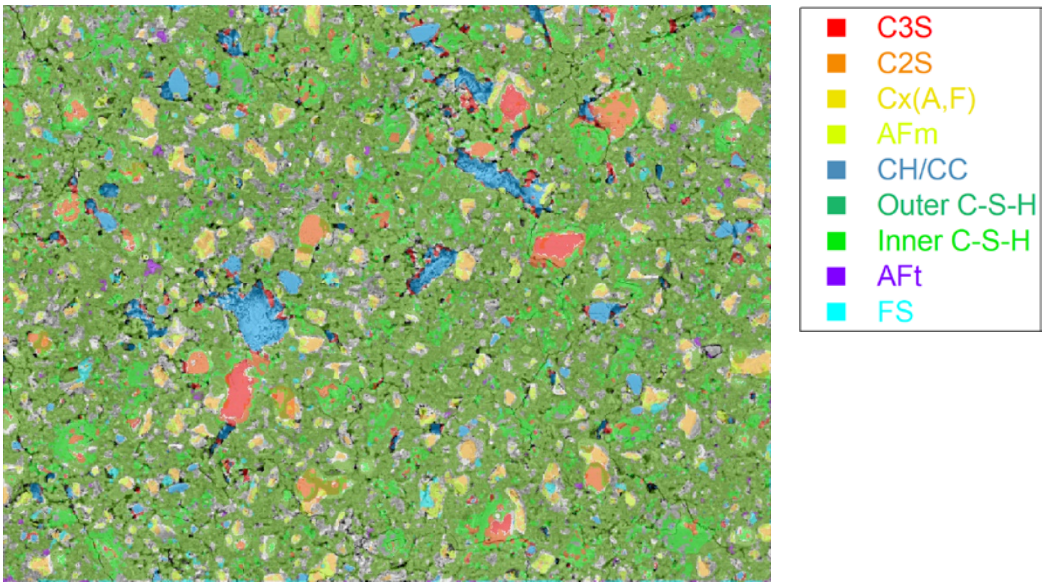

Figure 6.13 Identified phases by stoichiometries as overlays of the phase masks on the BSE image

Figure 6.13 displays the separated regions corresponding to various phases. The inner C-S-H phase was found surrounding the C_2S and C_3S particles. Some of them were observed in the shape of particles formed by the completely hydrated C_3S and C_2S phases. Combining with the BSE image, most CH clusters were found in the pores, which can be distinguished from CC particles with smooth surfaces and neat edges. A group of small AFm particles precipitated adjacent to the anhydrous C_xAF phase or scattered around, formed in the space left from clinker dissolution. Some of them can be

identified as FS and AFt. The outer C-S-H as the matrix glued various phases as a composite mixture.

6.2.4 Quantitative data analysis

Based on the image treatments mentioned above, a composite image was obtained to display the detailed distribution of pores and phases. However, extracting quantitative data from only one image may cause a great error due to contingency; a very large pore or anhydrous grain would result in a remarkable difference in value. Reducing the scanning magnification can decrease the error effectively, but more sub-resolution phases became hard to be identified. Geogret *et al.* (Georget, Wilson & Scrivener 2021) proposed a feasible method for images at high magnification—to renormalize the big particles according to the normalized result from remaining regions. In this study, images with a 1.57 times larger scanning area were used for quantitative analysis. In addition, more maps for one sample were used for statistical analysis (listed in Appendix C). Although it was time-consuming work, it was an exploratory attempt for future work.

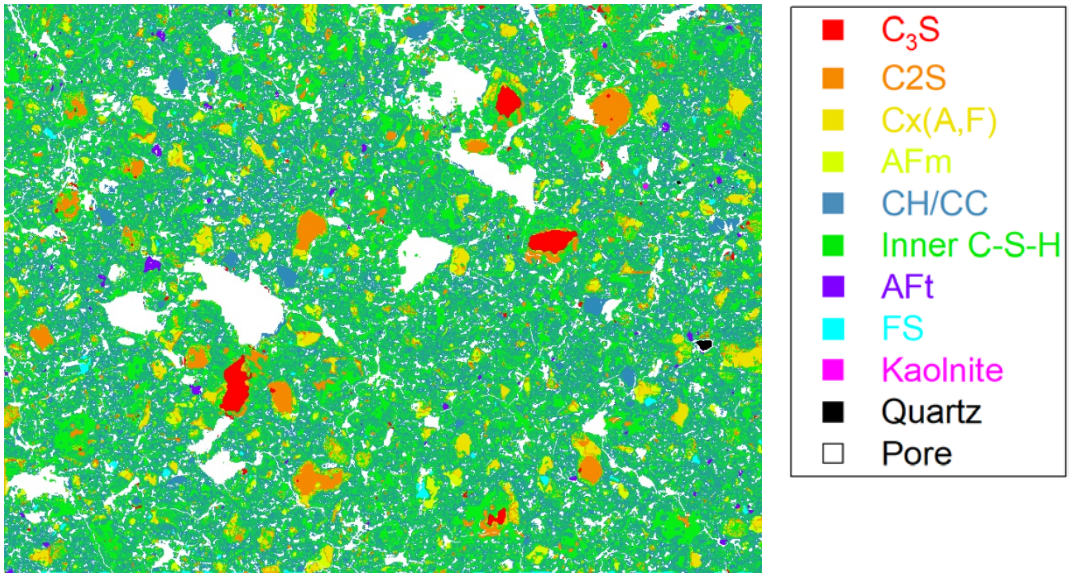

Figure 6.14 Composite image by ternary microstructure characterizing results

6.3 Experiment results

6.3.1 Morphology of hydrate phases

Figure 6.15 displays the SE micrographs of the cement paste after 28-day hydration with SW. Specific phases in the images can be identified by their typical micro morphologies and using the information from EDS points measurements. For instance, some crystals with high purity can be determined, such as CH as hexagonal platelet morphology (Plot 4) and AFt as hexagonal and prismatic crystals (Plot 10). The growing CH crystal thickened as a function of time (Plot 15). Although sealed curing was conducted to insulate CO_2 exposure, the carbonates can still be observed due to the self-contained CC in cement. Since the chloride was more competitive than carbonate to bind AFm phases, the initially dissolved carbonate would carbonate the CH phase eventually. Early signs of nucleation of carbonized CH (Jiang et al. 2018) can be observed in Plot 1; the crystal nuclei were evenly distributed on the CH matrix. The elongated clusters morphology can be observed from the growing carbonate calcium in Plot 2. The magnesium from SW can be precipitated as the M-S-H hydrate phase (Lothenbach et al. 2015; Nied et al. 2016; Roosz et al. 2015) mixed with C-S-H phases (Plot 3) and Mg-Al hydrotalcite-like phase (Haha et al. 2011) (Plot 5 and 6). As the main hydrate phase, C-S-H (Plot 7) can link other ions such as aluminate or alkalis, due to its poorly crystalline structure (Richardson & Groves 1993; Richardson 2008).

Cement with a higher content of aluminate may lead to the aluminate incorporation by C-S-H to form C-A-S-H and change the chain length (L'Hôpital et al. 2015; Lothenbach, Scrivener & Hooton 2011; Myers et al. 2015). The phase can be determined on Plot 13 with a looser surface than C-S-H.

In Plot 8 and 9, the AFt phase was converted to carbo AFm phases. The higher chloride or sulfate content in some AFm phases indicated the formation of FS and sulfo-AFm phases, as shown in Plots 11, 12, and 14. The coexisted AFm phases indicated that the sulfate, carbonate (mainly from gypsum and CC in cement) and chloride (mainly from SW) compteted for the formation of AFms. Like solid solution, these phases had no remarkable differences in morphology, and no obvious boundary can be determined. This was analogous to a sponge with absorbed fresh water on one side and salt water on the other. Segmentation of area could only be performed by ion concentration. Therefore, it confirms the feasibility of characterizing cement phases by element ratio from EDS approach.

In terms of the evolution of morphology, more details are listed in Appendix B. Although SW boosts the earlier microstructure formation by accelerating the hydration, noticeable differences in phase morphology cannot be observed at the late stage. However, issues should be considered regarding its stability. Since the microstructure of SW samples was developed in a stable condition with various ions involved, the main hydrate phase's volume, C-S-H, inevitably changed from element incorporation (L'Hôpital et al. 2015) or increased chemical shrinkage (Vafaei et al. 2022). Once the volume change is reversible, the stability of the structure may be sensitive to the long-term service environment.

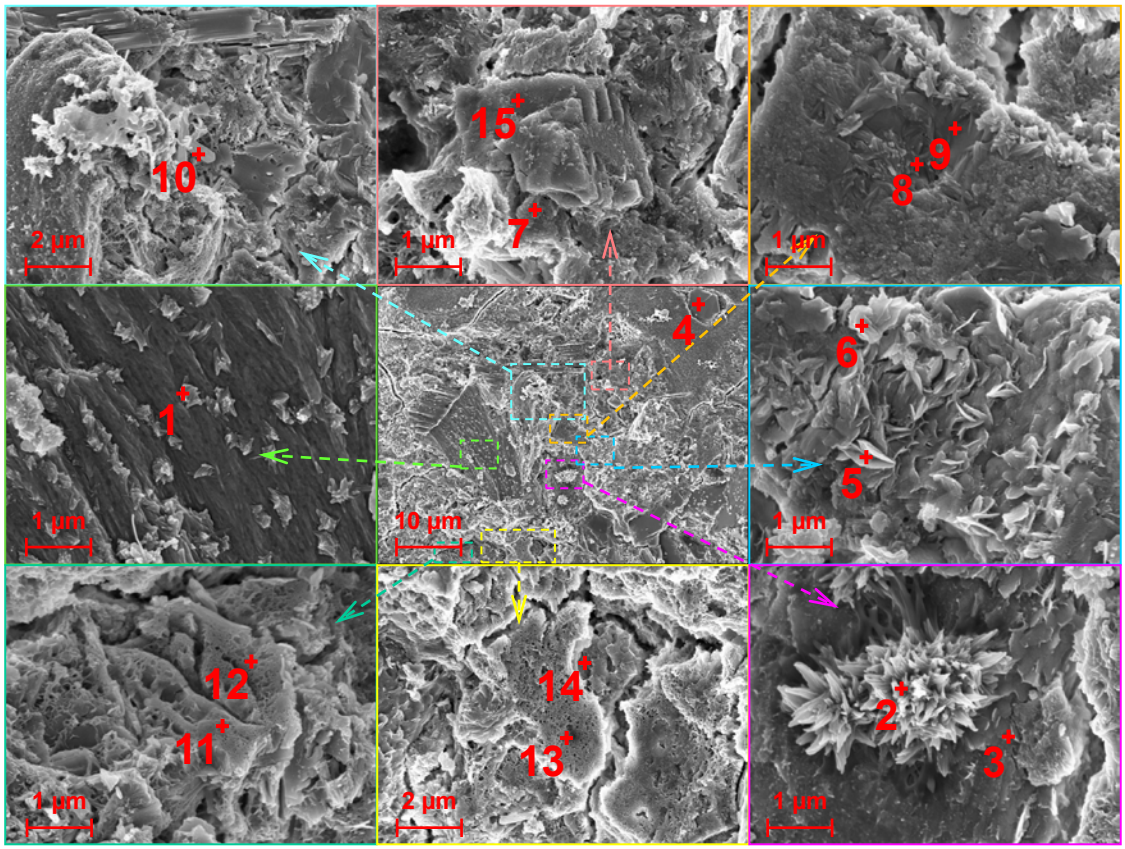

(a) FESEM images of hydrated OPC in SW at 28 days.

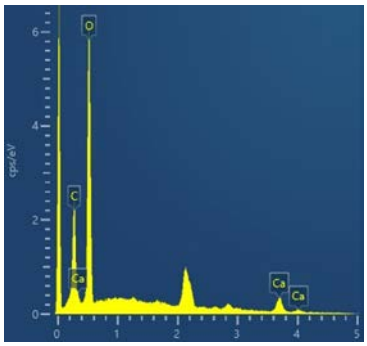

(b) Plot 1 (carbonized CH)

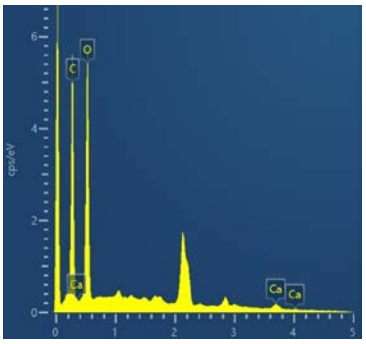

(c) Plot 2 (Carbonized CH)

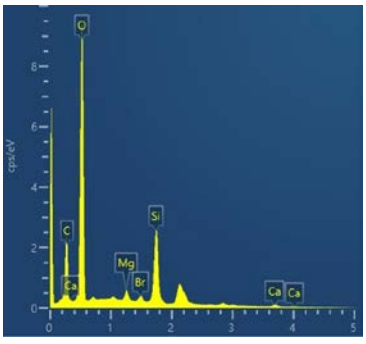

(d) Plot 3 (C-S-H/M-S-H)

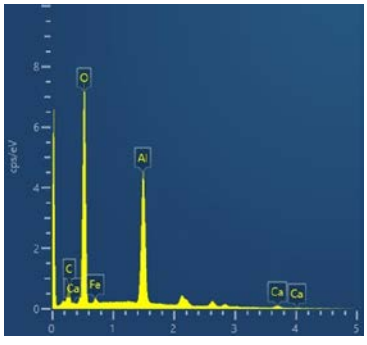

(d) Plot 4 (CH)

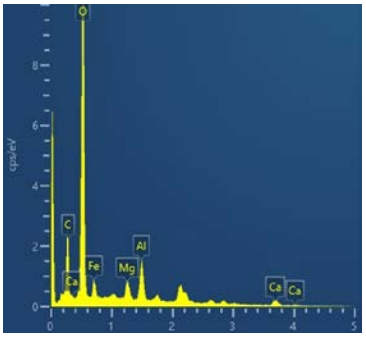

(f) Plot 5 (Mg-Al

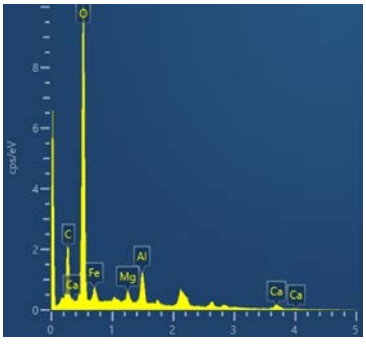

(g) Plot 6 (Mg-Al

hydrotalcite) hydrotalcite)

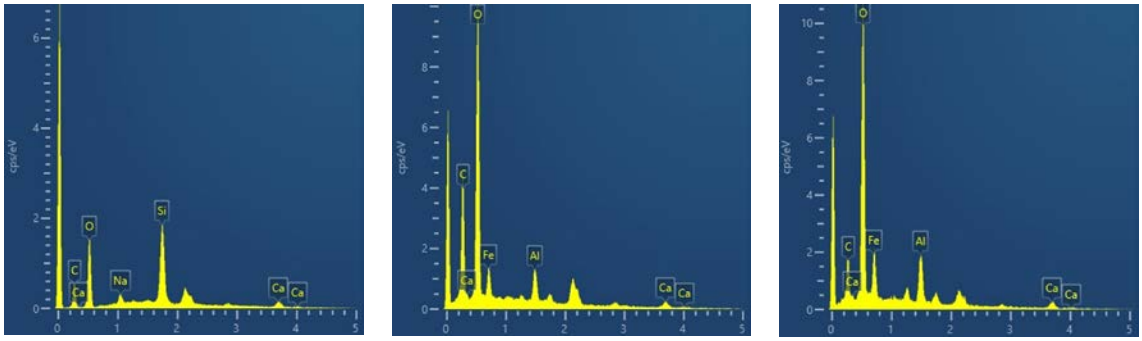

(f) Plot 7 (C-S-H) (g) Plot 8 (Carbo-AFm) (h) Plot 9 (Carbo-AFm)

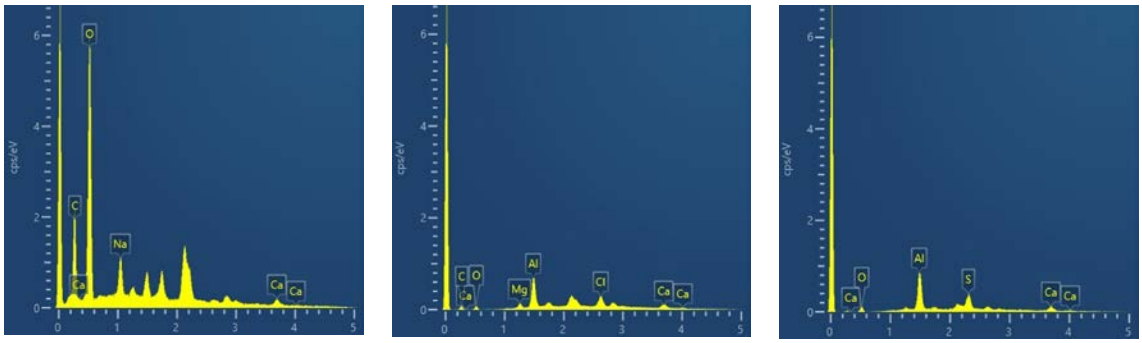

(i) Plot 10 (AFt) (j) Plot 11 (FS) (h) Plot 12 (Sulfo-AFm)

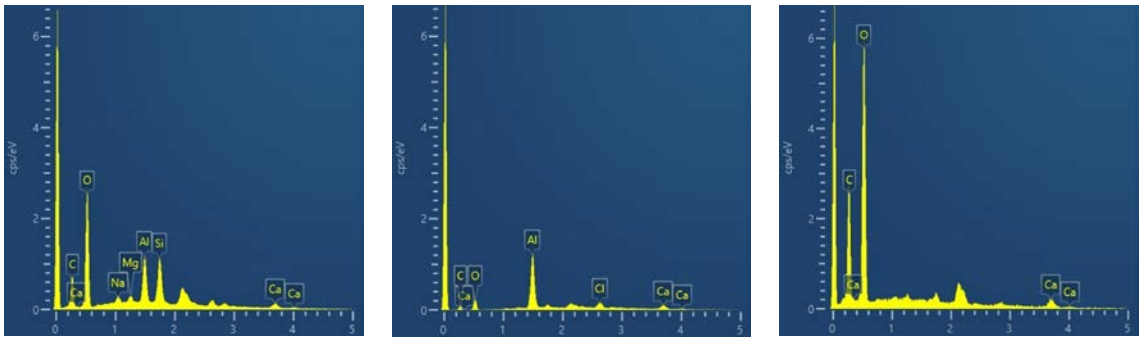

(i) Plot 13 (C-A-S-H) (j) Plot 14 (FS) (k) Plot 15 (CH)

Figure 6.15 EDS identification of OPC paste with SW at 28 days.

6.3.2 Statistical result of microstructure characterization

The volume of all identified phases and pores can be counted from the ternary composite images obtained by image treatment. Statistic results of the areas corresponding to various phases were presented in Figure 6.16 through BSE greyscale segmentation method and EDS mapping method. The standard deviation of the data set

extracted from the composite images was calculated and displayed as the error bar on the top of the columns. It can be observed that the concentration of values was high due to the short error bar, which increased the reliability of the average results. If needed, the volume content of phases can also be converted to the mass content based on the density of identified cement phases (Balonis & Glasser 2009) (Soin, Catalan & Kinrade 2013).

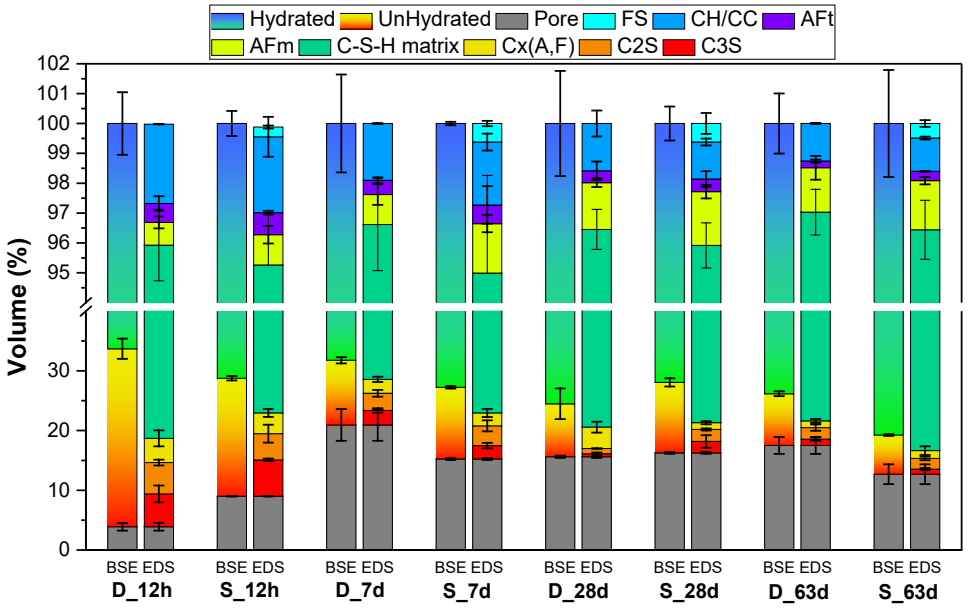

(a) Regional statistic results of composite digital images

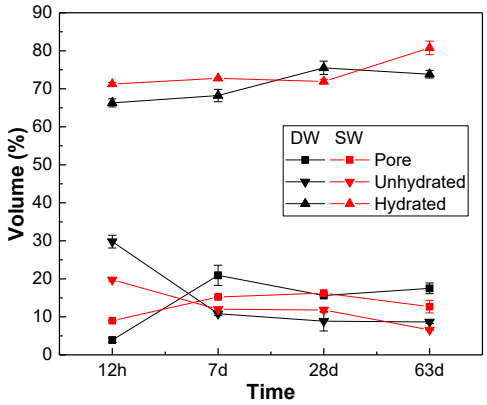

(b) Statistical results by BSE segmentation method

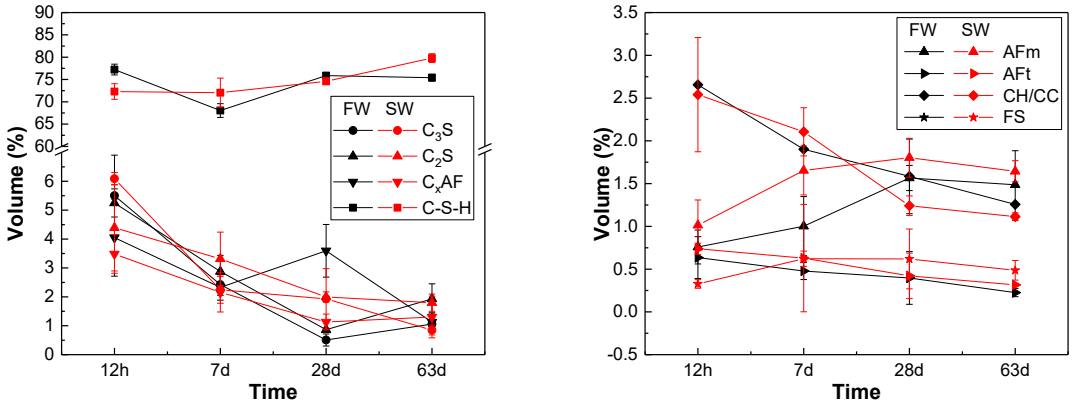

(c) Statistical results by EDS mapping method

Figure 6.16 Statistical result of various phases (in volume) through the two methods of microstructure characterization.

By comparison of the two methods, the total volume of anhydrous phases obtained by the EDS method was 30-50% lower than those from the BSE method. It was because the EDS method was more sensitive than the BSE method to identify whether the clinker was hydrated or not. This difference was significant at the early stage when more remained anhydrous phase to magnify the effect.

As for the sub-resolution phases, it can still be concluded that more AFt formed in samples with SW, although the AFt cannot be accurately quantified at this magnification. Freidel's salt can be observed from the early stage of hydration, but the content hardly increased in the following stages. Furthermore, it was found to coexist with other AFm phases (Sulfo-AFm and Carbo-AFm, as detected in Figure 6.15). However, other AFms were not detected in the typical phase identification method XRD (Cai et al. 2021; Cao et al. 2020; Li, Li, et al. 2020b; Li, Jiang, et al. 2021) or predicted by thermodynamic modelling (Balonis et al. 2010) from the hydrated cement with SW. It was because using the EDS method can only define the phase with the chloride ratio higher enough to the stoichiometry of FS. For those mixed with other phases, the

chloride content was diluted and thus had to be defined as other AFms. Increasing the magnification might be an effective way to separate these phases.

Compared to the long-term cured samples, an interesting result can be observed that the 12h cured sample has the lowest porosity, which seems illogical. Normally, the pores were from the space left from clinker dissolution after the adjacent cement matrix was formed and hardened. The porosity in 12h-cured DW samples was accordingly lower than the SW samples, considering SW can stimulate cement hydration, and the hydration degree of SW samples was higher than that of DW samples at the same curing age. As the hydration continues, the formed hydrates fill the pores gradually. Therefore, the porosity of cement paste seems to start from low to high and then to low throughout the whole hydration process. It can also explain the significant difference in porosity between the two samples after 12 hours and 7 days of curing.

At the late stage, the porosity of the cement matrix in the SW samples was comparable to, or lower than, that in the DW samples. It might be due to the higher content of AFt or AFms directly shown in the figure (sub-resolution AFt phases were not fully counted), filling the pores. At the late stage of 63 days, the space left from AFt conversion caused a slight increase of porosity in DW samples. However, the porosity of SW samples was decreased at the same time. It indicated more AFt could be retained at the late stage, being affected by ions from SW. By comparing the results of the two characterizing methods, EDS identifying method can perform a detailed phase separation. Increasing the scanning magnification would be conducive to quantifying small-size phases, while the time-cost factor should also be considered.

6.4 Discussion

6.4.1 Characterization methods of pore

MIP is routinely used for porosity characterization. Previous studies (Li, Gao, et al. 2020) found that the MIP samples required a certain hardness and quantity to obtain accurate results. The image analysing method, which directly extracts data with various strategies (Fang & Zhang 2020; Scrivener 2004; Wong, Head & Buenfeld 2006) on BSE greyscale segmentation, has been proposed as a feasible alternative. However, the study found that the segmented area was sensitive to the threshold value. A sudden change can be observed when the solid phase inside the pore was selected. Combining SE and BSE images can accurately profile the pore area, which benefited from the two imaging mechanisms. The samples do not require hardness but polishing and conductivity, which can ensure high quality and avoid beam drift.

6.4.2 Characterization methods of phases

The TG was a quantitative method with high accuracy for cement phases. However, since the inevitable overlapping of dehydration temperature, the reliable quantification phases were limited (typically CH and CC (Li, Li, et al. 2020b)). Rietveld quantitative XRD was widely accepted to characterize low-level phases by calibration and determine peak broadening (Taylor 1997). The accuracy of quantification depends highly on the well-defined content of phases from standard reference. However, the amorphous phases cannot be directly determined due to the lack of reference. Other quantitative methods are required to help verify the accuracy of Rietveld refinement, or else the quantitative reliability will be significantly reduced (Soin, Catalan & Kinrade 2013).

Image analysis from BSE-EDS hypermaps has been proposed as a suitable method with a reasonable degree of precision to characterize cement phases (Durdziński et al. 2015)

(Kocaba, Gallucci & Scrivener 2012). The information from these hypermaps is abundant but, unfortunately, it was hard to tap the value efficiently without a programming background. The framework developed by Geogret *et al*. (Georget, Wilson & Scrivener 2021) provided an easy-to-use interpreter with a graphical interface, significantly optimizing the quantitative analysis of microstructure. Although this method requires a high demand for sample quality and instrument parameters (they directly affect the accuracy of the data and the workload afterwards), it is a promising quantitative characterization alternative to link the microscopic and submicroscopic domains.

6.5 Conclusions

This chapter studied the microstructure of OPC paste formed from hydration with SW. The quantitative characterization method of the pore and cement phases was investigated and discussed in detail, as well as the identification and morphology of the phases.

The hydrate phases detected in Chapter 5 were identified by EDS point analysis. A notable result was that the various AFm phases coexisted in SW samples, including FS, monosulfoaluminate and monocarboaluminate. These hydrocalumite-like phases were similar and unable to be distinguished by morphology. Therefore, determining atomic ratio by the EDS method contributed to identifying these phases accurately. In addition, the effect of SW, such as stimulating cement hydration, hindering AFt decomposition and reducing porosity, can also be observed by SEM-EDS techniques, which shows its great applicability for microscopic characterization.

The study found that BSE images were more suitable for segmenting areas for smaller pores, while SE images were more suitable for larger pores, inside which no hydrate

phases can be observed. By combining SE and BSE images, the area for pores in the microstructure can be accurately segmented with lower data errors. Information from EDS hypermaps was of great value for phase identification. After the data processing of denoising, region segmentation, manual identification, and imaging calibration, the region of various phases can be separated effectively. Although a higher magnification was required to ensure the accurate result of finer phases such as AFt, the EDS hypermaps can identify most of the cement phases and provide detailed distribution of the phases on microstructure images with low data error. Therefore, with the advancing EDS detectors and optimizing algorithm, this method was promising to achieve efficient and highly adaptable quantification of cement phases.

CHAPTER 7. CONCLUSIONS AND RECOMMENDATIONS

7.1 RETROSPECTION

The primary purpose of this PhD thesis is to, in view of the various ions effect, conduct a fundamental study on the hydration characteristics of Portland cement in SW. As characterizing cement hydration requires combined experimental, modelling and numerical research at different hydration stages, the following works have been performed in the study.

In Chapter 3, the compositions of hardened cement pastes made with DW and SW at different hydration times are studied. Identification of the clinker phases, hydrate phases and pore solution is performed using TG, XRD and ICP-OES analysing methods. Rietveld refinement approach is adopted to characterize the composition of the solid phases as a function of time. The characterization result reveals the evolution of cement phases with DW and SW, to be the experimental support for subsequent research.

Based on the experimental results, the MPK model combined with thermodynamic modelling was developed to simulate the cement hydration process in Chapter 4. Parameters of the MPK model are adjusted from experimental data to adapt to predicting the dissolution rate of clinker phases in SW. The optimized model is validated by comparing the results obtained by experimental quantification and thermodynamic computing. The good agreement indicates that the modelling was of a high reference value for hydration simulation in SW.

Chapter 5 studies the effect of natural SW on the heat evolution, phase evolution, pore-size distribution and mechanical performance of OPC. An accurate quantification

method from the TG/DSC test was developed to help correct QXRD and characterise the evolution of various phases. Based on the determined phase evolution, the testing results of the exothermic rate, pore-size distribution and mechanical strength are fundamentally explained. The suitability of natural sea sand for cement mortar preparation is evaluated by compressive and flexural strength development.

Chapter 6 studies the microstructure of OPC formed from hydration with SW. In addition to the morphology of hydrate phases, the micro-scale ROI are studied by image and numerical analysis. Approaches are developed to quantitatively study the pores and phases through information extracted from SE and BSE images. The quantitative characterization of phases is conducted by image and data treatment from EDS hypermaps. The microstructure characterization results from developed approaches are compared through statistical analysis to evaluate their reliability and applicability.

7.2 GENERAL CONCLUSIONS

The conclusions regarding the related work have been given in each chapter of the thesis. In this section, some general conclusions are drawn in combination with the achievements from former research and the results of the current study.

Using SW as mixing water may not have a noticeable effect on the ultimate strength of cement composite. However, poor workability should be considered in actual concrete manufacturing due to the short setting time, high drying shrinkage and enhanced exotherm from rapid hydration at the early stage.

Both experimental and simulation results show that the ions from SW mainly affect the hydration and precipitation of Al-bearing cementitious phases. Therefore, the effect of SW on cement hydration will be magnified by using cementitious materials with a higher content of aluminate.

Although the chloride can be chemically bound by FS or physically adsorbed by C-S-H phases, the higher chloride content in pore solution shows that the binding effect by cement is limited—Even not counting that chloride is probably released from reversible binding. Therefore, it is not an ideal solution to use mineral admixture to protect steel reinforcement from corrosion; the binding effect is poor, and the mechanical strength is sacrificed.

More AFt phases are measured at the advanced stage of hydration in SW. These AFts can remain stable due to the high chloride and sulfate ions concentration in the pore solution. However, once it is exposed to fresh water, such as the long-term washed by rain, AFt may decompose from diluted pore solution and leave space, which may be unfavourable to the structural stability.

7.3 MAIN SCIENTIFIC CONTRIBUTIONS AND FINDINGS

The main scientific contribution and findings of this study are listed in the followings:

(1) Identify the phase compositions of cement clinker, cement hydrates, and pore solutions of pastes made with DW and SW. Quantitatively characterize the phase evolution of PC over the hydration time.

(2) Simulate the cement hydration process in SW by combining the thermodynamic model and the optimized MPK model. A good agreement can be observed in simulation and experiment results, showing the high reliability of the modified MPK model for PC hydration in SW

(3) Investigate the hydration characteristics and mechanical strength development of SW mortar with sea sand. Establish a connection between macroscopic property

differences and hydration characteristics. Propose the mechanism explanations to support performance evaluation.

(4) Investigate microstructural hydration features of Portland cement with SW. Special attention was paid to characterize the pore, hydrated and anhydrous phases quantitatively, which combines the latest microscopy and image and data processing techniques. The quantitative characterization methods of pore and cement phases were developed and discussed in detail, as well as the identification and morphology study of the phases.

7.4 RECOMMENDATIONS FOR FURTHER RESEARCH

The goal of SW-mixed concrete is to alleviate the shortage of freshwater resources by developing water resources while ensuring safety. Considerable efforts have been invested in improving the performance of SWC for a wider-scope application. Based on the experience and findings from the experimental process and simulation calculation, the following proposals may help to promote the application of SWC:

The current study proposed a modelling approach in chapter 4 to simulate the hydration system with SW. It helps to reveal the SW influence on microstructure and mechanical performance and contributes to designing the cement composite for better incorporation with SW to meet the actual engineering requirements.

The effect of SCMs, such as fly ash, slag, metakaolin, limestone and nanoparticles (e.g. nano titanium dioxide, nano alumina, nano calcium carbonate, nano silica and nano clays) on the performance improvement of SWC is worth investigating. In other words, combining cement composite to investigate the optimum dosage of SCMs for improving poor workability, high autogenous shrinkage, severe exotherm, etc., from the adverse effect of SW.

The current study on cement composite is based on the constant curing condition and laboratory specimens. However, in practical application conditions, the change of temperature and humidity by alternating day and night incorporated with complex environmental factors and size effect should be considered and require more studies on the shrinkage and durability.

Appendices

Appendix A. Phase segmentation for the related samples

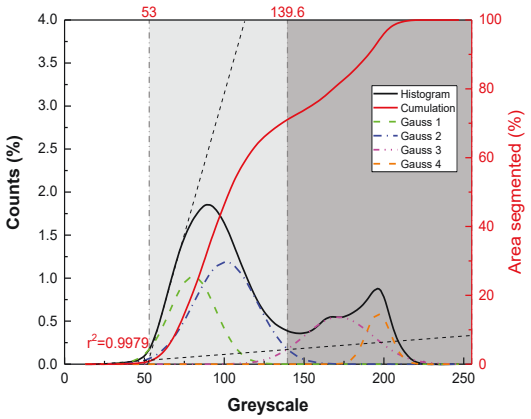

(a) D12h_1

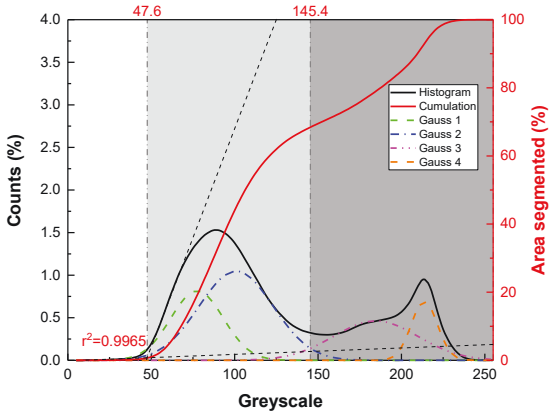

(b) D12h_2

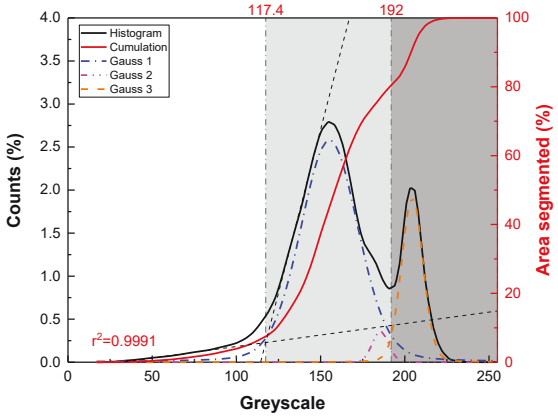

(c) S12h_1

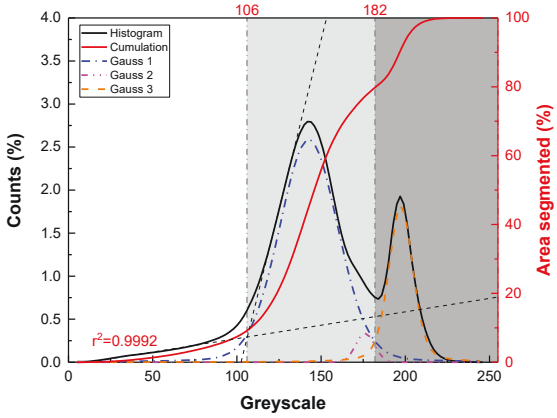

(d) S12h_2

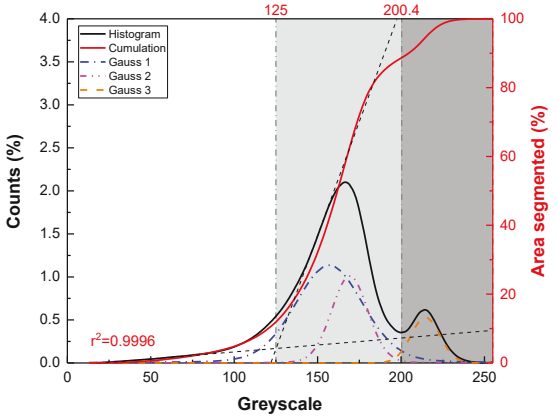

(e) D7d_2

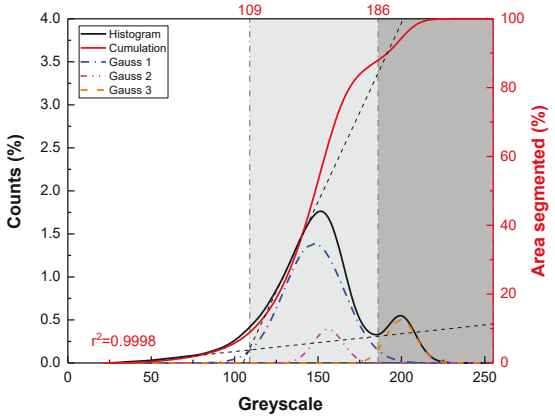

(f) D7d_2

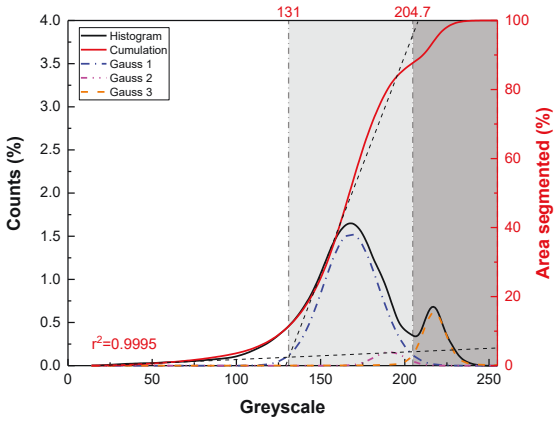

(g) S7d_1

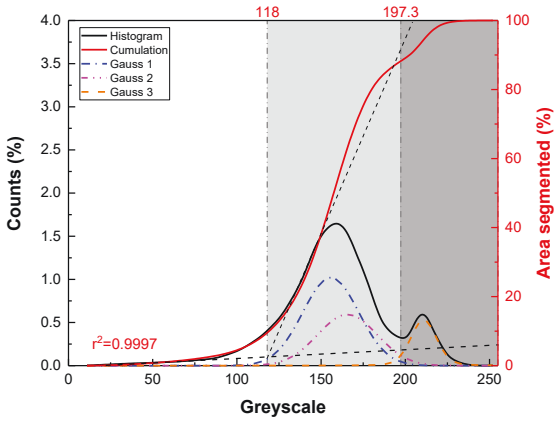

(h) S7d_2

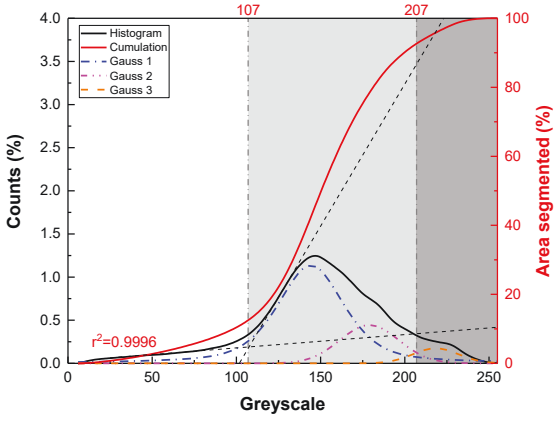

(m) D28d_1

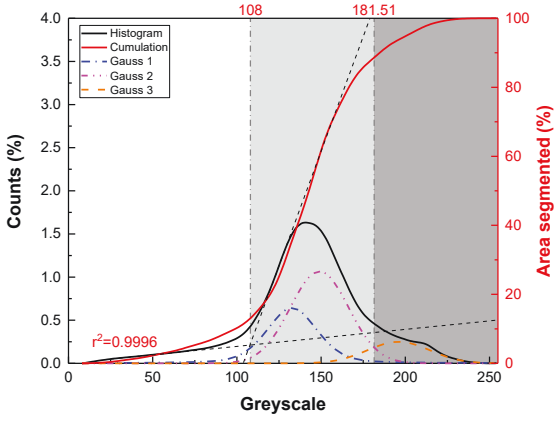

(n) D28

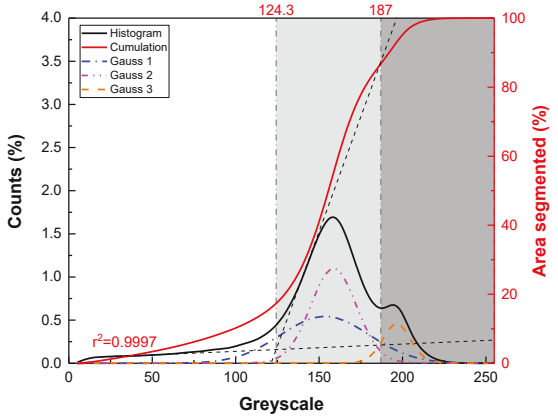

(o) S28

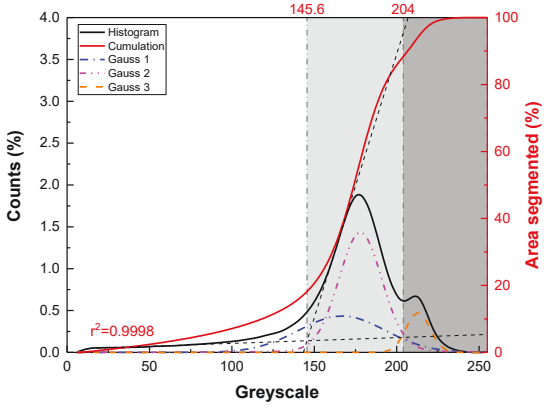

(p) S28

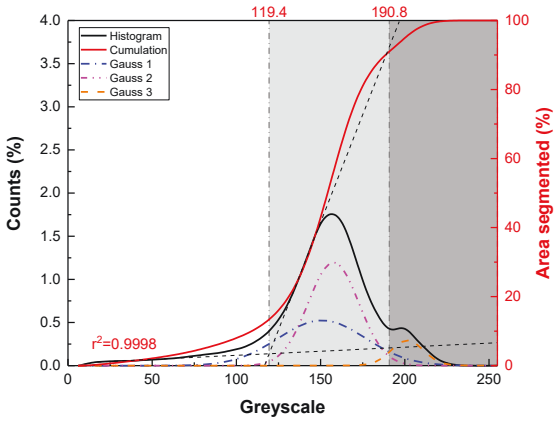

(q) D63

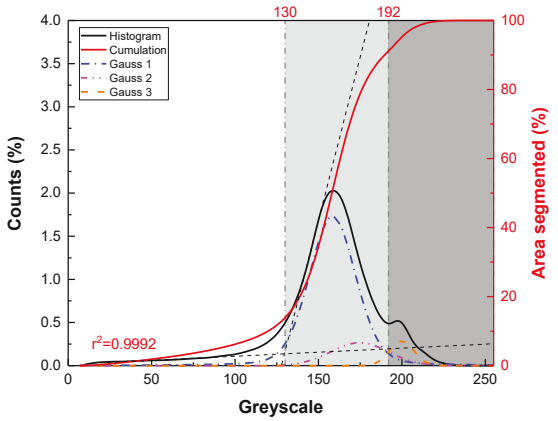

(r) D63

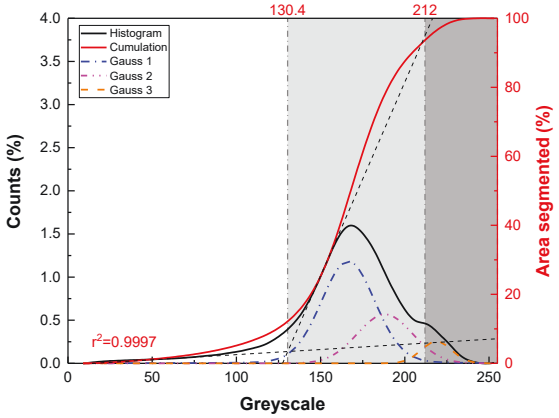

(u) S63

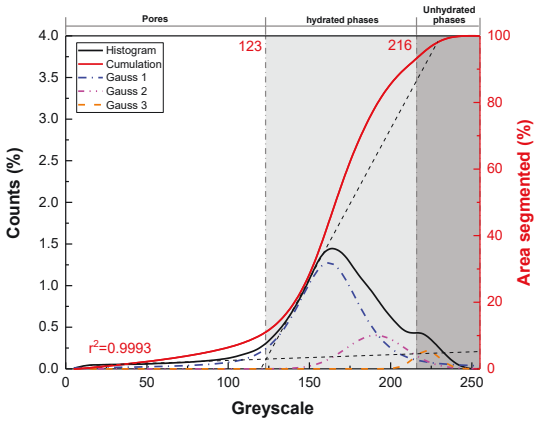

(v) S63

Figure A.1 Determination of threshold values for testing samples at different curing ages.

Appendix B. Morphology analysis of phase

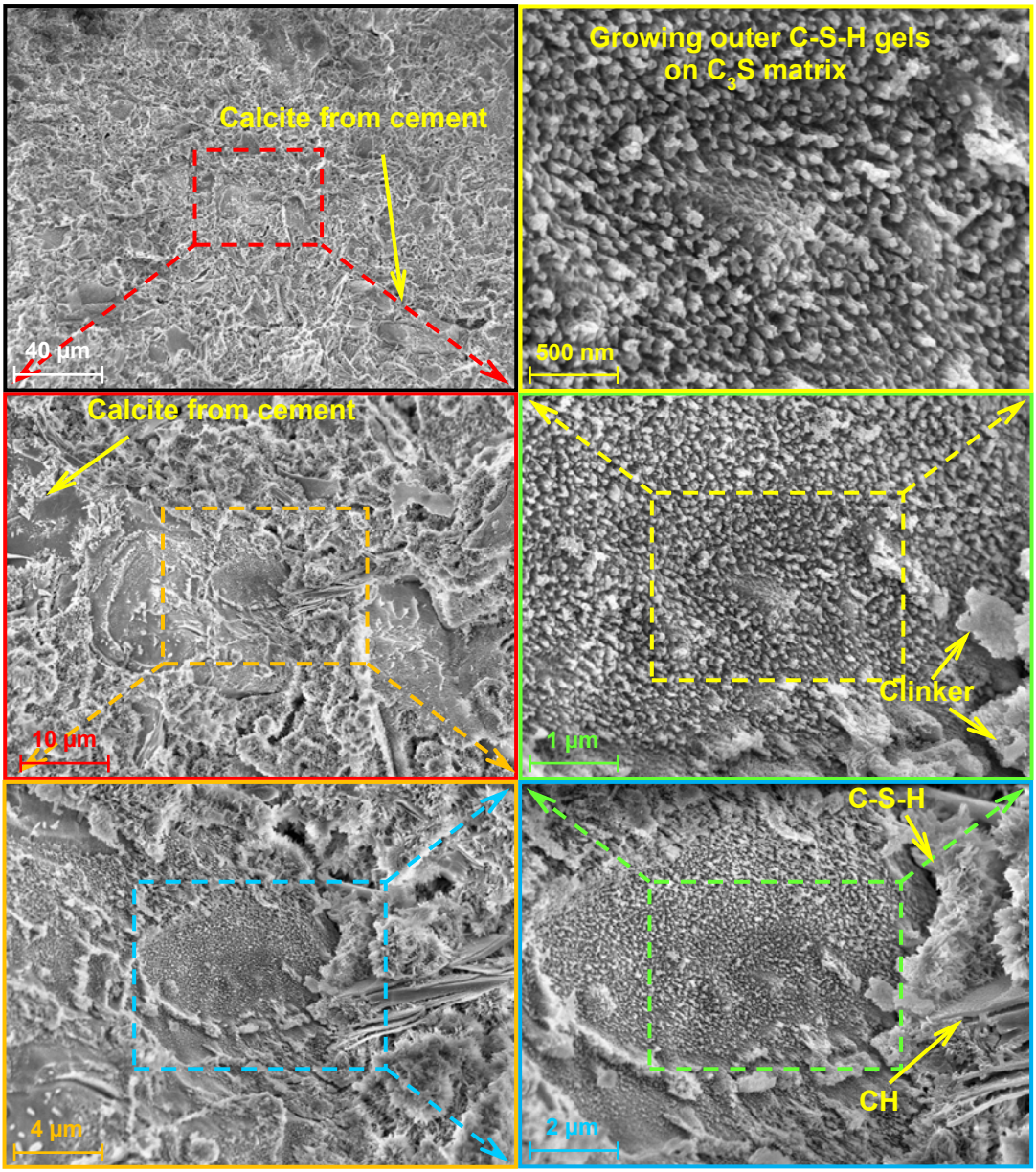

(a) 12-hour hydrated Cement paste with DW.

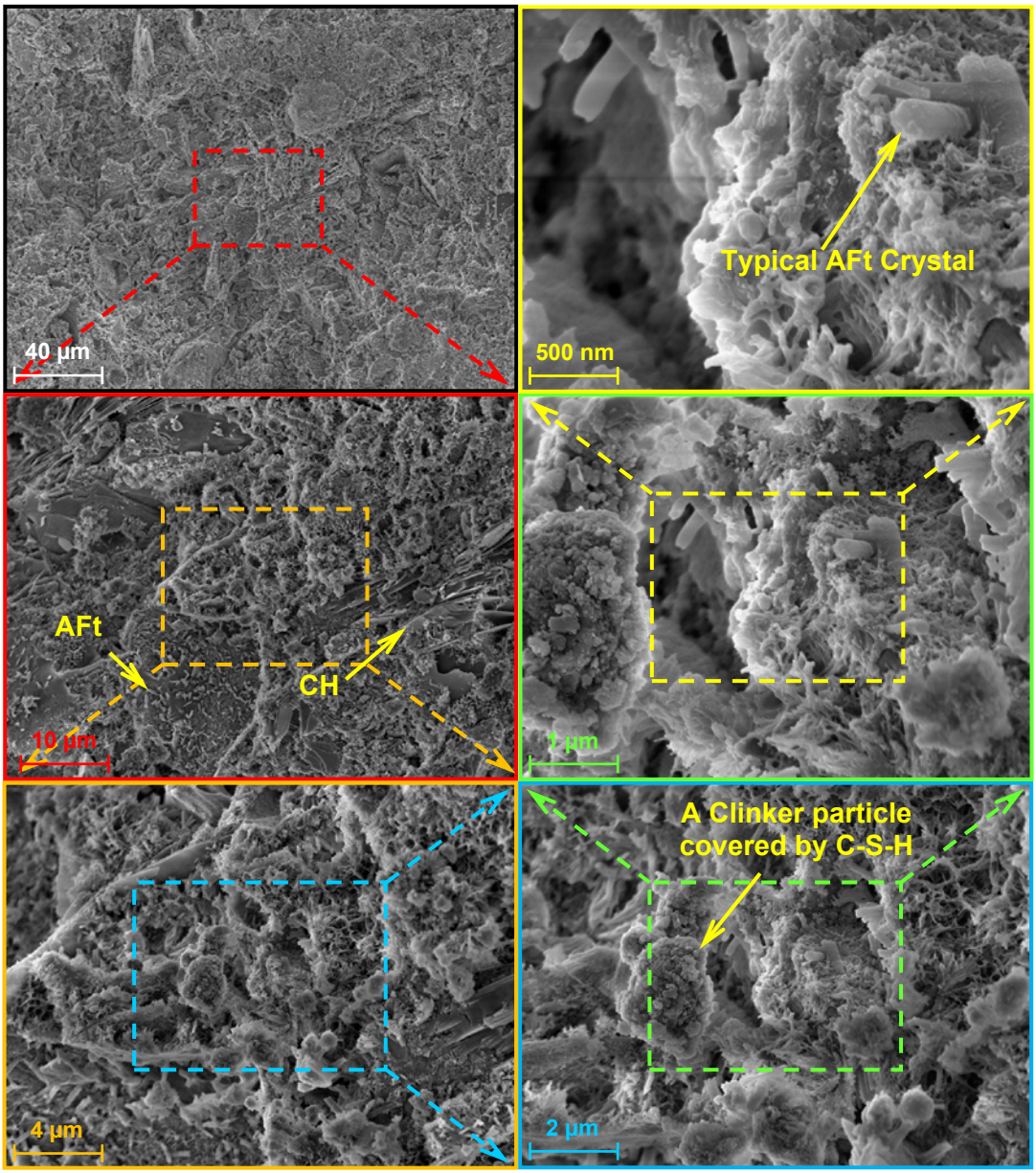

(b) 12-hour hydrated Cement paste with SW

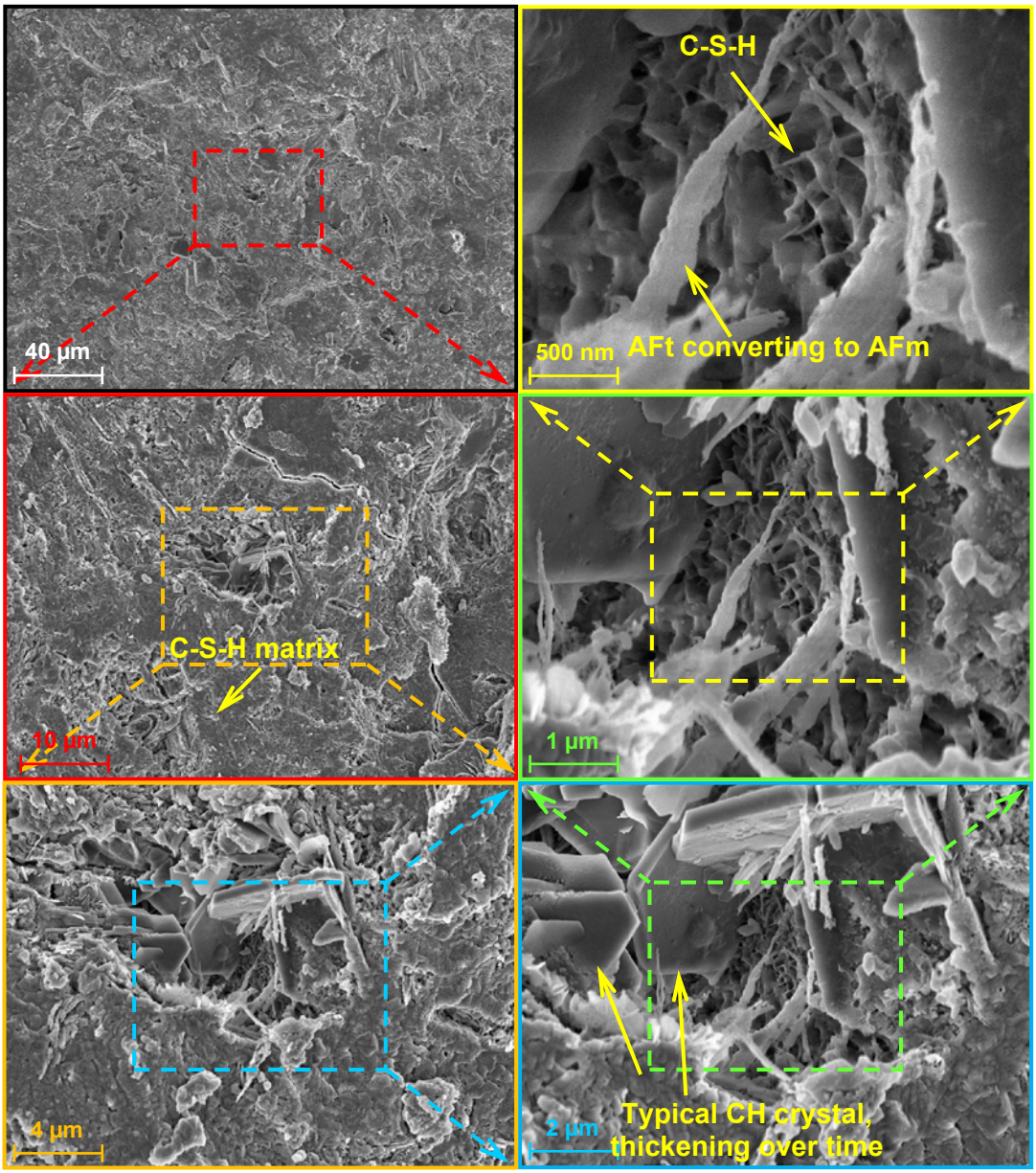

(c) 28-day hydrated Cement paste with DW

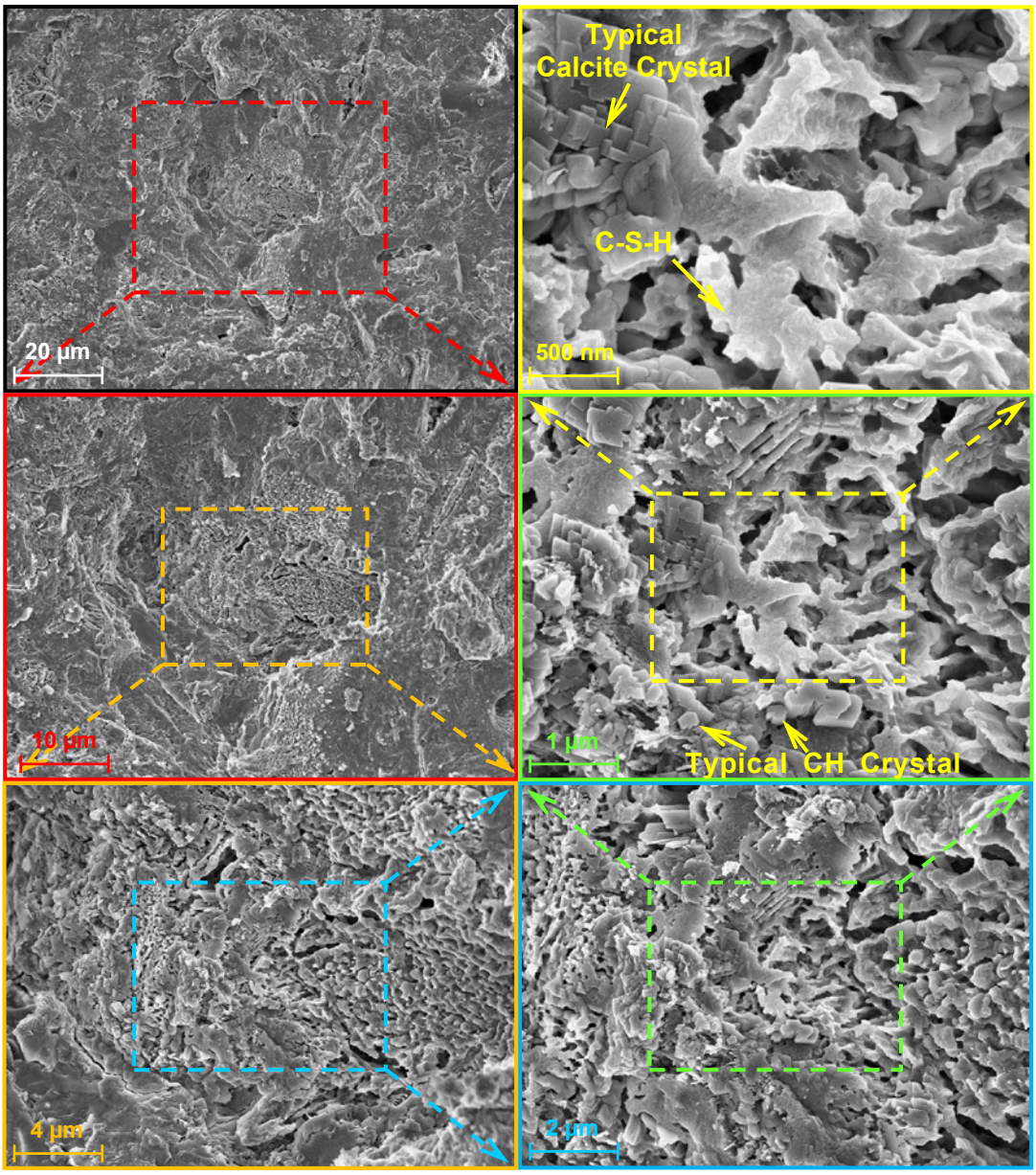

(d) 28-day hydrated Cement paste with SW

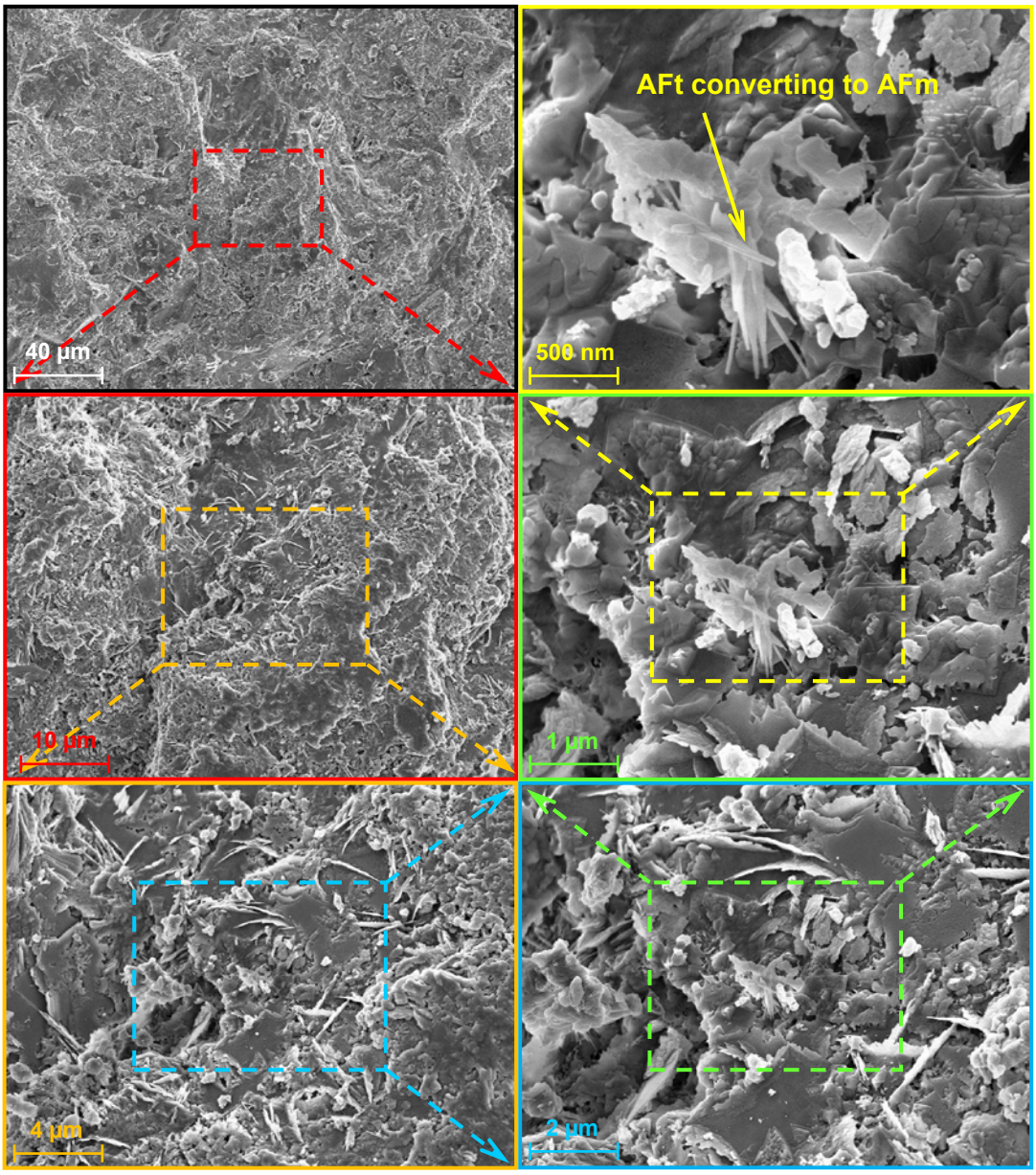

(e) 63-day hydrated Cement paste with DW

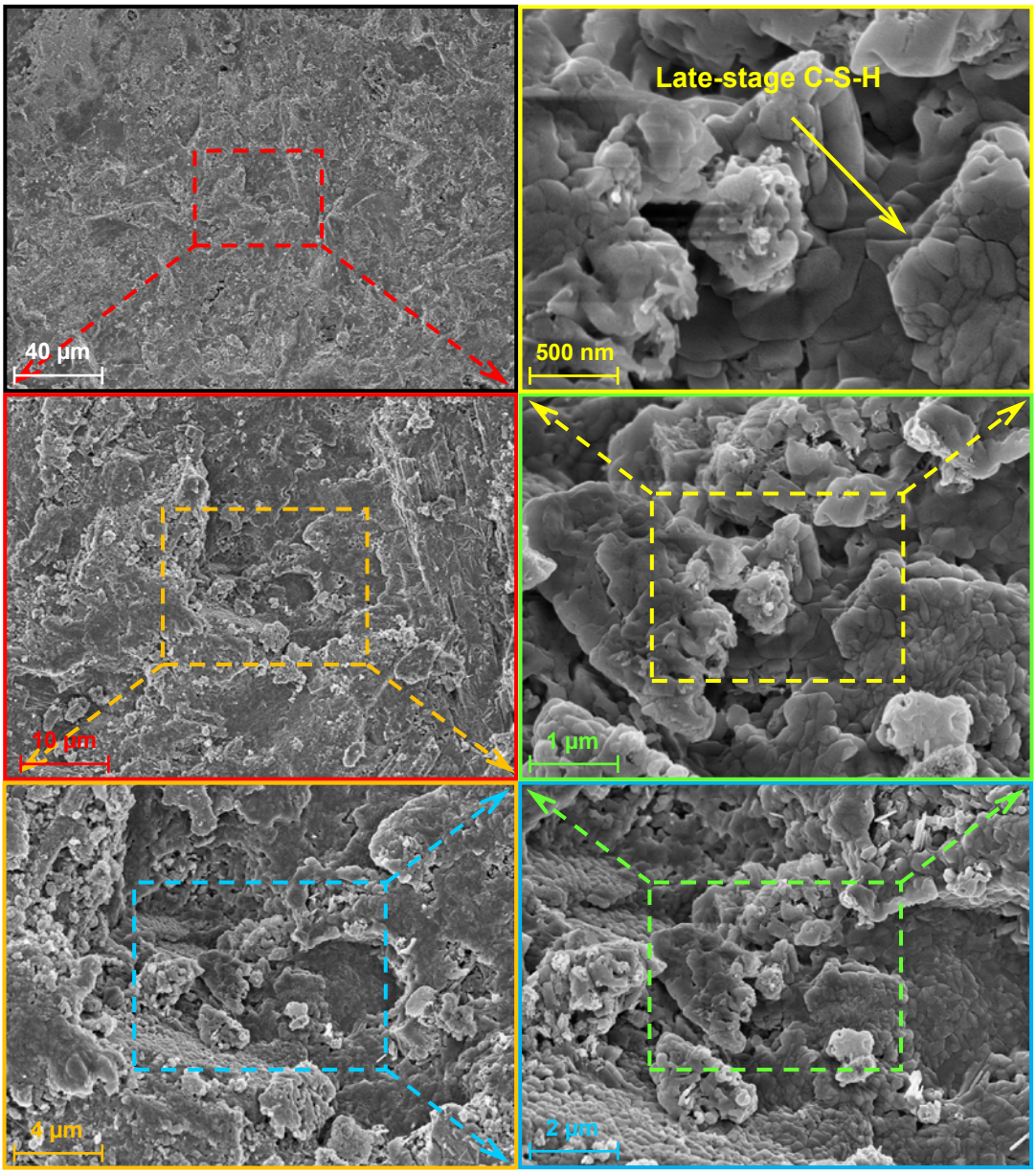

(f) 63-day hydrated Cement paste with SW

Figure B.1 FESEM images of OPC paste at various curing ages.

Appendix C. Phase quantification results

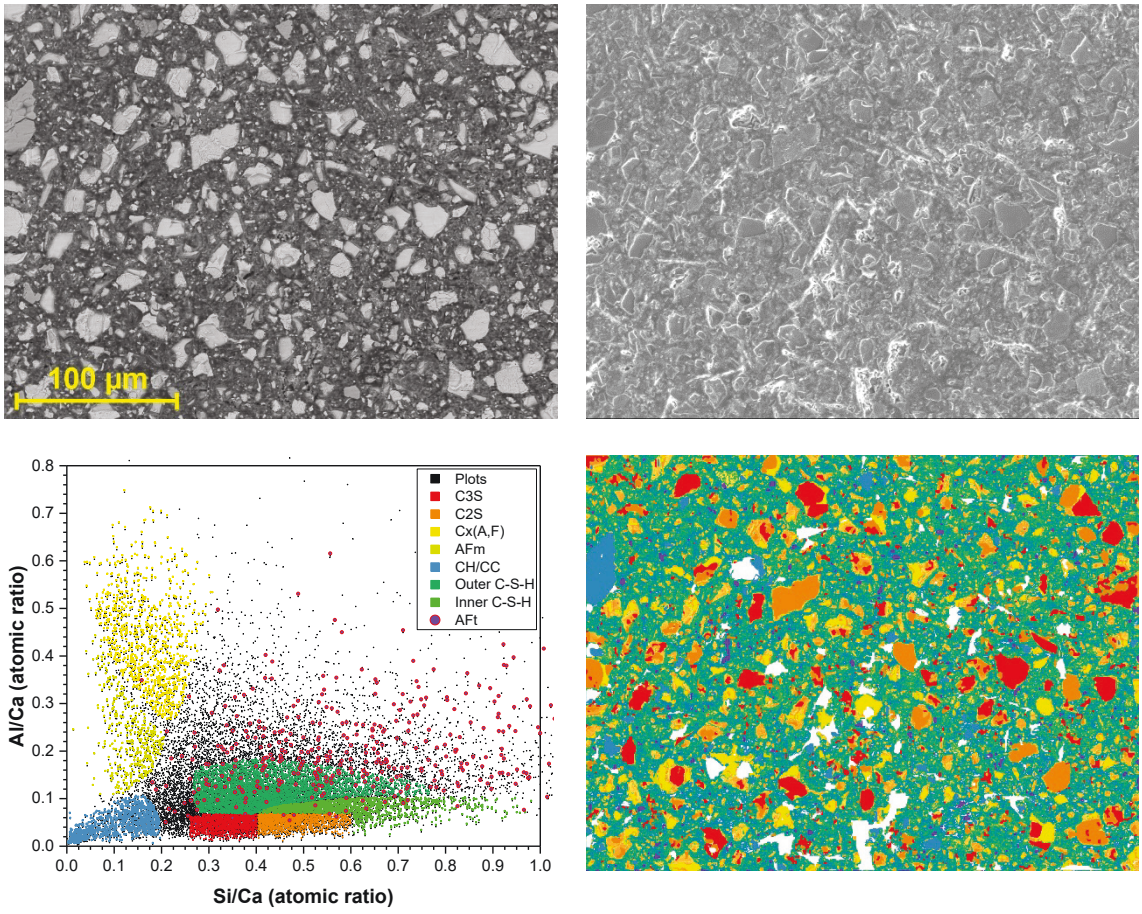

Figure C.1 Image and data treatment results for D12h_1

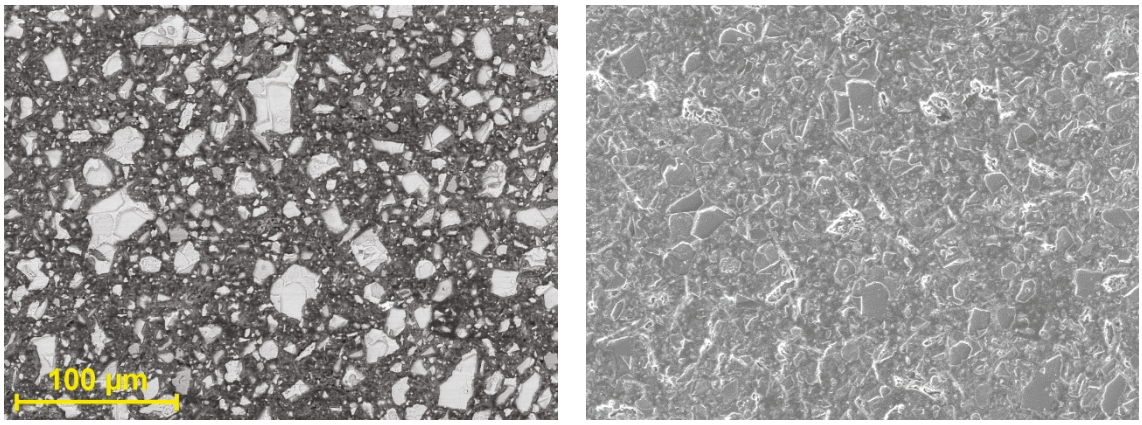

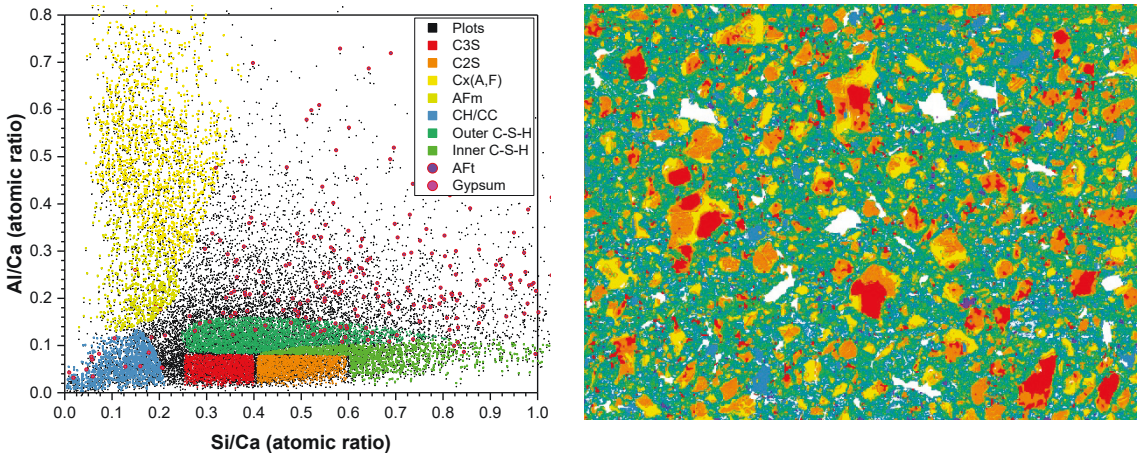

Figure C.2 Image and data treatment results for D12h_2

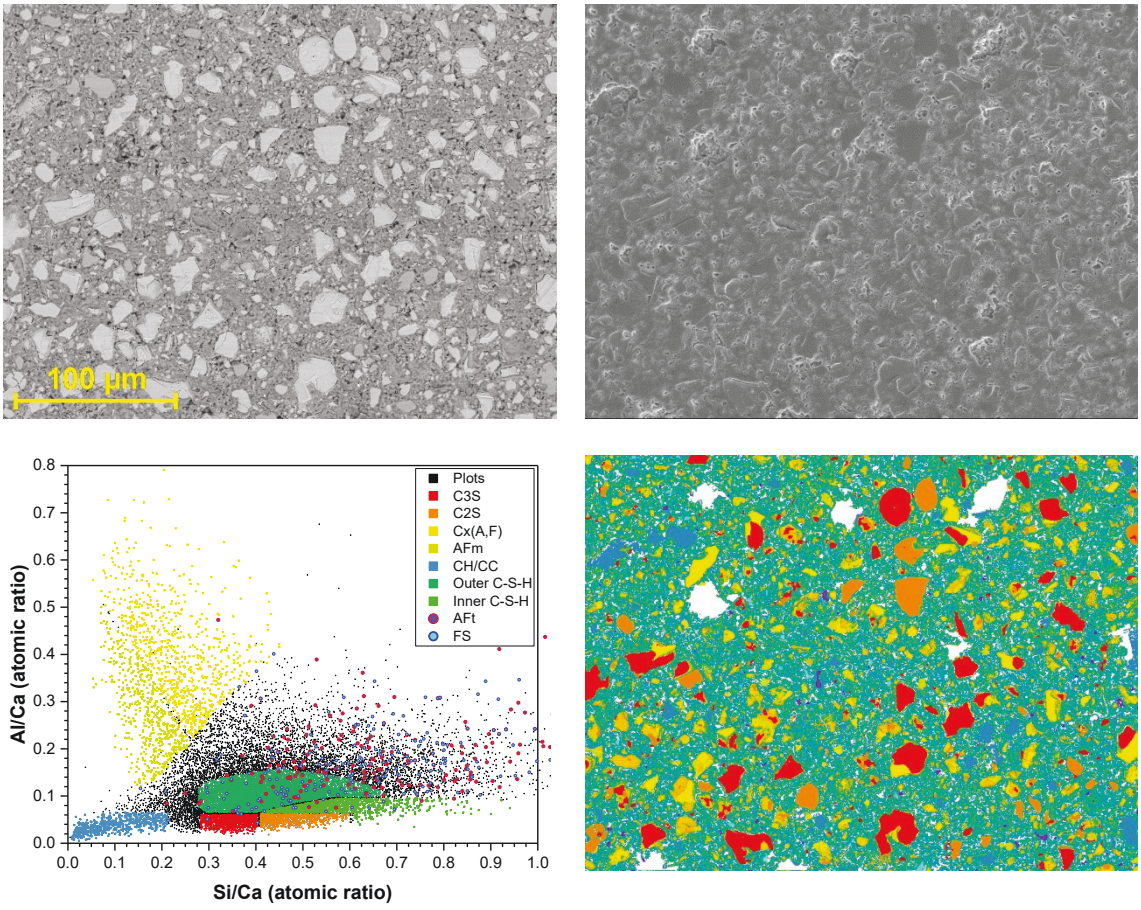

Figure C.3 Image and data treatment results for S12H_1

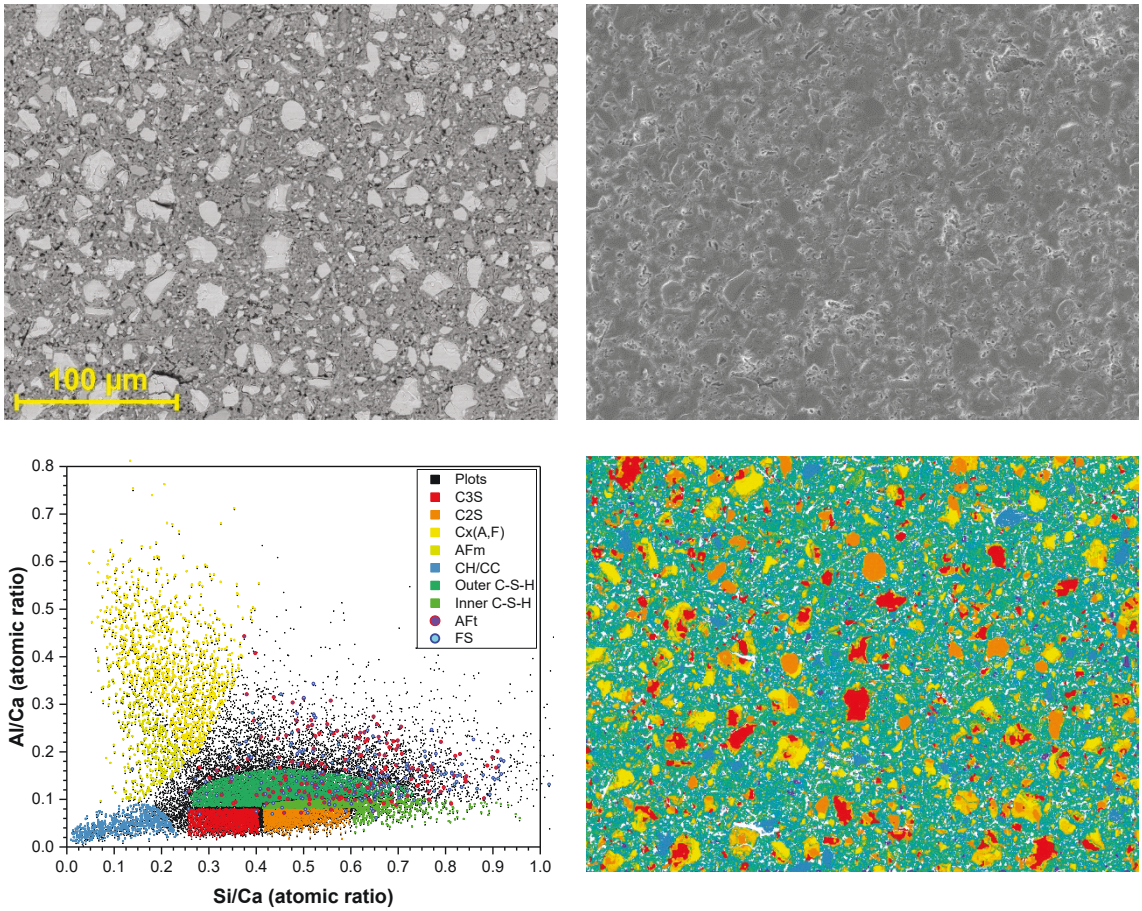

Figure C.4 Image and data treatment results for S12H_2

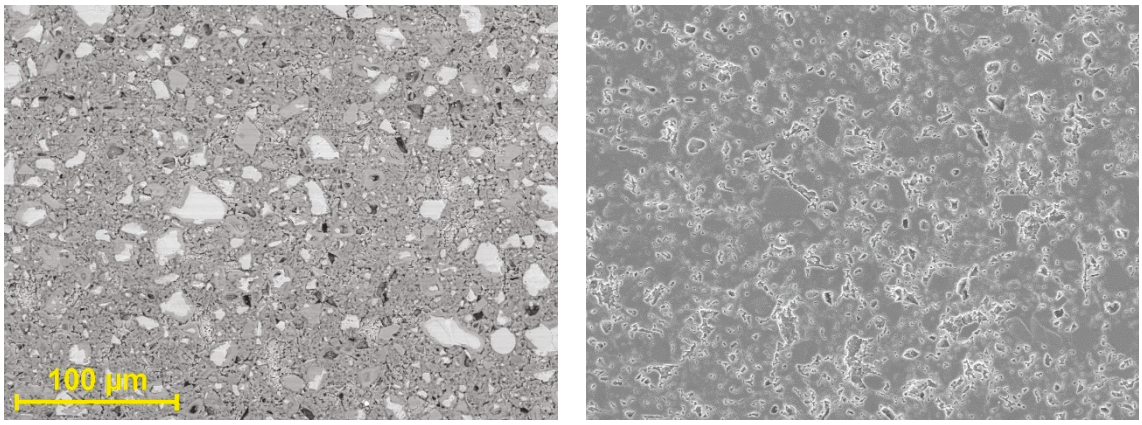

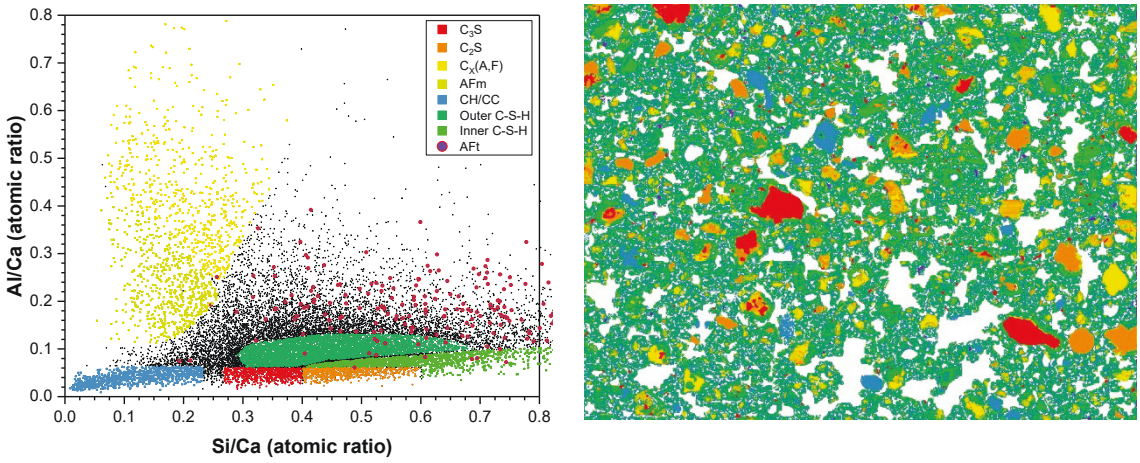

Figure C.5 Image and data treatment results for D7d_1

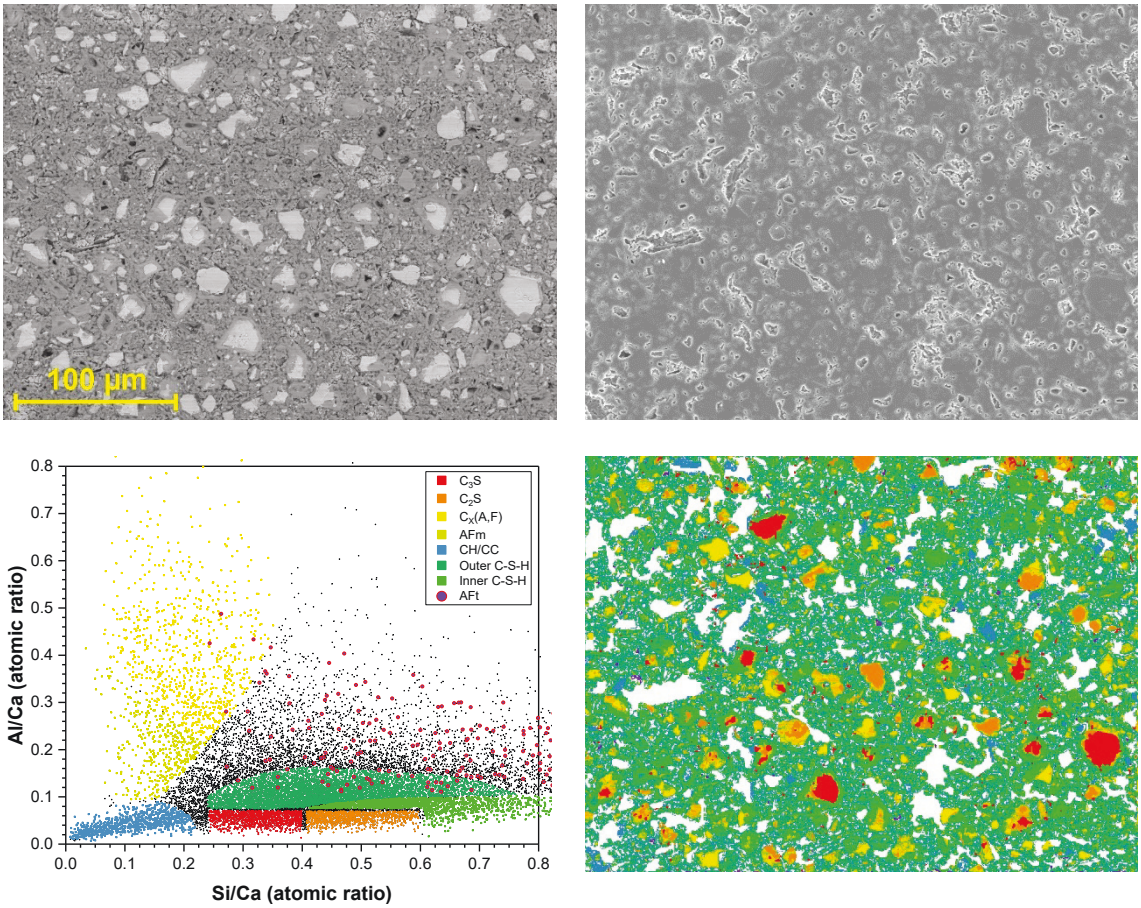

Figure C.6 Image and data treatment results for D7d_2

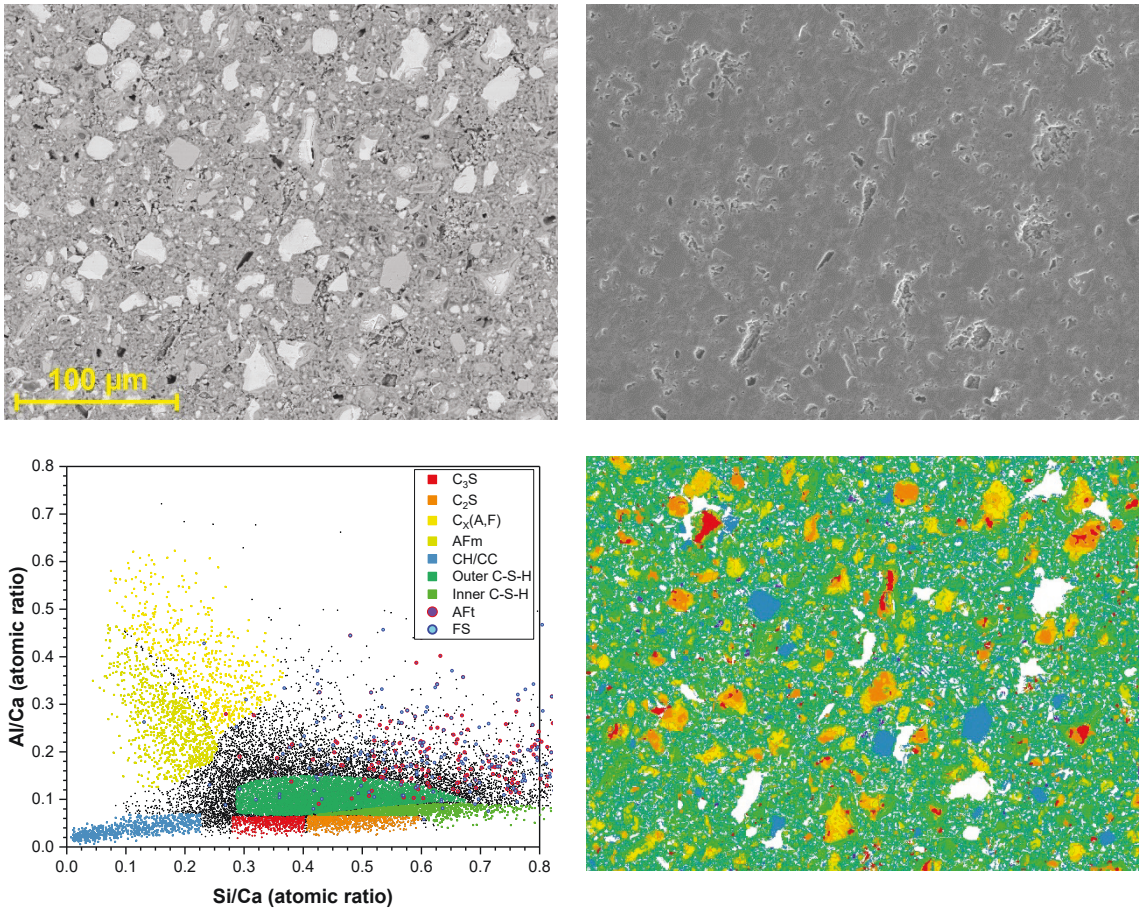

Figure C.7 Image and data treatment results for S7d_1

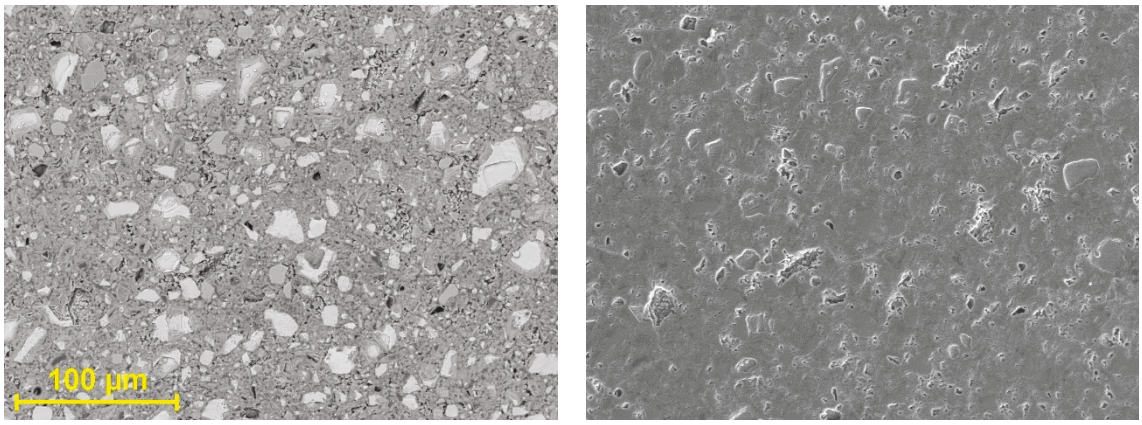

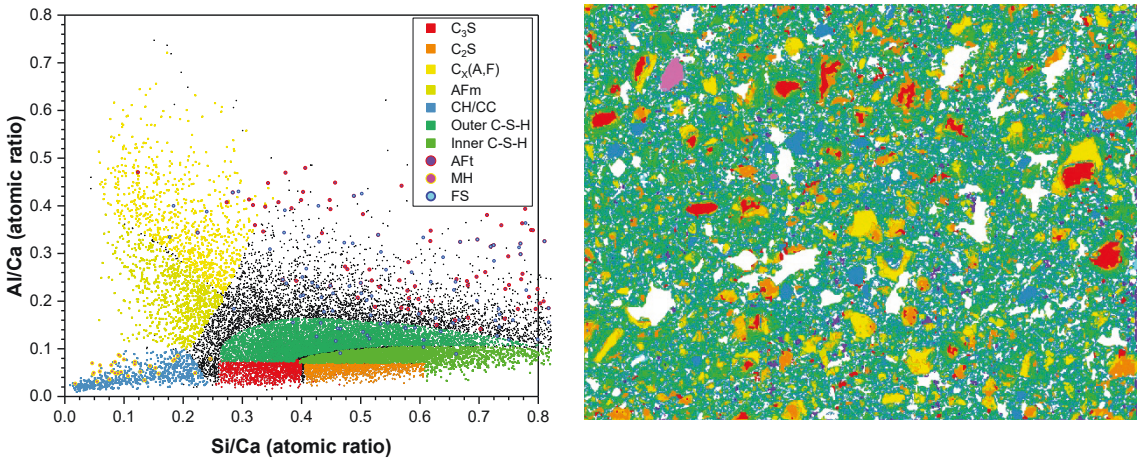

Figure C.8 Image and data treatment results for S7d_2

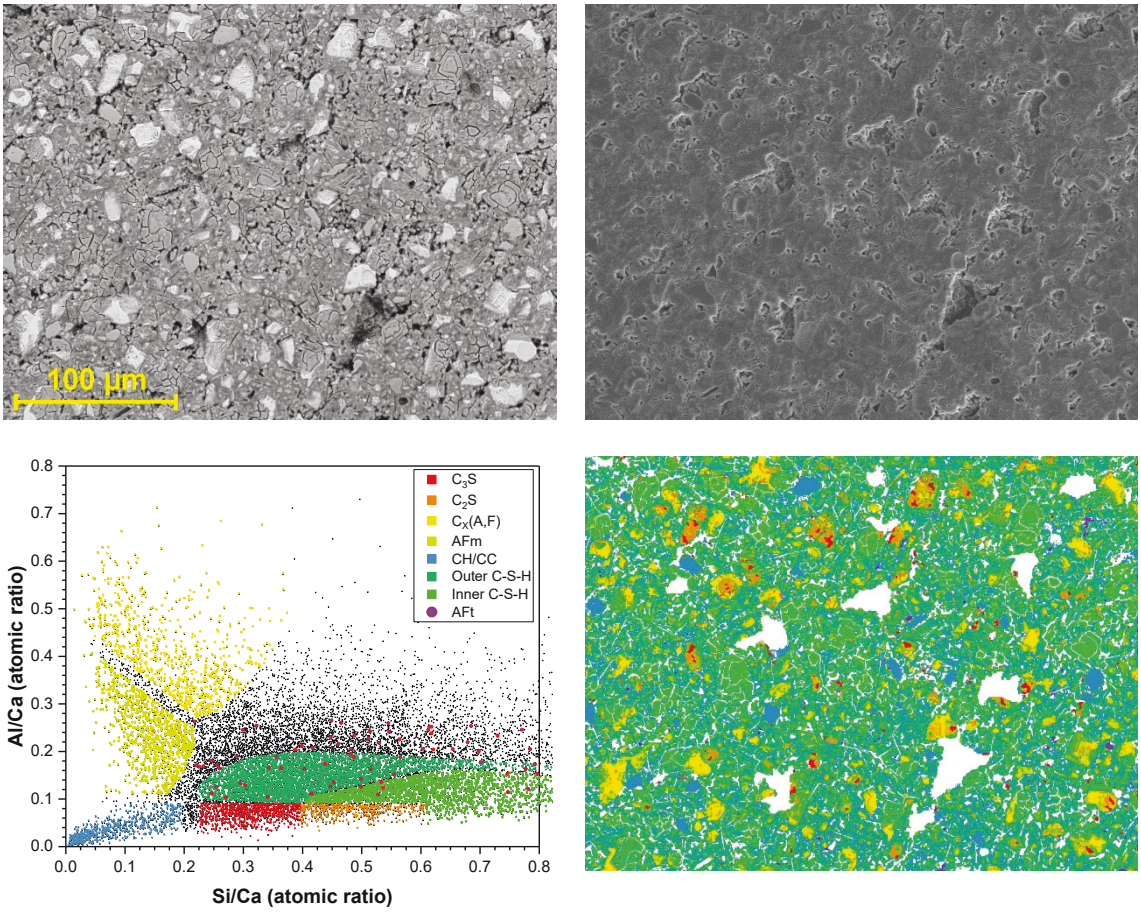

Figure C.9 Image and data treatment results for D28_1

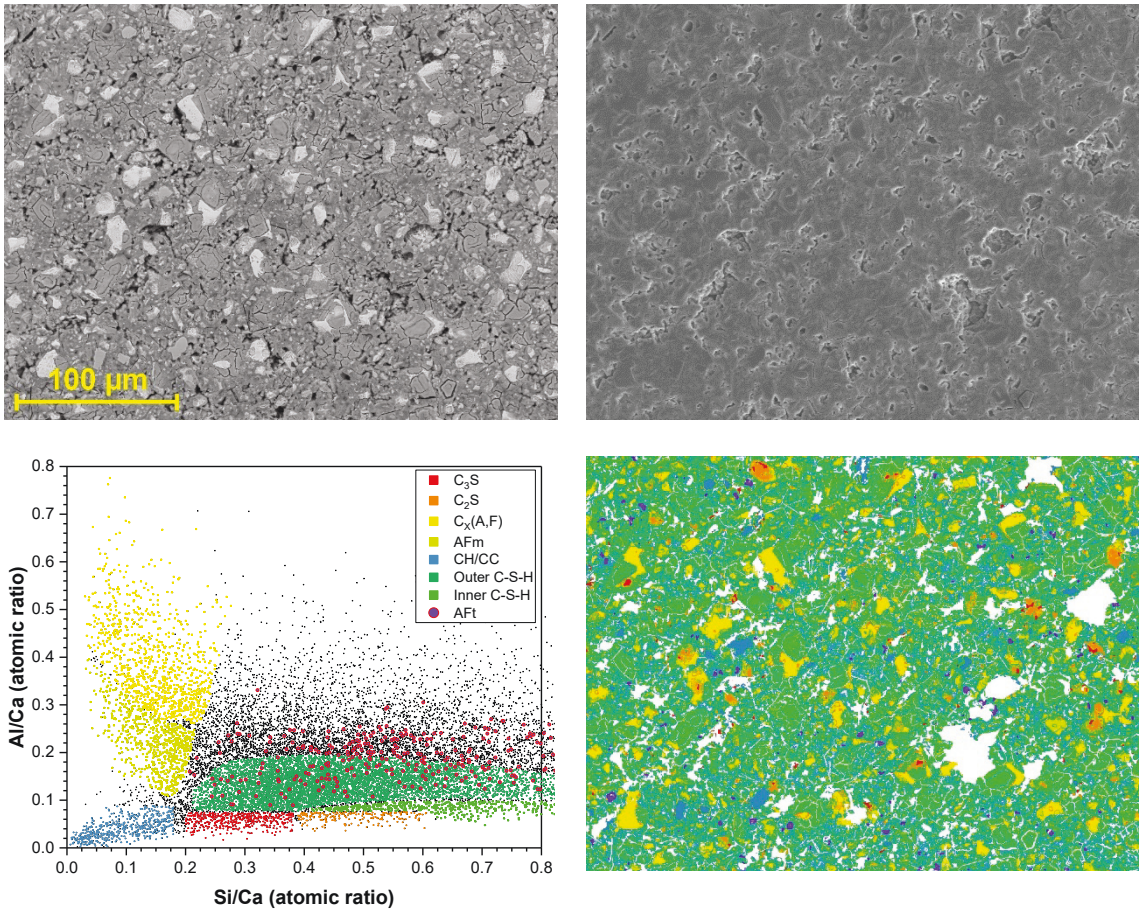

Figure C.10 Image and data treatment results for D28_2

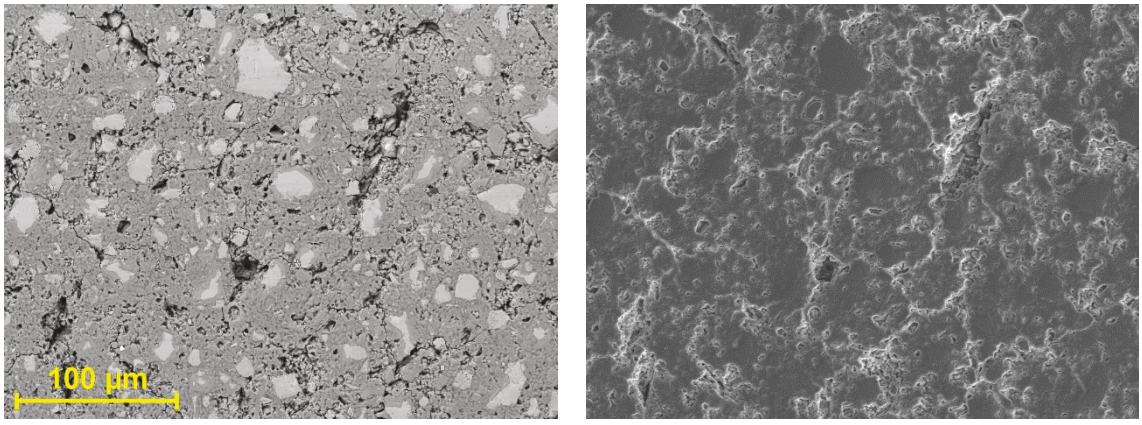

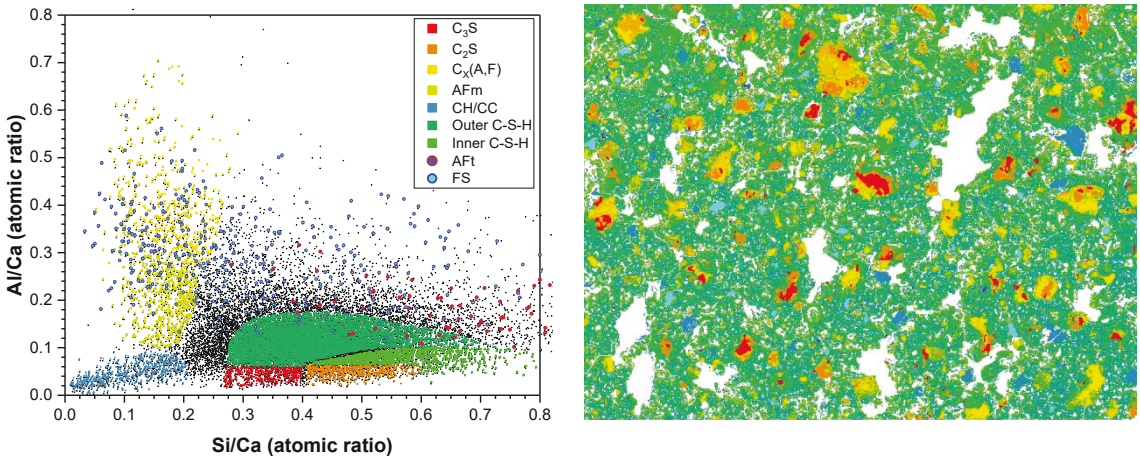

Figure C.11 Image and data treatment results for S28d_1

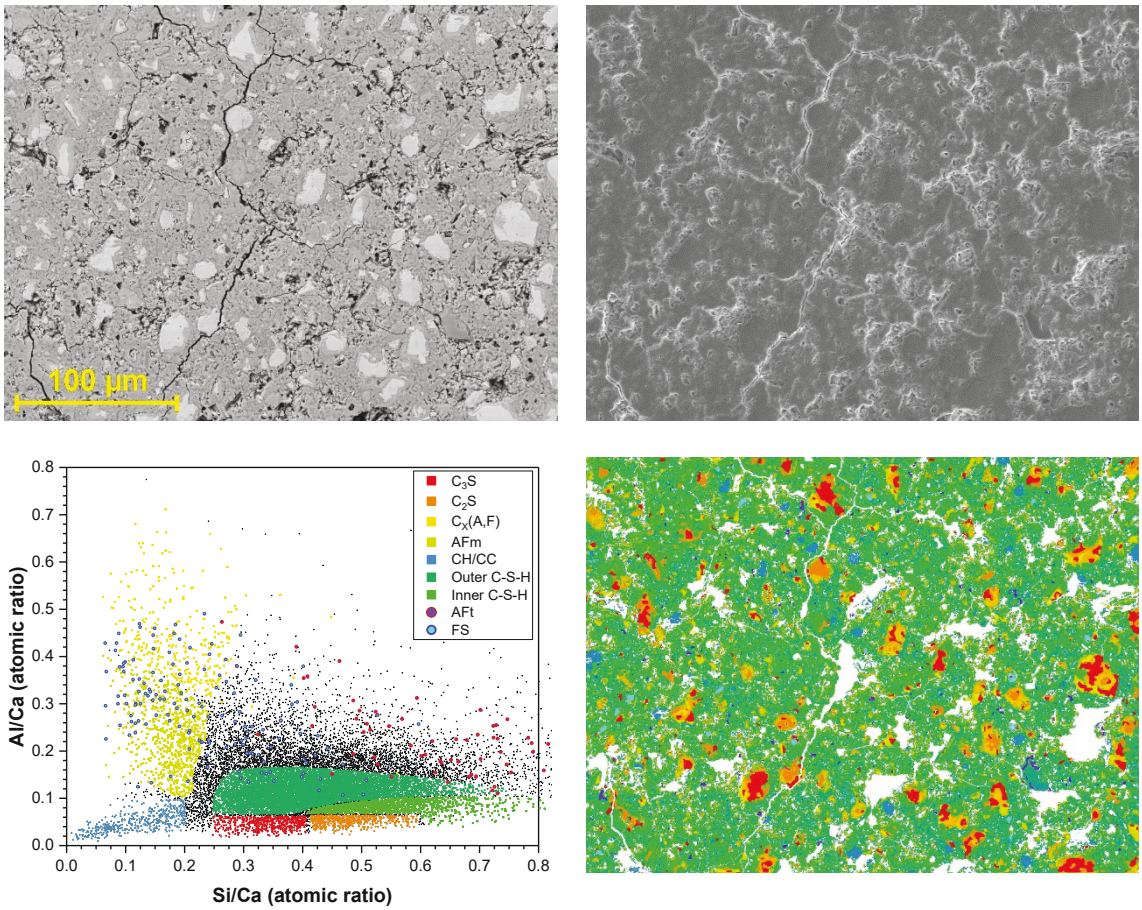

Figure C.12 Image and data treatment results for S28d_2

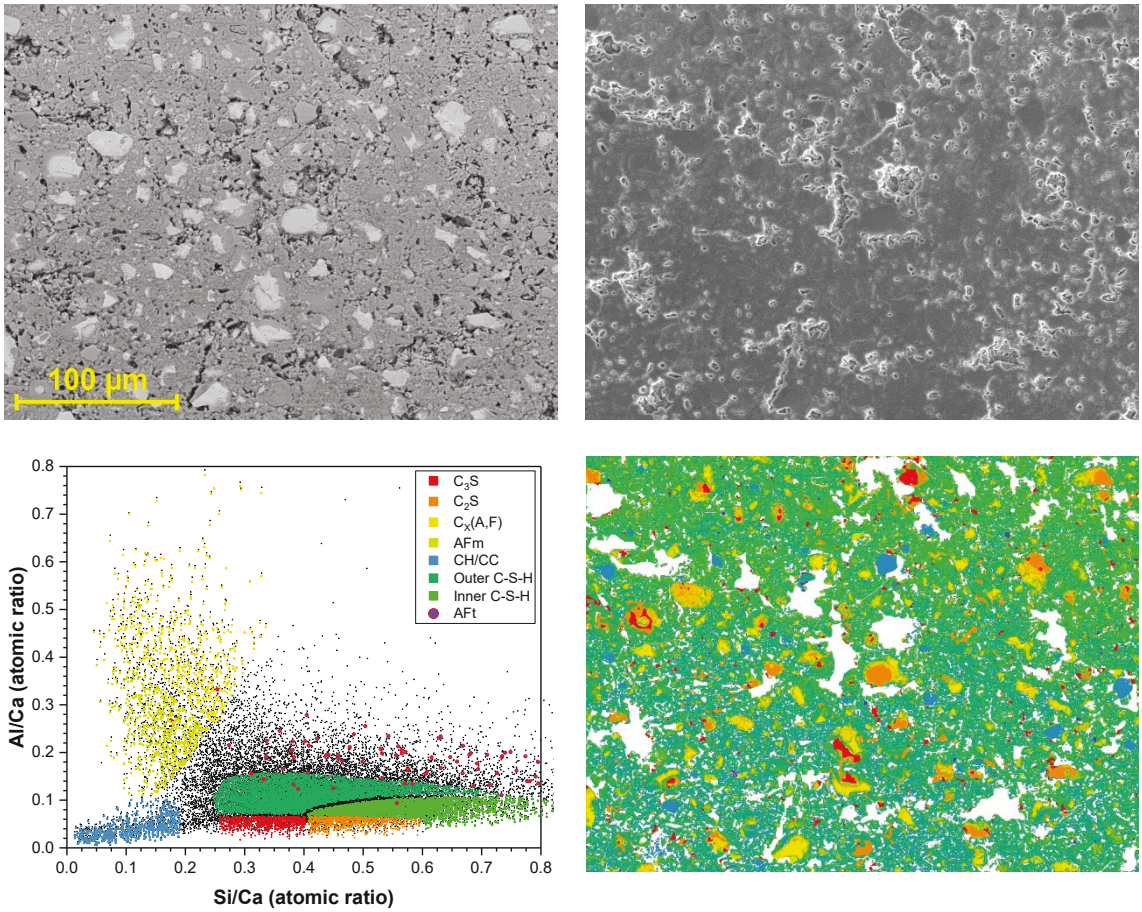

Figure C.13 Image and data treatment results for D63d_1

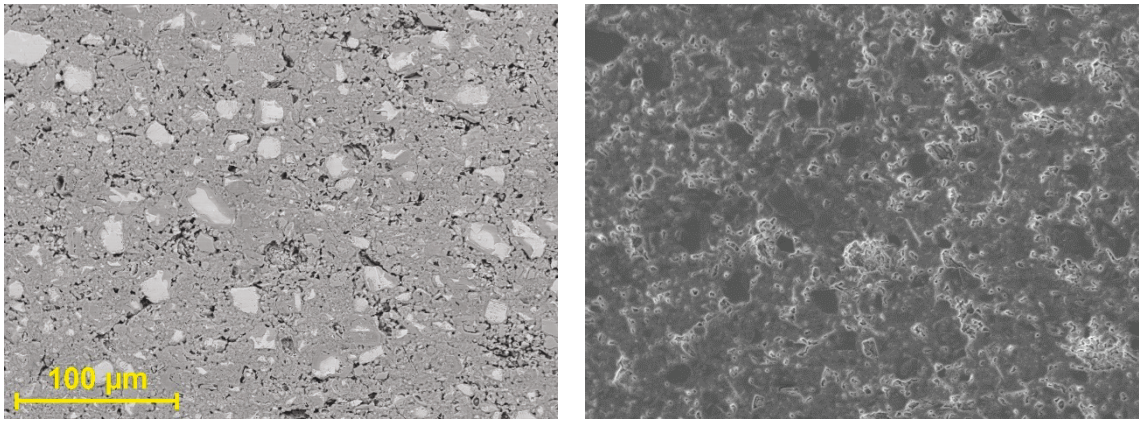

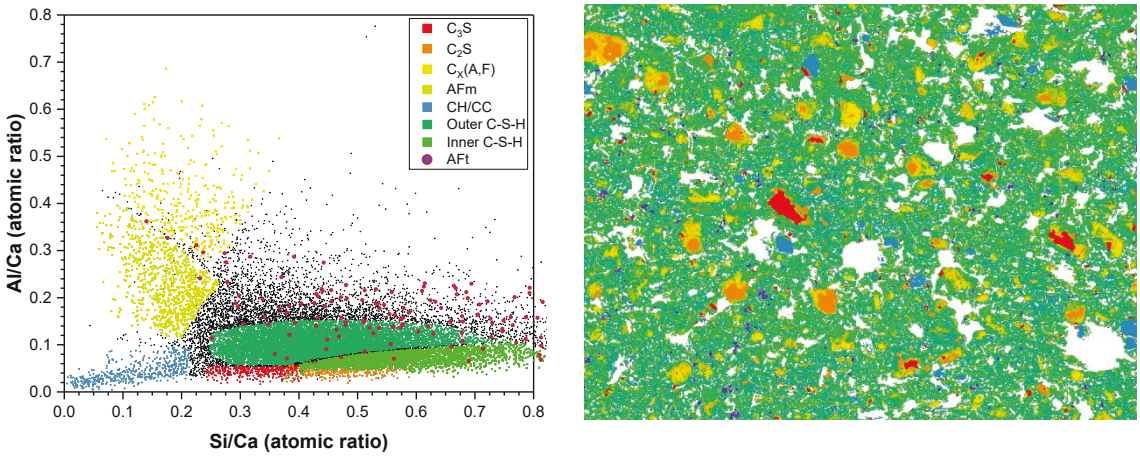

Figure C.14 Image and data treatment results for D63d_2

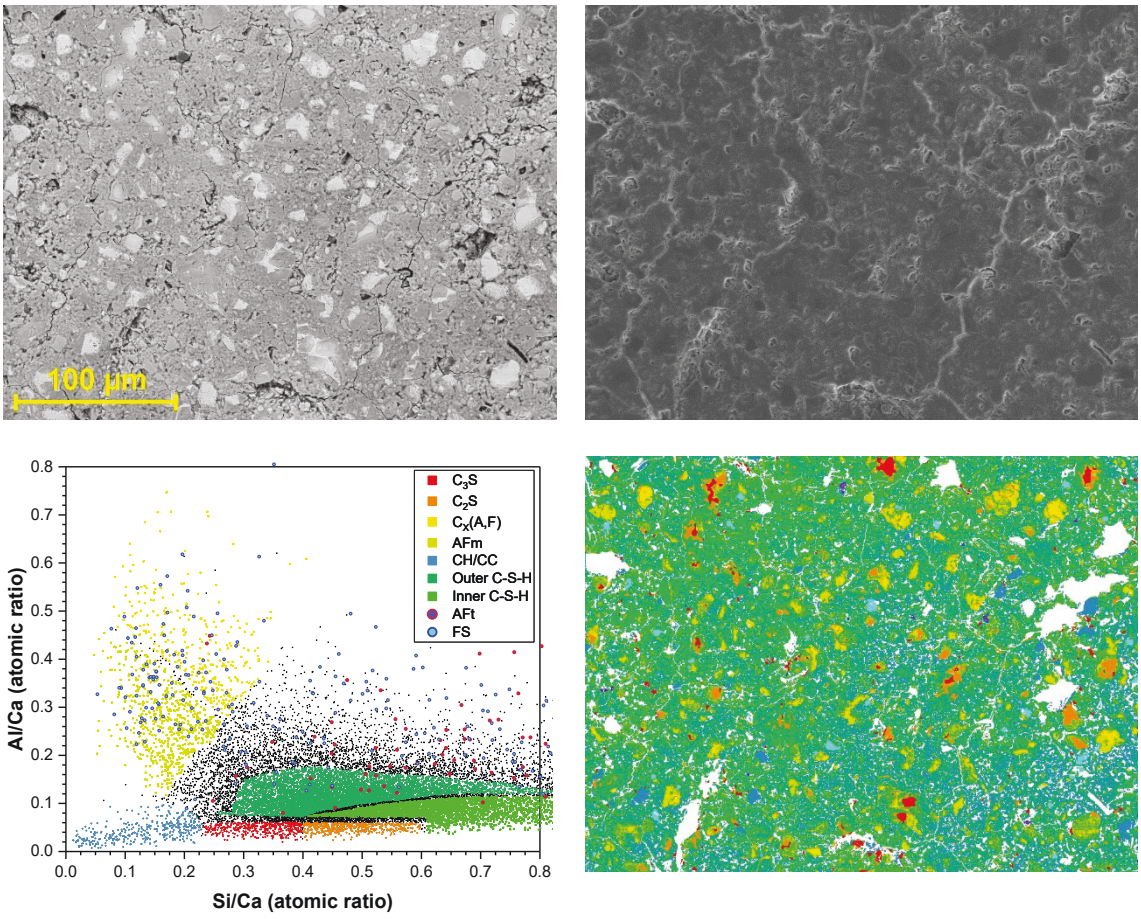

Figure C.15 Image and data treatment results for S63d_2

REFERENCES

Abrams, D.A. 1924, *Tests of impure waters for mixing concrete*, Structural Materials Research Laboratory.

Achanta, R., Shaji, A., Smith, K., Lucchi, A., Fua, P. & Süsstrunk, S. 2012, 'SLIC superpixels compared to state-of-the-art superpixel methods', *IEEE transactions on pattern analysis and machine intelligence*, vol. 34, no. 11, pp. 2274-82.

Ahmed, A., Guo, S., Zhang, Z., Shi, C. & Zhu, D. 2020, 'A review on durability of fiber reinforced polymer (FRP) bars reinforced seawater sea sand concrete', *Construction and Building Materials*, vol. 256, p. 119484.

Akinkurolere, O., Jiang, C. & Shobola, O. 2007, 'The influence of salt water on the compressive strength of concrete', *Journal of Engineering and Applied Sciences*, vol. 2, no. 2, pp. 412-5.

AS 3972 2010, *General purpose and blended cements*, Australia Standards, Australia.

ASTM 2013, *ASTM D1141-98: Standard Practice for the Preparation of Substitute Ocean Water*, ASTM International, West Conshohocken, PA.

Autelitano, F., Rinaldi, M. & Giuliani, F. 2019, 'Winter highway maintenance strategies: Are all the sodium chloride salts the same?', *Construction and Building Materials*, vol. 226, pp. 945-52.

Bachtiar, E., Tjaronge, M., Djamaluddin, R. & Sampebulu, V. 2015a, 'Compressive Strength and Slump Flow of Self Compacting Concrete Uses Fresh Water and Sea Water', *ARPN Journal of Engineering and Applied Science*, vol. 10, no. 6, pp. 2373-7.

Bachtiar, E., Tjaronge, M.W., Djamaluddin, R. & Sampebulu, V. 2015b, 'Compressive strength and slump flow of self compacting concrete uses fresh water and sea water', *ARPN Journal of Engineering and Applied Sciences*, vol. 10, pp. 2373-7.

Balonis, M. & Glasser, F.P. 2009, 'The density of cement phases', *Cement and Concrete Research*, vol. 39, no. 9, pp. 733-9.

Balonis, M., Lothenbach, B., Le Saout, G. & Glasser, F.P. 2010, 'Impact of chloride on the mineralogy of hydrated Portland cement systems', *Cement and Concrete Research*, vol. 40, no. 7, pp. 1009-22.

Barberon, F., Baroghel-Bouny, V., Zanni, H., Bresson, B., Malosse, L. & Gan, Z. 2005, 'Interactions between chloride and cement-paste materials', *Magnetic resonance imaging*, vol. 23, no. 2, pp. 267-72.

Beaudoin, J.J., Ramachandran, V.S. & Feldman, R.F. 1990, 'Interaction of chloride and C S H', *Cement and Concrete Research*, vol. 20, no. 6, pp. 875-83.

Birnin-Yauri, U. & Glasser, F. 1998a, 'Friedel's salt, Ca2Al (OH) 6 (Cl, OH)· 2H2O: its solid solutions and their role in chloride binding', *Cement and Concrete Research*, vol. 28, no. 12, pp. 1713-23.

Birnin-Yauri, U. & Glasser, F. 1998b, 'Friedel's salt, $Ca_2Al(OH)_6(Cl, OH)\cdot 2H_2O$: its solid solutions and their role in chloride binding', *Cement and Concrete Research*, vol. 28, no. 12, pp. 1713-23.

Birnin-Yauri, U.A. & Glasser, F.P. 1998c, 'Friedel's salt, Ca2Al(OH)6(Cl,OH)·2H2O: its solid solutions and their role in chloride binding', *Cement and Concrete Research*, vol. 28, no. 12, pp. 1713-23.

Black, L., Breen, C., Yarwood, J., Deng, C.-S., Phipps, J. & Maitland, G. 2006, 'Hydration of tricalcium aluminate (C 3 A) in the presence and absence of

gypsum—studied by Raman spectroscopy and X-ray diffraction', *Journal of Materials Chemistry*, vol. 16, no. 13, pp. 1263-72.

Bogue, R.H. 1955a, 'The chemistry of Portland cement'2nd edn, Reinhold Publishing Corp, New York, p. 790.

Bogue, R.H. 1955b, *The chemistry of Portland cement*, vol. 79, LWW.

Bonavetti, V., Rahhal, V. & Irassar, E. 2001, 'Studies on the carboaluminate formation in limestone filler-blended cements', *Cement and Concrete Research*, vol. 31, no. 6, pp. 853-9.

Brown, P. & Bothe, J. 2004, 'The system CaO-Al2O3-CaCl2-H2O at 23±2 °C and the mechanisms of chloride binding in concrete', *Cement and Concrete Research*, vol. 34, no. 9, pp. 1549-53.

Browne R. D. & Baker A. F. (1979), *The reinforcement of structural concrete in a marine environment, in developments in concrete technology-I (F. D. Lydon (Ed.)*, vol. 1, Applied Science Publishers, Ltd., London

Cai, Y., Xuan, D., Hou, P., Shi, J. & Poon, C.S. 2021, 'Effect of seawater as mixing water on the hydration behaviour of tricalcium aluminate', *Cement and Concrete Research*, vol. 149, p. 106565.

Cao, Y., Guo, L., Chen, B. & Wu, J. 2020, 'Thermodynamic modelling and experimental investigation on chloride binding in cement exposed to chloride and chloride-sulfate solution', *Construction and Building Materials*, vol. 246, p. 118398.

Chalhoub, C., François, R. & Carcasses, M. 2019, 'Determination of chloride threshold initiating corrosion: A new set-up taking the localized aspect of corrosion into account', *Cement and Concrete Research*, vol. 124, p. 105825.

Chambolle, A. 2004, 'An algorithm for total variation minimization and applications', *Journal of Mathematical imaging and vision*, vol. 20, no. 1, pp. 89-97.

Chang, H., Feng, P., Lyu, K. & Liu, J. 2019, 'A novel method for assessing C-S-H chloride adsorption in cement pastes', *Construction and Building Materials*, vol. 225, pp. 324-31.

Cheewaket, T., Jaturapitakkul, C. & Chalee, W. 2010, 'Long term performance of chloride binding capacity in fly ash concrete in a marine environment', *Construction and Building Materials*, vol. 24, no. 8, pp. 1352-7.

Cheng, S., Shui, Z., Sun, T., Huang, Y. & Liu, K. 2018, 'Effects of seawater and supplementary cementitious materials on the durability and microstructure of lightweight aggregate concrete', *Construction and Building Materials*, vol. 190, pp. 1081-90.

Choi, Y.-S., Kim, J.-G. & Lee, K.-M. 2006, 'Corrosion behavior of steel bar embedded in fly ash concrete', *Corrosion Science*, vol. 48, no. 7, pp. 1733-45.

Claisse, P. 2005, 'Transport properties of concrete', *Concrete International*, vol. 27, no. 1, pp. 43-8.

Clark, B. & Brown, P. 1999, 'The formation of calcium sulfoaluminate hydrate compounds: Part I', *Cement and concrete research*, vol. 29, no. 12, pp. 1943-8.

Costoya Fernández, M.M. 2008, *Effect of particle size on the hydration kinetics and microstructural development of tricalcium silicate*, EPFL.

Csizmadia, J., Balázs, G. & Tamás, F.D. 2001, 'Chloride ion binding capacity of aluminoferrites', *Cement and Concrete Research*, vol. 31, no. 4, pp. 577-88.

Cwirzen, A., Sztermen, P. & Habermehl-Cwirzen, K. 2014, 'Effect of Baltic seawater and binder type on frost durability of concrete', *Journal of materials in civil engineering*, vol. 26, no. 2, pp. 283-7.

D-98, A. 2008, 'Standard practice for the preparation of substitute ocean water', *ASTM International*.

Dalziel, J. & Gutteridge, W. 1986a, 'The influence of pulverized-fuel ash upon the hydration characteristics and certain physical properties of a Portland cement paste'Research and Development Division, Slough, p. 28.

Dalziel, J. & Gutteridge, W. 1986b, *The influence of pulverized-fuel ash upon the hydration characteristics and certain physical properties of a Portland cement paste*, Cement and Concrete Association, Slough.

Damidot, D., Birnin-Yauri, U. & Glasser, F. 1994, 'Thermodynamic investigation of the CaO-Al~ 2O~ 3-CaCl~ 2-H~ 2O system at 25 C and the influence of Na~ 2O', *Cemento*, vol. 91, pp. 243-.

Damidot, D. & Glasser, F.P. 1992, 'Thermodynamic investigation of the CaO Al2O3 CaSO4 H2O system at 50°C and 85°C', *Cement and Concrete Research*, vol. 22, no. 6, pp. 1179-91.

De Weerdt, K., Colombo, A., Coppola, L., Justnes, H. & Geiker, M.R. 2015, 'Impact of the associated cation on chloride binding of Portland cement paste', *Cement and Concrete Research*, vol. 68, pp. 196-202.

De Weerdt, K. & Justnes, H. 2015, 'The effect of sea water on the phase assemblage of hydrated cement paste', *Cement and Concrete Composites*, vol. 55, pp. 215-22.

De Weerdt, K., Lothenbach, B. & Geiker, M.R. 2019, 'Comparing chloride ingress from seawater and NaCl solution in Portland cement mortar', *Cement and Concrete Research*, vol. 115, pp. 80-9.

De Weerdt, K., Orsáková, D. & Geiker, M.R. 2014, 'The impact of sulphate and magnesium on chloride binding in Portland cement paste', *Cement and Concrete Research*, vol. 65, pp. 30-40.

Dhir, R.K., El-Mohr, M.A.K. & Dyer, T.D. 1996, 'Chloride binding in GGBS concrete', *Cement and Concrete Research*, vol. 26, no. 12, pp. 1767-73.

Dhondy, T., Remennikov, A. & Shiekh, M.N. 2019, 'Benefits of using sea sand and seawater in concrete: a comprehensive review', *Australian Journal of Structural Engineering*, vol. 20, no. 4, pp. 280-9.

Dong, W., Li, W., Tao, Z. & Wang, K. 2019, 'Piezoresistive properties of cement-based sensors: review and perspective', *Construction and Building Materials*, vol. 203, pp. 146-63.

Doyle, M.W. & Havlick, D.G. 2009, 'Infrastructure and the environment', *Annual Review of Environment and Resources*, vol. 34, pp. 349-73.

Durdziński, P.T., Dunant, C.F., Haha, M.B. & Scrivener, K.L. 2015, 'A new quantification method based on SEM-EDS to assess fly ash composition and study the reaction of its individual components in hydrating cement paste', *Cement and Concrete Research*, vol. 73, pp. 111-22.

Egüez Álava, H., De Belie, N. & De Schutter, G. 2016, 'Proposed mechanism for the formation of oxychloride crystals during sodium chloride application as a deicer salt in carbonated concrete', *Construction and Building Materials*, vol. 109, pp. 188-97.

Eisemann, E. & Durand, F. 2004, 'Flash photography enhancement via intrinsic relighting', *ACM transactions on graphics (TOG)*, vol. 23, no. 3, pp. 673-8.

Ekolu, S.O., Thomas, M.D.A. & Hooton, R.D. 2006, 'Pessimum effect of externally applied chlorides on expansion due to delayed ettringite formation: Proposed mechanism', *Cement and Concrete Research*, vol. 36, no. 4, pp. 688-96.

Elakneswaran, Y., Nawa, T. & Kurumisawa, K. 2009, 'Electrokinetic potential of hydrated cement in relation to adsorption of chlorides', *Cement and Concrete Research*, vol. 39, no. 4, pp. 340-4.

Erdoğdu, Ş., Bremner, T. & Kondratova, I. 2001, 'Accelerated testing of plain and epoxy-coated reinforcement in simulated seawater and chloride solutions', *Cement and Concrete Research*, vol. 31, no. 6, pp. 861-7.

Erniati, Tjaronge, M.W., Djamaluddin, R. & Sampebulu, V. 2015, 'Compressive strength and slump flow of self compacting concrete uses fresh water and sea water'.

Etxeberria, M., Fernandez, J.M. & Limeira, J. 2016, 'Secondary aggregates and seawater employment for sustainable concrete dyke blocks production: Case study', *Construction and Building Materials*, vol. 113, pp. 586-95.

Etxeberria, M., Gonzalez-Corominas, A. & Pardo, P. 2016, 'Influence of seawater and blast furnace cement employment on recycled aggregate concretes' properties', *Construction and Building Materials*, vol. 115, pp. 496-505.

Fang, G. & Zhang, M. 2020, 'The evolution of interfacial transition zone in alkali-activated fly ash-slag concrete', *Cement and Concrete Research*, vol. 129, p. 105963.

Farnam, Y., Dick, S., Wiese, A., Davis, J., Bentz, D. & Weiss, J. 2015, 'The influence of calcium chloride deicing salt on phase changes and damage development in cementitious materials', *Cement and Concrete Composites*, vol. 64, pp. 1-15.

Farnam, Y., Wiese, A., Bentz, D., Davis, J. & Weiss, J. 2015, 'Damage development in cementitious materials exposed to magnesium chloride deicing salt', *Construction and Building Materials*, vol. 93, pp. 384-92.

Farnam, Y., Zhang, B. & Weiss, J. 2017, 'Evaluating the use of supplementary cementitious materials to mitigate damage in cementitious materials exposed to calcium chloride deicing salt', *Cement and Concrete Composites*, vol. 81, pp. 77-86.

Fierens, P. & Verhaegen, J. 1976, 'Hydration of tricalcium silicate in paste—kinetics of calcium ions dissolution in the aqueous phase', *Cement and Concrete Research*, vol. 6, no. 3, pp. 337-42.

Florea, M.V.A. & Brouwers, H.J.H. 2012, 'Chloride binding related to hydration products: Part I: Ordinary Portland Cement', *Cement and Concrete Research*, vol. 42, no. 2, pp. 282-90.

Forgy, E.W. 1965, 'Cluster analysis of multivariate data: efficiency versus interpretability of classifications', *biometrics*, vol. 21, pp. 768-9.

Frias, M., Goñi, S., García, R. & Vigil de La Villa, R. 2013, 'Seawater effect on durability of ternary cements. Synergy of chloride and sulphate ions', *Composites Part B: Engineering*, vol. 46, pp. 173-8.

Friedel, P. 1897, 'Sur un chloro-aluminate de calcium hydraté se maclant par compression', *Bulletin Soc. Franc. Minéral*, vol. 19, pp. 122-36.

Friedmann, H., Amiri, O. & Aït-Mokhtar, A. 2008, 'Physical modeling of the electrical double layer effects on multispecies ions transport in cement-based materials', *Cement and Concrete Research*, vol. 38, no. 12, pp. 1394-400.

Fritzmann, C., Löwenberg, J., Wintgens, T. & Melin, T. 2007, 'State-of-the-art of reverse osmosis desalination', *Desalination*, vol. 216, no. 1-3, pp. 1-76.

Gabrovšek, R., Vuk, T. & Kaučič, V. 2006, 'Evaluation of the hydration of Portland cement containing various carbonates by means of thermal analysis', *Acta Chim. Slov*, vol. 53, pp. 159-65.

Galan, I. & Glasser, F.P. 2015, 'Chloride in cement', *Advances in Cement Research*, vol. 27, no. 2, pp. 63-97.

Galan, I., Perron, L. & Glasser, F.P. 2015, 'Impact of chloride-rich environments on cement paste mineralogy', *Cement and Concrete Research*, vol. 68, pp. 174-83.

Georget, F., Wilson, W. & Scrivener, K.L. 2021, 'edxia: Microstructure characterisation from quantified SEM-EDS hypermaps', *Cement and Concrete Research*, vol. 141, p. 106327.

Ghazy, A. & Bassuoni, M.T. 2017, 'Resistance of concrete to different exposures with chloride-based salts', *Cement and Concrete Research*, vol. 101, pp. 144-58.

Ghorab, H.Y., Hilal, M. & Antar, A. 1990, 'Effect of mixing and curing waters on the behaviour of cement pastes and concrete Part 2: Properties of cement paste and concrete', *Cement and concrete research*, vol. 20, no. 1, pp. 69-72.

Glasser, F.P., Marchand, J. & Samson, E. 2008, 'Durability of concrete—degradation phenomena involving detrimental chemical reactions', *Cement and Concrete Research*, vol. 38, no. 2, pp. 226-46.

Gruber, K.A., Ramlochan, T., Boddy, A., Hooton, R.D. & Thomas, M.D.A. 2001, 'Increasing concrete durability with high-reactivity metakaolin', *Cement and Concrete Composites*, vol. 23, no. 6, pp. 479-84.

Guo, M., Hu, B., Xing, F., Zhou, X., Sun, M., Sui, L. & Zhou, Y. 2020, 'Characterization of the mechanical properties of eco-friendly concrete made with untreated sea sand and seawater based on statistical analysis', *Construction and Building Materials*, vol. 234, p. 117339.

Guo, Q., Chen, L., Zhao, H., Admilson, J. & Zhang, W. 2018, 'The effect of mixing and curing sea water on concrete strength at different ages', *MATEC Web of Conferences*, vol. 142, EDP Sciences, p. 02004.

Haddad, R.A. & Akansu, A.N. 1991, 'A class of fast Gaussian binomial filters for speech and image processing', *IEEE Transactions on Signal Processing*, vol. 39, no. 3, pp. 723-7.

Haha, M.B., Lothenbach, B., Le Saout, G. & Winnefeld, F. 2011, 'Influence of slag chemistry on the hydration of alkali-activated blast-furnace slag—Part I: Effect of MgO', *Cement and Concrete Research*, vol. 41, no. 9, pp. 955-63.

Hajibabaee, A. & Ley, M.T. 2015, 'Impact of Wet and Sealed Curing on Curling in Cement Paste Beams from Drying Shrinkage', *ACI Materials Journal*, vol. 112, no. 1.

Hamad, J., Ha, C., Kennedy, M.D. & Amy, G.L. 2013, 'Application of ceramic membranes for seawater reverse osmosis (SWRO) pre-treatment', *Desalination and Water Treatment*, vol. 51, no. 25-27, pp. 4881-91.

Harrisson, A., Winter, N. & TAYLOR, H.W. 1987, 'X-ray microanalysis of microporous materials', *Journal of materials science letters*, vol. 6, no. 11, pp. 1339-40.

Hirao, H., Yamada, K., Takahashi, H. & Zibara, H. 2005, 'Chloride binding of cement estimated by binding isotherms of hydrates', *Journal of Advanced Concrete Technology*, vol. 3, no. 1, pp. 77-84.

Hong, S.-Y. & Glasser, F. 1999, 'Alkali binding in cement pastes: Part I. The CSH phase', *Cement and Concrete Research*, vol. 29, no. 12, pp. 1893-903.

Hosokawa, Y., Yamada, K., Johannesson, B. & Nilsson, L.-O. 2006, 'Models for chloride ion bindings in hardened cement paste using thermodynamic equilibrium calculations', *2nd International RILEM symposium on advances in concrete through science and engineering*.

Hou, D., Li, T., Han, Q. & Zhang, J. 2018, 'Insight on the sodium and chloride ions adsorption mechanism on the ettringite crystal: Structure, dynamics and interfacial interaction', *Computational Materials Science*, vol. 153, pp. 479-92.

Islam, M.M., Islam, M.S., Al-Amin, M. & Islam, M.M. 2012a, 'Suitability of sea water on curing and compressive strength of structural concrete', *Journal of Civil Engineering (IEB)*, vol. 40, no. 1, pp. 37-45.

Islam, M.M., Islam, M.S., Al-Amin, M. & Islam, M.M. 2012b, 'Suitability of sea water on curing and compressive strength of structural concrete', *J. Civil Eng*, vol. 40, pp. 37-45.

Jain, S. & Pradhan, B. 2020, 'Fresh, mechanical, and corrosion performance of self-compacting concrete in the presence of chloride ions', *Construction and Building Materials*, vol. 247, p. 118517.

Japan Concrete Institute 2015, *JCI Technical Committee Report on the Use of Seawater in Concrete*.

Jiang, J., Zheng, Q., Hou, D., Yan, Y., Chen, H., She, W., Wu, S., Guo, D. & Sun, W. 2018, 'Calcite crystallization in the cement system: morphological diversity, growth mechanism and shape evolution', *Physical Chemistry Chemical Physics*, vol. 20, no. 20, pp. 14174-81.

Jones, C., Ramanathan, S., Suraneni, P. & Hale, W.M. 2020, 'Calcium oxychloride: A critical review of the literature surrounding the formation, deterioration, testing procedures, and recommended mitigation techniques', *Cement and Concrete Composites*, p. 103663.

Jones, E., Oliphant, E. & Peterson, P. 2019, 'SciPy: Open source scientific tools for Python [http://www. scipy. org/]', *Go to reference in article*.

Jones, M.R., Macphee, D.E., Chudek, J.A., Hunter, G., Lannegrand, R., Talero, R. & Scrimgeour, S.N. 2003, 'Studies using 27Al MAS NMR of AFm and AFt phases and the formation of Friedel's salt', *Cement and Concrete Research*, vol. 33, no. 2, pp. 177-82.

Juilland, P., Gallucci, E., Flatt, R. & Scrivener, K. 2010, 'Dissolution theory applied to the induction period in alite hydration', *Cement and Concrete Research*, vol. 40, no. 6, pp. 831-44.

Julio-Betancourt, G.A. 2009, 'Effect of de-icer and anti-icer chemicals on the durability, microstructure, and properties of cement-based materials', University of Toronto.

Justnes, H. 1998, 'A review of chloride binding in cementitious systems', *Nordic Concrete Research-Publications-*, vol. 21, pp. 48-63.

Katano, K., Takeda, N., Ishizeki, Y. & Iriya, K. 2013a, 'Properties and application of concrete made with sea water and un-washed sea sand'.

Katano, K., Takeda, N., Ishizeki, Y. & Iriya, K. 2013b, 'Properties and application of concrete made with sea water and un-washed sea sand', *Proceedings of Third International conference on Sustainable Construction Materials and Technologies*.

Kaushik, S. & Islam, S. 1995, 'Suitability of sea water for mixing structural concrete exposed to a marine environment', *Cement and Concrete Composites*, vol. 17, no. 3, pp. 177-85.

Kawamura, M. & Takeuchi, K. 1996, 'Alkali-silica reaction and pore solution composition in mortars in sea water', *Cement and Concrete Research*, vol. 26, no. 12, pp. 1809-19.

Khatibmasjedi, M. 2018, 'Sustainable concrete using seawater and glass fiber reinforced polymer bars', University of Miami.

Khatibmasjedi, M., Ramanthan, S., Suraneni, P. & Nanni, A. 2019, 'Shrinkage behavior of cementitious mortars mixed with seawater', *Advances in Civil Engineering Materials*, vol. 8, no. 2, pp. 64-78.

Khoury, G., Majorana, C., Pesavento, F. & Schrefler, B. 2002, 'Modelling of heated concrete', *Magazine of concrete research*, vol. 54, no. 2, pp. 77-101.

Kocaba, V., Gallucci, E. & Scrivener, K.L. 2012, 'Methods for determination of degree of reaction of slag in blended cement pastes', *Cement and Concrete Research*, vol. 42, no. 3, pp. 511-25.

Kong, Y. & Hay, J. 2003, 'The enthalpy of fusion and degree of crystallinity of polymers as measured by DSC', *European Polymer Journal*, vol. 39, no. 8, pp. 1721-7.

Krstulović, R. & Dabić, P. 2000, 'A conceptual model of the cement hydration process', *Cement and concrete research*, vol. 30, no. 5, pp. 693-8.

Kulik, D. 2010, 'Gems 2, software', *http://gems.web.psi.ch/*, PSI Villingen, Switzerland.

Kulik, D.A. 2011, 'Improving the structural consistency of CSH solid solution thermodynamic models', *Cement and Concrete Research*, vol. 41, no. 5, pp. 477-95.

Kumar, A., Bishnoi, S. & Scrivener, K.L. 2012, 'Modelling early age hydration kinetics of alite', *Cement and Concrete Research*, vol. 42, no. 7, pp. 903-18.

L'Hôpital, E., Lothenbach, B., Le Saout, G., Kulik, D. & Scrivener, K. 2015, 'Incorporation of aluminium in calcium-silicate-hydrates', *Cement and Concrete Research*, vol. 75, pp. 91-103.

Lambert, P., Page, C.L. & Short, N.R. 1985, 'Pore solution chemistry of the hydrated system tricalcium silicate/sodium chloride/water', *Cement and Concrete Research*, vol. 15, no. 4, pp. 675-80.

Le Saoût, G., Lothenbach, B., Hori, A., Higuchi, T. & Winnefeld, F. 2013, 'Hydration of Portland cement with additions of calcium sulfoaluminates', *Cement and Concrete Research*, vol. 43, pp. 81-94.

Levitus, S., Locarnini, R.A., Boyer, T.P., Mishonov, A.V., Antonov, J.I., Garcia, H.E., Baranova, O.K., Zweng, M.M., Johnson, D.R. & Seidov, D. 2010, 'World ocean atlas 2009'.

Li, H., Farzadnia, N. & Shi, C. 2018, 'The role of seawater in interaction of slag and silica fume with cement in low water-to-binder ratio pastes at the early age of hydration', *Construction and Building Materials*, vol. 185, pp. 508-18.

Li, L.G., Chen, X.Q., Chu, S.H., Ouyang, Y. & Kwan, A.K.H. 2019, 'Seawater cement paste: Effects of seawater and roles of water film thickness and superplasticizer dosage', *Construction and Building Materials*, vol. 229, p. 116862.

Li, P., Gao, X., Wang, K., Tam, V.W. & Li, W. 2020, 'Hydration mechanism and early frost resistance of calcium sulfoaluminate cement concrete', *Construction and Building Materials*, vol. 239, p. 117862.

Li, P., Li, W., Sun, Z., Shen, L. & Sheng, D. 2021, 'Development of sustainable concrete incorporating seawater: A critical review on cement hydration, microstructure and mechanical strength', *Cement and Concrete Composites*, vol. 121, p. 104100.

Li, P., Li, W., Yu, T., Qu, F. & Tam, V.W. 2020a, 'Investigation on early-age hydration, mechanical properties and microstructure of seawater sea sand cement mortar', *Construction and Building Materials*, vol. 249, p. 118776.

Li, P., Li, W., Yu, T., Qu, F. & Tam, V.W.Y. 2020b, 'Investigation on early-age hydration, mechanical properties and microstructure of seawater sea sand cement mortar', *Construction and Building Materials*, vol. 249, p. 118776.

Li, Q., Geng, H., Shui, Z. & Huang, Y. 2015, 'Effect of metakaolin addition and seawater mixing on the properties and hydration of concrete', *Applied Clay Science*, vol. 115, pp. 51-60.

Li, W., Jiang, Z., Lu, M., Long, W., Xing, F. & Liu, J. 2021, 'Effects of Seawater, NaCl, and Na 2 SO 4 Solution Mixing on Hydration Process of Cement Paste', *Journal of Materials in Civil Engineering*, vol. 33, no. 5, p. 04021057.

Li, Y., Zhao, X. & Raman, R.S. 2018, 'Mechanical properties of seawater and sea sand concrete-filled FRP tubes in artificial seawater', *Construction and Building Materials*, vol. 191, pp. 977-93.

Li, Y., Zhao, X., Singh, R.R. & Al-Saadi, S. 2016, 'Experimental study on seawater and sea sand concrete filled GFRP and stainless steel tubular stub columns', *Thin-Walled Structures*, vol. 106, pp. 390-406.

Linderoth, O., Johansson, P. & Wadsö, L. 2020, 'Development of pore structure, moisture sorption and transport properties in fly ash blended cement-based materials', *Construction and Building Materials*, vol. 261, p. 120007.

Loser, R., Lothenbach, B., Leemann, A. & Tuchschmid, M. 2010, 'Chloride resistance of concrete and its binding capacity – Comparison between experimental results and thermodynamic modeling', *Cement and Concrete Composites*, vol. 32, no. 1, pp. 34-42.

Lothenbach, B., Kulik, D.A., Matschei, T., Balonis, M., Baquerizo, L., Dilnesa, B., Miron, G.D. & Myers, R.J. 2019, 'Cemdata18: A chemical thermodynamic database for hydrated Portland cements and alkali-activated materials', *Cement and Concrete Research*, vol. 115, pp. 472-506.

Lothenbach, B., Le Saout, G., Gallucci, E. & Scrivener, K. 2008, 'Influence of limestone on the hydration of Portland cements', *Cement and Concrete Research*, vol. 38, no. 6, pp. 848-60.

Lothenbach, B., Nied, D., L'Hôpital, E., Achiedo, G. & Dauzères, A. 2015, 'Magnesium and calcium silicate hydrates', *Cement and Concrete Research*, vol. 77, pp. 60-8.

Lothenbach, B., Scrivener, K. & Hooton, R. 2011, 'Supplementary cementitious materials', *Cement and concrete research*, vol. 41, no. 12, pp. 1244-56.

Lothenbach, B. & Winnefeld, F. 2006, 'Thermodynamic modelling of the hydration of Portland cement', *Cement and Concrete Research*, vol. 36, no. 2, pp. 209-26.

Luping, T. & Nilsson, L.-O. 1993, 'Chloride binding capacity and binding isotherms of OPC pastes and mortars', *Cement and Concrete Research*, vol. 23, no. 2, pp. 247-53.

Machner, A., Zajac, M., Ben Haha, M., Kjellsen, K.O., Geiker, M.R. & De Weerdt, K. 2018, 'Chloride-binding capacity of hydrotalcite in cement pastes containing dolomite and metakaolin', *Cement and Concrete Research*, vol. 107, pp. 163-81.

Malhotra, V. 1999, 'Making concrete" greener" with fly ash', *Concrete international*, vol. 21, no. 5, pp. 61-6.

Mangat, P. & Molloy, B. 1995, 'Chloride binding in concrete containing PFA, gbs or silica fume under sea water exposure', *Magazine of concrete research*, vol. 47, no. 171, pp. 129-41.

Matschei, T., Lothenbach, B. & Glasser, F. 2007a, 'The AFm phase in Portland cement', *Cement and Concrete Research*, vol. 37, no. 2, pp. 118-30.

Matschei, T., Lothenbach, B. & Glasser, F.P. 2007b, 'The AFm phase in Portland cement', *Cement and Concrete Research*, vol. 37, no. 2, pp. 118-30.

Mehta, K.P. 2001, 'Reducing the environmental impact of concrete', *Concrete international*, vol. 23, no. 10, pp. 61-6.

Mehta, P. 1999, 'Concrete technology for sustainable development - an overview of essential elements', *Concrete Technology for a Sustainable Development in the 21st Century*, vol. 83.

Mehta, P.K. 2002, 'Greening of the concrete industry for sustainable development', *Concrete international*, vol. 24, no. 7, pp. 23-8.

Mehta, P.K. 2009, 'Global concrete industry sustainability', *Concrete international*, vol. 31, no. 2, pp. 45-8.

Mesbah, A., Rapin, J.P., François, M., Cau-dit-Coumes, C., Frizon, F., Leroux, F. & Renaudin, G. 2011, 'Crystal Structures and Phase Transition of Cementitious Bi-Anionic AFm-(Cl−, CO32−) Compounds', *Journal of the American Ceramic Society*, vol. 94, no. 1, pp. 261-8.

Midgley, H.G. & Illston, J.M. 1984, 'The penetration of chlorides into hardened cement pastes', *Cement and Concrete Research*, vol. 14, no. 4, pp. 546-58.

Miller, S.A., Horvath, A. & Monteiro, P.J. 2016, 'Readily implementable techniques can cut annual CO2 emissions from the production of concrete by over 20%', *Environmental Research Letters*, vol. 11, no. 7, p. 074029.

Miller, S.A., Horvath, A. & Monteiro, P.J. 2018, 'Impacts of booming concrete production on water resources worldwide', *Nature Sustainability*, vol. 1, no. 1, pp. 69-76.

Miller, S.A. & Moore, F.C. 2020, 'Climate and health damages from global concrete production', *Nature Climate Change*, vol. 10, no. 5, pp. 439-43.

Mohammed, T.U., Hamada, H. & Yamaji, T. 2004, 'Performance of seawater-mixed concrete in the tidal environment', *Cement and concrete research*, vol. 34, no. 4, pp. 593-601.

Montanari, L., Suraneni, P., Tsui-Chang, M., Khatibmasjedi, M., Ebead, U., Weiss, J. & Nanni, A. 2019, 'Hydration, pore solution, and porosity of cementitious pastes made with seawater', *Journal of Materials in Civil Engineering*, vol. 31, no. 8, p. 04019154.

Monteiro, P.J., Miller, S.A. & Horvath, A. 2017, 'Towards sustainable concrete', *Nature materials*, vol. 16, no. 7, p. 698.

Moore, E., Vand erPlas, J., Laxalde, D., Perktold, J., Cimrman, R., Henriksen, I., Quintero, E., Harris, C., Archibald, A. & Ribeiro, A. 2020, 'SciPy 1.0: fundamental algorithms for scientific computing in Python', *Nature Methods*.

Myers, R.J., L'Hôpital, E., Provis, J.L. & Lothenbach, B. 2015, 'Effect of temperature and aluminium on calcium (alumino) silicate hydrate chemistry under equilibrium conditions', *Cement and Concrete Research*, vol. 68, pp. 83-93.

Neville, A. 2001, 'Seawater in the mixture', *Concrete international*, vol. 23, no. 1, pp. 48-51.

Neville, A.M. 1995, *Properties of concrete*, vol. 4, Longman London.

Newbury, D.E. & Ritchie, N.W. 2015, 'Performing elemental microanalysis with high accuracy and high precision by scanning electron microscopy/silicon drift detector energy-dispersive X-ray spectrometry (SEM/SDD-EDS)', *Journal of materials science*, vol. 50, no. 2, pp. 493-518.

Nied, D., Enemark-Rasmussen, K., L'Hopital, E., Skibsted, J. & Lothenbach, B. 2016, 'Properties of magnesium silicate hydrates (MSH)', *Cement and Concrete Research*, vol. 79, pp. 323-32.

Nilsson, L., Poulsen, E., Sandberg, P., Sørensen, H.E. & Klinghoffer, O. 1996, 'HETEK, Chloride penetration into concrete, State-of-the-Art, Transport processes, corrosion initiation, test methods and prediction models', *Denmark, ISSN/ISBN*, pp. 0909-4288.

Nishida, T., Otsuki, N., Ohara, H., Garba-Say, Z.M. & Nagata, T. 2013, 'Some considerations for applicability of seawater as mixing water in concrete', *Journal of Materials in Civil engineering*, vol. 27, no. 7, p. B4014004.

Nishida, T., Otsuki, N., Ohara, H., Garba-Say, Z.M. & Nagata, T. 2015, 'Some considerations for applicability of seawater as mixing water in concrete', *Journal of Materials in Civil engineering*, vol. 27, no. 7, p. B4014004.

Nixon, P., Page, C., Canham, I. & Bollinghaus, R. 1988, 'Influence of sodium chloride on alkali-silica reaction', *Advances in cement research*, vol. 1, no. 2, pp. 99-106.

Odler, I. & Dörr, H. 1979, 'Early hydration of tricalcium silicate II. The induction period', *Cement and Concrete Research*, vol. 9, no. 3, pp. 277-84.

Oliphant, T.E. 2007, 'Python for scientific computing', *Computing in science & engineering*, vol. 9, no. 3, pp. 10-20.

Otsuki, N. 1985, 'Research on the influence of chloride on corrosion of the embedded steel bars in concrete', *Report of the port and harbour research institute, ministry of transport*, vol. 24, no. 3, pp. 183-5.

Otsuki, N., Furuya, D., Saito, T. & Tadokoro, Y. 2011, 'Possibility of sea water as mixing water in concrete', *Conference on Our World in Concrete & Structures. Tokyo Institute of Technology, Japan*.

Otsuki, N., Nishida, T., Yi, C., Nagata, T. & Ohara, H. 2014, 'Effect of blast furnace slag powder and fly ash on durability of concrete mixed with seawater', *4th Int. Conf. Durab. Concr. Struct.*

Park, S.S., Kwon, S.-J. & Song, H.-W. 2011, 'Analysis technique for restrained shrinkage of concrete containing chlorides', *Materials and structures*, vol. 44, no. 2, pp. 475-86.

Parrot, L. 1984, 'Prediction of cement hydration', *Proceedings of the British Ceramic Society*, vol. 35, pp. 41-53.

Peduzzi, P. 2014, 'Sand, rarer than one thinks. UNEP Global Environmental Alert Service (GEAS)'.

Peterson, K., Julio-Betancourt, G., Sutter, L., Hooton, R.D. & Johnston, D. 2013, 'Observations of chloride ingress and calcium oxychloride formation in laboratory concrete and mortar at 5°C', *Cement and Concrete Research*, vol. 45, pp. 79-90.

Petschnigg, G., Szeliski, R., Agrawala, M., Cohen, M., Hoppe, H. & Toyama, K. 2004, 'Digital photography with flash and no-flash image pairs', *ACM transactions on graphics (TOG)*, vol. 23, no. 3, pp. 664-72.

Plusquellec, G. & Nonat, A. 2016, 'Interactions between calcium silicate hydrate (C-S-H) and calcium chloride, bromide and nitrate', *Cement and Concrete Research*, vol. 90, pp. 89-96.

Powers, T.C. & Brownyard, T.L. 1946, 'Studies of the physical properties of hardened Portland cement paste', *Journal Proceedings*, vol. 43, pp. 101-32.

Qiao, C., Suraneni, P., Chang, M.T. & Weiss, J. 2018, 'Damage in cement pastes exposed to MgCl 2 solutions', *Materials and Structures*, vol. 51, no. 3, p. 74.

Qiao, C., Suraneni, P., Nathalene Wei Ying, T., Choudhary, A. & Weiss, J. 2019, 'Chloride binding of cement pastes with fly ash exposed to CaCl2 solutions at 5 and 23 °C', *Cement and Concrete Composites*, vol. 97, pp. 43-53.

Qiao, C., Suraneni, P. & Weiss, J. 2018a, 'Damage in cement pastes exposed to NaCl solutions', *Construction and Building Materials*, vol. 171, pp. 120-7.

Qiao, C., Suraneni, P. & Weiss, J. 2018b, 'Flexural strength reduction of cement pastes exposed to CaCl2 solutions', *Cement and Concrete Composites*, vol. 86, pp. 297-305.

Radlinska, A., Rajabipour, F., Bucher, B., Henkensiefken, R., Sant, G. & Weiss, J. 2008, 'Shrinkage mitigation strategies in cementitious systems: A closer look at differences in sealed and unsealed behavior', *Transportation Research Record*, vol. 2070, no. 1, pp. 59-67.

Rasheeduzzafar, Ehtesham Hussain, S. & Al-Saadoun, S.S. 1991, 'Effect of cement composition on chloride binding and corrosion of reinforcing steel in concrete', *Cement and Concrete Research*, vol. 21, no. 5, pp. 777-94.

Richardson, I. & Groves, G. 1993, 'The incorporation of minor and trace elements into calcium silicate hydrate (C S H) gel in hardened cement pastes', *Cement and Concrete Research*, vol. 23, no. 1, pp. 131-8.

Richardson, I.G. 2008, 'The calcium silicate hydrates', *Cement and concrete research*, vol. 38, no. 2, pp. 137-58.

Roosz, C., Grangeon, S., Blanc, P., Montouillout, V., Lothenbach, B., Henocq, P., Giffaut, E., Vieillard, P. & Gaboreau, S. 2015, 'Crystal structure of magnesium silicate hydrates (MSH): The relation with 2: 1 Mg–Si phyllosilicates', *Cement and Concrete Research*, vol. 73, pp. 228-37.

Rosenberg, A.M. 1964, 'Study of the mechanism through which calcium chloride accelerates the set of portland cement', *Journal Proceedings*, vol. 61, pp. 1261-70.

Rossen, J. & Scrivener, K. 2017, 'Optimization of SEM-EDS to determine the C–A–S–H composition in matured cement paste samples', *Materials Characterization*, vol. 123, pp. 294-306.

Scrivener, K., Snellings, R. & Lothenbach, B. 2016, *A practical guide to microstructural analysis of cementitious materials*, vol. 540, Crc Press Boca Raton, FL, USA:.

Scrivener, K.L. 2004, 'Backscattered electron imaging of cementitious microstructures: understanding and quantification', *Cement and concrete Composites*, vol. 26, no. 8, pp. 935-45.

Scrivener, K.L., Juilland, P. & Monteiro, P.J. 2015, 'Advances in understanding hydration of Portland cement', *Cement and Concrete Research*, vol. 78, pp. 38-56.

Scrivener, K.L., Patel, H., Pratt, P. & Parrott, L. 1986, 'Analysis of phases in cement paste using backscattered electron images, methanol adsorption and thermogravimetric analysis', *MRS Online Proceedings Library (OPL)*, vol. 85.

Sena-Cruz, J., Pereira, E., Freitas, N., Pereira, E. & Soares, S.R.R. 2018, 'Bond behaviour between GFRP rods and concrete produced with seawater: an experimental research', *9th International Conference on Fibre-Reinforced Polymer (FRP) Composites in Civil Engineering (CICE2018)*, pp. 1-8.

Shi, X., Xie, N., Fortune, K. & Gong, J. 2012, 'Durability of steel reinforced concrete in chloride environments: An overview', *Construction and Building Materials*, vol. 30, pp. 125-38.

Shi, X., Yang, Z., Liu, Y. & Cross, D. 2011, 'Strength and corrosion properties of Portland cement mortar and concrete with mineral admixtures', *Construction and Building Materials*, vol. 25, no. 8, pp. 3245-56.

Shi, Z., Geiker, M.R., De Weerdt, K., Østnor, T.A., Lothenbach, B., Winnefeld, F. & Skibsted, J. 2017, 'Role of calcium on chloride binding in hydrated Portland cement–metakaolin–limestone blends', *Cement and Concrete Research*, vol. 95, pp. 205-16.

Shi, Z., Geiker, M.R., Lothenbach, B., De Weerdt, K., Garzón, S.F., Enemark-Rasmussen, K. & Skibsted, J. 2017, 'Friedel's salt profiles from thermogravimetric analysis and thermodynamic modelling of Portland cement-based mortars exposed to sodium chloride solution', *Cement and Concrete Composites*, vol. 78, pp. 73-83.

Shi, Z., Shui, Z., Li, Q. & Geng, H. 2015, 'Combined effect of metakaolin and sea water on performance and microstructures of concrete', *Construction and Building Materials*, vol. 74, pp. 57-64.

Sierra, R. 1975, 'Contribution to the kinetic study of the hydration of tricalcium silicate', *BULL LIAISON LAB PONTS CHAUSS*, no. 77.

Sikora, P., Cendrowski, K., Abd Elrahman, M., Chung, S.-Y., Mijowska, E. & Stephan, D. 2019, 'The effects of seawater on the hydration, microstructure and strength development of Portland cement pastes incorporating colloidal silica', *Applied Nanoscience*, pp. 1-12.

Sikora, P., Cendrowski, K., Elrahman, M.A., Chung, S.-Y., Mijowska, E. & Stephan, D. 2019, 'The effects of seawater on the hydration, microstructure and strength development of Portland cement pastes incorporating colloidal silica', *Applied Nanoscience*, pp. 1-12.

Skibsted, J. & Snellings, R. 2019, 'Reactivity of supplementary cementitious materials (SCMs) in cement blends', *Cement and Concrete Research*, vol. 124, p. 105799.

Smolczyk, H.G. 1968, 'Chemical Reactions of strong Chloride-Solution with Concrete', *Proceedings of the 5^< th> International Congress on the Chemistry of Cement, 1968*, pp. 274-80.

Soares, S., Freitas, N., Pereira, E., Nepomuceno, E., Pereira, E. & Sena-Cruz, J. 2020, 'Assessment of GFRP bond behaviour for the design of sustainable reinforced seawater concrete structures', *Construction and Building Materials*, vol. 231, p. 117277.

Soin, A.V., Catalan, L.J. & Kinrade, S.D. 2013, 'A combined QXRD/TG method to quantify the phase composition of hydrated Portland cements', *Cement and concrete research*, vol. 48, pp. 17-24.

Spragg, R., Jones, S., Bu, Y., Lu, Y., Bentz, D., Snyder, K. & Weiss, J. 2017, 'Leaching of conductive species: Implications to measurements of electrical resistivity', *Cement and Concrete Composites*, vol. 79, pp. 94-105.

Stark, J. & Bollmann, K. 2000, 'Delayed ettringite formation in concrete', *NORDIC CONCRETE RESEARCH-PUBLICATIONS-*, vol. 23, pp. 4-28.

Sugiyama, D. 2008, 'Chemical alteration of calcium silicate hydrate (C–S–H) in sodium chloride solution', *Cement and Concrete Research*, vol. 38, no. 11, pp. 1270-5.

Sumranwanich, T. & Tangtermsirikul, S. 2004, 'A model for predicting time-dependent chloride binding capacity of cement-fly ash cementitious system', *Materials and Structures*, vol. 37, no. 6, p. 387.

Suraneni, P., Azad, V.J., Isgor, B.O. & Weiss, W.J. 2016, 'Calcium oxychloride formation in pastes containing supplementary cementitious materials: Thoughts on the role of cement and supplementary cementitious materials reactivity', *RILEM Technical Letters*, vol. 1, pp. 24-30.

Suryavanshi, A.K., Scantlebury, J.D. & Lyon, S.B. 1995, 'The binding of chloride ions by sulphate resistant portland cement', *Cement and Concrete Research*, vol. 25, no. 3, pp. 581-92.

Suryavanshi, A.K., Scantlebury, J.D. & Lyon, S.B. 1996, 'Mechanism of Friedel's salt formation in cements rich in tri-calcium aluminate', *Cement and Concrete Research*, vol. 26, no. 5, pp. 717-27.

Sutherland, W.J., Barnard, P., Broad, S., Clout, M., Connor, B., Côté, I.M., Dicks, L.V., Doran, H., Entwistle, A.C. & Fleishman, E. 2017, 'A 2017 horizon scan of emerging issues for global conservation and biological diversity', *Trends in Ecology & Evolution*, vol. 32, no. 1, pp. 31-40.

Sutter, L., Peterson, K., Touton, S., Van Dam, T. & Johnston, D. 2006, 'Petrographic evidence of calcium oxychloride formation in mortars exposed to magnesium chloride solution', *Cement and Concrete Research*, vol. 36, no. 8, pp. 1533-41.

Sutter, L., Van Dam, T., Peterson, K.R. & Johnston, D.P. 2006, 'Long-term effects of magnesium chloride and other concentrated salt solutions on pavement and structural Portland cement concrete', *Transportation research record*, vol. 1979, no. 1, pp. 60-8.

Swaddiwudhipong, S., Chen, D. & Zhang, M.-H. 2002, 'Simulation of the exothermic hydration process of Portland cement', *Advances in cement research*, vol. 14, no. 2, pp. 61-9.

Tamas, F.D. 1966, 'Acceleration and retardation of Portland cement hydration by additives', *Highway Research Board Special Report*, no. 90.

Taylor, H.F. 1987, 'A method for predicting alkazi ion concentrations in cement pore solutions', *Advances in Cement Research*, vol. 1, no. 1, pp. 5-17.

Taylor, H.F. 1997, *Cement chemistry*, vol. 2, Thomas Telford London.

Taylor, H.F.W. 1992, *Cement Chemistry*, Academic Press.

Theissing, E. 1980, 'The Combining of Sodium Chloride and Calcium Chloride by the Hardened Portland Cement Compounds C_3S, C_2S, C_3A and C_4AF', *Proceedings of the 7th International Congress on the Chemistry of Cement, 1980*, pp. 823-8.

Thomas, M.D.A. & Bamforth, P.B. 1999, 'Modelling chloride diffusion in concrete: Effect of fly ash and slag', *Cement and Concrete Research*, vol. 29, no. 4, pp. 487-95.

Thomas, M.D.A., Hooton, R.D., Scott, A. & Zibara, H. 2012, 'The effect of supplementary cementitious materials on chloride binding in hardened cement paste', *Cement and Concrete Research*, vol. 42, no. 1, pp. 1-7.

Ting, M.Z.Y., Wong, K.S., Rahman, M.E. & Selowara Joo, M. 2020, 'Mechanical and durability performance of marine sand and seawater concrete incorporating silicomanganese slag as coarse aggregate', *Construction and Building Materials*, vol. 254, p. 119195.

Toby, B.H. 2006, 'R factors in Rietveld analysis: How good is good enough?', *Powder diffraction*, vol. 21, no. 1, pp. 67-70.

Tomasi, C. & Manduchi, R. 1998, 'Bilateral filtering for gray and color images', *Sixth international conference on computer vision (IEEE Cat. No. 98CH36271)*, IEEE, pp. 839-46.

Torres, A., Brandt, J., Lear, K. & Liu, J. 2017, 'A looming tragedy of the sand commons', *Science*, vol. 357, no. 6355, pp. 970-1.

Tritthart, J. 1989, 'Chloride binding in cement II. The influence of the hydroxide concentration in the pore solution of hardened cement paste on chloride binding', *Cement and Concrete Research*, vol. 19, no. 5, pp. 683-91.

Truc, N.N. & Van Vu, N. 2018, 'Partial replacement of natural sand by granulated blast furnace slag (GBFS) in fine aggregate for concrete: practical application in Vietnam', *International Multidisciplinary Scientific GeoConference: SGEM: Surveying Geology & mining Ecology Management*, vol. 18, pp. 523-30.

Vafaei, D., Ma, X., Hassanli, R., Duan, J. & Zhuge, Y. 2022, 'Microstructural behaviour and shrinkage properties of high-strength fiber-reinforced seawater sea-sand concrete', *Construction and Building Materials*, vol. 320, p. 126222.

van der Walt, S., Schönberger, J., Nunez-Iglesias, J., Boulogne, F., Warner, J., Yager, N., Gouillart, E. & Yu, T., 't contributors (2014). scikit-image: Image processing in python', PeerJ.

Wang, J., Liu, E. & Li, L. 2018, 'Multiscale investigations on hydration mechanisms in seawater OPC paste', *Construction and Building Materials*, vol. 191, pp. 891-903.

Wang, J., Xie, J., Wang, Y., Liu, Y. & Ding, Y. 2020, 'Rheological properties, compressive strength, hydration products and microstructure of seawater-mixed cement pastes', *Cement and Concrete Composites*, vol. 114, p. 103770.

Wang, X., Sadati, S., Taylor, P., Li, C., Wang, X. & Sha, A. 2019, 'Material characterization to assess effectiveness of surface treatment to prevent joint deterioration from oxychloride formation mechanism', *Cement and Concrete Composites*, vol. 104, p. 103394.

Wegian, F.M. 2010, 'Effect of seawater for mixing and curing on structural concrete', *The IES Journal Part A: Civil & Structural Engineering*, vol. 3, no. 4, pp. 235-43.

Wong, H., Head, M. & Buenfeld, N. 2006, 'Pore segmentation of cement-based materials from backscattered electron images', *Cement and concrete research*, vol. 36, no. 6, pp. 1083-90.

Xiao, J., Qiang, C., Nanni, A. & Zhang, K. 2017, 'Use of sea-sand and seawater in concrete construction: Current status and future opportunities', *Construction and Building Materials*, vol. 155, pp. 1101-11.

Yeginobali, A. 1984, 'Sulfate resistance of mortars mixed with sea waters', *Proc., 3rd International Conference on Durability of Building Materials and Components*, pp. 55-65.

Yogarajah, E., Nawa, T. & Kurumisawa, K. 2018, 'Influence of Surface Electrical Properties of C–S–H on Chloride Binding in Slag-Blended Cementitious Materials', *J. Mater. Civ. Eng*, vol. 30, p. 04018064.

Yoon, S., Ha, J., Chae, S.R., Kilcoyne, D.A., Jun, Y., Oh, J.E. & Monteiro, P.J. 2016, 'Phase changes of monosulfoaluminate in NaCl aqueous solution', *Materials*, vol. 9, no. 5, p. 401.

Yoon, S., Ha, J., Chae, S.R., Kilcoyne, D.A. & Monteiro, P.J.M. 2014, 'X-ray spectromicroscopic study of interactions between NaCl and calcium silicate hydrates', *Magazine of Concrete Research*, vol. 66, no. 3, pp. 141-9.

Younis, A., Ebead, U. & Judd, S. 2018, 'Life cycle cost analysis of structural concrete using seawater, recycled concrete aggregate, and GFRP reinforcement', *Construction and Building Materials*, vol. 175, pp. 152-60.

Younis, A., Ebead, U., Suraneni, P. & Nanni, A. 2018, 'Fresh and hardened properties of seawater-mixed concrete', *Construction and Building Materials*, vol. 190, pp. 276-86.

Yu, C., Wu, Q. & Yang, J. 2017, 'Effect of seawater for mixing on properties of potassium magnesium phosphate cement paste', *Construction and Building Materials*, vol. 155, pp. 217-27.

Yuan, Q., Shi, C., De Schutter, G., Audenaert, K. & Deng, D. 2009, 'Chloride binding of cement-based materials subjected to external chloride environment – A review', *Construction and Building Materials*, vol. 23, no. 1, pp. 1-13.

Zhou, Y., Hou, D., Jiang, J. & Wang, P. 2016, 'Chloride ions transport and adsorption in the nano-pores of silicate calcium hydrate: Experimental and molecular dynamics studies', *Construction and Building Materials*, vol. 126, pp. 991-1001.

Zibara, H. 2001, 'Binding of external chlorides by cement pastes', National Library of Canada= Bibliothèque nationale du Canada.